Theory and simulation of solubility and partitioning in polymers: Application of SAFT-γ Mie and molecular dynamics simulations

TASCHE, JOS

Theory and simulation of solubility and partitioning in polymers: Application of SAFT-γ Mie and molecular dynamics simulations

Jos Tasche

A thesis submitted for the degree of
Doctor of Philosophy

Durham University
Chemistry Department
United Kingdom
March 2018

Contents

Abstract

The solubility and compatibility of polymer mixtures is one of the crucial limitations in the development of a large variety of plastic products such as adhesives. Changes in solubility can change the mechanical, optical and olfactory properties significantly. In this work, theory, simulation and experiment were used to study the solubility and partitioning in polymer systems. The recently published SAFT-γ Mie equation of state was implemented into a stand-alone program together with all algorithms for parametrising new models and predicting phase equilibria. An analysis of the transferability of low-molecular weight Mie potential parameters for predicting the miscibility of polymer mixtures and partitioning of oligomers in polymer systems revealed the need for new models optimised for polymers. A systematic overview and analysis of available and typical experimental polymer data concluded that pure-component polymer-melt densities and cloud-point temperatures (liquid–liquid equilibria) are the best and most practical choice for parametrising new SAFT-γ Mie models. New polymer models were developed for a range of pure polymers, several binary mixtures and one ternary polymer mixture. All models showed very good agreement with the experimental data included in the model development. Good agreement was found for predicted properties and conditions not included in the parametrising process. Coarse-grained (CG) force fields were developed with the help of the SAFT-γ Mie equation of state. Excellent agreement was found for the direct translation of Mie potentials to CG force fields for modelling properties of low-molecular weight compounds and densities of polymer melts. Coarse-grained models for molecular dynamics (MD) simulations of polymer phase equilibria are more challenging to develop due to greater computa-

tional resource requirements and less perfect agreement between SAFT-γ Mie and MD force fields. The challenges were demonstrated and discussed for a polystyrene solution and a binary mixture of polystyrene and polyisoprene. The synergistic power of SAFT-γ Mie and MD simulations was used for developing coarse-grained models for describing the surface of a oligomer/polymer blend. Pure-component parameters were optimised within SAFT-γ Mie. In MD simulations, the SAFT-γ Mie CG model reproduced experimental partial-density surface profiles as a function of blend composition without the need to rescale length scales. Oligomer surface enrichment, wetting transition and wetting layers were correctly predicted with a single model.

Declaration

The material contained within this thesis has not previously been submitted for a degree at Durham University or any other university. The research within this thesis has been conducted by the author unless indicated otherwise.

Jos Tasche, 2018

Acknowledgements

I would like to thank my supervisor Mark R Wilson for his support, scientific guidance, and the fun working environment he has provided.

I would like to thank Marc Hamm for all the fruitful discussions, support in developing HammR and providing experimental data for the ternary polymer mixture.

I would like to thank Torsten Lindner and Gabriela Schäfer and Russell DeVane for all the great discussions, Richard and Elise and Salvatore for the successful collaborations, Todd Mansfield for providing DSC and GPC data for the polymer mixtures, Doug for measuring the heat capacities, and Stephen for helping with the rheometer viscosity measurements.

I would like to thank Vasilis Papaioannou and Costas Pantelides for providing the gSAFT software, and George Jackson for allowing me to use the HELD algorithm.

I am grateful for the computer facilities provided by the Durham University High Performance Computing service and all the quick and competent support from Henk. Also thank you to Martin for solving so many technical problems.

Thank you to everyone who has made the atmosphere in 200X so enjoyful in the past years. A special thank you to Rom, Valentina, Martin, Sarah, Matteo, Andrew, Daniel, Jim, Tom, Golda and Jon.

Most importantly, a big thank you to my family and Julia.

Publications

J. Tasche, M. Hamm, M. R. Wilson, SAFT-γ Mie Equation of State Software Package for the Development of Coarse-Grained Force Fields, *in preparation*.

J. Tasche, E. F. D. Sabattié, R. L. Thompson, M. R. Wilson, Bulk and Surface of Oligomer/Polymer Systems Modelled with SAFT-γ Mie and Molecular Dynamics Simulations, *in preparation*.

T. D. Potter, J. Tasche, E. L. Barrett, M. Walker and M. R. Wilson, Development of New Coarse-Grained Models for Chromonic Liquid Crystals: Insights from Top-down Approaches, *Liquid Crystals*, 2017, **0**, 1–11, DOI: 10.1080/02678292.2017.1342005.

E. F. D. Sabattié, J. Tasche, M. R. Wilson, M. W. A. Skoda, A. Hughes, T. Lindner and R. L. Thompson, Predicting Oligomer/Polymer Compatibility and the Impact on Nanoscale Segregation in Thin Films, *Soft Matter*, 2017, DOI: 10.1039/C7SM00048K.

Glossary

polymer	chain-like large molecule made of a repeated single or repeated few units
oligomer	short polymer
monomer	chemical unit which is repeated in oligomers and polymers
bead	spherical unit in SAFT models and MD simulation force fields, which can represent a single atom or a group of atoms
tackifier	an oligomer which can improve the tack of rubber-like polymers
plasticiser	an oligomer which can plasticise rubber-like polymers
cloud point	condition (temperature or pressure) at which a polymer solution or mixture becomes cloudy/hazy, indicating the onset of phase separation
CPC	cloud point curve
PVT	pressure/volume/temperature data triplets, effectively density values at a range of temperatures and pressures
VLE	vapour–liquid equilibrium
LLE	liquid–liquid equilibrium

LCST	lower critical solution temperature
UCST	upper critical solution temperature
MD	molecular dynamics (simulations)
CG	coarse graining/coarse grained
DSC	differential scanning calorimetry
EoS	equation of state
TPT1	first-order thermodynamic perturbation theory
SAFT	statistical association fluid theory
SAFT-γ Mie	heteronuclear version of SAFT-VR Mie published in 2014
SAFT-VR Mie	homonuclear version of SAFT published in 2013 using Mie potentials
Mie potential	interaction potential function used in SAFT-VR Mie, in SAFT-γ Mie and in molecular (dynamics) simulations
ϵ_{ij}	energetic parameter of the Mie potential for the interaction between bead i and j
σ_{ij}	size parameter of the Mie potential for the interaction between bead i and j
$\lambda_{\mathrm{r},ij}$	repulsive exponent of the Mie potential for the interaction between bead i and j
$\lambda_{\mathrm{a},ij}$	attractive exponent of the Mie potential for the interaction between bead i and j
ρ	density
η	packing fraction, volume fraction of beads, $\eta \approx 0.74$ corresponds to close-packing of equal spheres

A	Helmholtz free energy
G	Gibbs free energy
T	temperature
V	volume
P	pressure
M_{n}	number-average molecular weight
M_{w}	weight-average molecular weight
PDI	polydispersity index (PDI = $M_{\mathrm{w}}/M_{\mathrm{n}}$)
k_{ij}	correction factor for the energetic Mie potential parameter ϵ for the interaction between bead i and j
k_{B}	Boltzmann constant
R	ideal gas constant
ν	number of beads per group only used in SAFT-γ Mie, not SAFT-VR Mie
S_k	shape factor, only used in SAFT-γ Mie, not SAFT-VR Mie

Chapter 1

Introduction

Industrial equilibrium properties of polymer systems are crucial for the development of products made from a mixture of polymers and oligomers such as tackifiers, plasticisers and other additives to meet specific properties and application requirements. Also, in the process of plastic recycling, the compatibility of different polymers, compatibilisers and solvents is relevant.[1] When polymers are used in the analysis of organic compounds in water systems a piece of plastic can be submerged to passively sample compounds. For the subsequent determination of the concentration of the studied compounds their accurate partition constant between the passive sampler and water is necessary.[2]

The prediction of solubilities and partitioning of molecules between different solvents has been of interest for a long time.[3] Experimental measurements of thermophysical data on liquids and polymers, especially in slowly equilibrating systems, are often expensive and very time consuming. Predicting the compatibility of polymer systems of low viscosity is therefore not only attractive for screening materials, but also due to the fact that computational predictions could potentially be faster than experiments. The prediction of partitioning is not only of scientific but also of industrial interest as the migration of solutes from a host system can change the mechanical, optical and olfactory properties significantly.[4]

Examples of equilibrium properties of polymer systems are the compati-

bility (qualitatively) of different polymers and oligomers, solubility (quantitatively) of one compound in another compound or mixture, and the partition ratio (quantitatively) of one polymer between two polymer phases. A visualisation is presented in Fig. 1.1.

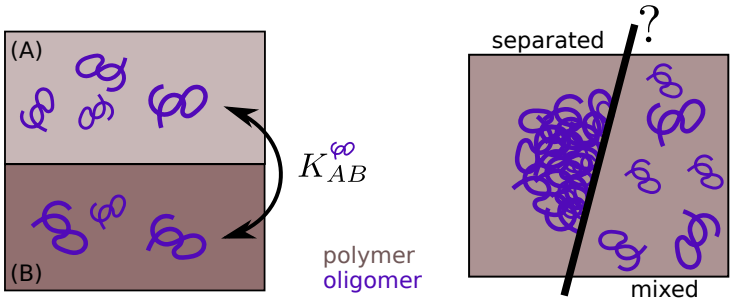

Figure 1.1: Visualisation of two key properties analysed and predicted in this work. (left) The partition coefficient, K_{AB}, is visualised as the concentration ratio of a short polymer (purple curl) of two polymer phases A and B (shaded boxes) in contact, and (right) the compatibility of a short polymer in a single-phase matrix. Polymers can agglomerate and phase separate, or homogeneously mix with the polymer matrix. The terms compatibility, miscibility and solubility are used synonymously in this work to describe how thermodynamically stable a mixture of polymers is.

This chapter introduces the background and terminology needed for the remainder of the dissertation. After an introduction to the thermodynamics of phase equilibria, an overview of approaches to solubility and phase separation, as well as an overview of approaches to coarse graining, are presented. In Chap. 2, the scope and aims of this work are stated. In Chap. 3, a separate introduction to the statistical associating fluid theory (SAFT) with focus on the incarnations SAFT-VR Mie and SAFT-γ Mie and their application to polymer systems is given. In Chap. 4, details on our implementation of the SAFT-VR Mie and SAFT-γ Mie and additional algorithms for calculating phase equilibria are presented. In Chap. 5, first we use published SAFT-γ Mie parameters to predict the miscibility and partition coefficients of polymer mixtures. In a second step new SAFT-γ Mie parameters are developed for a range of pure and multicomponent polymer systems. In Chap. 6, SAFT-γ Mie parameters are applied in molecular dynamics simula-

tions to predict polymer-melt densities, polymer mixture solubilities and the surface of oligomer/polymer films. In Chap. 7, the conclusion of this work and potential future work are described.

1.1 Thermodynamics of phase equilibria

From the partition function Q of a system, which is a description of the accessibility of the states of a system, the Helmholtz free energy A can be determined and consequently other thermodynamic properties obtained

$$A = -Nk_{\mathrm{B}}T \ln Q. \tag{1.1}$$

In thermodynamics it is often convenient to define ideal states and express deviations for real systems. In terms of the Helmholtz energy, the deviation from the ideal state is often referred to as *residual* property

$$A^{\mathrm{real}} = A^{\mathrm{ideal}} + A^{\mathrm{residual}}. \tag{1.2}$$

Once the Helmholtz free energy A of a system is known, its derived properties can be computed by evaluating first and second derivatives. The expressions can be obtained by considering the definition of the Helmholtz free energy

$$\mathrm{d}A = -S\mathrm{d}T - P\mathrm{d}V + \sum_i \mu_i \mathrm{d}N_i. \tag{1.3}$$

Within the canonical ensemble (NVT-ensemble), in which the number of particles N, the temperature T and the volume V are constant, three properties can be obtained by considering the variation of one of the three parameters at a time while keeping the others constant. Those three properties are the pressure P, the chemical potential μ_i and the entropy S

$$-\left(\frac{\partial A}{\partial V}\right)_{N,T} = P \tag{1.4}$$

$$\left(\frac{\partial A}{\partial N_i}\right)_{V,T} = \mu_i \tag{1.5}$$

$$-\left(\frac{\partial A}{\partial T}\right)_{N,V} = S \tag{1.6}$$

A list of more thermodynamic properties expressed in terms of the Helmholtz free energy can, e.g. be found in Refs 5–8 and a selection in Chap. 4.

1.1.1 Definition of ideal

Ideal behaviour of pure compounds is defined in this work as the behaviour of an ideal gas. Ideal gas particles are without particle volume and without interactions (apart form elastic collisions) between them. Alternatively, an ideal system can be defined via the change in internal energy U,

$$\left(\frac{\partial U}{\partial T}\right)_{N,V} = C_{\mathrm{V}}^{\mathrm{ideal}} = \text{const.} \tag{1.7}$$

where $C_{\mathrm{V}}^{\mathrm{ideal}}$ is the heat capacity at constant volume. The change in internal energy is constant with respect to temperature. For a monoatomic particle, the heat capacity is $C_{\mathrm{V}}^{\mathrm{ideal}} = \frac{3}{2}RT$, for a diatomic particle $C_{\mathrm{V}}^{\mathrm{ideal}} = \frac{5}{2}RT$, and the heat capacity increases with more complex particle structures which possess more translational, rotational and vibrational degrees of freedom to store kinetic energy. For polymers, the number of degrees of freedom become almost impossible to determine from first principle, which is why the ideal heat capacity of polymers is typically obtained from correlated empirical data.[9,10]

Ideal behaviour of mixtures is defined as ideal according to Raoult's law. With Raoult's law the pressure is a linear combination of its components. Properties are proportional to the mole fraction of the components, which is a good description for compounds of similar structure. It is worth emphasising that ideal mixtures are always miscible due to the gain in entropy of mixing by increasing the accessible volume for each compound.

Excess vs Residual

Residual properties are defined as non-ideal contributions of a system of one or more compounds, while excess properties describe non-ideal contributions of properties *upon mixing*, which are differences between the pure and mixed states.

$$B^{\mathrm{r}} = B - B^{\mathrm{ideal}} \tag{1.8}$$

$$B^{\mathrm{E}} = B_{\mathrm{mix}} - B^{\mathrm{ideal}}_{\mathrm{mix}} = B^{\mathrm{r}} - \sum_i B^{\mathrm{r}}_i \tag{1.9}$$

where property B for component i is B_i, B^{E} is the excess property, B^{r} is the residual property and B_{mix} the property upon mixing. The excess and mixing properties differ for Helmholtz free energy, Gibbs free energy and entropy as they show non-zero ideal contributions of mixing ($B^{\mathrm{ideal}}_{\mathrm{mix}}$). For many other properties excess and mixing contributions are the same.

1.1.2 Phase equilibrium

The state of equilibrium of a closed system (energy transfer but no mass transfer is possible) can be defined as having the same temperature, the same pressure and the same chemical potential throughout the system. For a system of k phases and m components this corresponds to[8]

$$T^{(1)} = T^{(2)} = T^{(3)} = \cdots = T^{(k)} \tag{1.10}$$

$$p^{(1)} = p^{(2)} = p^{(3)} = \cdots = p^{(k)} \tag{1.11}$$

$$\mu_1^{(1)} = \mu_1^{(2)} = \mu_1^{(3)} = \cdots = \mu_1^{(k)} \tag{1.12}$$

$$\mu_2^{(1)} = \mu_2^{(2)} = \mu_2^{(3)} = \cdots = \mu_2^{(k)} \tag{1.13}$$

$$\mu_3^{(1)} = \mu_3^{(2)} = \mu_3^{(3)} = \cdots = \mu_3^{(k)} \tag{1.14}$$

$$\vdots$$

$$\mu_m^{(1)} = \mu_m^{(2)} = \mu_m^{(3)} = \cdots = \mu_m^{(k)} \tag{1.15}$$

The free energy of mixing A^{mix}_{NVT} in a canonical ensemble for a binary

mixture can be defined as

$$A^{\text{mix}}_{NVT} = A_{NVT} - A^{\text{pure1}}_{N_1V_1T} - A^{\text{pure2}}_{N_2V_2T} \tag{1.16}$$

$$= A_{NVT} - x_1 A^{\text{pure1}}_{NVT} - (1 - x_1) A^{\text{pure2}}_{NVT} \tag{1.17}$$

where $N = N_1 + N_2$, $V = V_1 + V_2$ and $x_1 = \frac{N_1}{N_1+N_2}$.

Mixtures are fully miscible if they show a negative energy of mixing and a positive curvature with respect to the composition

$$A^{\text{mix}}_{NVT} < 0 \tag{1.18}$$

$$\left(\frac{\partial^2 A^{\text{mix}}}{\partial (N_1/N_2)^2}\right)_{NVT} > 0. \tag{1.19}$$

1.2 Approaches to solubility and phase separation

This section gives a short overview of approaches and methods to determine solubilities and phase separation properties. This overview is not meant to be exhaustive, but starts with a few general principles and common properties by which models can be grouped and classified, and is followed by a selection of approaches which are introduced separately. The methods that will be introduced in this section are solubility parameters, the Flory–Huggins theory, the universal quasichemical activity-coefficients method (UNIFAC), COSMO-RS, the Ornstein–Zernike equation approach, molecular dynamics simulations, dissipative particle dynamics (DPD), and equations of state.

Each model or group of models has a different approach to describe non-ideal deviations. It varies from a pure empirical function describing the total deviation, to a molecular-model-based expression using microscopic physical parameters to express each type of interaction separately. Nevertheless, independent of the degree of complexity of the models, each well performing model uses at least a few parameters that have been fitted to experimental data. There is no pure *ab initio* method for determining solubilities and polymer phase separation accurately to date.

A simple way to divide models into two groups is to separate group-contribution (GC) models from non-GC models. GC models offer specific parameter sets for individual chemical functional groups and allow the prediction of properties of molecules by assuming the contribution of functional groups/ building block to the properties are the same for each molecular structure they are part of. Non-GC models need to be parametrised for each system or compound and do not allow the combination of parameters.

For many model groups, both non-GC and GC versions exist. Examples are UNIQUAC[11]/ UNIFAC,[12] SAFT-VR[13,14]/ SAFT-γ,[15,16] Wilson[17]/ ASOG, and COSMO-RS[18]/ COSMO*frag*.[19]

1.2.1 Solubility parameters

Solubility parameters provide a simple way to predict solubilities. One-dimensional (Hildenbrand)[20] and three-dimensional (Hansen)[21] solubility parameters are tabulated for a large range of solvents and polymers, and can be determined both experimentally and by computational methods (e.g., molecular dynamics[22] and Monte Carlo simulations,[23] equations of state[5,24] and COSMO-RS[24,25]). The shorter the distance between the solubility parameters in the one-dimensional (Hildebrand) or three-dimensional (Hansen) space, the more likely it is that the corresponding compounds are miscible. A sphere around the solubility data of a compound, such as a polymer, can be determined in the 3-dimensional space, which includes all solvents that are predicted to dissolve this polymer.

The current database of the Hansen solubility parameters (HSP) comprises experimentally determined results for 1200+ chemicals, more than 10,000 calculated parameters, and data for more than 500 polymers.[26] It is the collected experience of more than 40 years of applying Hansen solubility parameters, and can often be a quick and simple tool for predicting solubilities.

The Hildebrand solubility parameter δ is obtained from the cohesive en-

ergy E_{C} (energy to turn a liquid into a gas)[20]

$$\delta^2 = \frac{E_{\mathrm{C}}}{V}. \tag{1.20}$$

The HSP divides the cohesive energy density into 3 specific contributions

$$\delta^2 = \delta_{\mathrm{D}}^2 + \delta_{\mathrm{P}}^2 + \delta_{\mathrm{H}}^2, \tag{1.21}$$

where δ_{D}, δ_{P} and δ_{H} are the dispersion, polar and hydrogen bonding solubility parameters, respectively. The separation of the cohesive energy density into the three components is usually performed on the basis of molar volume, dipole moment, refractive index and critical temperature.[27]

Solubility parameters describe the non-combinatorial Gibbs free energy of mixing of compounds A and B

$$\Delta G_{\mathrm{non-comb}}^{\mathrm{mix}} = \phi_{\mathrm{A}}\phi_{\mathrm{B}}V_{\mathrm{mix}}(\delta_{\mathrm{A}} - \delta_{\mathrm{B}})^2, \tag{1.22}$$

where ϕ_A and ϕ_B are volume fractions and V_{mix} the volume of the mixture. Solubility parameters, however, do not (at least not fully) account for the entropy of mixing[27] and the free-volume effects (molecular size differences).[27,28] Therefore, the HSP are often used in combination with the Flory–Huggins theory,[27,29] which includes ideal combinatorial contributions (see next section). Further corrections can be applied such as an approach to account for the difference in molecular size.[27] Another computational route to solubility parameters are atomistic molecular dynamics simulations, even for polymers.[30]

Hansen notes that one of the problems with the HSP is their low accuracy caused by obtaining the parameters as differences between large numbers.[27] Although deviations for non-simple compounds are known, the simple empirical expressions are still widely used today. One of the approaches to improve the description is a molecular-shape dependent correction factor recently derived by Hughes *et al.*.[31]

1.2.2 Flory–Huggins theory

The Flory–Huggins (FH) approach for determining the Gibbs free energy of mixing is a simple model designed for polymer systems, and despite its simplicity is still in extensive use today.[27,28,32–36] The Gibbs free energy of mixing of two polymers can be expressed as[36]

$$\frac{\Delta G^{\mathrm{mix}}}{k_{\mathrm{B}}T} = \frac{\phi \ln \phi}{v_1 N_1} + \frac{(1-\phi)\ln(1-\phi)}{v_2 N_2} + \frac{\chi_{12}\phi(1-\phi)}{v_r}, \tag{1.23}$$

where ϕ is the volume fraction of component 1, and N_i and v_i are the number of monomers and volume of a single monomer in component i, respectively. ϕ/v_1N_1 corresponds to the molecular number fraction of component 1. The volume v_r is an (arbitrary) reference volume, which needs to agree with the reference volume for which the binary interaction parameter χ_{12} has been determined.

The first two terms in Eq. (1.23) describe combinatorial/entropic contributions, while the third in principle accounts for enthalpic interactions. As the χ_{12} parameter is often fitted to experimental data, in practice it also accounts for not-considered combinatorial effects and shortcomings of the entropic part. The χ_{12} parameter is a measure of antipathy between compound 1 and 2. The larger χ_{12}, the more favourable are like interactions (1–1; 2–2) compared to unlike interactions (1–2).

The combinatorial part accounts for molecular size differences and, therefore, gives an important improvement over ideal descriptions for polymer systems of different degrees of polymerisation and polymer–solvent systems.

The χ_{12} parameters are usually determined experimentally. A popular method is the application of the random phase approximation (RPA) to neutron scattering profiles from homogeneous polymer mixtures.[36] Also solubility parameters, like the Hansen solubility parameter (HSP), can be used to obtain χ_{12} parameters. FH can be connected to solubility parameters by the following equation

$$\chi_{12} = \phi_1\phi_2 v_r(\delta_1 - \delta_2)^2. \tag{1.24}$$

Equations (1.23) and (1.24) do not (explicitly) account for free-volume differences. Milner *et al.*[35] have shown that the free-volume contribution to χ_{12} is typically 0.3 in units of χ_{12}. Although it is influenced by thermal expansion coefficients, molecular-volume differences, temperature, and other exceptions are known,[36] often 0.34 is added to χ_{12} in Eq. (1.24) as a rule of thumb.[27,36]

1.2.3 UNIFAC

Activity-coefficient approaches to solubility use activity-coefficient parameters as a means to describe the non-ideal behaviour, which is the correction factors to Raoult's law.

The universal quasichemical activity-coefficients **(UNIQUAC)**[11] method and its group-contribution version, the universal quasichemical functional-group activity-coefficients **(UNIFAC)**[12] method, are popular acitivity coefficient methods. In contrast to methods such as the Flory–Huggins approach they are derived from 'local composition fractions'[37] or 'surface fractions'[38] instead of 'volume fraction'. Free energy changes are described by the local composition and how it deviates from a random distribution. Additional methods based on the 'local composition' theory are the Wilson[17] and the Non-Random Two-Liquid (NRTL)[39] model.

The UNIFAC method uses tabulated surface and volume contributions and binary interaction parameters; while the surface and volume contributions are usually derived from the van der Waals radii, the binary interaction parameters are fitted to experimental data.

The activity coefficient of compound i, γ_i, within UNIFAC is defined as a sum of combinatorial and energetic parts, where the first arises due to size and shape differences and the second due to energetic interaction differences[37]

$$\ln \gamma_i = \ln \gamma_i^{\text{comb}} + \ln \gamma_i^{\text{res}}. \tag{1.25}$$

As there are different versions of the UNIFAC method, there is no universal set of parameters. The versions differ, e.g., in their detailed expressions, by how the temperature dependency is implemented, which equilibrium data

was used for the parametrisation, and by its main application. An overview can be found in Ref. 37.

The UNIFAC model, and especially the extended model **UNIFAC-FV**[12] including free-volume (FV) considerations, have been applied to polymer systems with good results, see for example Refs 28,40–42. Its success can at least partially be attributed to the large group-contribution set of functional groups for which parameters are available. The interaction parameters were correlated to the largest available set of experimental thermophysical data: the Dortmund Databank. As an activity-coefficient method, UNIFAC is limited to liquid–liquid mixtures (and liquid–vapour assuming ideal vapour) and can not be used for volumetric properties such as densities without additional tools. Within the framework of UNIFAC the development of additional parameters is not possible by using new experimental data, in case the available parameter set might not perform well enough on the polymer systems of interest.[38]

1.2.4 COSMO-RS

The COnductor-like Screening model for Realistic Solvents (COSMO-RS)[18,43] is a predictive tool, which combines quantum chemical calculations and statistical thermodynamics. Binary interaction parameters are determined from molecular surface charges obtained from a quantum chemical calculation. By using these quantum-chemically-obtained interaction parameters, COSMO-RS is not limited to fields where experimental data is known, but can also be used for systems which were not considered in its development.

To obtain the essential molecular surface charges, the quantum chemical COSMO method[44] is used: An initial solute molecule structure is chosen and its corresponding molecular surface shape determined. The electron density of the molecular structure is calculated in a quantum chemical single-point calculation. The electrostatic potential that arises from the electron density and nuclear positions is mapped on the molecular surface. A solvent with properties of a perfect conductor (infinite permittivity) is assumed to surround the molecule, which screens the surface charges fully, by adapting its

own charges (the conductor-like screening charges) to be the same magnitude as the molecular surface's charges but of opposite sign. In the first iteration process, the conductor-like screening charges are included as additional external charges in the next quantum chemical repetition until self-consistency is achieved. The second iteration process optimises the molecular structure, in which the atom positions are adjusted until the (local) minimum-energy structure is obtained. For each step in the structure optimisation, new adapted self-consistent conductor-like screening charges are calculated.

In summary, the quantum chemical aspect of the method adapts the electron distribution and atom positions towards the lowest energy, while the COSMO aspect follows in mirroring the negative of its surface potential mimicking a surrounding solvent with perfect conductor properties at each iteration.

Important parameters in the COSMO method are the choice of the quantum chemical (QC) method and the choice of surface shape construction.

A characteristic profile, the so-called σ-profile, is generated by plotting the electrostatic surface charges against its size of area of occurrence on the molecule's surface. The beautiful colour-coded molecular surfaces and the analytical σ-profile are interesting results on their own and indicate detailed molecular properties.

COSMO assumes a solvent environment of infinite permittivity as it allows any surface charge to be compensated/screened. A simple correction term was published in 2008[45] to reduce the screened charge as a function of the "experimental" solvent's permittivity.

To account for more than one geometrical conformation—which is important especially for flexible molecules—additional molecular structures and their σ-profiles are included. The calculation of the additional σ-profiles and an additional self-consistent iteration, however, increase the computational effort significantly.

QC calculations can not be performed on whole polymer chain as they are computationally too demanding. Instead, oligomers (trimers, tetramers, pentamers,...) are calculated, then the terminal monomers are cut-off and the remaining pseudo-monomer is repeated to reach the targeted chain length.

The choice of cuts in the original oligomer introduces small charge errors at the cuts. Multiplying the pseudo-monomer also multiplies the error. Especially for polar polymers, this error is significant. COSMOlogic, the company behind COSMO-RS, advises to not to use repetitions of 100 or more, even if cuts are made at rather non-polar bonds.[46] For more information on COSMO-RS the reader is directed to Ref. 44.

Both UNIFAC and COSMO-RS are based on the same expressions for the combinatorial entropy*. The combinatorial parts are determined from molecular volumes and surface areas instead of macroscopic volume fractions.[38] The most important difference between UNIFAC and COSMO-RS is that the binary interactions between segment types in UNIFAC are fitted to experimental data, while COSMO-RS derives them from surface charges obtained in the quantum chemical calculations.

1.2.5 Ornstein–Zernike equation/ integral equation theory

Integral equation theories have been used to describe mesoscopic structural and thermodynamic properties of polymer melts.[47,48] Guenza and coworkers solve the Ornstein–Zernike equation using the hypernetted chain-closure (HNC) and the reference molecular mean spherical approximation (R-MMSA) to develop coarse-grained force fields for polymers. Polymers are modelled at mesoscopic level as colloidal particles interacting with soft potentials. Each polymer chain is described with one or more units, which each are larger than the persistence length of the polymer chain. When one bead is used only, the size is comparable to the radius of gyration of the polymer. An analytical equation of state has been developed based on this approach.[48] Results for the volume dependency of the pressure (compressibility) for one temperature and the intermolecular correlation function between the coarse-grained particles were shown to be comparable to results of united-atom simulations.[48] While it is remarkable how both structural and thermodynamic properties are cap-

*Combinatorial entropy is the mole and volume-fraction-dependent ideal entropy also used in the Flory–Huggis theory, see Sec. 1.2.2.

tured simultaneously with this approach for polymer melts, for mixtures of polymers only structural properties have been predicted.[49,50] Further work seems to be necessary to achieve agreement for thermodynamic properties such as miscibility of polymer mixtures.

1.2.6 Molecular dynamics simulation

Molecular dynamics (MD) simulations and Monte Carlo (MC) simulations are the two most important particle-based molecular simulation methods. MD uses equations of motion to evolve the trajectory of particles, which enables studying time-dependent and time-averaged properties. In MC simulations, new configurations are sampled based on random numbers and the Boltzmann factor of the (potentially accepted) new state. Configurations in MC simulations are changed by explicitly defined types of moves, which can range from simple rotations to deleting and regrowing of molecular parts.

In molecular dynamics simulations, Newton's equation of motion is solved for particles that interact by a set of classical potentials that account for bond stretching, bond bending, torsional restrictions, dispersion and electrostatics. Using available atomistic force fields is usually too computationally demanding to be applied routinely to phase equilibria in polymer systems. Coarse-grained force fields (see next section) can speed up calculations by reducing the number of units, sampling phase space quicker and allowing a larger time step to progress in time faster.

The simplest and most naive approach to determine partition coefficients from MD simulations, e.g., for an oligomer between two polymer phases, would be direct counting of oligomer molecules in both phases in an equilibrated system. However, if the frequency of migration of the oligomers between the polymer phases is low at the conditions of interest, the process of equilibration is computationally expensive. To improve the accuracy of the predicted partition coefficient either the dynamics of the equilibrated system need to be studied over a longer time or the size of the system needs to be increased or both.

For low-frequency migration processes for which the direct counting method

is not appropriate, a different migration path can be studied. Such a path might even be non-physical. As the free energy is a state function and, hence, free-energy differences are independent of the considered path, computationally advantageous (unphysical) transitions lead to the same results. Solutes, e.g., can be gradually "grown" into the solvent phase. For example, Garrido *et al.*[51] have demonstrated good agreement between predicted and experimental octanol–water partition coefficients for a range of solvents. One advantage of the thermodynamic integration approach is its ability to systematically improve the predictions by reusing simulation results of lower accuracy, which is possible because the growth process is divided in independent simulations.

Also Monte Carlo simulations have successfully been applied to determining solubilities. The Grand Canonical Monte Carlo (GCMC) simulation technique (μVT ensemble), and a modern version with polymer-tailored Monte Carlo moves has been applied to the solubility of alkanes and oligomer in polyethylene.[52]

1.2.7 Dissipative particle dynamics

Dissipative particle dynamics (DPD) is a popular approach for mesocale simulations capturing hydrodynamic behaviour.[53,54] The force between particles is a sum of three contributions.

The conservative force is softly repulsive at small interparticle distances and linearly vanishing towards the cutoff distance (equal to the particle diameter). The dissipative force (drag force) effectively introduces fluid resistance opposite to the direction of flow. A random force sampled from a Gaussian distribution for each particle pair is also applied.

Interactions can be derived from the Flory–Huggins theory demonstrated by Groot and Warren.[55] Recently, an alternative to deriving interaction parameters was presented by Fraaije *et al.*[56] Their methodology is based on residual free energies of mixing, which can be obtained from other predictive (group-contribution) methods such as COSMO-RS and UNIFAC.

In its original form, DPD is an canonical ensemble (NVT) simulation

technique. Constant volume conditions are required to model condensed fluids due to the purely repulsive interactions. Using net-attractive interactions, for example by adding a density dependent force (multibody DPD),[57–59] allows the modelling of condensed fluids naturally, and makes the modelling of vapour–liquid equilibria and other larger density changes possible.

Larger time steps can be used in DPD compared to molecular dynamics simulations due to the soft interactions, effectively allowing longer simulation times.

Polymer solutions,[60] blends and complex fluids have been modelled with DPD. In particular micelles, lamellar structures and other heterogeneous fluids with microphase separations can be captured easily. The reader is referred to an overview article[61] for further details.

1.2.8 Equation-of-state approaches

Equations of state (EoS) are expressions relating thermodynamic properties such as temperature, volume, density, free energy and pressure. While simpler equations of state differ by how many empirical parameters are required and how they are combined to describe the thermodynamic phase space, more advanced EoS methods use molecular-structure related parameters and allow therefore the link to other methods like molecular dynamics simulations.

Van der Waals (vdW) introduced in 1873[62] two empirical parameters a and b to improve the ideal gas equation of state. The corresponding additional terms account in a simple and brilliant way for free-volume effects and particle interactions

$$\left(P + a\frac{N^2}{V^2}\right)(V - Nb) = NRT \tag{1.26}$$

A number of adjustments have been proposed to the vdW EoS leading to improved descriptions. Examples are the Redlich–Kwong (RK), Soave–Redlich–Kwong (SRK), Peng–Robinson (PR)[38] and Panayiotou–Vera EoS.[28] They all have in common that they can be rearranged into a polynomial that

is third order in volume and are therefore referred to as **cubic** EoS. The determination of the volume in cubic EoS is mathematically equivalent to finding the root of a cubic function. Cubic equations of state extended by a Wertheim-type[63–68] association term are referred to as cubic-plus-association (CPA) EoS. CPAs are still in extensive use, e.g. for high pressure systems in the petroleum industry,[38,69] but applications to polymer systems can be found also.[70]

Parameters in equation-of-state approaches are often defined with the help of the theory of corresponding states. It assumes that the relative behaviour of compounds is similar and is mainly influenced by the individual critical temperature and pressure values. Some equations of state use the critical temperature–pressure pair as the only or most important information for its parametrisation.[38]

An advanced equation of state based on a detailed molecular model is the statistical association fluid theory (SAFT).[71] **SAFT** is based on a perturbation approach for describing interactions between monomers starting from a hard-sphere fluid[72,73] as reference and Wertheim's thermodynamic perturbation theory[74–79] for describing the formation of chains and additional association interactions. While SAFT-γ incarnations have been improved by higher order perturbation terms to almost perfectly reproduce a range of thermodyamic experimental data for spherical molecules, chains are described with the first-order perturbation term (i.e., they are assumed to be fully flexible with no bond and dihedral angle preference or restriction). This description has been found to be a good approximation for liquid densities,[16] but for mixtures of polymers of different chain lengths where the stiffness of chains, its surface accessibility and coiled structures are important it is not expected to be as predictive as for more spherical molecules. Satisfactory correlations and predictions from pure-component parameters have been shown for polymer–solvent systems within SAFT-HS,[80] PC-SAFT[81,82] and SAFT-VR.[83] See Chap. 3 for further details on SAFT in general and SAFT-VR Mie and SAFT-γ Mie in particular.

1.3 Approaches to coarse graining

Coarse graining (CG) is the process of parametrising a model of lower resolution. Lower resolution is usually specified in comparison to an atomistic model. In the context of molecular simulations, atomistic models are referred to as full-resolution models, while models with one bead per heavy atom (referred to as united-atom resolution) or one bead per monomer are models with typical coarse-grained resolutions. Fig. 1.2 visualises a polymer model with different degrees of coarse graining.

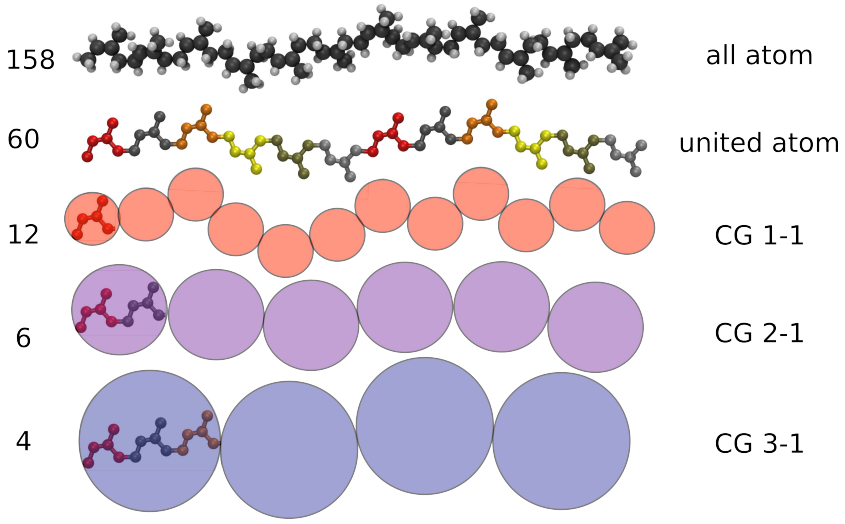

Figure 1.2: Polymer model representations with different degrees of coarse graining. The number of beads (left column) of a 12mer of polyisoprene reduces from the full-resolution all-atom (top), via the united-atom resolution to even further coarse-grained models, which lump one, two or three monomers into one coarse-grained bead.

Coarse-grained models lead to faster simulations compared to their higher-resolution equivalent, because of three reasons: Firstly, the smaller number of beads reduces the number of interactions to determine. Secondly, the free-energy landscape is smoother leading to faster diffusion. Thirdly, the interaction potentials of coarser systems are usually softer, which allows an increase in the time step within MD simulations. Coarse-grained models allow access to longer time scales and larger length scales.

Coarse-grained potentials are typically developed as a temperature-independent potential and are, therefore, state dependent.[84] State dependency describes the inability of models to accurately represent the system over a wide range of temperature and pressure conditions. The mapping of the position of the beads of the finer model onto the position of the beads of the coarser model, e.g., by using the centre of mass, is clearly influenced by temperature, i.e., kinetic energy and intramolecular restrictions of the individual beads. An optimal choice of temperature-independent coarse-grained potentials by including several state points in the CG potential development, however, can reduce the state dependency.

Coarse graining is concerned with a balance between reducing the number of particles and still retaining as much molecular structure as necessary for the properties of interest to be described accurately. While versatile and transferable coarse-grained force fields are available at the united-atom resolution (e.g., TraPPE[85] and NERD[86]), the transferability of coarse-grained force fields at the resolution of several heavy atoms per bead is often limited.

Coarse-graining methods can be divided into "bottom-up" and "top-down" approaches. Bottom-up approaches take models of higher resolution (usually atomistic models) as the reference for parametrising coarse-grained models. Top-down approaches employ models of lower resolution, usually macroscopic experimental values, to inform new models.

Coarse graining aims to integrate out unnecessary information and to only retain those of interest. The most important criteria for good coarse-grained descriptions are the *representability* of the reference model or reference experimental system and *transferability* to new conditions and new models by, e.g., extending the chain length or combining beads differently than during the parametrisation process.

For overviews and comparisons of coarse-graining methods the reader is referred to Refs 87–92.

1.3.1 Bottom-up

Bottom-up coarse-graining methods use finer-grained models to inform the coarse-grained model. Typically the CG model is optimised to reproduce the structural properties or the forces obtained from the finer model.

Iterative Boltzmann Inversion (IBI)

A common bottom up approach is the iterative Boltzann inversion (IBI).[93] The coarse-grained potential V_i is iteratively optimised by the inverted Boltzmann factor of the ratio of the property distribution function g_i of the tabulated interaction potential V_i and the target distribution function g_{target}

$$V_{i+1} = V_i + k_{\text{B}}T \ln\left(\frac{g_i}{g_{\text{target}}}\right). \tag{1.27}$$

The distribution functions are typically radial distributions, angular distributions, bond-length distributions and torsional distribution functions. This method has also been successfully applied to polymer systems.[94–97] The disadvantage of IBI, however, is that it can be a time-consuming method, while the obtained CG force fields are often only accurate for a narrow pressure/temperature range.[98] Moore *et al.* have extended IBI to multiple thermodynamic states (MS-IBI) and have presented force fields of improved transferability compared to a single-state IBI.[99]

Relative-entropy method

The relative-entropy method by Shell[100] uses the probability of configurations to be observed in simulations to define the fitness of coarse-grained models. The best coarse-grained model minimises the relative entropy S_{rel}, which is a measure of the loss of information upon coarse graining

$$S_{\text{rel}} = \sum_i p_{\text{target}}(i) \ln \frac{p_{\text{target}}(i)}{p_{\text{model}}(i)}, \tag{1.28}$$

where $p_{\text{target}}(i)$ and $p_{\text{model}}(i)$ are the probability of configuration i in the target and model system, respectively. While similar results compared to IBI methods can be obtained, one advantage of the relative-entropy method is the possibility to use analytical potentials. The relative entropy is a flexible and generalised approach to analyse and develop models. Despite the flexibility and advantages, the relative-entropy method has so far only been applied to a limited number of systems.[100,101]

Force Matching

In the force-matching approach (also referred to as multi-scale CG approach, MS-CG) by Izvekov and Voth[102,103] the forces acting between the coarse-grained particles for each simulation snapshot are optimised to best match the forces of the finer-grained simulation. The coarse-grained interaction potentials are spline functions, for which the coefficients are optimised by solving a set of linear equations. Applications of the force-matching approach have been published for several low molecular weight compounds.[84,102–105]

1.3.2 Top-down

Top-down coarse-graining methods use mesoscopic, macroscopic or experimental properties to inform the coarse-grained model. Typically the CG model is optimised to thermodynamic experimental data.

MARTINI approach

The MARTINI force field[106] is a set of coarse-grained force fields at a similar degree of coarse graining (3 or 4 heavy atoms per bead), which are systematically parametrised to match experimental partition coefficients. The group-contribution nature of the set of beads allows the quick development of new coarse-grained MARTINI models by mapping available beads onto new structures of interest.[107] The MARTINI methodology has mostly been applied to biomolecular systems,[106,108,109] but also applications to polymers were published.[110–112]

Statistical Association Fluid Theory

The Statistical Association Fluid Theory (SAFT) offers an analytical link between coarse-grained force fields and thermodynamic properties such as density, pressure, solubility or liquid–liquid equilibrium compositions. The advantage of SAFT approaches is the speed with which the properties can be calculated and, hence, the parametrisation can be performed. The faster calculation of target properties for model force fields compared to molecular simulations makes it possible to parametrise a force field not only to one state point, but to a set of thermodynamic properties at a range of temperatures and pressures. The range of conditions included in the parametrisation process improves the transferability of the CG force fields significantly.[6,113–115] See Chap. 3 for further details on SAFT in general and SAFT-VR Mie and SAFT-γ Mie in particular.

Chapter 2

Statement of aims

The aim of this work is threefold. First, we aim to develop our own implementation of the SAFT-γ Mie theory together with all required solvers and optimisers to apply and develop SAFT-γ Mie models. Second, we aim to assess the accuracy of SAFT-γ Mie correlations and predictions for thermodynamic properties of polymer systems. Third, we aim to analyse how well SAFT-γ Mie models perform as force fields in coarse-grained molecular dynamics simulations.

A new implementation of the SAFT-γ Mie equation of state together with algorithms for liquid–liquid equilibria for multicomponent systems and Mie-parameter estimation will be developed. An interface to the HELD code will be provided, to allow the calculation of multicomponent vapour–liquid equilibria. The code and solvers will be rigorously tested and details of the development and testing presented. See the results in Chap. 4.

A systematic and comprehensive analysis on how well the most recent SAFT incarnation SAFT-γ Mie can be applied to polymer systems will be conducted. A literature search will be performed to assess the accessibility of experimental data for parametrising SAFT models. An overview of the experimental data will be presented and the suitability of different data types compared and tested. New tailored SAFT-γ Mie parameters for pure-component polymer melts, binary polymer mixtures and ternary polymer mixtures will be parametrised. The polymer models will be examined on

how accurately they can correlate, extrapolate and predict the experimental reference data. See the results in Chap. 5.

The link between SAFT-γ Mie and molecular dynamics simulations will be investigated for polymeric systems. The properties of low molecular compounds, oligomeric and polymeric melts and mixtures will be simulated. While the focus will be on homogeneous bulk properties, also the surface of an oligomer/polymer mixture will be simulated and compared to experimental surface density profiles. See the results in Chap. 6.

A more detailed introduction to the statistical associating fluid theory (SAFT), and SAFT-γ Mie in particular, is provided in Chap. 3. The chapter also includes an overview and comparison of the most relevant SAFT incarnations for polymers and MD simulations.

Chapter 3

SAFT

The statistical association fluid theory (SAFT) is a beautifully elegant combination of equations of state (EoS) and radial distribution functions (RDF) of simpler fluids. Although the underlying EoS and RDFs usually describe simple pure components and their mixtures, the full SAFT EoS can model gases, supercritical fluids, vapour–liquid equilibria (VLE) and liquid–liquid equilibria (LLE), alkanes, polar compounds, hydrogen bonding compounds such as alcohols and water, and also polymer solutions and complex mixtures. The numerous excellent developments and analyses of more than two decades of SAFT history have brought accurate SAFT versions, strategies for developing new model parameters and best uses of component characteristic parameters. Also the limitations of the respective SAFT incarnations have been discussed extensively.[64–66,116]

This section is aimed at providing a brief introduction to SAFT, and the SAFT-γ Mie incarnation in particular. Emphasis will be put on the link to molecular simulations (Monte-Carlo and molecular dynamics) and the application of SAFT to polymers.

Several aspects and background information of the SAFT EoS are not discussed in this chapter. For the derivation of the SAFT equation the reader is referred to the original work by Wertheim,[74–79] the original SAFT publication,[117] a heuristic derivation by Müller and Gubbins[64] and an excellent review by Zmpitas and Gross[118] who give a pedagogical introduction to and

the analysis of the foundation of the central SAFT equations. For an overview of SAFT modifications and incarnations, the reader is referred to the popular SAFT reviews from 2001[64] and 2002.[65] For all equations of the SAFT-γ Mie incarnation, see the original publications by Lafitte and coworkers.[14,16]

The *non*-associating form of the SAFT theory will be discussed in this work, because the association terms are not required for the description of non-polar compounds and their mixtures. For details on the association extension, which is recommended for hydrogen-bonding compounds such as water, the reader is referred to the original work[117] and the most recent extension by Dufal *et al.*[119] comparing several newly developed equations for the associating Helmholtz contribution in SAFT-VR Mie for describing water in particular.

Providing an overview of SAFT versions is difficult. Very many SAFT modifications have been suggested over the years and then applied to a large range of different systems. A comparison between them can be difficult due to the use of sometimes unsystematic names and the lack of a widely agreed set of test cases.* While most incarnations have been applied to alkanes, where usually excellent behaviour is found, not all SAFT versions have been applied to polymers. A very brief introduction to the SAFT equations and history of incarnations is given in this section. Some of the most used adjectives for SAFT versions are explained. The focus, again, will be on SAFT versions applied to polymers or linked to simulations. For excellent comprehensive reviews and overviews over the range of SAFT theories and applications the reader is referred to Refs 64–66,116

*This was also brought up and discussed in the closing session at the SAFT 2015 conference in Houston, a major international conference celebrating, in 2015, 25 years of SAFT.

3.1 SAFT backbone

One way of expressing the essential backbone of the non-associating version of SAFT is the Helmholtz energy for a pure compound is

$$\frac{A^{\mathrm{SAFT}}}{Nk_{\mathrm{B}}T} = \ln(\rho\Lambda^3) - 1 \; + \; m_{\mathrm{s}}a_{\mathrm{seg}} \; - \; (m_{\mathrm{s}} - 1)\ln g_{\mathrm{seg}}(\sigma_{\mathrm{contact}}). \tag{3.1}$$

where the ideal contribution is[72]

$$\frac{A^{\mathrm{ideal}}}{Nk_{\mathrm{B}}T} = \ln(\rho\,[\Lambda(T)]^3) - 1. \tag{3.2}$$

Here, Λ is the temperature-dependent de Broglie wavelength of the molecular particles, and ρ is the number density of particles. This term captures all kinetic contributions and reduces, as expected, to the ideal gas equation for the volume derivative $P = \partial A^{\mathrm{ideal}}/\partial V = Nk_{\mathrm{B}}T/V$. The ideal contribution is not unique to SAFT, but used for other equations of state, too. See Sec. 4.3.3 for more details.

The monomer contribution

$$\frac{A^{\mathrm{mono}}}{Nk_{\mathrm{B}}T} = \; m_{\mathrm{s}}a_{\mathrm{seg}} \tag{3.3}$$

captures the change in Helmholtz energy due to the repulsion and attraction of individual monomers. The energy per monomer segment a_{seg} is multiplied by the chain length m_{s} of the SAFT model.

The chain contribution

$$\frac{A^{\mathrm{chain}}}{Nk_{\mathrm{B}}T} = -(m_{\mathrm{s}} - 1)\ln g_{\mathrm{seg}}(\sigma_{\mathrm{contact}}). \tag{3.4}$$

captures the change in Helmholtz energy due to the covalent bond of monomers forming a linear chain. It relies on the value of the radial distribution function of the monomer system at the contact distance $g_{\mathrm{seg}}(\sigma_{\mathrm{contact}})$, which quantifies the likelihood of two monomers temporarily being separated by the distance $\sigma_{\mathrm{contact}}$.[†] The corresponding energy change $\ln g_{\mathrm{seg}}(\sigma_{\mathrm{contact}})$ is multiplied by

[†]Assuming the interaction potential of the (reference) monomer fluid is zero at the

the number of bonds $(m_s - 1)$ of the linear chain model to obtain the energy contribution for forming a chain of length m_s. Eq. (3.3) is the result of the first-order thermodynamic perturbation theory (TPT1) using a 2-body distribution function only. Higher order TPT, which involves many-body distribution functions, and therefore captures also bond angles and dihedrals, is challenging to express in tractable analytical equations. TPT1 has been the standard level of description for the chain forming term. The three contributions of the SAFT expression are visualised in Fig. 3.1.

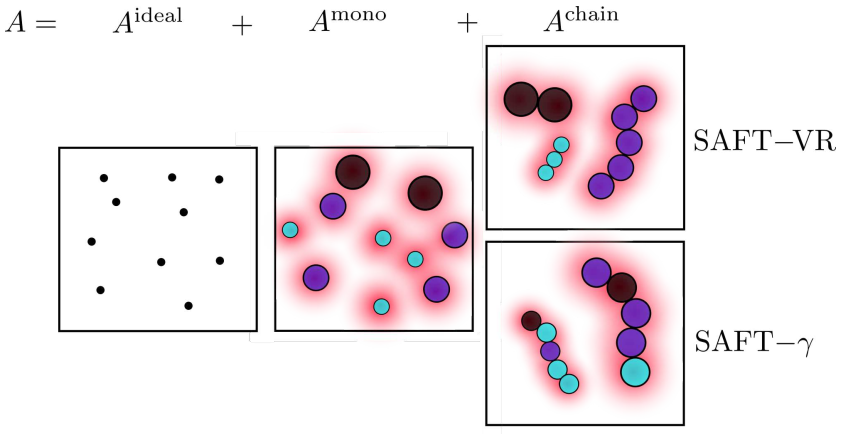

Figure 3.1: Schematic illustration of the three contributions to the Helmholtz free energy of the non-associating form of SAFT. The first represents the ideal contribution of a non-interacting monomeric system (using the proper model architecture—usually chains—instead of the monomers here is only necessary for the comparison between states at different temperatures, e.g., entropy, heat capacity and speed of sound, as vibrational and rotational contributions do not cancel out in those cases), the second the monomer interactions and the third the contribution due to the formation of bonds. In SAFT-VR, homonuclear chains are formed. In SAFT-γ, heteronuclear chain are described by deriving averaged Mie potential parameters of all types per chain (indicated by averaged bead size). Also in SAFT-γ the chain contribution uses homonuclear chains, but the homonuclear chains represent heteronuclear chains due to the averaged parameters.[15,16,120]

Before SAFT was published, equations of state typically did not separate

bond length σ_{contact}. This is for example true for tangentially bonding hard spheres and Mie potentials. For fused spheres or other interaction types the $g_{\text{seg}}(\sigma_{\text{contact}})$ is multiplied by the Boltzmann factor of the potential at σ_{contact}.

monomer interactions and the chain forming terms. Perturbations accounting for dispersion and non-spherical shape (chains) were directly applied to simple reference fluids such as the hard-sphere EoS.[73,121] With SAFT, the reference fluid is extended such that the molecular shape can be non-spherical, i.e. chains of more than one monomer. Association interactions, which can describe hydrogen bonding, can also be included in the reference fluid. SAFT therefore provides an improved "molecular model". Perturbations and improvements can then be applied to the monomer interaction, chain character and associating interaction separately if required, and the basic chain character and associating interaction does not have to be part of the perturbations. SAFT has become more predictive than earlier EoS and the better-defined molecular model provides a closer connection to molecular simulations.[117]

SAFT incarnations mainly differ by what expressions are used for a_{seg} and $g_{\text{seg}}(\sigma)$. This includes the expressions for the reference fluids, the type of interaction potential and the number of perturbations included.

EoS and RDFs of the reference fluids are often polynomials fitted to results of molecular simulations.[117,122,123] They are required as a function of all parameters, such as density, temperature and composition, which is why the simulation-based EoS can practically not be obtained for the full system including all interactions and cases, but typically the hard-sphere[73,121] and Lennard–Jones monomer fluids[122] are used.

3.2 Molecular models

The molecular model in SAFT theories is typically a linear chain of spherical segments. Special adjustments to effectively describe rings[114] or branches[124] have been made, but are seldom. A range of adjectives are used to classify SAFT incarnations and the underlying molecular model. Some of the most important adjectives will be briefly explained.

"Associating" vs **"non-associating"** indicates whether the SAFT equation includes an extra term for association, usually referred to as a^{assoc}.

"Homonuclear" vs **"heteronuclear"** vs **"group-contribution" (GC)** indicates whether chains can be composed of only one type (homonuclear) or

several types of monomers (heteronuclear). "Group-contribution approach" usually refers to a methodology for heteronuclear models, for which a large set of parameters has already been developed, which can be assembled to form new predictive models. Heteronuclear SAFT versions do not necessarily have expressions for the chain contribution of the Helmholtz energy that use a heteronuclear model, but rather refer to the functionality that is provided by the overall theory. For example, SAFT-γ SW[120] and Mie[16] are referred to as heteronuclear models but use effective parameters (derived from a heteronuclear model) with a homonuclear chain for the chain term a^{chain}, see Fig. 3.1. Effective parameters are introduced to allow fused chains with the same model.

"Fused" vs **"tangent"** indicates the covalent bond type in the SAFT model. In most SAFT incarnations, model chains have monomers tangentially touching neighbouring monomers. In tangential models the bond lengths are identical to the bead diameter (or the arithmetic mean of bead diameters of unequal sized beads). Allowing the overlap of beads with bond lengths shorter than the bead diameters is referred to as a fused model.

"Hard-sphere" (HS) vs **"square-well" (SW)** vs **"variable range" (VR)** vs **"Lennard–Jones" (LJ)** refers to the underlying type of interaction potential between beads. HS potentials are only repulsive, while SW and LJ potentials are repulsive at short and attractive at medium distances. Earlier SAFT versions with SW potentials provided parameters for the well-depths (energetic) and bead diameter (size). The variable-range models also allowed adjustment for the width of the well, which controls the range of distances with attractive potential values.

A range of interaction potentials have been incorporated into SAFT versions. Square-well potentials have probably been the most widely used potential.[15,64,65,80,82,125,126] Square-well potentials were first implemented as 2-parameter potentials, i.e. with an energetic and size parameter. In the variable-range (VR) version of the SAFT theory, a third parameter for the width of the well is added to make the SAFT-VR SW[125,127] theories a 3-parameter EoS (not counting the chain length as a parameter). Also the Lennard–Jones (LJ) potential,[117,125,128–131] the Mie potential,[13,14] Yukawa

(Y),[125,132,133] Sutherland (S),[125] step potentials,[134] and recently also SAFT version with the Morse potential[135] have been published. Discontinuous potentials such as the SW, step and hard-sphere potentials can be applied in Monte-Carlo (MC) simulations, which has been used to verify the respective SAFT EoS.[136–140] Continuous potentials such as the Lennard–Jones and Mie potentials can be used in both MC and MD simulations allowing a wider range of applications. The hard-sphere, Yukawa and Sutherland potentials are either purely repulsive or purely attractive. Applying only one of them is not sufficient to capture phase equilibria. They are typically applied in SAFT theories to capture parts of another richer potential to allow the separation of a reference and perturbation contribution. For example the hard-sphere potential can be used to describe the repulsive part of square-well potentials[117] and the Sutherland potentials the repulsive part of Mie potentials.[13,14]

3.3 Polymers

Many SAFT versions have been applied to polymer systems. One of the common methodologies is extrapolating SAFT parameters which were fitted to the homologous alkane series to longer alkanes and polyethylene.[16,80,83,127,141,142] For pure polymers, usually only the melt densities as a function of temperature and pressure are considered,[16,80] while for longer alkanes also VLE properties have been predicted.[141]

For mixtures involving polymers, usually not mixtures of several polymers, but mixtures of a single polymer with gases and solvents have been studied. Typical properties of interest of such systems are vapour pressures,[81,126,143] solubility,[83,126,144] cloud-point pressures[83,124,124,127] and cloud-point curves in composition space.[81,83,126,143]

Rarely have solubility or cloud points of polymer blends been studied. Ghonasgi and Chapman[128] studied oligomer blends of 25mers, but to our knowledge no miscibility predictions of high-molecular-weight polymer blends were published.

For polymers, PC-SAFT is probably the most prominent SAFT incarnation, which has been applied to a large range of polymer and copolymer

solutions.[81,82,116,143]

Real polymers usually show a molecular weight distribution rather than chains of the exact same length. Rarely, the polydispersity of the polymer is included in the model explicitly, see for example ref.[81,116,145] The polydispersity of polymers can be described explicitly by a multi-component mixture of several individual pseudocomponents of different molecular weight, see for example ref.[81] While increasing the number of (pseudo)components make the phase equilibria calculations more expensive, several strategies were presented to simplify and speed up calculations of polydisperse polymer systems.[145–149] Jog and Chapman[147] have speeded up the calculations by rearranging the SAFT-HR[80] algorithm to reuse terms that do not differ between pseudocomponents. Sun *et al.*[149] proposed a method to approximate the molecular weight distribution with a Gaussian quadrature method, which reduces the number of components for the same accuracy significantly. Neither method has been applied to the SAFT-VR Mie equation of state.

3.4 Molecular simulation

SAFT theories have, since the beginning, been verified againsts results of MC simulations[16,128,137] and often correlations of large sets of simulation data have been incorporated into SAFT versions as reference fluid descriptions[73,121,150] or to inform perturbations.[14,117]

In connection with molecular dynamics simulations, the SAFT-VR Mie has probably been the most prominent SAFT incarnation. SAFT-VR Mie has been used to develop molecular simulation force fields.[6,114,115,151,152] The continuous Mie potential of the SAFT-VR Mie theory allows the direct transfer of the model parameters to MD simulations. Excellent agreement between theory (SAFT) and simulation (MD) was found for carbon dioxide,[6] model mixtures of crude oil,[153] alkane mixtures,[154] carbon dioxide/alkane mixtures,[155] organic solvents,[156] carbon dioxide/water mixture,[157] VLE and PVT of dichlormethene, bromochlormethane and bibromomethane,[158] VLE of a range of Mie potentials,[159] carbon dioxide, CF_4, SF_6, a refridgerant, decane, eicosane,[115] pure water,[151] and binary and ternary mixtures of water,

carbon dioxide and alkanes.[152]

However, even discontinuous square-well interaction, which are easier to apply in MC than MD simulations, have been used to speed up the development of continuous force fields by correlating the parameters of the discontinuous square-well potential and the continuous Mie potential in an intermediate step.[160]

3.5 SAFT-γ Mie

SAFT-γ Mie[16] is the group-contribution and heteronuclear version of SAFT-VR Mie.[14] SAFT-γ Mie and SAFT-VR Mie are part of a line of systematic improvements of the SAFT-VR family. As part of this development higher-order perturbations have been added and the molecular model was made more flexible and representative. While two SAFT versions are sometimes referred to as SAFT-VR Mie, in this work we refer to the older version as SAFT-VR Mie 2006[13] and use SAFT-VR Mie for the SAFT-VR Mie 2013[14] version.

In the monomer contribution (see Eq. (3.3)) of SAFT-γ Mie, for a_{seg} the hard-sphere fluid is taken as the reference fluid using an empirical equations of state[73,121,150] for a^{HS}. The Mie potential interactions of the monomer fluid are introduced by adding perturbation terms up to third order with the Barker and Henderson high-temperature perturbation expansion[72]

$$a_{\text{seg}} = a^{\text{HS}} + \frac{a_1}{k_{\text{B}}T} + \frac{a_2}{(k_{\text{B}}T)^2} + \frac{a_3}{(k_{\text{B}}T)^3}. \tag{3.5}$$

The third-order perturbation term was optimised to effectively account for even higher-order terms. The third term a_3 was added with the SAFT-VR Mie[14] version, while previous versions comprised terms up to second order.

In the chain contribution (see Eq. (3.4)) of SAFT-γ Mie, the radial distribution function $g^{\text{Mie}}(\sigma)$ is also described with a Barker and Henderson high-temperature expansion. The expansion is applied to the logarithm of the RDF and evaluated up to second order (SAFT-VR Mie 2006 was evalu-

ated up to first order)

$$g^{\mathrm{Mie}}(\sigma) = g_d^{\mathrm{HS}}(\sigma)\ \exp\left(\frac{\epsilon}{k_{\mathrm{B}}T}\ \frac{g_1(\sigma)}{g_d^{\mathrm{HS}}(\sigma)} + \left(\frac{\epsilon}{k_{\mathrm{B}}T}\right)^2\ \frac{g_2(\sigma)}{g_d^{\mathrm{HS}}(\sigma)}\right). \tag{3.6}$$

The reference-fluid radial distribution function g_d^{HS}, describes a hard-sphere fluid of spheres with diameter d. The temperature-dependent effective hard-sphere diameter d accounts for the softness of the Mie potential and is shorter or equal to σ. The contact distance, i.e., the bond length, is still taken as σ.

All SAFT-VR Mie and SAFT-γ Mie equations or details on the derivations and approximations are found in the original puplications by Lafitte *et al.* 2013[14] and Papaioannou *et al.* 2014.[16] The notation of this chapter closely follows the notation of the original papers.

Mie potential

The Mie potential is a generalised Lennard–Jones potential

$$V_{ij}^{\mathrm{Mie}} = C_{ij}\epsilon_{ij}\left[\left(\frac{\sigma_{ij}}{r_{ij}}\right)^{\lambda_{\mathrm{r},ij}} - \left(\frac{\sigma_{ij}}{r_{ij}}\right)^{\lambda_{\mathrm{a},ij}}\right] \tag{3.7}$$

with

$$C_{ij} = \frac{\lambda_{\mathrm{r},ij}}{\lambda_{\mathrm{r},ij} - \lambda_{\mathrm{a},ij}}\left(\frac{\lambda_{\mathrm{r},ij}}{\lambda_{\mathrm{a},ij}}\right)^{\frac{\lambda_{\mathrm{a},ij}}{\lambda_{\mathrm{r},ij}-\lambda_{\mathrm{a},ij}}}, \tag{3.8}$$

where ϵ_{ij} and σ_{ij} are the well depth and the segment size, respectively. $\lambda_{\mathrm{r},ij}$ and $\lambda_{\mathrm{a},ij}$ are the repulsive and attractive exponents, respectively, while $\lambda_{\mathrm{r},ij} = 12$ and $\lambda_{\mathrm{a},ij} = 6$ is the Lennard–Jones potential. The influence of the four Mie potential parameters on the shape of the potential curve, on VLE properties and on free energies of mixing of blends are illustrated in Fig. 3.2.

For mixtures and heteronuclear compounds, additional interactions between unlike segments are required. The parameter estimations can be made based on the like interaction parameter values following rules that are called combining rules or mixing rules. The combining rules recommended by

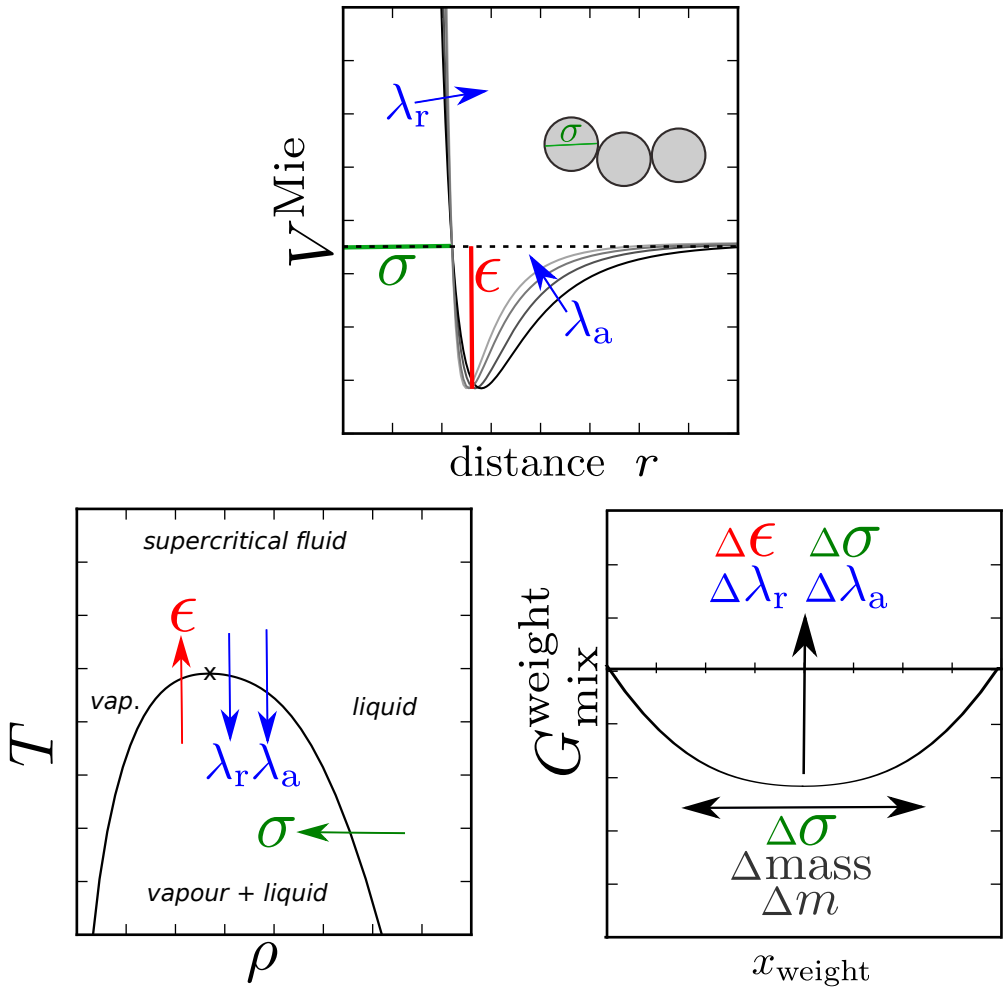

Figure 3.2: Influence of the Mie potential parameters on (top) potential curve and (left) vapour–liquid equilibrium densities. (Right) The influence of the dissimilarity of Mie potential parameter values in a binary blend expressed for Gibbs free energy of mixing, where Δm is the difference in chain length. The unlike interactions were obtained with the combining rules in Equations (3.9)-(3.11) with k_{ij}=0. Note that only the most dominant influence of each parameter is demonstrated, which is especially true for the vapour–liquid equilibrium curve. The influence of the Mie parameters on polymer-melt densities and polymer cloud-point temperatures is presented in a later chapter (Fig. 5.11 and Fig. 5.20).

Lafitte *et al.* 2013 are

$$\sigma_{ij} = \frac{\sigma_{ii} + \sigma_{jj}}{2}, \tag{3.9}$$

$$\lambda_{ij} - 3 = \sqrt{(\lambda_{ii} - 3)(\lambda_{jj} - 3)}, \tag{3.10}$$

$$\epsilon_{ij} = (1 - k_{ij}) \frac{\sqrt{\sigma_{ii}^3 \sigma_{jj}^3}}{\sigma_{ij}^3} \sqrt{\epsilon_{ii} \epsilon_{jj}}, \tag{3.11}$$

where k_{ij} is a correction factor to express deviations which are often needed to reproduce experimental data. A correction factor is usually first applied to the energetic parameter before other unlike parameters are adjusted to further improve the model.

In SAFT-γ Mie, not only heteronuclear chains are possible, but also the notion of a group is introduced. A group has two more parameters but can only have one type of bead. The first additional parameter is the number of beads ν in the group, which is adjustable and can be a positive non-integer value. The second additional parameter is the shape factor S_k, which is another attribute of a group. The shape factor scales the number of beads per group. Since ν and S_k are multiplied at all occurrences in the SAFT-γ Mie equations, they could be combined into a single parameter. However, the typical value range shows that they are intended to separate two physical phenomena. The S_k is intended to model chains with fused bonds, where $(1 - S_k)$ is the degree of overlap. S_k is therefore intended to be *less* or equal to unity. ν allows larger chemical units to be combined into one group. Larger chemical units, which are best modelled with more than one bead and are not expected to be applied in other compounds as a fraction alone, can be combined into a convenient group. ν is intended to be *larger* or equal to unity.

The fused-chain model is not directly used in the a^{chain} term of SAFT-γ Mie, as drastic assumptions and approximations would have to be made to

derive a practical expression. Instead, an equivalent chain length of tangentially bonded spheres is used, which were shown to give comparable results to MC simulations of fused chains.[161] Using an effective chain length of tangentially bonded spheres needed for allowing fused chains loses the heteronuclear nature of the chain model. Effective averaged Mie potentials are used instead of accounting for each covalent bond type individually. Papaioannou *et al.* 2014[16] showed that the predictions with effective homonuclear chain models were almost indistinguishable from the predictions of the heteronuclear chain model. See the illustrated molecular models in Fig. 3.1.

SAFT-γ Mie is equivalent to SAFT-VR Mie for compounds of only one type of bead per chain (homonuclear) and the additional group parameters S_k and ν are set to unity.[‡]

3.6 Limitations and assumptions

SAFT-γ Mie and SAFT-VR Mie allow a simple but powerful description of homogeneous fluids. Starting from an accurate description of spherical particles interacting with Mie potentials, the particles are covalently bonded in pair-wise tangential connections to form chains. The description of spherical particles and short chains for homogeneous fluid properties is excellent.[14,16]

For application of polymers, limitations arise due to the way the chains are formed within TPT1.[162] Firstly, no information about bond angles, dihedrals and overall chain flexibility is included. As a result, chains are modelled as fully flexible, while effectively being more stretched out than expected for polymer structures,[64] which at least partially coil up due to entropic reasons. Secondly, the order of beads in chains can not be influenced, they are effectively modelled as an average over all random combinations. As a result, differences between random, alternating and block copolymers are not captured in the molecular model. Thirdly, the chain model is strictly linear. Describing large rings or branched chains either requires effective parameters or slight adjustments to the chain expression.

[‡]Strictly speaking the product nS_kn_{seg} in SAFT-γ Mie has to be equal to the chain length n in SAFT-VR Mie.

As a fluid theory, SAFT does not capture solids, such as vitrified or crystallised polymers. Options to capture solids are mentioned in the next section.

As the fluid is described as being homogeneous, no structural effects or larger ordering is captured. Surfaces, interfaces and liquid crystal phases, such as a nematic phases, can not be modelled with the SAFT equations alone.

The next section introduces options to add additional terms to SAFT or join SAFT with other theories to extend its capability.

3.7 Theories joint with SAFT

The capabilities of the SAFT theory are often extended with additional terms or by combining theories. The desired capabilities are typically inhomogeneous properties, either as macroscopic properties of solids or as microscopic structural properties of interfaces and surfaces.

Solids and solid–liquid equilibria have been described with SAFT by using a Helmholtz energy term for the solid phase.[163] To account for the crystallinity in semicrystalline polyethylene Paricaud *et al.* have employed Flory theory.[83] The solubility of gases and liquids in polymers below their glass transition temperature has been successfully modelled with the non equilibrium extension of SAFT referred to as NE-SAFT.[164]

Surfaces and interfaces can be described by joining SAFT with the square gradient theory (SGT), which is also referred to as density gradient theory (DGT) or gradient theory (GT). The surface partial-density profiles and the depletion and enrichment of certain species at interfaces have been successfully described.[165–167] An alternative approach to describe surfaces and interfaces has been shown by joining SAFT with classical density functional theory (DFT).[168,169] Also a combination of SAFT, fundamental measure theory and DFT has been used to study partial-density profiles,[170,171] the adsorption of gases on activated carbon[170,172] and carbon dioxide in polystyrene.[171] Also polymer surface tensions have been described with the interfacial SAFT (iSAFT) DFT version by Dominik *et al.*[173]

3.8 SAFT in this work

In this work, we implement and apply the SAFT-γ Mie[16] theory. In Chap. 4 the SAFT-γ Mie[16] EoS and its earlier homonuclear version SAFT-VR Mie[14] EoS are implemented in a stand-alone computer program. In Chap. 5, SAFT-γ Mie parameters published by Dufal *et al.*,[174] making use of all heteronuclear, group-contribution and fused-sphere capabilities of the SAFT-γ Mie method, are applied to polymers. Additionally, new polymer models are developed with the SAFT-γ Mie theory. As the models are homonuclear, the models can also be referred to as SAFT-VR Mie models. In Chap. 6 we use SAFT-γ Mie models as coarse-grained force fields in molecular dynamics simulations.

Chapter 4

Implementation and testing of a SAFT-γ Mie code

This chapter covers the technical details of our SAFT-VR Mie and SAFT-γ Mie program. Firstly, we present an overview of the program building blocks and what units have been chosen throughout. Secondly, the details of the implementation of the SAFT-VR Mie core equations and the conversion to the generalised SAFT-γ Mie version are addressed. Thirdly, derived thermodynamic properties beyond the Helmholtz free energy are covered. Fourthly, optimisation algorithms are presented for obtaining pressure, vapour–liquid equilibria (VLE), liquid–liquid equilibria (LLE) and pure-component Mie potentials. Lastly, details are given for a module for generating tabulated potentials which are compatible with the GROMACS simulation software.[175–177]

This chapter should be read together with a copy of references 14 and 16. Not all definitions and equations of SAFT-γ Mie are repeated here, but the aim is to add additional insights and information only. A consistent notation between this work and Refs 14 and 16 is used.

4.1 Program structure and overview

The SAFT program developed in this work is made up of a set of building blocks. The building blocks in terms of functionality are shown in Fig. 4.1.

A scheme focusing on the user experience linking the main input and output information to the building blocks is found in Fig. 4.2. The latter reveals the Mie potential parameters as the heart of the SAFT program. The building blocks in terms of the code structure and corresponding file structure are summarised in Fig. 4.3. Fig. 4.3 and 4.2 also show the flow of information from input to output files at two levels of detail.

The SAFT core implementation is fully coded in Fortran. Other programming languages are used for the liquid-liquid equilibrium solver (R script) and for the analysis and plotting scripts (python). Input and output files are standard text files. The input file structure is designed to be similar to the input file structure of the GROMACS package.[175–177]

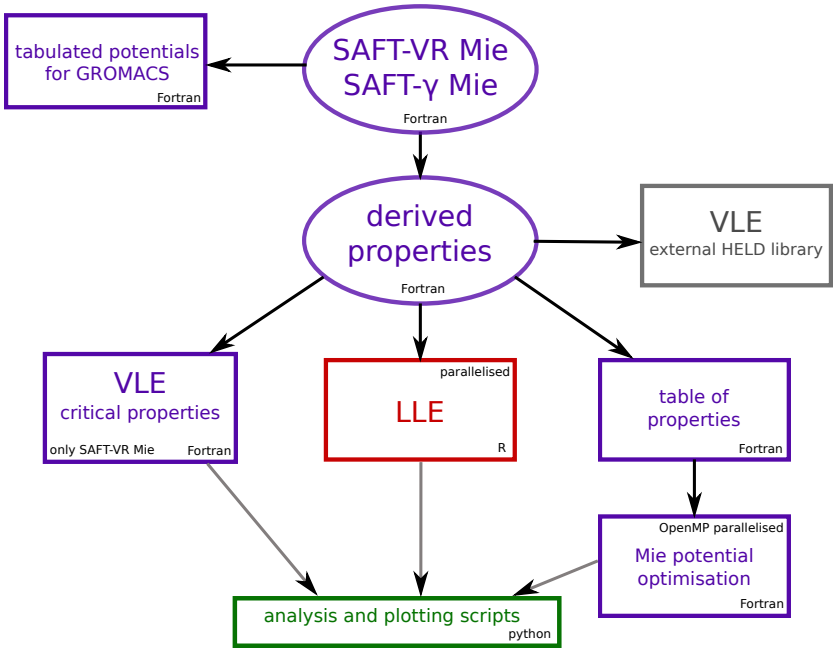

Figure 4.1: SAFT program modules in terms of functionality. Arrows denote dependencies. Colours are used to highlight programming language, while the name of the programming language is also given in the lower right corner of each element. Round contours represent elements which are used as libraries only, while square contours represent programs with integrated libraries.

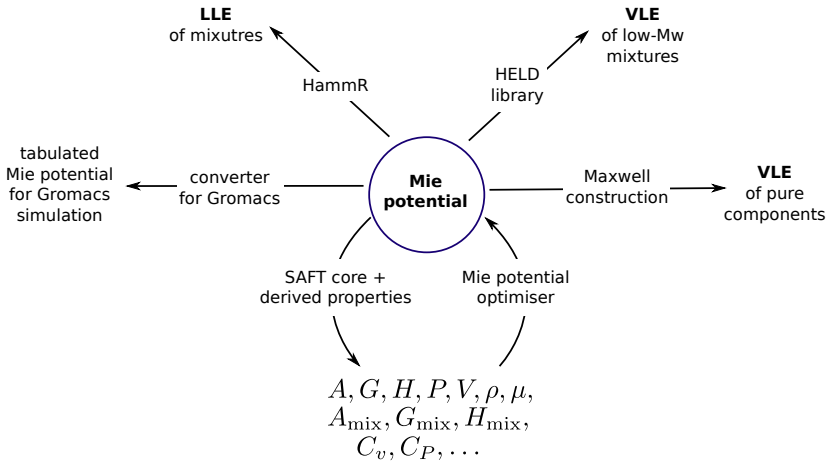

Figure 4.2: SAFT program functionality in terms of main input and output information. The Mie potential parameters are the heart of our SAFT program package. Arrows denote the flow of information.

4.2 Units

The units used in the SAFT implementation are mostly SI units. Deviations are the units for the Mie potential parameters σ in nanometres and ϵ in Kelvin (instead of metres and Joules, respectively), which were chosen to allow easier-to-handle numbers. The Helmholtz energy and its derivatives—pressure, chemical potential, entropy and heat capacity—are internally handled in reduced units. The units in the SAFT core and outer property shell differ in how particle number and volume are described. An overview of the units are presented in Tab. 4.1.

4.3 SAFT-VR Mie Helmholtz free energy

This section provides details on the development of a Fortran code of the SAFT-VR Mie EoS published in 2013 by Lafitte and coworkers[14] at the Imperial College London research group. The code is tested against available data published by the authors.

The Helmholtz free energy is almost fully calculated analytically. The only exception is the numerical integration for the effective hard-sphere di-

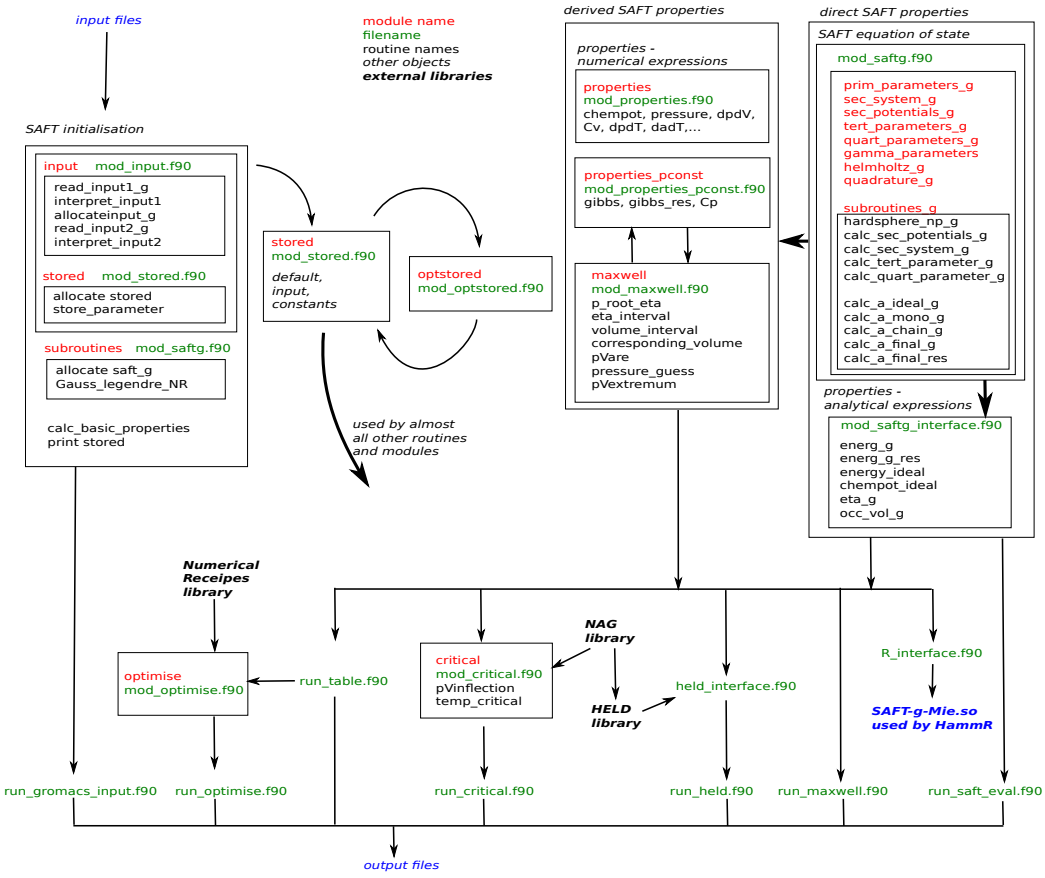

Figure 4.3: SAFT program modules in terms of code structure. The flow of information is highlighted with arrows. A legend for the colour coding is depicted at the top. Fortran modules are highlighted in red (their corresponding file names in green), and input and output text files in blue. The diagram shows the most important connections between elements of the Fortran code and interfaces to libraries.

Table 4.1: Units used in the SAFT code for different types of properties

property	example	SAFT core	property shell	HELD	input file
particle number	N	[ ]	mol	mol	mol
volume	V	nm^3	$\mathrm{m}^3\,\mathrm{mol}^{-1}$	$\mathrm{m}^3\,\mathrm{mol}^{-1}$	$\mathrm{m}^3\,\mathrm{mol}^{-1}$
temperature	T	K	K	K	K
length	σ	nm	nm	-	nm
mass	m_w	$\mathrm{g\,mol}^{-1}$	$\mathrm{g\,mol}^{-1}$	$\mathrm{g\,mol}^{-1}$	$\mathrm{g\,mol}^{-1}$
energy	a	[ ]	[ ]	[ ]	-
	ϵ	J	J	-	K(=J/k_B)
energy derivatives	P,S,μ,C_V	-	reduced by RT	reduced by RT	
pressure	P	-	m^{-3}(=Pa/RT)	m^{-3}	Pa
chemical potential	μ	-	mol^{-1}	mol^{-1}	-
entropy	S	-	K^{-1}	K^{-1}	-
heat capacity	C_V	-	K^{-1}	-	-

ameter. Properties beyond the Helmholtz free energy are calculated numerically with a high-accuracy finite-difference method (see next section). Such first and second derivatives are pressure, chemical potential, Gibbs energy and entropy.

The current program version comprises the SAFT-VR Mie and the generalised SAFT-γ Mie version, which is a heteronuclear group-contribution version using Mie potentials. The SAFT-VR Mie version can be used by setting the SAFT-γ-specific parameters, which are the so-called shape factor and the number of segments per group, equal to one and by only using one type of Mie potentials per compound. Details on the code conversion from SAFT-VR Mie to SAFT-γ Mie are given in Section 4.4.

4.3.1 Code structure - Helmholtz energy

The code is structured with the help of Fortran subroutines and modules. A scheme of the code structure is shown in Figure 4.4 (using a notation consistent with Lafitte *et al.* 2013[14]). The Helmholtz energies are evaluated in 4 stages—primary, secondary, tertiary and quaternary parameters. The

primary level uses the potential and system parameters directly provided in the input file, the secondary level evaluates basic parameters separately for potential and system parameters. On the tertiary and quaternary level, parameters derived from both strands are combined. Each of the four Helmholtz free-energy contributions are evaluated in a separate subroutine using the parameters from the previous four stages. The final Helmholtz free energy is obtained by summing up the four contributions.

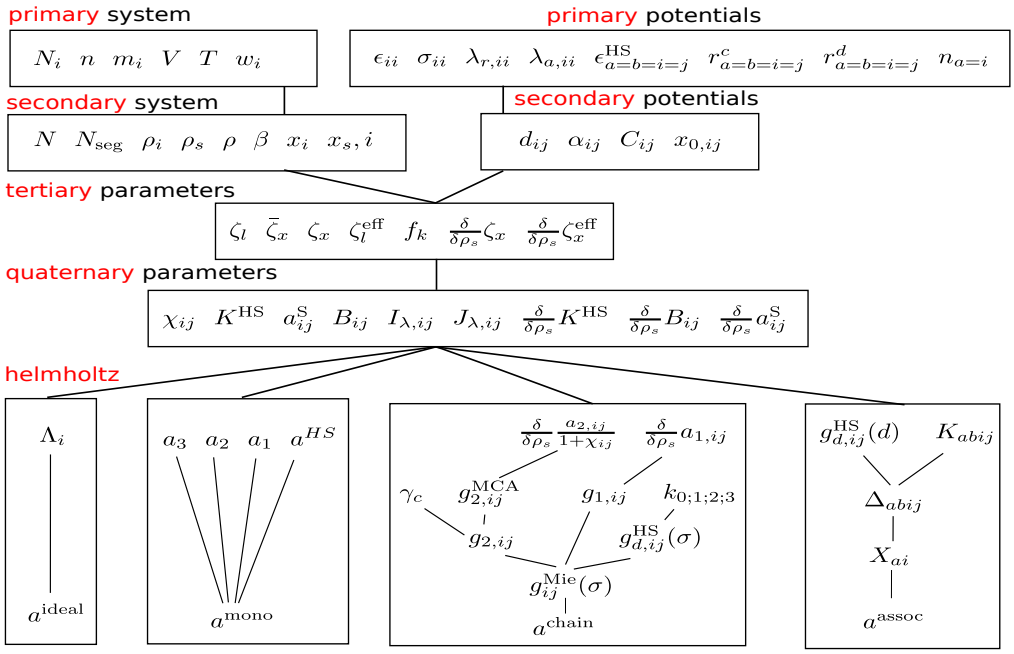

Figure 4.4: Schematic structure of the Fortran code for the SAFT-VR Mie theory. The variable notation is consistent with Ref. 14 for easy referring to the original publication. Each box corresponds to a subroutine, and each title (outside the boxes) indicates a separate module for variable declarations. The order of execution is from top to bottom, while order of execution of boxes on the same height is not important.

The minimal set of input parameters for evaluating the Helmholtz energy is one Mie potential parameter set (well depth ϵ_{ii}, segment diameter σ_{ii}, repulsive exponent $\lambda_{\mathrm{r},ii}$, attractive exponent $\lambda_{\mathrm{a},ii}$, shape factor S_k, number of beads per group ν and mass of the group w_i) and four system parameters (temperature T, volume V, number of molecules N_i and number of monomers

m_i per chain).

4.3.2 Assumptions and limitations

The non-associating version of SAFT-γ Mie has been implemented for this work. The equations for the associating Helmholtz energy contribution are part of the implementation, but the required solver for the mass action equation is not provided. The only interactions in our implementation are therefore the Mie potential interaction between monomers and the impact of the formation of chains. Additional interactions such as association or electrostatics require an extension of the code.

4.3.3 Ideal contribution

The ideal part of the Helmholtz energy of SAFT can be derived from the canonical partition function $Q(N, V, T)$. The real Helmholtz free energy in terms of the canonical partition function is:

$$a = \frac{A}{N k_\mathrm{B} T} = -\ln Q(N, V, T). \tag{4.1}$$

The full partition function has translational, rotational, vibrational and electronic contributions. By following the standard textbook derivation as e.g. found in Ref. 178 one can obtain a tractable expression (see Eq.(6.45) in Ref. 72) reinterpreted in Eq. (4.2) as a function of number of particles N, volume V and temperature T.

$$\begin{aligned} a^{\mathrm{ideal}} &= -1 + \sum_i^n x_i \ln(\rho_i \left[\Lambda_i(T)\right]^3) \\ &= -1 + \sum_i^n \frac{N_i}{N} \ln\left(\frac{N_i}{V} \left[\Lambda_i(T)\right]^3\right) \end{aligned} \tag{4.2}$$

where x_i is the mole fraction, ρ_i the number density and $\Lambda(T)$ the de Broglie wavelength of component i in the mixture of n components.* Λ^3 is often

*The equivalent expression in Lafitte *et al.*[14] misses brackets (Eq.(A1) therein), which is corrected in Papaioannou *et al.*[16] in Eq.(5).

referred to as the de Broglie volume.

For a monoatomic system, there are no rotational and vibrational contributions. For non-spherical multi-atomic compounds (e.g., polymers) the rotational and vibrational terms are not composition dependent, but only temperature dependent. The rotational and vibrational parts, therefore, cancel for composition and volume derivatives of the Helmholtz free energy (chemical potential, pressure, compressibility), but need to be considered for temperature derivatives (entropy, heat capacity, speed of sound). As we are not concerned with differences between states of different temperatures (apart from heat capacities in a later chapter where we will address the ideal contribution again), the rotational and vibrational contributions are neglected here.[179] The expression of de Broglie volume of monoatomic particles is used in our implementation for simplicity. As intended, the vibrational and rotational contributions are neglected, as monoatomic particles possess no rotational and vibrational degrees of freedom.

$$\Lambda_i = \frac{h}{\sqrt{2\pi m_{\mathrm{w},i} k_\mathrm{B} T}}. \tag{4.3}$$

where h is the Planck constant and $m_{\mathrm{w},i}$ the molar weight of compound i. As expected, Eq. (4.2) reduces to the ideal gas equation when expressed in terms of pressure

$$P = -\left(\frac{\partial A^{\mathrm{ideal}}}{\partial V}\right)_{N,T} = \frac{N k_\mathrm{B} T}{V} \tag{4.4}$$

For the implementation of the ideal Helmholtz free energy the separation of component-dependent from component-independent terms simplifies computations and allows one to provide N and V as logarithmic values $\ln N$ and $\ln V$, which can help improve numerical evaluations at extremely small and large N and V. For polymeric systems, where very small mole fractions are common, the logarithmic input can improve the stability of the returned

a^{ideal} values as exemplified in Eq. (4.5).

$$\begin{aligned} a^{\text{ideal}} &= -1 + \sum_i \frac{N_i}{N} \left(\ln N_i - \frac{3}{2} \ln m_i - \ln V - \frac{3}{2} \ln T + \ln \left(\frac{h}{\sqrt{2\pi k_\text{B}}} \right)^3 \right) \\ &= - \ln V - \frac{3}{2} \ln T - 1 + \ln \left(\frac{h}{\sqrt{2\pi k_\text{B}}} \right)^3 + \sum_i \frac{N_i}{N} \left(\ln N_i - \frac{3}{2} \ln m_i \right) \end{aligned} \tag{4.5}$$

The de Broglie volume here was chosen for a monoatomic particle for simplicity. It was not completely dropped (or set equal to unity) to retain the consistency of units. To accurately describe the temperature-dependent ideal contribution of chain models, such as needed for the heat capacity of polymers, all vibrational and rotational contributions have to be expressed in the de Broglie volume. Alternatively, the ideal contributions to the heat capacity are not obtained from the SAFT expressions but are taken from empirical data.[9,10] However, for properties at constant temperature, such as for densities, pressure and phase equilibria, the de Broglie volume is not important as long as it is used consistently for all compounds and phases. The simplest expression for the ideal Helmholtz energy (by dropping temperature-dependent and volume- and particle-number-*in*dependent terms) accounting for volume and concentration contributions is

$$a^{\text{ideal}} = - \ln \frac{V}{\text{nm}^3} + \sum_i \left(\frac{N_i}{N} \ln N_i \right). \tag{4.6}$$

4.3.4 Effective hard-sphere diameter

The effective hard-sphere diameter, d_{ij}, is a temperature-dependent parameter for the monomer size and is obtained by the integration of the Boltzmann factors of the Mie potential from the particle centre, $r = 0$, to the bond length

distance, $r = \sigma$.

$$d_{ij} = \int_0^{\sigma_{ij}} \left(1 - \exp\left(-\frac{u_{ij}^{\mathrm{Mie}}(r)}{k_{\mathrm{B}}T}\right)\right) \mathrm{d}r \tag{4.7}$$

$$= \sigma_{ij} - \int_0^{\sigma_{ij}} \exp\left(-\frac{u_{ij}^{\mathrm{Mie}}(r)}{k_{\mathrm{B}}T}\right) \mathrm{d}r \tag{4.8}$$

where $u_{ij}^{\mathrm{Mie}}(r)$ is the Mie potential between monomers i and j at a distance r. The diameter is used for the sphere size in the hard-sphere reference fluid (zeroth-order perturbation). The diameter d is temperature and Mie-potential-dependent, and is therefore not a constant during a typical set of Helmholtz energy calculations. But in calculations at constant temperature and constant Mie potential, it is transferable across other variables such as composition, pressure and number of components.

The function, which will be integrated to obtain d_{ij}, is almost constant in the integration interval, but drops sharply close to $r = \sigma$ (see Fig. 4.5). The shape of the integration area approaches a rectangular shape for increasing Mie potential parameters. Integration areas are plotted in Fig. 4.5 for three different Mie potentials.

The fully expanded expression of the effective hard-sphere diameter:

$$d_{ij} = \sigma_{ij} - \int_0^{\sigma_{ij}} \exp\left(-\frac{\epsilon}{k_{\mathrm{B}}T}\frac{\lambda_{\mathrm{r}}}{\lambda_{\mathrm{r}} - \lambda_{\mathrm{a}}}\left(\frac{\lambda_{\mathrm{r}}}{\lambda_{\mathrm{a}}}\right)^{\frac{\lambda_{\mathrm{a}}}{\lambda_{\mathrm{r}}-\lambda_{\mathrm{a}}}}\left[\left(\frac{\sigma}{r}\right)^{\lambda_{\mathrm{r}}} - \left(\frac{\sigma}{r}\right)^{\lambda_{\mathrm{a}}}\right]\right) \mathrm{d}r \tag{4.9}$$

helps in realising that an analytical integration is not straight forward. The python sympy package does not find a solution to the slightly simplified equation:

$$d^* = \int \exp\left(-r^{-\lambda_{\mathrm{r}}} + r^{-\lambda_{\mathrm{a}}}\right) \mathrm{d}r. \tag{4.10}$$

The solution for the even simpler expression $\int \exp(r^{-\lambda})\mathrm{d}r$ involves the complete and incomplete gamma functions hinting at the complexity of solving the full integral.

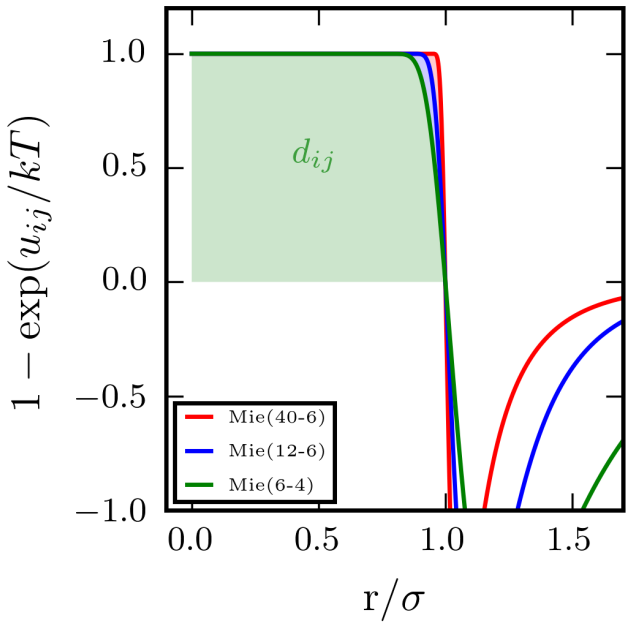

Figure 4.5: The effective hard-sphere diameter integral for three different Mie potentials for $\epsilon/k_{\mathrm{B}}T = 1$.

Hence, a numerical evaluation of the integral is pursued, instead. Refs 14, 16,180 report using the Gauss–Legendre quadrature method for the numerical evaluation of the effective hard-sphere diameter integral. In the following our results with the Gauss–Legendre quadrature and the technical possibilities in applying it to determine the effective hard-sphere diameter are described.

Application of NAG routines for constants and integration

We have used the NAG routine D01ARF,[181] which offers the integration of finite integrals with a method by Patterson[182] to a specified accuracy. The NAG routine produces accurate integrals for repulsive potentials of moderate steepness. For highly-repulsive Mie potentials, however, which have steeper potentials than the (24–6) Mie potential (tested with $\sigma = 0.4\,\mathrm{nm}$, $\epsilon/T \approx 1$), results are returned with errors up to 2% even if higher accuracies are requested. The NAG routine converged at its first iteration, being a 3-point Gauss–Legendre quadrature. Dividing the interval into parts, which were then integrated by D01ARF individually, could not prevent the early

convergence. As the SAFT-VR Mie 2013 theory is parametrised for highly-repulsive potentials up to $\lambda_r = 100$, the standard NAG routine for Gaussian quadrature is unfit for this integration.

Application of NAG routines for constants only

To manually set the number of points used in the integration scheme, we only partially used NAG routines for the evaluations. The Gaussian quadrature is a two-step evaluation. First, the parameters for the requested accuracy (number of points) are calculated, and secondly the actual evaluation of the integral is performed. For the first task, the NAG routine D01BCF[181] can be used to generate the weights and abscissae for any number of points. The actual quadrature integration was then performed with our own implementation without the help of a NAG routine. This allowed the number of points to be set manually and to obtain better accuracy.

In Figure 4.6 the effective hard-sphere diameter results are given as a function of the repulsiveness of the (λ_r–6) Mie potential for several different numbers of points of the Gauss–Legendre algorithm. It can be seen, that significant differences occur up to a 20-point quadrature. We can support the results by Paricaud[180] who found a 10-point quadrature sufficient for the (12–6) Lennard–Jones potential. However, our results are in contrast to the recommendation of Papaioannou *et al.*[16] who reported a 5-point Gauss–Legendre quadrature to be sufficient.

Application of Jacobi as alternatives to Legendre

The Gauss–Legendre quadrature almost equally spaces the function evaluations across the integration interval. A higher concentration of function evaluations toward the upper integration boundary is expected to improve the accuracy of the integration.

We have looked for other types of quadrature integration schemes, where in particular the Gauss–Jacobi quadrature was tested. The Gauss–Jacobi quadrature approximates functions which have singularities in the integration interval. Gauss–Jacobi is a generalised Gauss–Legendre quadrature. We investigated whether this scheme could better approximate the steep decrease at the upper boundary. Slightly better accuracies are only obtained for a very small number of conditions, overall the accuracies are improved by adjusting

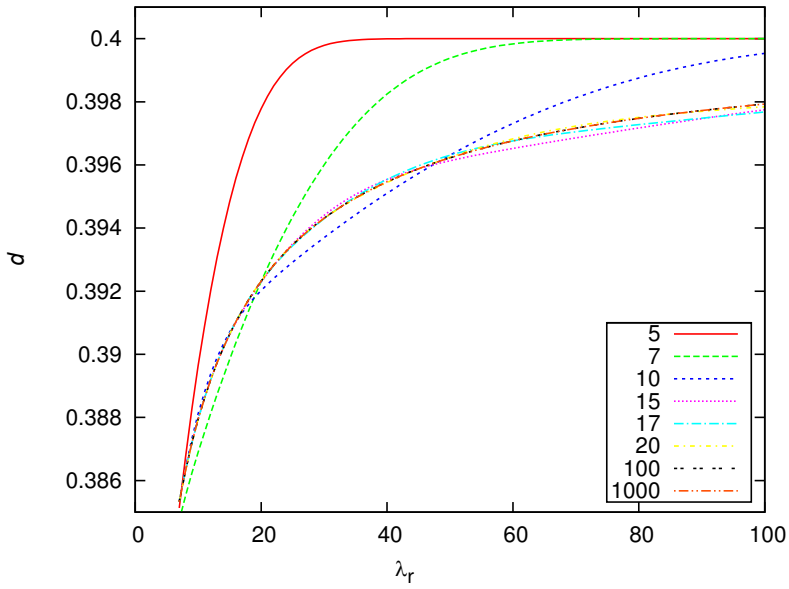

Figure 4.6: Effective hard-sphere diameter d in units of nm as a function of repulsive exponent λ_r of the (λ_r–6) Mie potential ($\sigma = 0.4\,\mathrm{nm}$, $\epsilon/k_\mathrm{B}T = 1$). The integrals are evaluated for several different numbers of points (see legend) of the Gauss–Legendre algorithm. More points in the integration lead to higher accuracies.

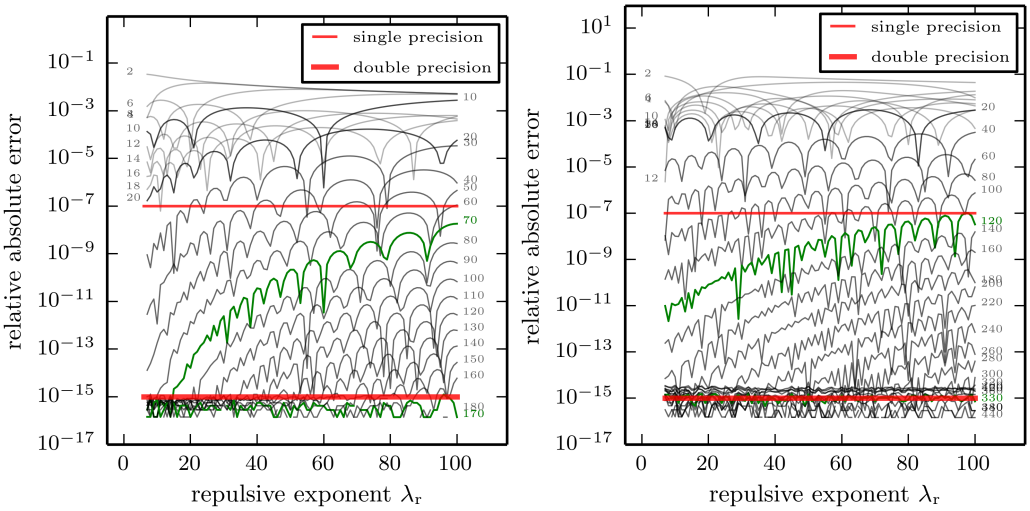

Figure 4.7: Relative error of effective hard-sphere diameter d for (left) typical parameters $\epsilon/k_\mathrm{B}T = 1$, $\lambda_a = 6$ and (right) challenging parameters $\epsilon/k_\mathrm{B}T = 0.001$, $\lambda_a = 30$ as a function of the repulsive exponent λ_r. The curves differ by the number of Gauss–Legendre quadrature points (integrand function calls) used to evaluate the integral, which are printed either at the start or end of the curve. Relative absolute errors are calculated with respect to a 30,000-point Gauss–Legendre quadrature ($|d_{30000} - d|/d_{30000}$), which is assumed exact in this context. The minimum error level of single and double precision is roughly highlighted by horizontal red lines. The data shows decreasing levels of error for increasing the number of points in the Gauss–Legendre quadrature integration.

the Gauss–Jacobi settings towards the values which correspond to the Gauss–Legendre quadrature. Interesting to note is that the sensitivity of accuracy with respect to the repulsive exponent vanishes in the Gauss–Jacobi scheme, while the Gauss–Legendre method offers smaller errors for smaller repulsive exponents (see Fig. 4.6). Overall no improved accuracy was found for the Gauss–Jacobi quadrature.

Approach independent of NAG routines

The integration scheme that is currently implemented is the Gauss–Legendre integration, for which the abscissae and weights are calculated via a Numerical Recipe (NR) routine[183] or read in from a file, and the integration is performed with our implementation. Using the NR routine makes the evaluation of d independent of NAG libraries and in the case of reading the abscissae and weights from a precalculated file even independent of external libraries.

The relative error of d was analysed as a function of its parameters ϵ, T, λ and σ. The relative error increases with decreasing $\epsilon/k_\mathrm{B}T$ ratio and increasing Mie potential exponents λ. The relative error as a function of number of quadrature points and λ_r is shown in Fig. 4.7 for a typical and a challenging set of values for the other parameters. For obtaining relative errors smaller than 10^{-14} (corresponding to double precision accuracy) for all tested combinations of Mie potential parameters and temperature more than 330 quadrature points were required. Our SAFT implementation therefore uses 330 points in the Gauss–Legendre quadrature for approximating the effective hard-sphere diameter d.

4.3.5 Sutherland potential

We used the data for the first-order term of a Sutherland fluid[†] a_1^S by Lafitte *et al.*[14] to evaluate our implementation of a_1^S. Figure 3 therein[14] is reproduced in the right column in Fig. 4.8 which perfectly agrees with results from our implementation given in the left column.

[†]The Sutherland potential comprises a short-range hard-core part (infinite energy) and a long-range attractive part of inverse power law.

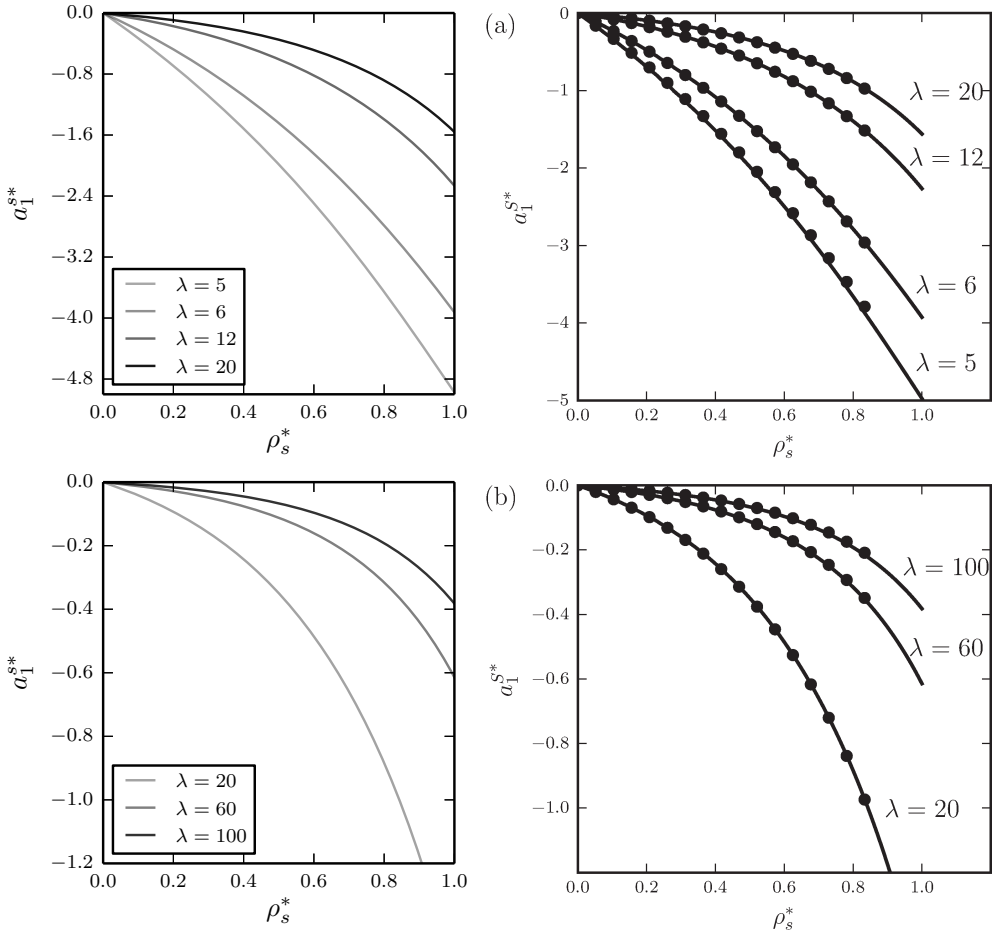

Figure 4.8: Sutherland potential $a_1^{\mathrm{S}*} = a_1^{\mathrm{S}}/\epsilon$ at different repulsive exponents λ. The right column of figures is taken from Ref. 14. The density, which is plotted in reduced units as $\rho_{\mathrm{s}}^* = N_{\mathrm{s}}\sigma_{\mathrm{S}}^3/V$ is reduced by σ_{S}, which is the particle size of the Sutherland potential (not σ of the Mie potential). In the SAFT-VR Mie notation for which the Sutherland potential is used as a perturbation, the Sutherland particle size is the effective hard-sphere diameter d. For consistency with the SAFT-VR Mie notation the reduced density is $\rho_{\mathrm{s}}^* = N_{\mathrm{s}}d^3/V$.

4.3.6 Monomer contribution

The monomer contribution a^{mono} to the Helmholtz free energy is calculated as a sum of the hard-sphere reference fluid contribution and three perturbations. The multi-component hard-sphere reference fluid is described by the expression of Boublík[150] and Mansoori et al.[121] (BM), which is the multi-component form of the pure-component Carnahan–Starling (CS) expression

$$a^{\text{HS,CS}} = \frac{4\eta - 3\eta^2}{(1-\eta)^2}, \tag{4.11}$$

where $\eta = \rho_S \pi d^3/6$ is the packing fraction of the hard-sphere fluid.[14] Our implementation of the hard-sphere expression was tested for the consistency between pure and multi-component expressions. Our BM expression correctly agrees with the CM expression for pure-component systems for all tested packing fractions.

In Fig. 4.9 our implementation of the perturbation terms to the hard-sphere fluid are compared with the data by Lafitte *et al.*[14] Agreement for all Mie potentials is found.

The SAFT program allows the automatic generation of Figures 4.8 and 4.9 as a test routine.The results are compared with reference values to test the SAFT core equations.

4.3.7 Chain contribution

The chain contribution a^{chain} to the SAFT-VR Mie Helmholtz energy uses derivatives of the first and second perturbation terms with respect to density, $\frac{\partial a_{1,ij}}{\partial \rho_S}$ and $\frac{\partial (a_{2,ij}/(1+\chi_{ij}))}{\partial \rho_S}$ (see Eq.(A35) and (A36) in Ref. 14). Recent SAFT-VR Mie[14,174] and SAFT-γ[16,184] publications do not provide analytical expressions and do not mention if their implementation employs numerical or analytical expressions. In this section we provide analytical expressions for these two first-order derivatives and present results for comparison against numerical calculations (See Fig. 4.10). The analytical derivatives were produced to improve the reliability of the SAFT implementation and speed up the code execution.

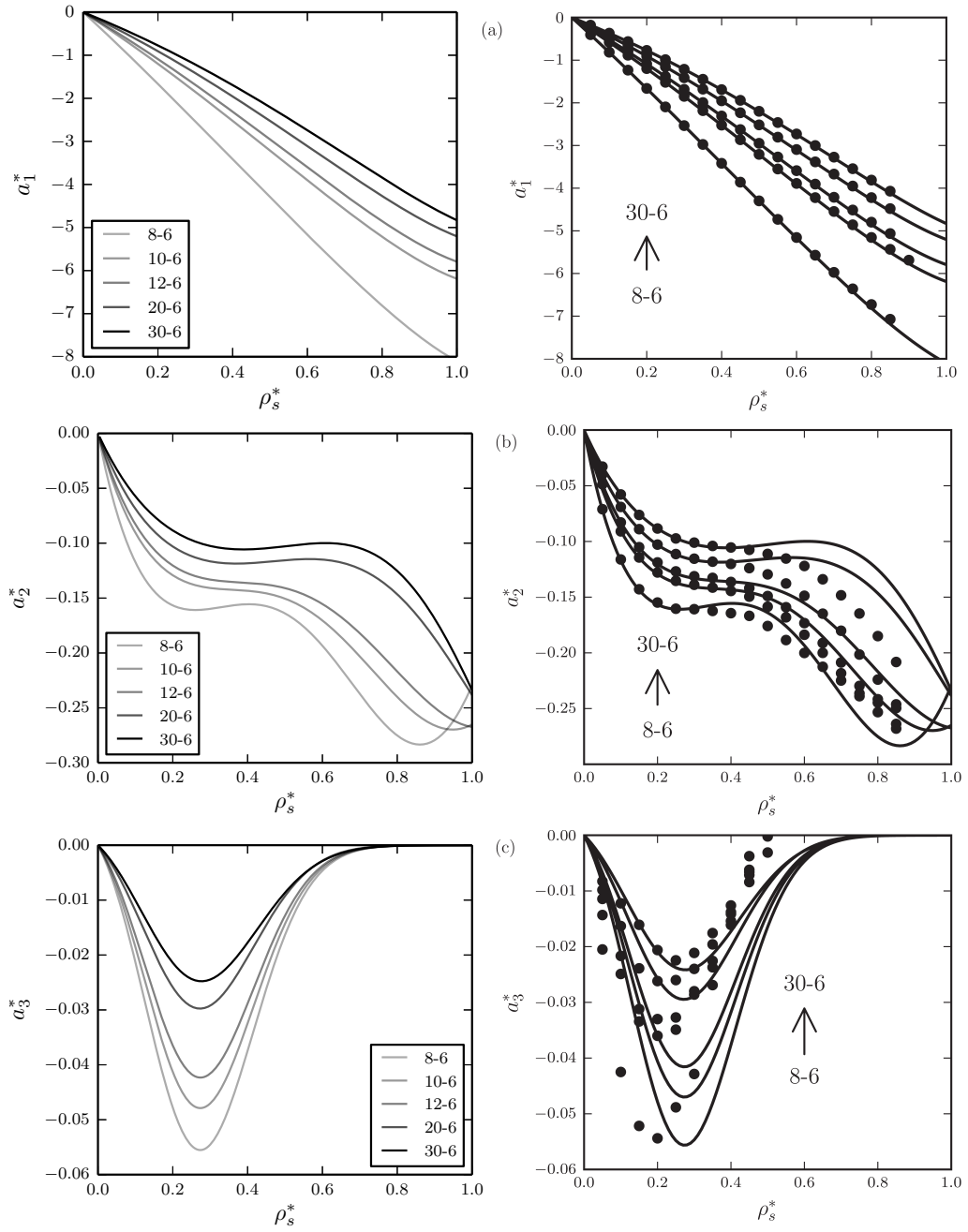

Figure 4.9: Comparison of our implementation (left column) and reproduced figures from Lafitte *et al.*[14] (Figure 2 therein) (right column) for the first $a_1^* = a_1/\epsilon$ (top), second $a_2^* = a_2/\epsilon^2$ (middle) and third $a_3^* = a_3/\epsilon^3$ (bottom) Barker and Henderson perturbation terms for different Mie potentials (8-6),(12-6),(14-6),(20-6) and (30-6) at a temperature $T^* = k_\mathrm{B}T/\epsilon = 1$. The circles in the figures taken from Ref. 14 represent values determined by Monte Carlo simulation.

Density derivatives

The density derivatives are provided for the SAFT-VR Mie theory, but can be easily converted to SAFT-γ Mie expressions with the steps summarised in the next section.

The first derivative of the pair-wise first-order perturbation $a_{1,ij}$ of the monomer term of SAFT-VR Mie a_1^{mono} with respect to the segment number density ρ_s used in the chain term a^{chain}

$$\begin{aligned}\frac{\partial a_{1,ij}}{\partial \rho_s} = C_{ij}\Bigg[& x_{0,ij}^{\lambda_{\text{a},ij}}\left(\frac{\partial}{\partial \rho_s}a_{1,ij}^{\text{S}}(\rho_s;\lambda_{\text{a},ij}) + \frac{\partial}{\partial \rho_s}B_{ij}(\rho_s;\lambda_{\text{a},ij})\right) \\ & -x_{0,ij}^{\lambda_{\text{r},ij}}\left(\frac{\partial}{\partial \rho_s}a_{1,ij}^{\text{S}}(\rho_s;\lambda_{\text{r},ij}) + \frac{\partial}{\partial \rho_s}B_{ij}(\rho_s;\lambda_{\text{r},ij})\right)\Bigg]\end{aligned} \tag{4.12}$$

The first derivative of the quantity B_{ij} with respect to the segment number density ρ_s

$$\begin{aligned}\frac{\partial B_{ij}}{\partial \rho_s} = C\Bigg(& \left[\frac{1-\zeta_x/2}{(1-\zeta_x)^3} + \frac{(2.5\zeta_x - \zeta_x^2)}{(1-\zeta_x)^4}\right] I_{ij}(\lambda) \\ & - \left[\frac{9(\zeta_x+\zeta_x^2)}{2(1-\zeta_x)^3} + \frac{9(\zeta_x+4\zeta_x^2+\zeta_x^3)}{2(1-\zeta_x)^4}\right] J_{ij}(\lambda)\Bigg),\end{aligned} \tag{4.13}$$

with

$$\zeta_x = \frac{\pi\rho_s}{6}\sum_{i=1}^{n}\sum_{j=1}^{n} x_{s,i}x_{s,j}d_{ij}^3, \tag{4.14}$$

and

$$\frac{\partial \zeta_x}{\partial \rho_s} = \frac{\zeta_x}{\rho_s}. \tag{4.15}$$

The first derivative with respect to the segment number density ρ_s of the

first-order perturbation to the Sutherland potential is

$$\frac{\partial}{\partial \rho_{\mathrm{s}}} a^{\mathrm{S}}_{1,ij}(\rho_s;\lambda) = -2\rho_s \left(\frac{\pi \epsilon_{ij} d_{ij}^3}{\lambda - 3}\right)\left[F(\lambda) + \rho_s \frac{\partial F(\lambda)}{\partial \rho_s}\right] \tag{4.16}$$

where

$$F(\lambda) = \frac{1 - \zeta_x^{\mathrm{eff}}(\lambda)/2}{(1-\zeta_x^{\mathrm{eff}}(\lambda))^3} \tag{4.17}$$

and

$$\frac{\partial F(\lambda)}{\partial \rho_s} = -\frac{\partial \zeta_x^{\mathrm{eff}}(\lambda)}{\partial \rho_s}\left[\frac{\zeta_x^{\mathrm{eff}}(\lambda) - 2.5}{(1-\zeta_x^{\mathrm{eff}}(\lambda))^4}\right]. \tag{4.18}$$

The first derivative with respect to the segment number density ρ_{s} of the pair-wise second-order perturbation of the monomer term reduced by $(1+\chi)$

$$\frac{\partial \frac{a_{2,ij}}{1+\chi_{ij}}}{\partial \rho_s} = \frac{1}{2}\epsilon_{ij} C_{ij}^2 \left(\frac{\partial K^{\mathrm{HS}}}{\partial \rho_s} D + K^{\mathrm{HS}} \frac{\partial D}{\partial \rho_s}\right) \tag{4.19}$$

where

$$\begin{aligned} D =& x_{0,ij}^{2\lambda_{\mathrm{a},ij}} \left(a^{\mathrm{S}}_{1,ij}(\rho_s; 2\lambda_{\mathrm{a},ij}) + B_{ij}(\rho_s; 2\lambda_{\mathrm{a},ij})\right) \\ &- 2x_{0,ij}^{\lambda_{\mathrm{a},ij}+\lambda_{\mathrm{r},ij}} \left(a^{\mathrm{S}}_{1,ij}(\rho_s; \lambda_{\mathrm{a},ij}+\lambda_{\mathrm{r},ij}) + B_{ij}(\rho_s; \lambda_{\mathrm{a},ij}+\lambda_{\mathrm{r},ij})\right) \\ &+ x_{0,ij}^{2\lambda_{\mathrm{r},ij}} \left(a^{\mathrm{S}}_{1,ij}(\rho_s; 2\lambda_{\mathrm{r},ij}) + B_{ij}(\rho_s; 2\lambda_{\mathrm{r},ij})\right), \end{aligned} \tag{4.20}$$

$$\begin{aligned} \frac{\partial}{\partial \rho_s} D =& x_{0,ij}^{2\lambda_{\mathrm{a},ij}} \left(\frac{\partial}{\partial \rho_s} a^{\mathrm{S}}_{1,ij}(\rho_s; 2\lambda_{\mathrm{a},ij}) + \frac{\partial}{\partial \rho_s} B_{ij}(\rho_s; 2\lambda_{\mathrm{a},ij})\right) \\ &- 2x_{0,ij}^{\lambda_{\mathrm{a},ij}+\lambda_{\mathrm{r},ij}} \left(\frac{\partial}{\partial \rho_s} a^{\mathrm{S}}_{1,ij}(\rho_s; \lambda_{\mathrm{a},ij}+\lambda_{\mathrm{r},ij}) + \frac{\partial}{\partial \rho_s} B_{ij}(\rho_s; \lambda_{\mathrm{a},ij}+\lambda_{\mathrm{r},ij})\right) \\ &+ x_{0,ij}^{2\lambda_{\mathrm{r},ij}} \left(\frac{\partial}{\partial \rho_s} a^{\mathrm{S}}_{1,ij}(\rho_s; 2\lambda_{\mathrm{r},ij}) + \frac{\partial}{\partial \rho_s} B_{ij}(\rho_s; 2\lambda_{\mathrm{r},ij})\right), \end{aligned} \tag{4.21}$$

and the quantity B_{ij} is given by

$$B_{ij} = C\left(\rho_s \frac{1-\zeta_x/2}{(1-\zeta_x)^3} I_{ij}(\lambda) - \rho_s \frac{9(\zeta_x + \zeta_x^2)}{2(1-\zeta_x)^3} J_{ij}(\lambda)\right) \tag{4.22}$$

and the first-order perturbation to the Sutherland potential is

$$a_{1,ij}^{\mathrm{S}}(\rho_s;\lambda) = -2\rho_s \left(\frac{\pi\epsilon_{ij}d_{ij}^3}{\lambda-3}\right) F(\lambda). \tag{4.23}$$

The isothermal compressibility of the hard-sphere reference fluid is

$$K^{\mathrm{HS}} = \frac{(1-\zeta_x)^4}{E}, \tag{4.24}$$

with

$$E = 1 + 4\zeta_x + 4\zeta_x^2 - 4\zeta_x^3 + \zeta^4, \tag{4.25}$$

and its first derivative

$$\frac{\partial}{\partial\rho_s}K^{\mathrm{HS}} = \frac{-4\zeta_x(1-\zeta_x)^3\Big(E + (1-\zeta_x)(1+2\zeta_x-3\zeta_x^2+\zeta_x^3)\Big)}{\rho_{\mathrm{s}}E^2}. \tag{4.26}$$

For details and expressions of the quantities χ, x_0, $I_{ij}(\lambda)$, $J_{ij}(\lambda)$, C_{ij}, ζ_x^{eff} see Refs 14,16.

Numerical data for the density derivatives $\frac{\partial a_{1,ij}}{\partial\rho_{\mathrm{s}}}$ and $\frac{\partial(a_{2,ij}/(1+\chi_{ij}))}{\partial\rho_{\mathrm{s}}}$ showing agreement between the results using the analytic expressions above and the numerical derivatives using finite differences is shown in Fig. 4.10.

Discrepancy for RDF at bond length

To account for the chain character of molecules, the radial distribution function of the monomer fluid is evaluated at the segment-diameter distance σ. The magnitude of this contact value $g^{\mathrm{Mie}}(\sigma)$ is given as a function of density for the Mie (12-6) and (30-6) potential in Figure 4c in Lafitte *et al.*[14] The figure is reprinted in this work in Fig. 4.11. Values obtained by our implementation for $g^{\mathrm{Mie}}(\sigma)$ agree with the reference results apart from a small deviation at $\rho_{\mathrm{S}}^* = 0.2$ for the steeper Mie (30-6) potential. The deviation is highlighted in Fig. 4.11 by a (red) arrow.

A fully independent code for $g^{\mathrm{Mie}}(\sigma)$ has been developed within Maple

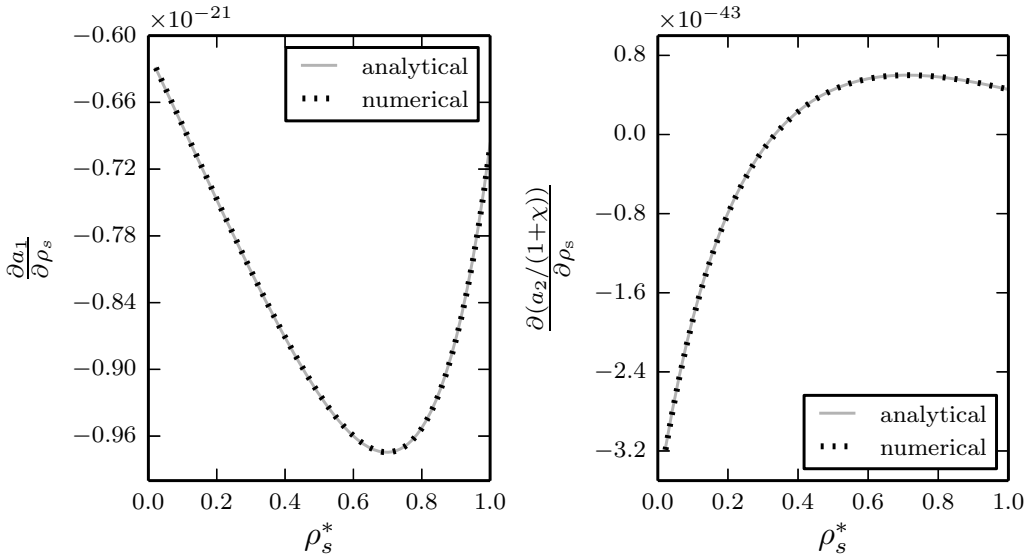

Figure 4.10: Comparison of analytical and numerical evaluations of the first derivatives of a_1 and a_2 with respect to number density of monomer particles ρ_s plotted against volume density of monomer particles $\rho_s^* = \rho_s \sigma^3$.

to analyse this deviation. The Maple code perfectly agrees with the results of the Fortran code (see Fig. 4.11). The authors E. Müller, G. Jackson and T. Lafitte have recalculated $g^{\text{Mie}}(\sigma)$ and confirmed our results to be correct. Their recalculated graph is shown in Fig. 4.11.

4.4 Converting SAFT-VR Mie to SAFT-γ Mie

A generalised version of the SAFT-VR Mie has been published in 2014 called SAFT-γ Mie.[16] In comparison to SAFT-VR Mie it allows a description of chains that consist of more than one type of Mie-potential spheres (heteronuclear model), see Fig. 4.12. A set of identical monomers can also be combined in a "group", which is described with two additionally parameters, that is the number of beads in the group, and a shape factor, which scales the contribution of the group to the molecular properties. The heteronuclear description allows the use of more detailed force fields. Another advantage is that pure-component data can be used to parametrise unlike interactions by using a model containing the two types of beads of interest. The parametrisation of

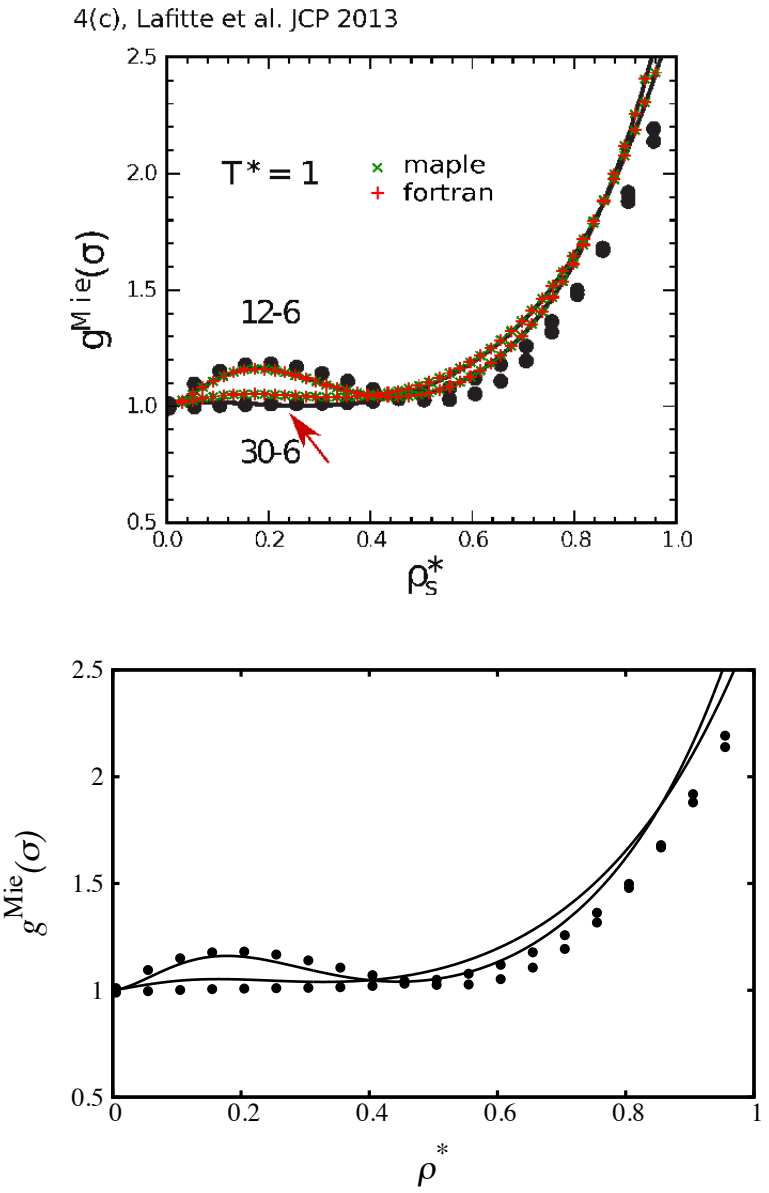

Figure 4.11: Contact value of the radial distribution function $g^{\text{Mie}}(\sigma)$ for the Mie (12-6) and (30-6) potential at a temperature $T^* = 1$. (Top) The results of our independent Fortran and Maple codes are overlaid in colour on Fig.4c from Ref. 14. The deviation is highlighted with an arrow. (Bottom) Recalculated results by Jackson *et al.*[185] Circles represent results by Monte Carlo simulations, see Ref.[14] for further details. Results by the SAFT-VR Mie expressions are represented by (top and bottom) continuous lines calculated by the Imperial College London group and (top) "x/+" calculated as part of this work.

unlike interactions based on pure-component data improves the prediction of unlike interactions in mixtures.[16]

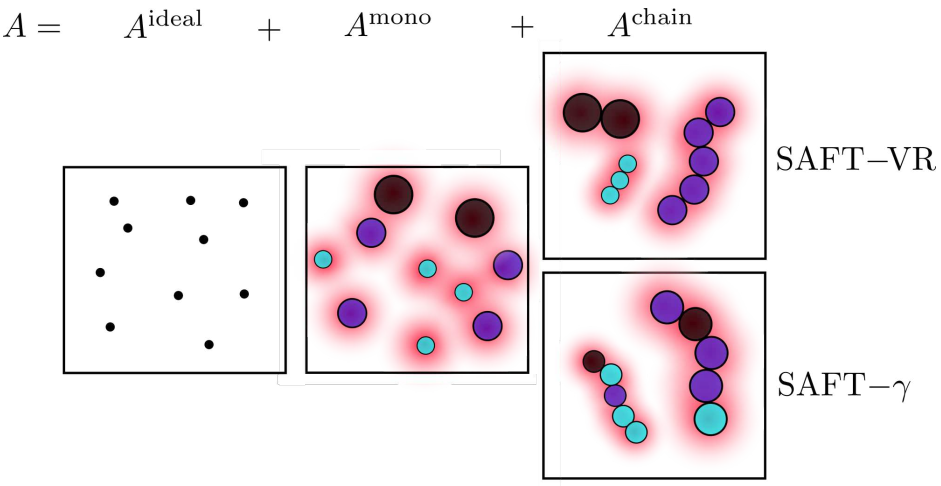

Figure 4.12: Visual representation of SAFT contributions, comparing SAFT-VR and SAFT-γ. SAFT-VR allows only one type of bead (Mie potential) per chain, while SAFT-γ models can be heterogeneous chains with different bead types (Mie potentials). In the chain term, the Mie potential types are averaged to a homogeneous description. SAFT-γ models can not capture in which order beads are in chains, but it is captured as an average of all combinations. One exception is the SAFT-γ version of McCabe and coworkers,[126,186] which they name GC-SAFT-VR. This SAFT version can capture the order of beads by using the number of bonds separating groups.

A list of the most important changes from VR to γ from a functionality perspective:

- Units/building blocks are called "**groups**" in SAFT-γ Mie, which increases flexibility for parameter estimations and makes setting up calculations easier.
- A group has **two more parameters** (6 in total) than the Mie potential in SAFT-VR Mie (4 in total).
- New parameters: **number of beads** ν per group and **shape factor** S_k, the product of both gives the number of beads of the group. While ν is typically a positive integer number, S_k is typically a floating point

number between zero and one. ν values larger than one are used for larger functional groups such as esters or when whole molecules are captured in one group, S_k values smaller than one are used for groups overlapping with other groups to capture fused connections such as for CH_2 groups ($S_{CH_2} = 0.22932$) in an alkane chain compared to methane ($S_{CH_4} = 1$).[16]

- Although 6 parameters per group are available, typically **only 4 parameters are optimised**. The parameters ν and S_k are not independent, only their product is. This reduces the overall available number to 5. The λ exponents are not fully independent, either. Most parameter estimation efforts[6,14,16,115,151] chose $\lambda_a = 6$ and only optimised λ_r, which reduces the overall number to 4. To summarize, the 4 remaining parameters influence the potential well depth (ϵ), the bead diameter (σ), the potential steepness/hardness (λ_r) and non-sphericity (number of beads, νS_k).

- Different bead types (now group types) can be combined in a single chain: Chains are still calculated as made of a single bead type, but now it is the weighted average of the monomer types, which effectively captures the **heterogeneity**.

While a version of a SAFT-γ EoS (using square-well potentials rather than Mie potentials) was already published in 2007,[15] which captured chain heterogeneity and the shape factor S_k, the SAFT-γ Mie 2014 is the first version to introduce ν for groups of more than one bead. The ν parameter is effectively part of the shape factor or the number of groups in SAFT-γ in the 2007 version. All three parameters have a similar effect, they change the number of beads per chain.

SAFT-γ Mie reduces to SAFT-VR Mie when compounds consist of only one group type (no heterogeneity) and the product of number of groups per chain and νS_k is used as n in SAFT-VR Mie.

The changes necessary to convert the Fortran SAFT-VR Mie code to a SAFT-γ Mie code can be summarised as renaming and addition of new variables. Additional variables are added for the new parameters (S_k,ν), for the

molecule-averaged parameters (denoted by a subscript z in our implementation because the molecular fraction z is used in Ref. 16) used in the chain contribution, and for the additional indices as groups and compounds are differentiated (i, j and k, l). The z-averaged variables are only component i specific, not bead pair k, l specific, and therefore have one fewer dimension. New adjusted copies of functions such as B and a_1^{S} are added to work with arguments of fewer dimensions.

4.5 Derived properties

In this section the approach to calculate derivative properties of the Helmholtz energy is presented. While analytical expressions can be obtained for at least the most part of the SAFT-VR Mie and SAFT-γ Mie equation, the complexity of the equation of state makes deriving *analytical* derivatives of the Helmholtz free energy a non-trivial task. We have developed *numerical* derivatives for the thermodynamic properties of interest instead. Numerical derivatives allow faster development of new derivatives and fewer additional lines of code. They offer also a more flexible implementation for future changes to the underlying equation of state as the derivatives only change with the set and shape of input variables, but not with other changes of the equation of state. For most changes of the equation of state, no changes of the numerical derivative code is needed.

A disadvantage of numerical over analytical derivatives is that extreme conditions and extreme input parameters can lead to less accurate results and have to be accounted for explicitly. Special considerations at extreme conditions and close to conditions where the Helmholtz free energy can not be evaluated will be reported in this chapter. Another disadvantage of numerical derivatives are often the longer execution times.

Beyond pure numerical derivatives, the cheapest improvements can be obtained by calculating the ideal contributions analytically. This improves in particular the performance in extreme conditions. In this work all ideal contributions are therefore calculated analytically. The equations are given in this section.

The derivative-property relations in this chapter are reported in normal and reduced units (reduced by RT) as the quantities in our implementation use these reduced units throughout.[‡] The notation for reduced variables used in this work is, that lower case letters represent variables reduced by RT, upper case represent unreduced variables. We use M for chemical potential and C for heat capacity to be consistent in the notation, and even reduce S and C_P by RT to be consistent in the conversion factor:

$$A/(RT) = a \tag{4.27}$$
$$G/(RT) = g \tag{4.28}$$
$$S/(RT) = s \tag{4.29}$$
$$H/(RT) = h \tag{4.30}$$
$$P/(RT) = p \tag{4.31}$$
$$M/(RT) = \mu \tag{4.32}$$
$$C_P/(RT) = c_P \tag{4.33}$$

All "ideal" quantities in this work are only translational kinetic ideal contributions, which do not explicitly account for vibrational and rotational motion. For differences between states at the same temperature the vibrational and rotational contributions cancel out, so derivatives with respect to number of particles (chemical potential) and volume (pressure) indirectly account for it. However, temperature derivatives (entropy, heat capacity) and quantities calculated from entropies (enthalpy, heat capacity) can not readily be compared with experimental values, but residual or changes upon mixing should be compared (for which the vibrational and rotational contributions vanish). See Sec. 4.3.3 and 4.5.8 for more details.

For equations of other thermodynamic quantities and similar relations the reader is referred to the text book by Michelsen and Mollerup,[7] which, unlike most other text books, expresses thermodynamic quantities in terms of Helmholtz energies.

[‡]Only in the Helmholtz SAFT core, and right before the quantities are printed to the output, they are handled in different units (see beginning of this chapter for more information on units).

How the thermodynamic quantities are derived from Helmholtz free energies is visualised in Fig. 4.13.

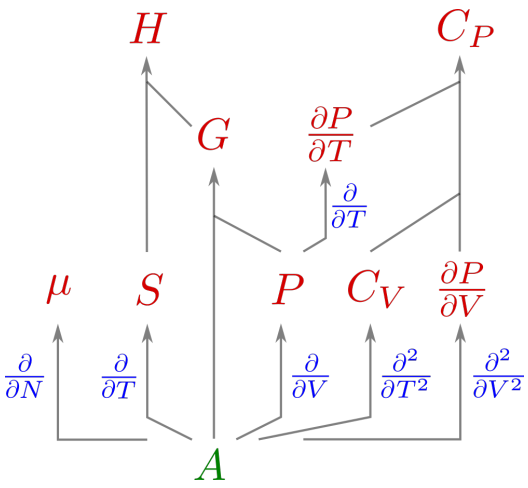

Figure 4.13: Overview of essential connections in the derivation of thermodynamic properties starting from the Helmholtz free energy A in this chapter.

4.5.1 Method

Numerical derivatives are determined from finite-difference approximations of the Helmholtz energy. The most inexpensive finite-difference approximation for the first derivative of function B with respect to x at the position x_0 is

$$\left.\frac{\partial B}{\partial x}\right|_{x_0} = \frac{\frac{1}{2}B(x_0 - h) + \frac{1}{2}B(x_0 + h)}{h} \tag{4.34}$$

where h is the step size. This most inexpensive first-derivative approximation is the 2-point finite-difference approximation. The step size is typically set to be as small as possible to approach the exact limit of a tangent, but large enough to avoid numerical instabilities.

In the same notation, the second derivative can be obtained from

$$\left.\frac{\partial^2 B}{\partial x^2}\right|_{x_0} = \frac{B(x_0 - h) - 2B(x_0) + B(x_0 + h)}{h^2} \tag{4.35}$$

which requires one more evaluation of B than the first derivative in their most inexpensive forms.

The 8-point finite-difference approximation using 8 evaluations of the function B is the default accuracy used in our implementation for both first and second-order derivatives. For function B, the first-order derivative is

$$\begin{aligned}\left.\frac{\partial B}{\partial x}\right|_{x_0} =& \frac{\frac{1}{280}B(x_0-4h)-\frac{4}{105}B(x_0-3h)+\frac{1}{5}B(x_0-2h)-\frac{4}{5}B(x_0-h)}{h} \\ &+\frac{\frac{4}{5}B(x_0+h)-\frac{1}{5}B(x_0+2h)+\frac{4}{105}B(x_0+3h)-\frac{1}{280}B(x_0+4h)}{h}\end{aligned} \tag{4.36}$$

This high level of accuracy is used in this work to minimise errors due to the finite-difference approximation.

As an example, the 8-point finite-difference approximation of the residual Helmholtz free energy with respect to volume, which is the residual pressure, is

$$\begin{aligned}P^{\mathrm{res}}(V_0) =& -\left(\frac{\partial A^{\mathrm{res}}}{\partial V}\right)_{N,T} \\ =& -\left[\frac{\frac{1}{280}A(V_0-4h)-\frac{4}{105}A(V_0-3h)+\frac{1}{5}A(V_0-2h)-\frac{4}{5}A(V_0-h)}{h}\right. \\ &\left.+\frac{\frac{4}{5}A(V_0+h)-\frac{1}{5}A(V_0+2h)+\frac{4}{105}A(V_0+3h)-\frac{1}{280}A(V_0+4h)}{h}\right].\end{aligned} \tag{4.37}$$

The coefficients for finite-difference expressions for the second-order derivative used in our implementation and for other accuracies can be found in Fornberg.[187]

4.5.2 Special adjustments

Special considerations were taken for the derivative with respect to particle number (chemical potential). In comparison to derivatives with respect to volume and temperature, which are typically not of interest at small values (or even zero), the particle number of a compound N_i is regularly set to small

values and also zero for determining chemical potentials. Setting the step size as a fraction of the value of N_i leads to numerical instabilities at small N_i. We implemented a constant step size of 10^{-5}, instead. A constant step size is possible due to the fact that the residual chemical potential approaches a constant value for $N_i \to 0$. For $N_i < 5h$ the finite-difference algorithm changes to a one-sided algorithm, only using function evaluations larger than N_i to avoid calculating non-physical conditions at $N_i < 0$.

We parallelised the numerical derivative evaluation with OpenMP, where all eight function evaluations were calculated on separate threads to investigate the potential speed up. The performance of the parallelised routine gave no significant speed up, which is most likely attributed to the extra initialisation and memory allocation. Numerical derivatives are therefore calculated in serial, while parallelisation is added at a higher level, see Sec. 4.6.

4.5.3 Pressure

Pressure is not an input parameter naturally in the SAFT equations expressed in terms of Helmholtz energies. Pressure can be obtained from the first derivative with respect to the system's volume

$$P^{\text{ideal}} = -\left(\frac{\partial A^{\text{ideal}}}{\partial V}\right)_{N,T} = \frac{RT}{V} \tag{4.38}$$

$$p^{\text{ideal}} = \frac{1}{V} \tag{4.39}$$

$$P^{\text{res}} = -\left(\frac{\partial A^{\text{res}}}{\partial V}\right)_{N,T} \tag{4.40}$$

$$p^{\text{res}} = -\left(\frac{\partial a^{\text{res}}}{\partial V}\right)_{N,T} \tag{4.41}$$

$$P = \frac{RT}{V} - \left(\frac{\partial A^{\text{res}}}{\partial V}\right)_{N,T} \tag{4.42}$$

$$p = \frac{1}{V} - \left(\frac{\partial a^{\text{res}}}{\partial V}\right)_{N,T}. \tag{4.43}$$

4.5.4 Gibbs free energy

Gibbs free energy can be expressed as the sum of Helmholtz energy and product of pressure and volume (PV)

$$\begin{aligned} G^{\text{ideal}} &= A^{\text{ideal}} + (PV)^{\text{ideal}} \\ &= A^{\text{ideal}} + RT, \end{aligned} \tag{4.44}$$

$$\begin{aligned} g^{\text{ideal}} &= a^{\text{ideal}} + (pV)^{\text{ideal}} \\ &= a^{\text{ideal}} + 1. \end{aligned} \tag{4.45}$$

$$\begin{aligned} G^{\text{res}} &= A^{\text{res}} + (PV)^{\text{res}} \\ &= A^{\text{res}} + PV - (PV)^{\text{ideal}} \\ &= A^{\text{res}} + PV - RT \end{aligned} \tag{4.46}$$

$$g^{\text{res}} = a^{\text{res}} + pV - 1 \tag{4.47}$$

$$G = A + PV \tag{4.48}$$

$$g = a + pV \tag{4.49}$$

4.5.5 Chemical potential

Chemical potential is the first derivative of the Helmholtz energy with respect to particle number N_i

$$M_i^{\text{ideal}} = \left(\frac{\partial A^{\text{ideal}}}{\partial N_i}\right)_{V,T,N_{i\neq j}} = \frac{RT}{N}\ln\left(\frac{N_i}{V}\Lambda_i^3\right) \tag{4.50}$$

$$\mu_i^{\text{ideal}} = \frac{1}{N}\left(\frac{\partial (a^{\text{ideal}}N)}{\partial N_i}\right)_{V,T,N_{i\neq j}} = \frac{1}{N}\ln\left(\frac{N_i}{V}\Lambda_i^3\right) \tag{4.51}$$

$$M_i^{\text{res}} = \left(\frac{\partial A^{\text{res}}}{\partial N_i}\right)_{V,T,N_{i\neq j}} \tag{4.52}$$

$$\mu_i^{\text{res}} = \frac{1}{N}\left(\frac{\partial (a^{\text{res}}N)}{\partial N_i}\right)_{V,T,N_{i\neq j}}. \tag{4.53}$$

4.5.6 Entropy

Entropy is the first derivative of the Helmholtz energy with respect to temperature. The equation for the ideal translational entropy is also known as the Sackur–Tetrode equation.[188–192§] Remember the ideal vibrational and rotational contributions are neglected at this stage, which need to be accounted

[§] Which can be derived with Stirling's approximation.

for when comparing states at different temperatures.

$$\begin{aligned} S^{\text{ideal}} &= -\left(\frac{\partial A^{\text{ideal}}}{\partial T}\right)_{V,N} \\ &= \frac{5}{2}RT - RT\sum_i \frac{N_i}{N}\ln\left(\frac{N_i}{V}\Lambda_i^3\right) \\ &= \frac{3}{2}RT - \frac{A^{\text{ideal}}}{T} \end{aligned} \tag{4.54}$$

$$\begin{aligned} s^{\text{ideal}} &= -\frac{1}{T}\left(\frac{\partial (a^{\text{ideal}}T)}{\partial T}\right)_{V,N} \\ &= \frac{5}{2} - \sum_i \frac{N_i}{N}\ln\left(\frac{N_i}{V}\Lambda_i^3\right) \\ &= \frac{3}{2} - \frac{a^{\text{ideal}}}{T} \end{aligned} \tag{4.55}$$

$$S^{\text{res}} = -\left(\frac{\partial A^{\text{res}}}{\partial T}\right)_{N,V} \tag{4.56}$$

$$s^{\text{res}} = -\frac{1}{T}\left(\frac{\partial (a^{\text{res}}T)}{\partial T}\right)_{N,V} \tag{4.57}$$

4.5.7 Enthalpy

Enthalpy can be expressed in terms of Helmholtz energy via the definition of the Gibbs free energy $G = H - TS$

$$\begin{aligned} H^{\text{ideal}} &= G^{\text{ideal}} + TS^{\text{ideal}} \\ &= A^{\text{ideal}} + RT + TS^{\text{ideal}} \end{aligned} \tag{4.58}$$

$$h^{\text{ideal}} = a^{\text{ideal}} + 1 + Ts^{\text{ideal}} \tag{4.59}$$

$$\begin{aligned} H^{\text{res}} &= G^{\text{res}} + TS^{\text{res}} \\ &= A^{\text{res}} + TS^{\text{res}} + PV - RT \end{aligned} \tag{4.60}$$

$$h^{\text{res}} = a^{\text{res}} + Ta^{\text{res}} + pV - 1 \tag{4.61}$$

$$H = A^{\text{ideal}} + A^{\text{res}} + PV + T(S^{\text{ideal}} + S^{\text{res}}) \tag{4.62}$$

$$h = a^{\text{ideal}} + a^{\text{res}} + pV + T(s^{\text{ideal}} + s^{\text{res}}) \tag{4.63}$$

4.5.8 Heat capacity

Heat capacities are second-order derivative quantities with respect to temperature. The ideal part can be approximated as a sum of translational, rotational, vibrational and electronic contributions. Using this approximation, the ideal part can be calculated using statistical mechanics for simple compounds of low molecular weight. For larger molecular weights, however, the vibrational and rotational parts are usually not known from first principles, but different approaches to derive C_V^{ideal} from experimental data are available. In this work we determine the ideal heat capacities from experimental C_P^{ideal} data. C_V^{ideal} are then obtained via

$$C_V^{\text{ideal}} = C_P^{\text{ideal}} - R, \tag{4.64}$$

$$c_V^{\text{ideal}} = c_P^{\text{ideal}} - \frac{1}{T}. \tag{4.65}$$

Heat capacity data c_P^{ideal} have been made available in a group-contribution scheme by Joback and Reid[9] and Coniglio and Daridon,[10] so predictions for almost any chemical structure is possible when data for the chemical moieties is available.

The residual heat capacities can be expressed in terms of Helmholtz energies as

$$C_P^{\text{res}} = T\left(\frac{\partial S}{\partial T}\right)_{p,N} = T\left(\frac{\partial[-\frac{\partial A^{\text{res}}}{\partial T}]_{V,N}}{\partial T}\right)_{p,N} \tag{4.66}$$

$$c_P^{\text{res}} = T\left(\frac{1}{T}\frac{\partial(sT)}{\partial T}\right)_{p,N} = T\left(\frac{1}{T}\frac{\partial[-\frac{\partial(a^{\text{res}}T)}{\partial T}]_{V,N}}{\partial T}\right)_{p,N} = -\left(\frac{\partial[\frac{\partial(a^{\text{res}}T)}{\partial T}]_{V,N}}{\partial T}\right)_{p,N} \tag{4.67}$$

$$C_V^{\text{res}} = T\left(\frac{\partial S}{\partial T}\right)_{V,N} = -T\left(\frac{\partial^2 A^{\text{res}}}{\partial T^2}\right)_{V,N} \tag{4.68}$$

$$c_V^{\text{res}} = T\left(\frac{1}{T}\frac{\partial (sT)}{\partial T}\right)_{V,N} = -T\left(\frac{1}{T}\frac{\partial^2 (a^{\text{res}}T)}{\partial T^2}\right)_{V,N} = -\left(\frac{\partial^2 (a^{\text{res}}T)}{\partial T^2}\right)_{V,N} \tag{4.69}$$

An alternative way of obtaining c_V^{res} in terms of a^{res} is

$$C_V^{\text{res}} = -2RT\left(\frac{\partial (A^{\text{res}}/RT)}{\partial T}\right)_{V,N} - RT^2\left(\frac{\partial^2 (A^{\text{res}}/RT)}{\partial T^2}\right)_{V,N} \tag{4.70}$$

$$c_V^{\text{res}} = -2\left(\frac{\partial a^{\text{res}}}{\partial T}\right)_{V,N} - T\left(\frac{\partial^2 a^{\text{res}}}{\partial T^2}\right)_{V,N} \tag{4.71}$$

Eq. (4.68) and Eq. (4.70) are equivalent. While the first uses the normal Helmholtz energy, the latter takes the derivative of the Helmholtz energy reduced by temperature. The equivalence can be seen from using the following easily-derivable relation

$$\left(\frac{\partial^2 B}{\partial x^2}\right) = 2\left(\frac{\partial (B/x)}{\partial x}\right) + x\left(\frac{\partial^2 (B/x)}{\partial x^2}\right). \tag{4.72}$$

An alternative way of obtaining C_P^{res} based on C_V^{res} is[7]

$$C_P^{\text{res}} = C_V^{\text{res}} - T\left(\frac{\partial P}{\partial T}\right)_{V,N}^2 \left(\frac{\partial P}{\partial V}\right)_{T,N}^{-1} \tag{4.73}$$

$$c_P^{\text{res}} = c_V^{\text{res}} - T\left(\frac{1}{T}\frac{\partial (pT)}{\partial T}\right)_{V,N}^2 \left(\frac{\partial p}{\partial V}\right)_{T,N}^{-1} \tag{4.74}$$

Our implementation provides all equations mentioned in this section for obtaining heat capacities, while the defaults are Eq. (4.68) and Eq. (4.73).

Our heat capacity implementation was validated by reproducing carbon dioxide and n-octane heat capacity (C_P) predictions of Avendaño *et al.* 2011.[6] This high-level property validated equations, units and numerical performance at the same time. While the overall shape and absolute values

of our predictions agreed very well with the predictions found in the figures in Ref. 6, a small number of segments differ by up to a few percent. Determining the cause of these smaller differences is challenging. We expect numerical differences of determining second order derivatives to be the cause. As we are not concerned in this work with the accuracy of heat capacities at the level of a few percent, these differences were not studied in further detail.

4.5.9 Property changes upon mixing

Changes upon mixing are defined as the difference between the properties of a mixed and a demixed system

$$\begin{aligned} B_{\text{mix}} &= B\left(V, T, \sum_i N_i\right) - \sum_i B(V, T, N_i) \\ &= B_{\text{mix}}^{\text{ideal}} + B_{\text{mix}}^{\text{res}} \\ &= B_{\text{mix}}^{\text{ideal}} + B^{\text{ex}} \end{aligned} \tag{4.75}$$

where the non-ideal change upon mixing is also called the excess quantity B^{ex}. The excess quantities are obtained from determining the changes upon mixing of the residual quantities.

The ideal changes upon mixing $B_{\text{mix}}^{\text{ideal}}$ for Helmholtz energy, Gibbs free energy, and entropy only differ by a prefactor $(-T)$. As there is no ideal change of enthalpy upon mixing, the excess enthalpy H^{ex} and enthalpy of

mixing H_{mix} are identical.

$$\begin{aligned} S_{\text{mix}} &= S_{\text{mix}}^{\text{ideal}} + S^{\text{ex}} \\ &= R \sum_i \frac{N_i}{N} \ln\left(\frac{V_i}{V}\right) + S^{\text{ex}} \end{aligned} \tag{4.76}$$

$$\begin{aligned} A_{\text{mix}} &= A_{\text{mix}}^{\text{ideal}} + A^{\text{ex}} \\ &= -RT \sum_i \frac{N_i}{N} \ln\left(\frac{V_i}{V}\right) + A^{\text{ex}} \\ &= -T S_{\text{mix}}^{\text{ideal}} + A^{\text{ex}} \end{aligned} \tag{4.77}$$

$$\begin{aligned} G_{\text{mix}} &= G_{\text{mix}}^{\text{ideal}} + G^{\text{ex}} \\ &= -RT \sum_i \frac{N_i}{N} \ln\left(\frac{V_i}{V}\right) + G^{\text{ex}} \\ &= -T S_{\text{mix}}^{\text{ideal}} + G^{\text{ex}} \end{aligned} \tag{4.78}$$

$$H_{\text{mix}} = H^{\text{ex}}. \tag{4.79}$$

4.6 Optimisations and solvers

Conditions and properties, which can not be calculated via non-repetitive calculations or derivatives as described in the previous section, but require iterative optimisations are the topic of this section. The conditions and properties covered in this section are the corresponding volume for a given pressure, the vapour–liquid equilibrium of a pure compound, the liquid–liquid equilibrium of a mixture of compounds, and the pure-component Mie potentials with which a set of experimental data is best reproduced.

The SAFT theory is typically expressed in terms of Helmholtz free energies, which describe systems at a specific number of molecules N, volume V and temperature T. The pressure P, however, is not an input variable. The pressure is not determined directly, but will be set by varying V until the target pressure is met. While simpler equations of state (e.g. cubic EoS) can also be solved with analytical schemes, the SAFT equations, which are higher-order in volume, are typically solved numerically.

The conditions of the thermodynamic equilibrium between vapour and

liquid of pure components can be determined by different means. One approach is to use the Maxwell equal-area rule (also referred to as Maxwell construction), where the optimisation is performed in pressure–volume space.

In case of phase-separating conditions, the details of the set of equilibrated phases is determined from searching for the compositions and set of phases with the lowest Gibbs free energy. Volume and composition of the phases are optimised, while the global ratio of compounds, the temperature and pressure are kept constant.

4.6.1 Pressure solver

When the volume V for the state of interest is given, the Helmholtz energy A can be calculated with V as a direct input. When the pressure P is given instead, P can not be used directly as an input, but the corresponding V value has to be determined.

Mainly two approaches are available for finding the corresponding volume: Finding the root of $\Delta P(V) = P(V) - P_0$ from the target pressure P_0 using, e.g., a Newton–Raphson algorithm, or minimising the Gibbs free energy $A(V) + P_0 V$ by varying V.

We have implemented the pressure root algorithm, whose details are described in this section. More details on minimising the Gibbs free-energy expression can be found in the Sec. 4.6.5, where the corresponding volume is determined at the same time as the composition of phases in equilibrium.

Pressure root algorithm Performing the optimisation in packing fraction space (not volume space) has several advantages. The boundaries of the possible solution space changes from $V \in [0; \infty]$ to $\eta \in [1; 0]$. The packing fraction space has a more convenient high-volume (vapour) boundary. In addition, the low-volume (liquid) boundary of the SAFT EoS is the sphere packing, which is more conveniently expressed in packing fraction as $\eta = 0.74$. The interval in which the pressure root algorithm searches for the solution is $\eta \in [0.74; 0]$.

The root finding is performed with the Newton–Raphson algorithm (NRA), which uses the pressure and the slope to approach the pressure root

$$\eta_{i+1} = \eta_i - w_{\text{damp}} \frac{\Delta P(\eta)}{\frac{\partial}{\partial \eta} \Delta P(\eta)}. \tag{4.80}$$

We define the convergence criterion in terms of pressure. Typically, the convergence criterion for the NRA is defined in term of η, e.g. as $\eta_{i+1} - \eta_i$ below a given threshold. The sensitivity ($\mathrm{dP}/\mathrm{d}\eta$) varies across the possible solution range. The high sensitivity for the liquid phase packing fraction means that even a high packing fraction accuracy leads to a low pressure accuracy. An overall increased packing fraction accuracy would be unnecessarily high for the vapour packing fraction as it has a lower sensitivity. Instead of setting several criteria, we define the convergence criterion in terms of pressure, as is ensures a consistent accuracy across the whole range

$$\frac{P_0 - P}{P_0} < 10^{-6}, \tag{4.81}$$

which ensures 6 significant figures of the input pressure value.

If no convergence is found after 200 Newton–Raphson cycles, the algorithm is restarted with either a new guided (when close to a solution) or a new random guess (when $1 \times 10^{-30} < \eta < 0.74$ or $\eta =$NaN). Random packing fractions are $\eta \in [0.05, 0.65]$ with the current time taken as a seed for the random number generator (`random_number`).

For polymers, starting with a low-volume initial guess ($0.5 < \eta < 0.6$) the corresponding volume for the liquid phase is found reliably. For low-molecular weight compounds or at conditions where the vapour phase becomes more stable, considering the vapour root solutions is important.

We have implemented a routine which searches for both vapour and liquid roots. It uses the compressibility (dP/dV) to determine if a stable solution was found. The unstable third root has a positive compressibility. Any optimisations, which are converged on the unstable third root are restarted with a slightly larger (+20%) or smaller (-66%) packing fraction away from the unstable solution (depending on which solution has not been found).

A disadvantage of the pressure root algorithm for the case of two stable

solutions is, that it does not immediately provide information on which is the more stable solution. A consequent Gibbs-free-energy comparison is used in our implementation to pick the more stable lower in energy solution.

4.6.2 VLE of pure components

This section covers our algorithm for finding pure-component vapour–liquid equilibria. Supporting our own attempts, Elliott and Lira mention that phase equilibrium algorithms can be “tedious and difficult to automate".[38] The typical approaches are the Maxwell equal-area rule,[15] van der Waals loop,[193] K-ratios, and nonlinear system of the equalities of pressures and chemical potentials.[15]

The latter method, the nonlinear system of the equalities of pressures and chemical potentials, is one of the least robust methods as it requires initial guesses to be close to the solution. In our attempt to implement this method, none of the randomly generated initial guesses led to a converged result.

Instead, we have implemented the Maxwell equal-area rule, as it is one of the more robust algorithms and utilises our pressure root algorithm (see previous section).

Maxwell equal-area rule The equal-area rule determines the pressure at which the enclosed areas in the PV-plain are of equal size, see Fig. 4.14. The pressure, for which the equal-area condition is satisfied, is the saturated-liquid pressure P_{sat}. The condition can be expressed as

$$0 = \int_{V_{\text{liq}}}^{V_{\text{vap}}} (P(V) - P_{\text{sat}}) \mathrm{d}V, \tag{4.82}$$

where the pressures at the volumes V_{liq} and V_{vap} are equal to the saturation pressure ($P(V_{\text{liq}}) = P(V_{\text{vap}}) = P_{\text{sat}}$). At conditions below the critical temperature and critical pressure, pressures can be obtained via (at least) three different volumes. The low and high-value volumes correspond to the liquid and vapour phase, respectively. The third (middle) volume is an unstable condition of positive compressibility (a slightly lower volume has a lower pressure). A horizontal pressure line at a pressure with three volumes,

together with the PV curve enclose two area elements. The size of the area elements is optimised in the Maxwell construction. The PV areas are larger at low temperatures and vanish when approaching the critical temperature. A pronounced minimum and maximum in the PV curve are found at medium temperature. Additional extrema appear at low temperatures. A single point of inflection occurs at the critical temperature, while no inflection point is found at higher temperatures.

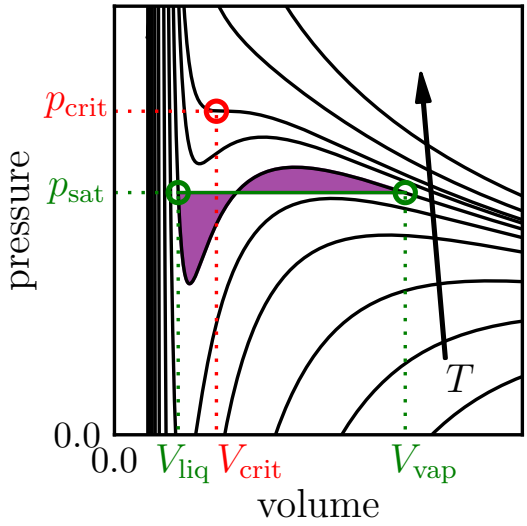

Figure 4.14: Pressure-volume curves for several temperatures with highlighted critical conditions. The vapour–liquid equilibrium conditions are shown for one temperature, where the shaded areas are of equal size following the Maxwell equal-area method.

The changing shape of the PV curve leads to challenges in implementing the Maxwell construction. The algorithm has to be able to neglect additional PV roots at low temperatures and, at the same time, pick up comparably small extrema at very similar volumes close to the critical temperature. At lower temperatures the contrast between the pronounced minimum and the flat and wide maximum increases.

Most of our efforts to implement a robust Maxwell algorithm was put into optimising initial volume and pressure guesses, step sizes of sweeps and sampling, the handling of exceptions, and improved restarting of unsuccessful extrema and pressure searches.

Our algorithm starts with determining the best list of temperatures to give a smooth VLE curve, then optimises the PV area, for which the pressure roots and the extrema are determined for each iteration:

- find T_{crit} ($P(V)$ curvature is zero)
- determine list of temperatures (more T closer to T_{crit})
- start with lowest T
- find $P(V)$ extrema ($P(V)$ slope is zero)
- derive a P guess for P_{sat} (slightly smaller than pressure of local maximum)
- optimise P to obtain equal PV areas (find P roots every iteration)
- print VLE results (T, P_{sat}, ρ_{l}, ρ_{v})
- continue with next temperature.

Our phase equilibrium code was validated with pure-compound coexistence curves from Avendaño *et al.*[115] We validated against SAFT-VR Mie models of CO_2, n-decane and eicosane.

4.6.3 Flash

A flash is the fast evaporation of an unstable liquid system. While the term “flash algorithm" is a frequently used term for phase equilibrium solvers, it is difficult to find a precise definition. It is usually[7,194] used to describe a phase equilibrium solver, which takes the global composition of a system (together with temperature, pressure or volume) as input, and determines the composition of the separated phases. Flash algorithms can be categorised based on whether temperature (isothermal), pressure (isobaric) or volume (isochoric) or a combination are kept constant. The flash algorithms discussed and developed in this work are isobaric-isothermal-flash (PT-flash) algorithms.

A range of approaches has been applied to solve flash problems. Successive substitution, Newton's method and Gibbs energy minimisation are three examples.[7]

4.6.4 VLE of mixtures (interface to the HELD algorithm)

For determining vapour–liquid equilibria of mixtures, we rely on the Helmholtz-free-energy Lagrangian dual (HELD)[195] algorithm, which is a PT-flash algorithm. HELD was developed by Frances Pereira and coworkers and provided as a compiled library package by the M&S group at Imperial College London. We have implemented a set of subroutines which allow the HELD solver to access the thermodynamic properties of our SAFT implementation, such as Helmholtz free energy, chemical potential and pressure. The set up was validated with binary mixture phase diagrams of both SAFT-VR Mie[14] and SAFT-γ Mie models.[184]

The HELD algorithm is a multicomponent-multiphase equilibrium solver, which was shown to work for VLE, LLE and LLLE system for compounds ranging from gases, solvents to polymers.[195] The HELD algorithm runs through three stages. At the first stage it performs a stability test to quickly determine stable phases. The stability test uses the tangent plane stability test and also a tunnelling algorithm with an exponential tunnelling function. At the second stage (if the system was found unstable) searches for candidate stable phases with a dual description. In the inner minimisation problem of the dual description, the volume and composition are optimised subject to minimising the Gibbs free energy of a single potential phase, which aims to satisfy the mechanical stability (equal pressure) and reaching the lowest Gibbs free energy,

$$\min_{V,\boldsymbol{x}} \; L(\boldsymbol{x}, V, \lambda^{\mathrm{Lag}}) = \min_{V,\boldsymbol{x}} \left(A(\boldsymbol{x}, V, T^0) + P^0 V + \sum_{i}^{N_\mathrm{c}-1} \lambda_i^{\mathrm{Lag}} (x_i^0 - x_i) \right), \tag{4.83}$$

where L is the Langrangian, N_c is the number of components, (x^0, T^0, P^0) the initial global conditions, and λ_i^{Lag} are the Lagrange multipliers, which are linked to the chemical potential

$$\lambda_{\mathrm{Lag},i} = \mu_i(\boldsymbol{x}, V, T^0) - \mu_{N_\mathrm{c}}(\boldsymbol{x}, V, T^0) \tag{4.84}$$

where i runs from 1 to $N_\mathrm{c} - 1$.

In the outer problem of the dual description, the Langrange multipliers are optimised subject to maximising the Lagrangian, which aims to satisfy the thermodynamic stability of equal chemical potentials

$$\max_{\lambda^{\mathrm{Lag}}} \Theta(\lambda^{\mathrm{Lag}}) \tag{4.85}$$

$$\Theta(\lambda^{\mathrm{Lag}}) = \min_{V,\boldsymbol{x}} \; L(\boldsymbol{x}, V, \lambda^{\mathrm{Lag}}). \tag{4.86}$$

The convergence criteria are set relatively loosely during the stable-phase-finding stage. The tighter convergence criteria are applied in the third stage, where the total Gibbs free energy of all collected stable phases is minimised

$$\min_{V,\boldsymbol{x}} \; G(\boldsymbol{x}, V) = \min_{\boldsymbol{V},\boldsymbol{x}} \; \sum_{n}^{\text{phases}} \left(A(\boldsymbol{x}_n, V_n, T^0) + P^0 V_n \right). \tag{4.87}$$

Note the sum over several phases in this stage. A convergence test is performed on the converged solution to ensure equality of chemical potentials. The equilibrium compositions of trace components are determined post-convergence by using the chemical potential of the phase with the largest composition for this component. The chemical potential of large compositions is more accurate because of their large contribution to the Gibbs free energy (larger sensitivity in the earlier optimisations) and therefore can be used to improve trace compositions.

The HELD algorithm in combination with our SAFT-γ Mie code runs reliably for VLE calculations for low-molecular weight systems. We encounter, however, convergence challenges for LLE of polymer systems. While a polymer solution (polymer and solvent) causes some convergence challenges, a

solution for a polymer mixture (also oligomer/polymer) was only very rarely found. The numerical derivatives of our code and the consistency between them are a potential complication. This is because of the typically similar energy of competing phases in LLE compared to VLE. The comparison between more similar phases requires more precise consideration. None of the performed tests, however, were able to narrow down the challenges we see with polymers.

Equilibrium properties of several binary mixtures are shown in Figures 4.15 and 4.16 calculated with our SAFT-γ Mie version and the HELD algorithm. The results agree with the results of the SAFT-γ authors in Refs 14,184.

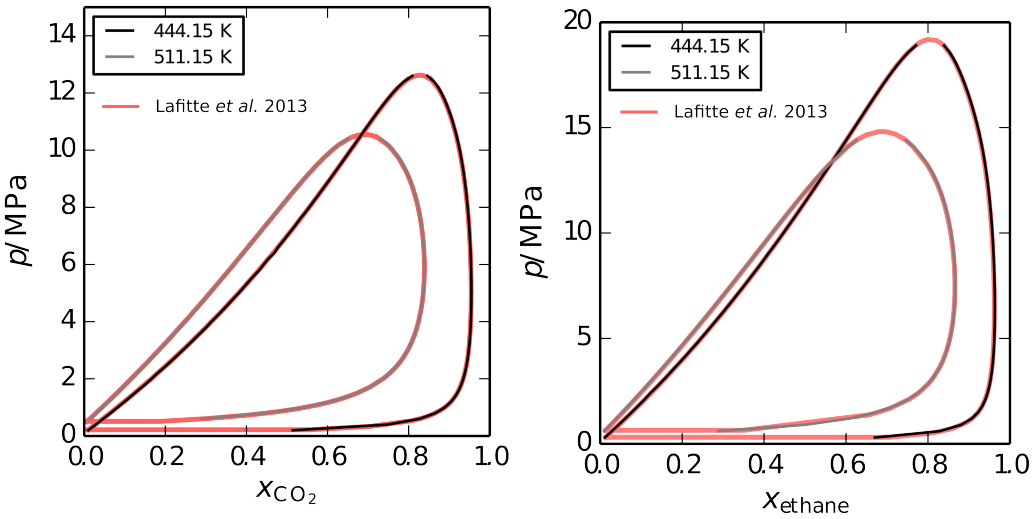

Figure 4.15: Vapour-phase equilibria of ethane + n-decane (left) and carbon dioxide + n-decane (right) at two different temperatures. Red continuous lines are taken from Ref. 14, grey and black lines are this work.

4.6.5 LLE of mixtures (HammR)

The HammR algorithm is a PT-flash algorithm designed for polymer mixtures. It determines the stability of liquid mixtures and provides equilibrium compositions of phase-separated liquid (polymer) phases. HammR is set up to automatically calculate whole LLE phase diagrams. A global optimisation is not performed but a large range of initial starting compositions and num-

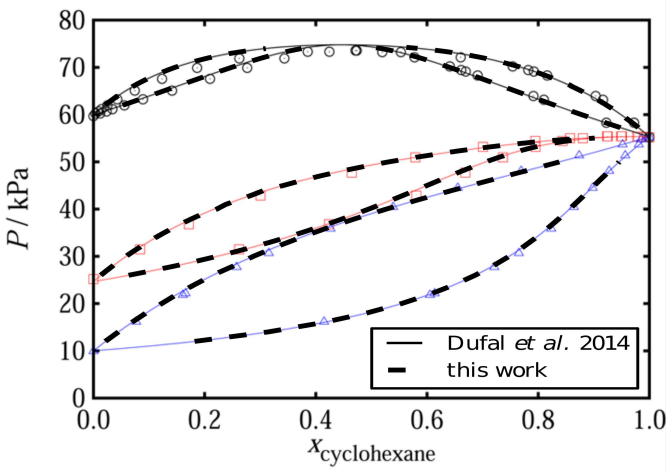

Figure 4.16: Vapour–liquid equilibria of three binary mixtures as a function cyclohexane mole fraction at a temperature of 335 K. Cyclohexane + n-ethyl acetate (circles), cyclohexane + n-propyl acetate (squares) and cyclohexane + n-butyl acetate (triangles) are experimental values, thin and coloured lines are SAFT-γ results from Ref. 184, thicker black lines are this work. Reprinted and adapted with permission from Dufal *et al., J. Chem. Eng. Data*, 2014, 59 (10), pp 3272–3288. Copyright (2014) American Chemical Society.

ber of phases are each optimised locally with the Broyden[196]–Fletcher[197]–Goldfarb[198]–Shanno[199] (BFGS) method, which is a quasi-Newton method. The user can easily set the number of compounds and number of phases, which are not hard-coded or restricted.

The HammR phase equilibrium solver is based on an unpublished phase equilibrium solver by Marc Hamm and has been adjusted to work with SAFT-γ Mie, improved for automated execution, and parallelised. HammR was developed in collaboration with Marc Hamm.

HammR shares some functionality with HELD. Both minimise the Gibbs free energy as $G = A + P^0V$ to determine the equilibrium conditions and improve the trace compositions using the chemical potential. However, HammR does not include a stability test and a stage for finding stable phase candidates. Instead of making smart initial guesses based on the solutions of the dual approach, HammR relies on multistart local optimisations spread across the search space. A set of reliable starting compositions is set as default, but

changes can be easily made in the input file.

The speed-up due to the stability test and candidate phase search, which HELD performs unlike HammR, is expected to have a lesser impact on LLE than on VLE, as smaller differences between phases (liquid/liquid vs vapour/liquid) require more elaborate searches.[7] In cases of strong liquid immiscibility with almost pure equilibrium phases, larger differences between the phases are present and a larger potential to speed up the calculations with smarter search algorithms is expected. However, we perform most LLE calculations at conditions where the phases are significantly mixed or are miscible. Therefore, the stability test and candidate phase search have not been a priority in our development.

The Gibbs free energy summed over all phases is minimised by optimising the volume V and composition $\boldsymbol{x}$ of each phase simultaneously at constant pressure P_0 and constant temperature T_0

$$G^* = \min_{\boldsymbol{V},\boldsymbol{x}} \sum_{n}^{\text{phases}} \left[A(\boldsymbol{x}_n, V_n, T^0) + P^0 V_n\right]. \tag{4.88}$$

HammR is written in R and relies on our Fortran routines (Sec. 4.3) for the Helmholtz energies (and corresponding volume, occupied volume, ideal properties). The **interface** to the Helmholtz energy and other basic SAFT routines of our Fortran code is provided via a shared object (*.so) file, which is loaded at the beginning of the HammR code. Available SAFT properties, among others, are the Helmholtz energy, pressure, occupied volume, corresponding volume, residual properties, chemical potential.

Several adjustments to the minimisation of the Gibbs free energy in Eq. (4.88) are made to improve the reliability (penalty-outside-volume boundaries), accuracy for polymers (logarithmic variables) and satisfy the mass-balance constraint (relative composition).

The **mass balance** is satisfied by only optimising relative compositions normalised by the compositions in an arbitrary phase. For the objective function, the absolute compositions are reconstructed using the total number of molecules per compound N_i. The compositions $\boldsymbol{x}_n$ in phase n are reformu-

lated relative to the population in, e.g., phase 1, to give the reduced-variable set $\boldsymbol{q}$. The number of variables is reduced by one per compound per phase, so that the size of $\boldsymbol{q}$ is $N_{\text{compo}}N_{\text{phase}} - N_{\text{compo}}$ (i.e., $N_{\text{compo}}(N_{\text{phase}} - 1)$), because with knowledge of the global composition $\boldsymbol{x}^0$, the composition of the last phase can be reconstructed).

$$\begin{aligned} q_{n,i} &= \frac{x_{n,i}}{x_{1,i}}, && n = 2, ..., N_{\text{phase}} \\ &= \frac{N_{n,i}}{N_{1,i}}, && n = 2, ..., N_{\text{phase}} \end{aligned} \tag{4.89}$$

$$\begin{aligned} \ln q_{n,i} &= \ln x_{n,i} - \ln x_{1,i}, && n = 2, ..., N_{\text{phase}} \\ &= \ln N_{n,i} - \ln N_{1,i}, && n = 2, ..., N_{\text{phase}} \end{aligned} \tag{4.90}$$

$$\begin{aligned} N_{n,i} &= N_{\text{tot},i} x_{n,i} \\ &= N_{\text{tot},i} \frac{\exp(\ln q_{n,i} - \ln q_i^{\max})}{\sum_n \exp(\ln q_{n,i} - \ln q_i^{\max})}, \text{ with } \ln q_{1,i} = 0 \end{aligned} \tag{4.91}$$

$$\begin{aligned} \ln N_{n,i} &= \ln N_{\text{tot},i} + \ln x_{n,i} \\ &= \ln N_{\text{tot},i} + \ln q_{n,i} - \ln q_i^{\max} - \ln \sum_n \exp(\ln q_{n,i} - \ln q_i^{\max}), \text{ with } \ln q_{1,i} = 0 \end{aligned} \tag{4.92}$$

where $\ln q_i^{\max} = \max_n(\ln q_{n,i})$ is chosen to shift the logarithmic values to avoid numerical problems. While the BFGS optimiser works in relative mole fraction space $\boldsymbol{q}$, the Helmholtz energy evaluations are naturally performed in absolute mole fraction space $\boldsymbol{x}$. Variable-space converter routines are applied for each communication.

To improve the accuracy of polymer and trace concentrations, the optimisations are performed on **logarithmic** variables $(\ln \boldsymbol{x}, \ln \boldsymbol{q})$, which inconveniently changes the lower search boundaries from zero to negative infinity, but at the same time provides higher sensitivity at low mole fractions.

Penalties are applied for volumes outside the specified liquid-volume range expressed in packing fraction as the range $\eta = [0.2, 0.68]$. The volume penalty is applied phase wise. It avoids unphysical high packing fractions near the close sphere packing threshold of $\eta = 0.74$ and avoids vapour phases at low packing fractions, where we have set the threshold at $\eta = 0.2$

Accounting for the mass-balance constraint, the logarithmic variables, and the volume-penalty features, the objective function optimised in HammR can be expressed as

$$O^* = \min_{\ln \boldsymbol{q}, \ln \boldsymbol{V}} O(\ln \boldsymbol{q}, \ln \boldsymbol{V}) \tag{4.93}$$

$$\begin{aligned} O(\ln \boldsymbol{q}, \ln \boldsymbol{V}) &= \sum_{n}^{\text{phases}} \left[G_n(\ln \boldsymbol{q}_n, \ln \boldsymbol{V}_n) + Y(V_n) \right] \\ &= \sum_{n}^{\text{phases}} \left[A\left(\ln x_n (\ln \boldsymbol{q}_n)_n, V_n, T^0\right) + P^0 V_n + Y(V_n) \right] \end{aligned} \tag{4.94}$$

$$Y(V_i, V_{\text{lower/upper}}) = N_i + (N - N_i)(1 - e^{-b^2})\left(e^b - 1\right) \tag{4.95}$$

$$b = \frac{\mathrm{d}(A + P^0 V)}{\mathrm{d}V_{\text{lower/upper}}}(V - V_{\text{lower/upper}}) \tag{4.96}$$

The **trace-component** mole fractions are improved post-convergence using the chemical potential of the same compound in the phase where it has the largest mole fraction, μ^{best}, which is expected to be the chemical potential of highest accuracy. The compositions are adjusted based on the deviation from μ^{best},

$$x_i = \frac{x_i - w_{\text{damp}}(\mu^{\text{best}} - \mu_i)}{N_i}, \tag{4.97}$$

which works reliably for small compositions as the chemical potential is monotonically increasing with composition in this range. A range of damping factors $w_{\text{damp}} = [1; 0.003]$ is tested and the successful improvement with the highest w_{damp} is used. Success is defined as a smaller variation in the chemical potential for each compound.

Equilibria are calculated assuming liquid phases to be more stable than vapour phases. If vapour phases are significantly more stable, HammR iterations often move beyond the lower packing fraction boundary of $\eta = 0.2$, which is reported together with a warning, that a VLE or VLLE might be more stable at the requested conditions.

Several more **technical features** are implemented to improve the perfor-

mance (parallel execution), the handling of polydisperse materials (component/material), automation of phase diagrams (skipping of failed attempts, loops over P,T,x),

Compounds can be specified in the input as **material or component** to facilitate introducing and handling of polydispersity. Several (pseudo)-components can be combined as materials. Composition results are reported for both components and materials in separated output files to allow easy analysis.

Additional optimisation methods apart from the BFGS method have also been implemented. The **Nelder-Mead (simplex) and genetic optimiser (GENOUD)**[200] solver can conveniently be turned on and off via an input flag.

For automatic generation of full LLE phase diagrams, **automatic batch** calculations can be executed, which run over a set range of temperatures, pressures, composition, and initial population guesses. Automatic skipping (try-except commands) of unsuccessful optimisation attempts is implemented to avoids unwanted program aborts.

HammR can be run in **parallel**. A bash script is provided in which only the number of processors has to be adjusted to the available hardware. The composition list is spread across the processors. Separate instances of R are launched. As no communication between the instances is required, the parallelisation scales perfectly with the number of available processors. The input files for each instance are adjusted to carry the unique `thread-ID`, which is picked up by HammR to find the right section of the composition list to work on. The current set up can run in parallel on a single node with several processors, but can not run across several nodes.

The result are saved in several different ways. Results of successful local optimisations are saved to a separate file for each $(T^0, P^0, \boldsymbol{x}^0)$ combination. The equilibrium results (lowest G for each $(T^0, P^0, \boldsymbol{x}^0)$) are saved to a summary file. This summary file is generated for both component and material level. Several python scripts are provided for automated analysis and plotting.

4.6.6 Mie potential optimisation

An optimisation routine is available to develop pure-component Mie potentials. The algorithm allows the optimisation of all 4 Mie parameters (ϵ,σ,λ_r,λ_a) simultaneously or a selection of them. Any thermodynamic property made available in the `table` module can be used in the Mie potential optimiser as the reference property; properties ranging from density, volume, pressure, free energy, energies of mixing and more are available. The underlying solver is a Nelder–Mead[201] (downhill simplex) algorithm, which is applied in a multistart approach. The optimisation is parallelised with OpenMP, which fully utilises multicore hardware to speed up execution times.

The performance of SAFT models is typically expressed in reference to experimental data as the average absolute deviation in percent (%AAD),

$$\%\mathrm{AAD} = \sum_{i=1}^{N_\mathrm{exp}} \frac{100 w_i}{N_\mathrm{exp}} \left| \frac{X_i^\mathrm{exp} - X_i^\mathrm{SAFT}}{X_i^\mathrm{exp}} \right| \tag{4.98}$$

where N_exp is the number of experimental reference points, w_i the weight for reference data point i and X is the thermodynamic property (e.g., density, energy or pressure) for which reference values X^exp are available and which are predicted with the tested SAFT model, X^SAFT. We use %AAD in the Mie potential optimisation as the core of the objective function O^*

$$O^* = \min_{\boldsymbol{\theta}} \left(\sum_{i=1}^{N_\mathrm{exp}} \frac{100 w_i}{N_\mathrm{exp}} \left| \frac{X_i^\mathrm{exp} - X_i^\mathrm{SAFT}(\boldsymbol{\theta})}{X_i^\mathrm{exp}} \right| + Y(\boldsymbol{\theta}) \right), \tag{4.99}$$

where the parameters to be optimised are

$$\boldsymbol{\theta} = (\epsilon, \sigma, \lambda_\mathrm{r}, \lambda_\mathrm{a}). \tag{4.100}$$

The objective function includes a penalty Y

$$Y(\boldsymbol{\theta}) = Y^\mathrm{outside} + Y^{\lambda-\mathrm{gap}}. \tag{4.101}$$

Y^outside penalises parameters outside a specified range. The penalty is quadratic

with the distance to the closest boundary and is normalised by the size of the acceptable value range ($\theta^{\mathrm{ub}} - \theta^{\mathrm{lb}}$).

$$Y(\boldsymbol{\theta}) = \sum_{j=1}^{N_\theta} \left(100 \frac{\theta_j^{\mathrm{ub}} - \theta_j}{\theta_j^{\mathrm{ub}} - \theta_j^{\mathrm{lb}}} \right)^2 \tag{4.102}$$

where N_θ is the number of parameters in $\boldsymbol{\theta}$. Eq. (4.102) is expressed for parameters θ larger than the upper boundary θ^{ub}. For determining the penalty for parameters smaller than the lower boundary, substitute upper boundary θ^{ub} with lower boundary θ^{lb} and vice versa in Eq. (4.102).

The second penalty $Y^{\lambda-\mathrm{gap}}$ ensures λ_{r} to be larger than λ_{a}, and adds a minimum difference of 1 to improve numerical stability

$$Y^{\lambda-\mathrm{gap}} = 100(\lambda_{\mathrm{r}} - \lambda_{\mathrm{a}} - 1)^2 \tag{4.103}$$

$Y^{\lambda-\mathrm{gap}}$ is only applied if $\lambda_{\mathrm{r}} - \lambda_{\mathrm{a}} \leq 1$.

One successful approach to perform Mie optimisations and plot results is to run (ϵ,σ) optimisations for fixed (λ_{r},λ_{a}) values. Equally spread (λ_{r},λ_{a}) values are automatically generated for a chosen value range. The results can be plotted in ($\lambda_{\mathrm{r}}, \lambda_{\mathrm{a}}$)-space with either ($\epsilon$,$\sigma$) included as colour and size of symbols, or quality of fit %AAD as colour of symbols. A python script is provided to produce these and other plots automatically.

As numerical solvers, we have tested available minimisation algorithms from the Numerical Recipe library,[183] which do not require explicit derivatives, but determine necessary information from function evaluations only. The Powell algorithm is not fit for the problem at hand, because parameters are optimised in turns or based on a specified vector of parameters. As the parameters are highly correlated and correlations differ from property to property and change with changing parameters, optimisations were either unsuccessful or highly specified to a type of property and area of phase space. The amoeba solver, which is a simplex algorithm by Nelder and Mead, instead, was found to be a flexible and successful optimiser, which finds the solutions even if started not close to the solution. The amoeba solver is

therefore applied as default.

4.7 Tabulated Mie potentials for GROMACS

To use Mie potentials as non-bonded interactions in the GROMACS[175–177] software package, the potentials have to be provided as look-up tables, which are tabulated forces and potentials with a fine spacing of 0.002 nm.[202] We have implemented a routine to automatically generate GROMACS compatible table files for Mie potential parameters provided in our default input file.

GROMACS offers two alternatives to specify tabulated potentials for which the potential U^{Mie} can be expressed as

$$\begin{aligned} U^{\mathrm{Mie}} &= K\epsilon\left[\left(\frac{\sigma}{r}\right)^{\lambda_\mathrm{r}} - \left(\frac{\sigma}{r}\right)^{\lambda_\mathrm{a}}\right] \\ &= K\epsilon\sigma^n\ r^{-\lambda_\mathrm{r}} + K\epsilon\sigma^m\ r^{-\lambda_\mathrm{a}} \\ &= Cu^{\mathrm{r}*}(r) + Au^{\mathrm{a}*}(r) \\ &= u^{\mathrm{r}}(r) + u^{\mathrm{a}}(r). \end{aligned} \tag{4.104}$$

Either $r^{-\lambda_\mathrm{r}}$ and $r^{-\lambda_\mathrm{a}}$, or $u^{\mathrm{r}*}(r)$ and $u^{\mathrm{a}*}(r)$ are provided in the table files. The two options differ by σ and ϵ. The first option is convenient for systems where the exponents $(\lambda_\mathrm{r}, \lambda_\mathrm{a})$ are the same for many or all interactions. It allows the reuse of the table files. However, for Mie potentials developed with SAFT the exponents typically differ between bead types. For general convenience and maximum automation we therefore provide the potentials fully in the table files as $u^{\mathrm{r}}(r)$ and $u^{\mathrm{a}}(r)$ by setting $C = A = 1$. A separate table file is used for each interaction, which is generated automatically by our implementation.

The look-up table is a numerical file of the potential contributions and their first-order derivatives given in seven columns whose column order corresponds to r, $\frac{1}{r}$, $-\frac{1}{r^2}$, $u^{\mathrm{r}}(r)$, $-u^{\mathrm{r}\prime}(r)$, $u^{\mathrm{a}}(r)$ and $-u^{\mathrm{a}\prime}(r)$. The radius r increment is 0.002 nm. Values need to be given up to 1 nm larger distances than the highest cut-off radius (`rvdw`,`rlist`,`rcoulomb` keywords) specified in the

GROMACS `grommp.mdp` input file.

The code was tested for a Lennard–Jones potential against the internal GROMACS-build look-up table. The initial steric energies of both simulations were identical.

4.8 How algorithms are used in this work

The SAFT-γ Mie algorithm with the derived properties and the pressure solver are the basis for all other algorithms used in this work, referred to as *basic* algorithms in this section.

The *basic* algorithms are used for testing the available Dufal 2014[184] group-contribution Mie potential parameter set on polymers, see Sec. 5.1.

The Maxwell construction (VLE of pure compounds) together with the *basic* algorithms is used for evaluating Mie potentials obtained via the corresponding state method of Mejia *et al.*[156] for describing like interactions, see Sec. 5.4.1.

The external HELD library together with the *basic* algorithms is used for calculating VLE of mixtures, see Chap. 6.

The HammR algorithm together with the *basic* algorithms is used for predicting LLE of polymer mixtures. Some derived properties and the pressure solver (written in Fortran 95) are substituted with new routines in the HammR environment (written in R) for improved performance, see Sec. 5.5.

The Mie potential optimisation algorithm together with the *basic* algorithms is used to develop new Mie potentials, see Sec. 5.4.2.

Chapter 5

Development of Mie potentials for polymers

This chapter covers our strategies for developing SAFT-γ Mie models for oligomers and polymers. Firstly, we summarise strategies employed by other groups with the SAFT equation of state. The SAFT-γ Mie parameter set by Dufal *et al.*[184] is applied to industrially relevant oligomer/polymer/polymer and oligomer/polymer mixtures to test the transferability of SAFT-γ Mie parameters from low molecular to polymer weight. A semi-comprehensive overview of experimental thermodynamic data of hydrocarbon polymers for the development of equation of state models is presented. We discuss the corresponding state principle as a short cut for the polymer model development and demonstrate why heat capacities and speed of sound data are challenging to utilise in the Mie potential parameter estimation of polymers. Pure-component SAFT-γ Mie models for a range of polymers are presented, which were successfully developed with liquid densities (PVT). SAFT-γ Mie models for binary and ternary mixtures are developed based on the pure-component models. The influence of individual unlike interaction parameters is analysed and challenges in the development of SAFT polymer models are discussed.

Most of the SAFT-γ Mie calculations in this section were performed with our own code presented and discussed in Chap. 4. For the development of

some of the unlike interactions we also employed the commercial SAFT-γ Mie implementation (gSAFT by PSE).[203] If not stated otherwise, our own SAFT implementation and solvers were applied.

5.1 Testing transferability of available parameters

The currently most advanced SAFT-γ Mie parameter set is the group-contribution (GC) parameter set at united-atom level by Dufal and coworkers.[184] Although the Mie potential parameters were developed with data from low-molecular weight compounds, it is straight-forward to apply them to higher molecular weight compounds, due to their group-contribution nature. To our knowledge, the parameters were not tested on polymers before. In this section we explore how accuracy of polymer compatibility predictions when Dufal's group-contribution parameters (GC-Dufal2014) are applied at molecular weights far beyond the tested range.

Our own SAFT-γ Mie implementation was used for the prediction of free energies of mixing and pseudo partition coefficients. The HELD algorithm was added to obtain VLE and LLE properties of the low molecular weight mixtures. The VLE and LLE properties were used as the reference to improve some of the unfitted unlike interactions of the GC-Dufal2014 set.

5.1.1 Polymer compatibility data

Three sources of experimental compatibility data of polymer mixtures were used in this evaluation. Qualitative experimental compatibility data (miscible vs. immiscible) was used from Sabattié *et al.*[204] and Mansfield[205] based on differential scanning calorimetry analysis (DSC) of glass transition temperature shifts. The data comprises three polymers in pairs with several different oligomers. Quantitative experimental compatibility data was used from Mansfield and Hamm[206] based on gel permeation chromatography (GPC) analysis of oligomer partitioning between two polymers. Brief details of the

relevant experiments are given below.

Experimental details

The experimental details of Mansfield and Hamm's work[206] comprises the preparation and analysis of polymer systems. An oligomer was added at a level of 5-15% by weight to one of the triblock copolymers in a microextruder. The oligomer loaded and a second unloaded triblock copolymer where both pressed into approximately 150 μm thick films, before being brought in contact to allow the oligomer to migrate between the polymer matrices. Four oligomers and the two triblock copolymers styrene–isoprene–styrene block copolymer (SIS) and styrene–hydrogenated-isoprene–styrene block copolymer (ShIS)* were mixed in pairs. The oligomer/triblock-copolymer pair was brought in contact with a styrene–butadiene–styrene block copolymer for at least two weeks. Gel permeation chromatography was used to determine the partitioning as the ratio of the oligomer signal integrals of both phases.

The experimental details of Mansfield's work[205] comprises the preparation of 50:50 weight percent polymer/oligomer blends via solution blending in tetrahydrofuran (THF) (with 250 ppm BHT) on microscope slides. The dried mixtures were analysed in DSC experiments at rates of 20 °C/ min. Two heat runs (to 180 °C and 300 °C) separated by a cool run were performed. The second heat run was used to determine glass transition temperatures.

The experimental details of Sabattié's DSC analysis and preparation details can be found elsewhere.[204]

Details including molecular weight, polydispersity and monomer ratio about the polymers and oligomers of all three studies are listed in Table 5.1. The polymers and oligomers cover a broad range of industrially relevant hydrocarbon polymeric compounds. Unsaturated (PI, PB, PS, PM, phPMI), saturated and hydrogenated (hPI, hPMI, phPMI, hPM), and aromatic (PS, PM, phPMI) compounds are included. Polymers from both C4 monomer streams (PiB, PiBB) and C9 monomer streams (PM, hPMI, phPMI) are covered.

*ShIS and SEPS are synonyms, because hydrogenated-1,4-PI and poly(ethylene)-alt-poly(propylene) (EP) describe identical structures.

Table 5.1: Details and notation of oligomers and polymers. Experimentally known details and assumption about missing information are listed. 204–206

name	compound	M_n /g mol^{-1}	M_w/M_n	monomer ratio	Ref.
PI[c]	polyisoprene	145 000[b]	1.1[b]	92.6% 1,4-linked[a] PI 7.4% 3,4-linked[a] PI	204–206
hPI[c]	hydrogenated polyisoprene	150 000[b]	1.1[b]	92.6% 1,4-linked[a] hPI 7.4% 3,4-linked[a] hPI	204–206
PB[c]	polybutadiene	133 000[b]	2.1[b]	90% 1,4-linked[a], 10% vinyl[a]	204–206
sq	squalane	423	1.0	-	204
PiB	polyisobutylene	900	-	-	204
PiBB+fur[d]	poly(isobutylene-*co*-1-butene) with terminal furandione group and linker (fur)	910	1.6	assumed 50% isobutylene, 50% 1-butene, 1 furandione group and linker per chain	206
PS1k	polystyrene	1000	"narrow"	-	205
PS4	polystyrene	418[e]	1	-	204
PM	poly(methylstyrene)	550	3.3	assumed no α methyl substitution	206
hPM	hydrogenated poly(methylstyrene)	700	1.8	100% saturation, assumed no α methyl substitution	205
hPMI	hydrogenated poly(methylstyrene-*co*-indene)	600	1.5	100% saturation, assumed: 50% methylstyrene with no α methyl substitution, 50% indene	205,206
phPMI	partially hydrogenated poly(methylstyrene-*co*-indene)	600	1.5	50% saturation, assumed: 50% methylstyrene with no α methyl substitution, 50% indene, equal saturation of all potential sites	205

[a] Measured for the Mansfield–Hamm data set[206] and assumed to be the same for the other two data sets.[204,205]

[b] Assumed to also be a good description for the mid block X of the SXS triblock copolymers in the context of oligomer compatibilities. The small influence of the exact polymer weight on the compatibility of oligomer/polymer mixtures supports this assumption. Measured for the Sabattié data set,[204] the other two data sets[205,206] are modelled as 1×10^6 g mol^{-1}.

[c] Also covers styrenic triblock copolymers. The styrenic blocks are neglected in the SAFT models as they are vitrified at all applied conditions.

[d] PiBB+fur is a polybutylene succinic anhydride.

[e] A styrene tetramer initiated and terminated with a hydrogen radical. The actual compound used in the DSC experiments was fully deuterated, but is treated as only containing hdyrogen in this context as the SAFT groups were developed on hydrogen-compounds. We assume no significant change in properties due to deuterium for the properties studied here.

5.1.2 Polymer models based on GC parameters

SAFT-γ models for the polymeric compounds in Tab. 5.1 are assembled based on the group-contribution Mie potential parameter set by Dufal *et al.* 2014.[184] The mapping of group parameters for the monomer structures are represented in Fig. 5.1. The chosen mapping accounts for all known experimental information about the compounds. The most important information for the development of SAFT-γ models was the molecular weight, the monomer types and monomer ratios. For the few chemical moieties for which no perfectly-matching group parameters are available in the parameter set (quaternary carbon >C<, the urea group, fully substituted sp^2 >C= carbon), we have chosen the closest-matching available group based on molecular weight and chemical nature, see Fig. 5.1. In the furandione group two ester groups were chosen for the urea moiety. To account for the uncertainty of the non-perfect choice of ester groups to capture the urea moiety, in addition to PiBB+fur (see Tab. 5.1 for details) we included a PiBB model without linker and furandione group. The choices for the quaternary carbon and the >C= group are further analysed for low-molecular weight compound mixtures later in this section.

The polystyrene blocks in the triblock copolymers are vitrified (temperature below glass transition) in contrast to the rubbery polyisoprene, polybutadiene and hydrogenated polyisoprene midblocks. We assume the migration of oligomers is impossible in and out of the vitrified high-molecular-weight polystyrene blocks, which is why the polystyrene blocks are neglected in the SAFT-γ Mie models. Oligomers of polystyrene in this work are rubbery (above their glass transition temperature) and are therefore explicitly included in the SAFT-γ Mie models.

All compounds are modelled as monodisperse. Unknown molecular weights of PI, hPI and PB polymers were set to $100\,\mathrm{kg\,mol^{-1}}$, which is in a range where free energies of mixing of oligomer/polymer mixtures are almost independent of the polymer weight. All calculations were performed at a temperature of 298 K and a pressure of 101 325 Pa.

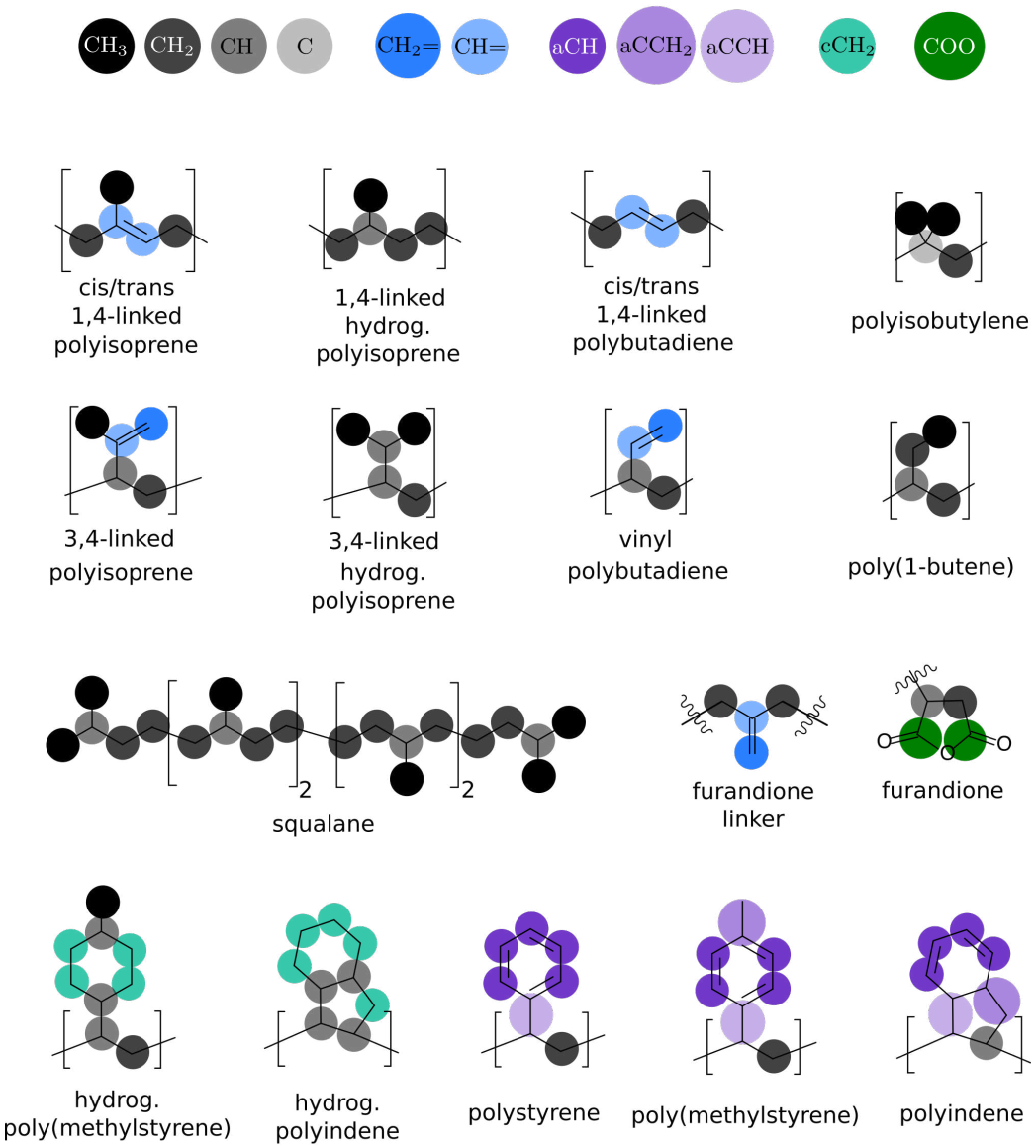

Figure 5.1: (Top) Colour code of groups taken from Dufal *et al.*[184] (Bottom) Monomer structures of oligomers and polymers overlaid with the mapping of groups. *Cis* and *trans* isomers are not differentiated in the GC-Dufal2014 parameter set.[184]

5.1.3 Compatibility and pseudo partition coefficient

The compatibility predictions are based on free energies of mixing of binary blends, ΔG_{mix}, as a function of oligomer weight fractions, w, which we express as

$$\Delta G_{\mathrm{mix}} = G_{\mathrm{o+p}} - x_{\mathrm{o}} G_{\mathrm{o}} - (1 - x_{\mathrm{o}}) G_{\mathrm{p}} \tag{5.1}$$

$$w = \frac{M_{\mathrm{o}} x_{\mathrm{o}}}{M_{\mathrm{o}} x_{\mathrm{o}} + M_{\mathrm{p}} x_{\mathrm{p}}} \tag{5.2}$$

where indices 'o' and 'p' denote oligomer and polymer, respectively, x are mole fractions and M the molecular mass for which the number-average molecular mass is used in case of polydisperse compounds.

Compatibility (only 1 phase present) is found for compositions with negative ΔG_{mix} and positive ΔG_{mix} curvature (convex). In cases of negative curvature (concave), the mixture is more stable when separated into two phases as it lowers the overall free energy, independent of the sign of ΔG_{mix}. Only those plots exhibit the relevant curvature that are plotted with consistently normalised quantities, e.g. by normalised by total weight or total number of molecules. Inconsistent normalisation significantly warps the graphs.

For the prediction of partition coefficients, the polymer pairs PI/PB and hPI/PB are made available for the oligomers to partition between. Phase separation is predicted in the hPMI/PI/PB and PiBB(+fur)/PI/PB systems as all binary pairs are incompatible. No true partition coefficient can be determined in these cases for significant oligomer concentrations larger than only traces. To allow a consistent and easy comparison of relative compatibility for all pairs, the difference between the free energies of mixing of the mixed phases at constant oligomer weight fraction is computed, which we call a pseudo partition coefficient.

We define the pseudo partition coefficient $\log K_{\mathrm{x/y}}(A)$ of oligomer A between polymers x and y as the difference of free energies of mixing

$$\log K_{\mathrm{x/y}}(A) = -\left[\Delta G^{\mathrm{x}}_{\mathrm{mix}}(A) - \Delta G^{\mathrm{y}}_{\mathrm{mix}}(A)\right] / RT. \tag{5.3}$$

The pseudo partition coefficients $\log K_{\mathrm{x/y}}(A)$ are not true partition coefficients, but rather are pseudo partition coefficients or driving forces as they are calculated from free energies of mixing of systems not necessarily in thermodynamic equilibrium and potentially at unstable conditions, but at the same weight composition.

5.1.4 Results and discussion

Free energies of mixing predictions for all oligomer/polymer pairs are plotted in weight-normalised quantities in Fig. 5.2a. Incompatibility is found for the majority of combinations and compositions. PiBB and hPMI oligomers are incompatible with PB and PI, and compatible in hPI. Inclusion of the furandione group in the PiBB+fur model shows slight incompatibility in hPI at high oligomer concentrations, but does not change the qualitative compatibility in PI and PB. PM oligomers are found to be compatible with PI and PB, while partially compatible in hPI.

The pseudo partition coefficient predictions in Fig. 5.2c reveal a positive driving force for most oligomers. The only negative partition coefficient is found for $\log K_{\mathrm{hPI/PB}}(\mathrm{PM})$. A positive pseudo partition coefficient $\log K_{x/\mathrm{PB}}$ describes oligomers which are less compatible in PB than in polymer x, and a negative $\log K_{x/\mathrm{PB}}$ describes oligomers less compatible in polymer x than in PB. The large positive $\log K_{x/\mathrm{PB}}$ values can be attributed to the large positive ΔG_{mix} for the oligomer–PB pairs found for all oligomers apart from the PM tackifier.

The absolute (pseudo) partition coefficient values predicted by SAFT are significantly larger than found in the experimental studies obtained from GPC experiments by Hamm and Mansfield,[206] see the comparison in Tab. 5.2. The experimental values are consistently positive and between 1.44 and 6.23, while the SAFT-γ Mie predictions are roughly between -2 and $+42$. As the $\log K_{\mathrm{PI/PB}}$ values for PiBB and hPMI in PI/PB are based on only incompatible pairs, the SAFT-γ Mie predictions are clearly in contrast to the experiment. Agreement, however, with the experimental results is found qualitatively on whether the driving force is larger in the PI/PB or h-PI/PB

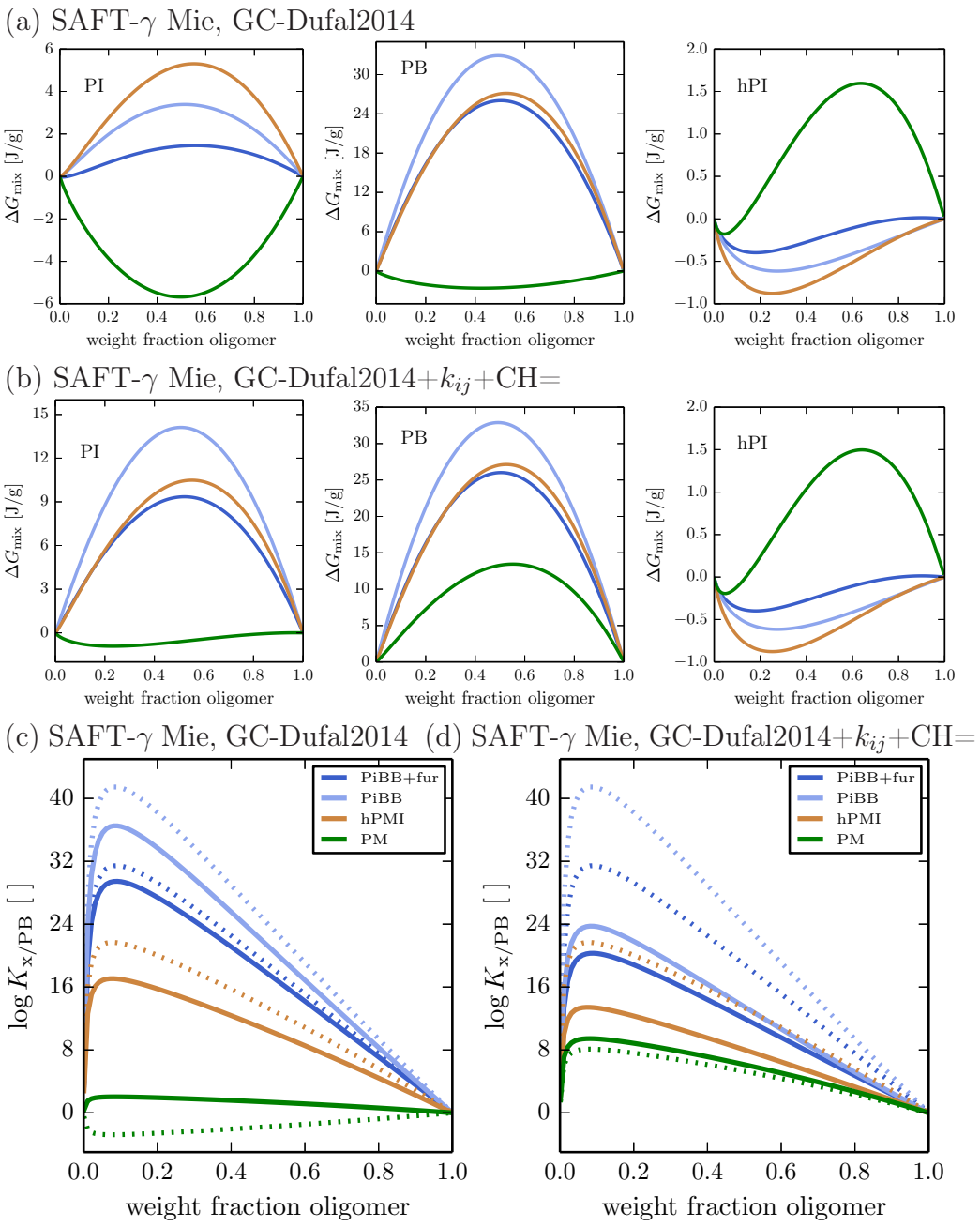

Figure 5.2: SAFT-γ Mie predictions for (a,b) free energies of mixing as a function of the oligomer weight fraction for oligomer/polymer pairs: Polyisoprene (left), polybutadiene (middle), hydrogenated polyisoprene (right). (c,d) Pseudo partition coefficients $\log K_{x/\mathrm{PB}}$ as a function of oligomer weight fraction: $\log K_{\mathrm{PI/PB}}$ (continuous lines) and $\log K_{\mathrm{hPI/PB}}$ (dotted lines). The legend in (c) also applies to (a,b).

system, effectively correctly capturing the effect of hydrogenation of the polymer matrix. Agreement is also found on the order of all (pseudo) partition coefficient apart from the order of hPMI/PI/PB and PM/PI/PB. The same inversion of hPMI/PI/PB and PM/PI/PB, however, is also predicted by the linear free-energy model (LFE),[206] hence the order of all (pseudo) partition coefficient agrees between SAFT-γ Mie and LFE without exceptions.

The SAFT model seems to capture the relative chemistry of the compounds, but does not perform well on the absolute compatibility of pairs of oligomers and polymers.

Table 5.2: Comparison between experimental partitioning,[206] linear free-energy partitioning predictions[206] and SAFT-γ Mie pseudo partitioning predictions. As quantitative agreement was not achieved, the order of partition coefficient values for each method is given as "rank" in brackets. Rank numbers highlighted in green agree with experiment, while red highlights disagreement with experiment. The SAFT predictions of the pseudo partition coefficient are reported for 33% (w/w) of oligomer.

system		(pseudo) partition coefficient (rank)			
polymer pair	oligomer	exp.[206]	LFE[206]	SAFT-γ Mie +GC-Dufal2014	SAFT -γ Mie +GC-Dufal2014 +k_{ij}+CH=
PI/PB	PiBB+fur	3.42 (#2)	3.13 (#2)	23.4[a] (#2)	16.0 (#2-3)
PI/PB	hPMI	1.49 (#5)	2.65 (#4)	13.6[a] (#4)	10.5 (#4)
PI/PB	PM	2.11 (#4)	2.44 (#5)	1.71 (#5)	7.76 (#5)
hPI/PB	PiBB+fur	6.23 (#1)	7.21 (#1)	24.9 (#1)	24.9 (#1)
hPI/PB	hPMI	2.27 (#3)	3.03 (#3)	17.3 (#3)	17.3 (#3-2)
hPI/PB	PM	1.44 (#6)	1.98 (#6)	−2.25[a] (#6)	6.67 (#6)

[a] Predicted phase separation of the oligomer into a third phase as the oligomer is not fully compatible with either polymer.

SAFT-γ Mie predictions for the qualitative compatibility data of a range of oligomer/polymer is compared in Tab. 5.3 with experimental results obtained from the shift of glass transition temperatures in DSC measurements.[204,205]

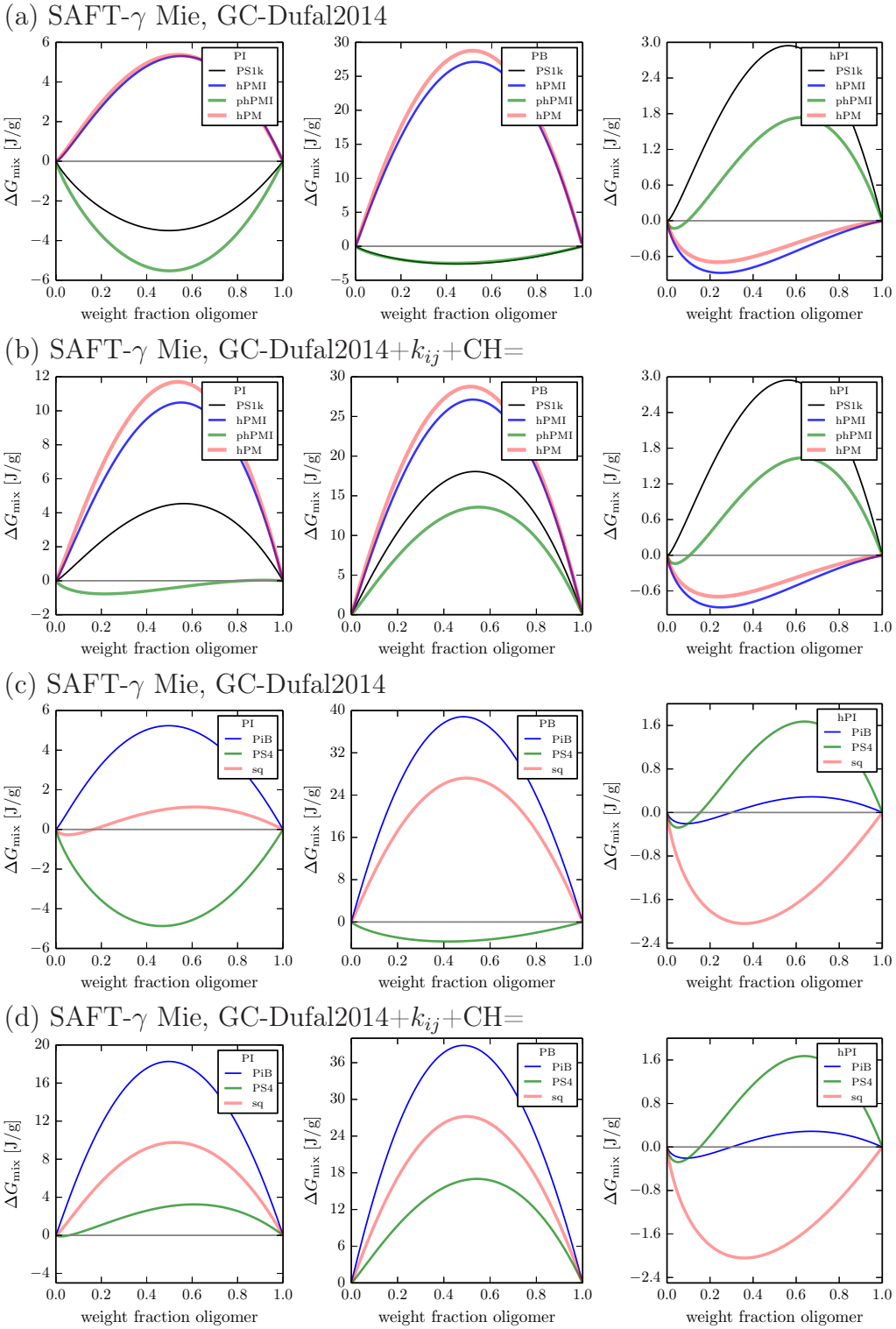

Figure 5.3: SAFT-γ Mie predictions for free energies of mixing for oligomer/polymer blends. The polymers are polyisoprene (left column), polybutadiene (middle column) and hydrogenated polyisoprene (right column). The SAFT-γ Mie group-contribution parameter set by Dufal *et al.*[184] 2014 was used (a,c) alone and (b,d) with two improved k_{ij} values and informed choice of the (CH=) group.

Table 5.3: SAFT-γ Mie predictions for the number of phases in equilibrium for several oligomer/polymer pairs compared with experimental DSC results.[204,205] "1" phase denotes compatibility, "1-2" phases partial compatibility, and "2" phases incompatibility. The solubility limit for predicted partial compatibility is given as oligomer weight percentages in brackets.

polymer	oligomer	experimental	SAFT-γ Mie +GC-Dufal2014	SAFT -γ Mie +GC-Dufal2014 +k_{ij}+CH=
hPI	PS4	2 [a]	1-2 (5%)	1-2 (5%)
hPI	PS1k	2 [b]	2	2
hPI	squalane	1 [a]	1	1
hPI	PiB	1 [a]	1-2 (15%)	1-2 (15%)
hPI	hPM	1 [b]	1	1
hPI	hPMI	1 [b]	1	1
hPI	phPMI	1-2 [b]	1-2 (5%)	1-2 (5%)
PI	PS4	1-2 [a]	1	1-2 (2%)
PI	PS1k	2 [b]	1	2
PI	squalane	1 [a]	1-2 (10%)	2
PI	PiB	1-2 [a]	2	2
PI	hPM	1? [b,c]	2	2
PI	hPMI	1? [b,c]	2	2
PI	phPMI	1 [b]	1	1-2 (40%)
PB	PS4	1-2 [a]	1	2
PB	PS1k	2 [b]	1	2
PB	squalane	1 [a]	2	2
PB	PiB	2 [a]	2	2
PB	hPM	2? [b,c]	2	2
PB	hPMI	1? [b,c]	2	2
PB	phPMI	1 [b]	1	2

[a] Sabattié *et al.* 2015[204]

[b] Mansfield 2015[205] Compatibility statement only for a 50/50 weight percent mixture.

[c] Experiment not conclusive[205]

A poor agreement of the SAFT model predictions with the DSC experiments is found as agreement is only found in 8 cases and disagreement is found in 9 cases.

SAFT-γ Mie model parameter improvements

Some of the poor performance correlates with unlike interactions, which relied on combining rules in the Dufal parameter set and were not explicitly fitted to experimental data. The two unfitted unlike interactions with the highest contribution in this work were identified based on the number of beads in the compound models. The overview in Fig. 5.4 reveals the olefinic-aromatic (aCH/CH=) and cycloaliphatic-aromatic (aCH/cCH2) interactions to be the most important unfitted interactions for the systems in this work. Solvent mixtures which exclusively rely on (or are dominated by) these interactions are chosen to inform these unlike interactions. SAFT-γ Mie predictions for these solvent mixtures were compared with experimental data to test the performance of the combining rule and adjustments were made to the unlike interaction parameter k_{ij} when needed. Recall, that k_{ij} was defined as the correction factor to the energetic unlike interaction parameter as

$$\epsilon_{ij} = (1 - k_{ij}) \frac{\sqrt{\sigma_{ii}^3 \sigma_{jj}^3}}{\sigma_{ij}^3} \sqrt{\epsilon_{ii} \epsilon_{jj}} \tag{5.4}$$

and is typically the first correction factor to be invoked to adjust unlike interactions to improve the performance of SAFT-γ Mie models.

The olefinic–aromatic interactions are tested in benzene mixtures with ethene, propene and butadiene. The (CH2=) bead was tested therefore first before the (CH=) was tested and adjusted. The prediction of ethene/benzene vapour pressures as (2 CH2=)/(6 aCH) at 293 K and 313 K at several compositions reveals the best agreement with experimental data for the combining rule of (CH2=)/(aCH). Using the validated (CH2=)/(aCH) interaction, the olefinic-aromatic interaction (CH=)/(aCH) is tested in models for propene/benzene and propene/butadiene mixtures. Dew and bubble point (start of vapour condensation and start of liquid boiling, respectively) predic-

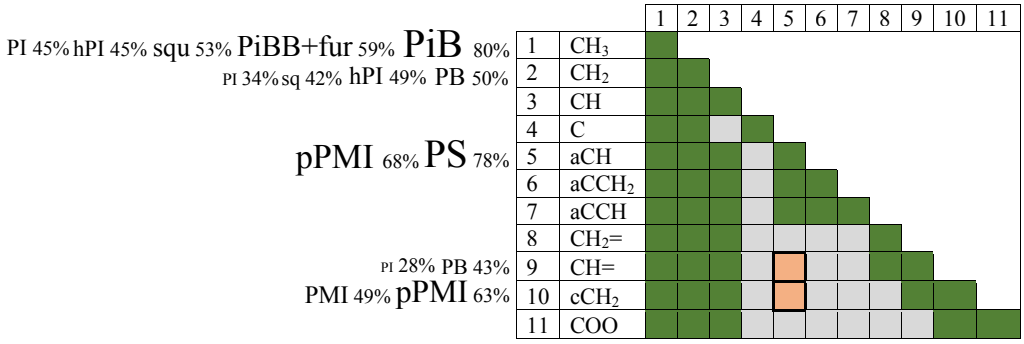

Figure 5.4: Extract from the GC-Dufal2014 group parameter set.[184] Green denotes interactions fitted by Dufal and coworkers, grey highlights interactions derived with combining rules, and the two red and stronger contoured pairs are fitted in this work. The percentage of the groups for each compound are added to visualise the relative importance of the interactions. The percentage is calculated based on the number of beads used for each compound i, while the number of bead type k is calculated accounting for the shape factor as $\nu_{i,k}\nu_k^* S_k$. Only percentages equal or larger than 28% are shown for the sake of clarity and to highlight only the most dominant groups in the polymer models.

tions across the whole composition range were compared with experiments, see Fig. 5.5. We found a readjusted $k_{ij} = 0.22$ to give a significantly better agreement than the combining rule for both mixtures. The combining rule hugely overestimated the interaction strength.

The cycloalkane–aromatic interaction was tested with boiling and bubble point temperatures of a cyclohexane/benzene mixture. The comparison in Fig. 5.5 reveals how the azeotropic mixture is better described with $k_{ij} = 0.01$ than with the combining rule.

Further testing of additional unlike interactions was attempted, but no mixture data was found which is dominated by those interactions and did not require parametrisation of completely new bead types. Further attempts were made, for example, for the cyclic aromatic (aCCH and aCCH2) groups interacting with olefinic and cycloalkane groups, and the olefinic (CH2=) group interacting with the cycloalkane group.

For validating the replacement for the fully substituted olefinic group (>C=), which is not part of the Dufal 2014 parameter set, the two closest-

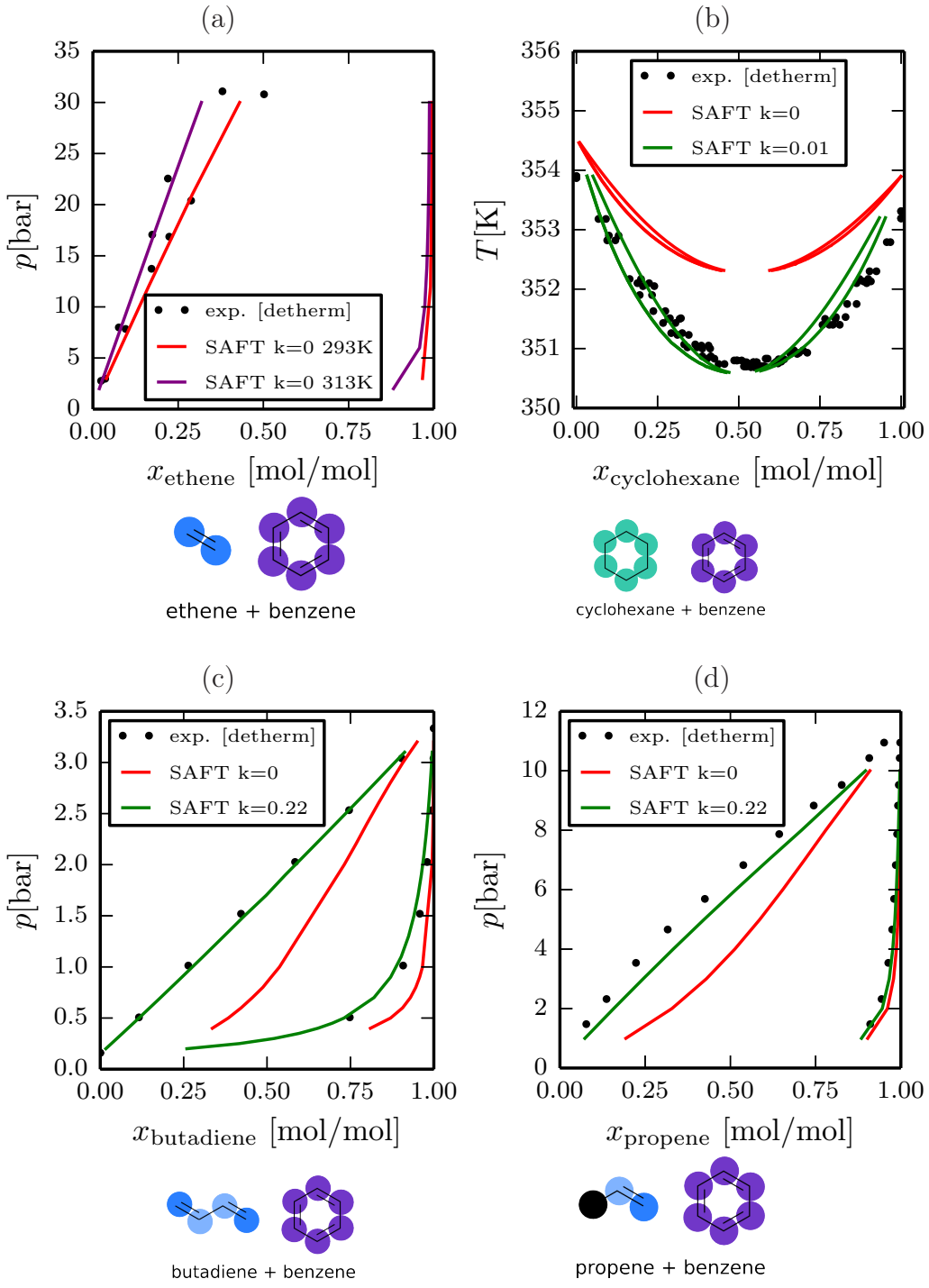

Figure 5.5: Vapour–liquid equilibria (VLE) of binary mixtures calculated with SAFT-γ Mie using the GC-Dufal2014 parameter set.[184] The unlike interactions are tested and adjusted. (a) ethene/benzene at T = 293.15 K and 313.15 K, k(CH2=/aCH) tested, (b) cyclohexane/benzene at P = 101300 Pa, k(cCH2/aCH) adjusted, (c) benzene/butadiene at T = 303.15 K, k(CH=/aCH) adjusted, (d) propene/benzene at T = 298.15 K, k(CH=/aCH) tested, All experimental data (symbols) was retrieved from the DETHERM database.[207]

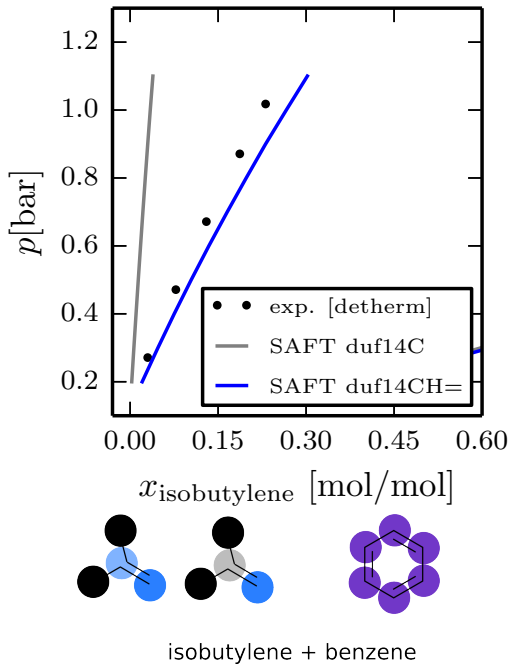

Figure 5.6: Comparison of vapour–liquid equilibria predictions for two SAFT-γ Mie models of the isobutylene/benzene mixture at $T = 298.15$ K. As no dedicated parameters are available for the fully substituted olefinic group (>C=), the closest matching beads (CH=, blue) and (C, grey) of the Dufal *et al.*[184] parameter set are compared. All experimental data (symbols) was retrieved from the DETHERM database.[207]

matching groups are tested. The weight consistent (>C<) and the chemically similar (>CH=) group are tested for vapour pressures of an isobutylene–benzene mixture. The chemically similar (>CH=) group gives a far better agreement with the experimentally observed data, see Fig. 5.6.

All previous predictions were recalculated using the improved GC-Dufal-2014 parameter set by including the two adjusted parameters k(CH=/aCH)= 0.22 and k(cCH2/aCH)= 0.01 together with the validated choice of (>CH=) for the missing (>C=) group. The improved parameter set performs slightly better in predicting the oligomer/polymer compatibilities. The new SAFT-γ Mie predictions for all previously studied mixtures are presented in Tables 5.2 and 5.3. All (pseudo) partition coefficients are now correctly positive and the relative position to each other is significantly improved, as can, for example be seen in better differentiation of the PI/PB/PiBB+fur and hPI/PB/PiBB+fur results. The relative agreement with the LFE results has become even better. New correct predictions are found for the two PS/PI mixtures and the PS1k/PB blend, but a worse performance for the PB/phPMI mixture. Overall the improved parameter set gives 10 correctly and 7 incorrectly predicted compatibilities. Worse performances were found for the arguably most complex mixtures PB/phPMI and PI/phPMI which are composed of several monomer types, isomers and partial hydrogenation. In conclusion, the updated parameter set has led to a systematic improvement.

Two additional trends are studied with the GC-Dufal2014 parameter set to further evaluate the transferability to larger molecular weights. The trends are the influence of the oligomer molecular weight and the degree of hydrogenation of unsaturated oligomers.

Influence of oligomer molecular weight

A range of alkane chains has been modelled to study the influence of molecular weight of the oligomer on the pseudo partition coefficient. Linear alkane chains of the length of n-hexane, n-hexadecane, n-C_{30}, n-C_{60}, n-C_{120}, n-C_{240} and n-C_{480} are modelled. The structures and their mapping are shown in

Fig. 5.7a.

Predictions for the free energies of mixing in Fig. 5.7b-d overall reveal improved compatibility for reduced molecular weights of the oligomers, which follows the known trend caused by the increasing stabilising influence of the ideal entropy of mixing for smaller molecular weights. While alkanes of all modelled chain lengths are predicted to be compatible with hPI, none are compatible with PB. In PI, the compatibility reduces from fully compatible (n-C_6 and n-C_{16}), via partial compatibility to incompatibility (n-C_{240} and n-C_{480}).

The pseudo partition coefficients in Fig. 5.7e reveal a high driving force for all oligomer chain lengths. Both longer chain length of the oligomer as well as the hydrogenation of hPI compared to PI leads to larger $\log K_{x/\mathrm{PB}}$ values. The trend of increased $\log K_{x/\mathrm{PB}}$ values for longer chain lengths agrees with GPC experiments.[206] It is important to note again that $\log K_{x/\mathrm{PB}}$ values have been calculated for all pairs, even those predicted to be incompatible.

Counter-intuitively, the weight normalised energy of mixing for PB in Fig. 5.7c is almost independent of the oligomer chain length. Even a slight increase of ΔG_{mix} with oligomer molecular weight is found, although the entropy of mixing with larger negative contributions at smaller molecular weights is expected to favour a mixed system. As the chains are terminated with CH_3 groups, the relative composition of groups changes with molecular weight. This change of composition seems to have a larger positive contribution to ΔG_{mix} than the entropy of mixing has a negative contribution.

Influence of oligomer hydrogenation

The influence of degree of hydrogenation (fraction of unsaturated bonds) of the oligomer on the partition coefficient was studied by a range of of linear C_{16} hydrocarbon chains. The two extreme cases are the unsaturated hexadec-2,4,6,8,10,12,14-ene and the fully saturated n-hexadecane. The degree of hydrogenation is modelled by substituting (CH=) with (CH_2) groups in 14 steps. The mapping and structures are represented in Fig. 5.8a.

The free energies of mixing analysis in Fig. 5.8b-d shows better compati-

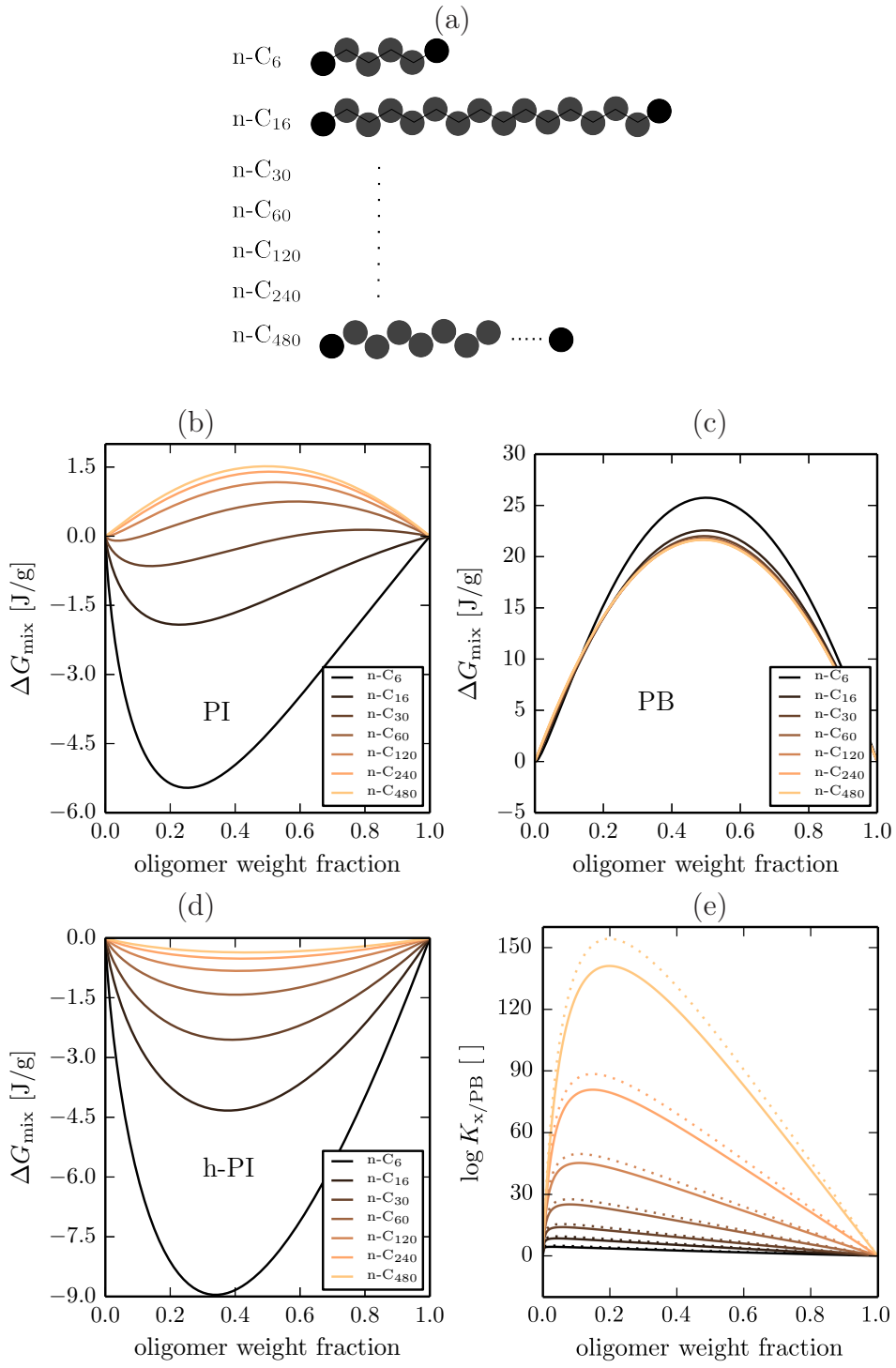

Figure 5.7: Compatibility predictions for oligomer/polymer pairs with oligomers of varying molecular weight. (a) The oligomers differ by their number of CH_2 groups and correspond to different chain lengths. Free energies of mixing as a function of the oligomer weight fraction in (b) polyisoprene, (c) polybutadiene and (d) hydrogenated polyisoprene. (e) Pseudo partition coefficients $\log K_{x/\mathrm{PB}}$ as a function of oligomer weight fraction: $\log K_{\mathrm{PI/PB}}$ (continuous lines) and $\log K_{\mathrm{h-PI/PB}}$ (dotted lines).

bility for hydrogenated C_{16} hydrocarbon in PI and hPI, and rather unsaturated C_{16} hydrocarbons in PB. The best compatibilities are found for C_{16} with 4 double bonds in PB, C_{16} with 1 double bond in PI and fully saturated C_{16} in hPI. The ratio of saturated and unsaturated groups of the best-compatible tackifiers roughly agrees with the ratios found in the respective polymers and supports expectations.

In summary, the best compatibility is found when the fractions of olefinic groups roughly agree between the oligomer and polymer, confirming the expectation that chemically similar compounds are more compatible.

5.1.5 Conclusion

We applied the currently most comprehensive group-contribution Mie potential parameter set by Dufal *et al.*[184] to oligomer/polymer mixtures of molecular weights far beyond the molecular weight range it was developed for. In summary, we find the predictions to correctly capture the relative chemistry, but show a poor performance in predicting quantitative partition coefficients of oligomers between two immiscible polymers, and compatibilities in oligomer/polymer blends both quantitatively and qualitatively.

The order of free energy of mixing differences matches the experimentally observed order of partition ratios with only one exception, although in many cases incompatibility is predicted where compatibility is found experimentally. In comparison with predictions of an independent LFE model,[206] the SAFT-γ Mie predictions match the order of free energy of mixing differences of the LFE model without exceptions. Also the gaps between the predicted values agree better with the LFE model predictions than with the experimental findings. The influence of the oligomer molecular weight and the oligomer degree of hydrogenation is correctly captured by the SAFT-γ Mie calculations using the GC-Dufal2014 parameter set.

We were able to show a systematic improvement to the GC-Dufal2014 parameters by testing and adjusting two unlike interactions with VLE data of low molecular weight mixtures. Predictions for both pseudo partition coefficients and for oligomer/polymer compatibilities saw an improvement in

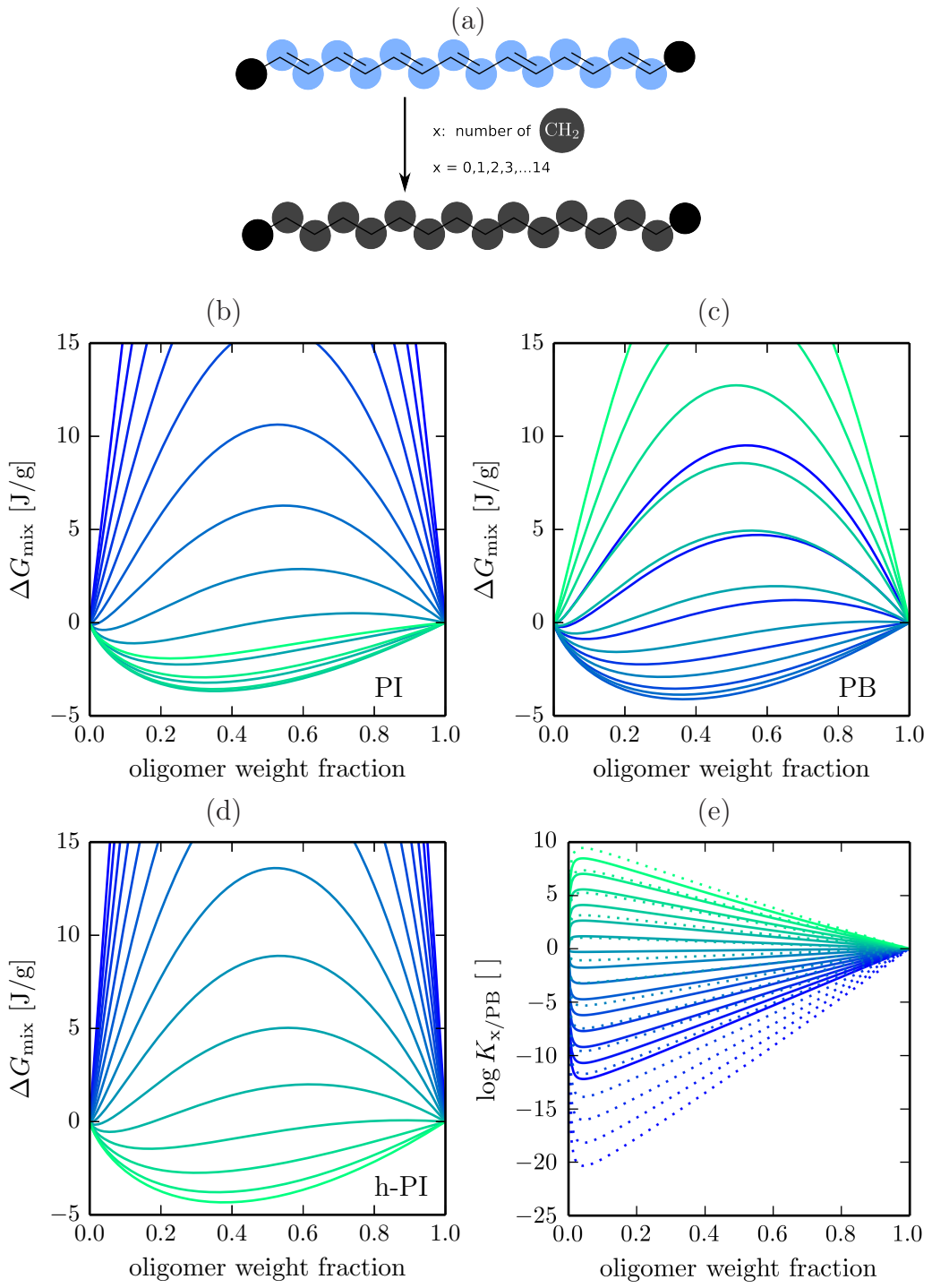

Figure 5.8: Compatibility predictions for oligomer/polymer pairs with C_{16} oligomers of varying degree of hydrogenation. (a) The 15 C_{16} oligomers differ by their ratio of (CH=) to (CH_2) groups and correspond to different degrees of hydrogenation, from unsaturated (blue bead, dark blue lines) to fully saturated (grey bead, bright green lines). Free energies of mixing of oligomer–polymer pairs as a function of the oligomer weight fraction in (b) polyisoprene, (c) polybutadiene and (d) hydrogenated polyisoprene. (e) Pseudo partition coefficients $\log K_{x/\mathrm{PB}}$ as a function of oligomer weight fraction: $\log K_{\mathrm{PI/PB}}$ (continuous lines) and $\log K_{\mathrm{h-PI/PB}}$ (dotted lines).

the agreement with experimental results.

We do not expect to see further improvements in the predictions by accounting for the polydispersity of the oligomers and polymers, because including polydispersity is expected to further reduce the compatibilities.[147]

Our findings suggests the local chemistry and in particular the relative chemistry is correctly captured with the GC-Dufal2014 parameter set applied to polymers, but not all high-molecular-weight effects are represented correctly when the number of beads in the SAFT-γ Mie model is simply adjusted to match the polymer weight.

Molecular-weight-transferable parameter sets of older SAFT versions not only scale the number of beads, but introduce additional fitted parameters to also scale the energetic parameter and number of beads per monomer unit.[80,81,83] The two additional parameters are estimated based on experimental data available at several molecular weights. The additional experimental data makes the development of these parameter sets more expensive and prohibit the development if no data is available or can be measured.

The challenges to reproduce the experimental data in this section are at least partially attributed to the lack of chemical information of the compounds in this study. For most compounds the detailed monomer ratio was not known. Furthermore SAFT predictions are expected to be most reliable when applied to situations of similar reduced properties (T/T_{crit} and P/P_{crit}),[64] while the reduced properties of the predictions in this section are far lower than used during the parameter estimation due to the (experimentally inaccessible) large T_{crit} and P_{crit} of polymers. In addition, approximations in the SAFT theory are less well suited to predict properties of long chains due to the linear approximation used for the many-body distribution function of the monomer reference fluid.[115]

5.2 Approaches to developing new SAFT-γ Mie models for polymers

Applying SAFT-γ Mie parameters beyond the molecular weight range they are optimised for did not lead to accurate predictions of polymer compatibilities. No dedicated SAFT-γ Mie parameters for polymer mixtures are available, either. New polymer models will therefore be developed in this work. In this section, a few approaches, best practices, important considerations, ideas and aspects to developing new SAFT models are summarised. This summary compiles a few selected insights from many groups around the world who successfully developed models for equations of states.

Several types of experimental data in the parameter estimation help balance thermodynamic properties and improve the transferability due to more physically relevant parameter values.[14] It was shown that the inclusion of polymer solution VLE data improves the pure-component polymer parameters in PC-SAFT models.[116] One of the biggest strengths of equations of state such as SAFT-γ Mie is the ability to calculate properties quickly for a given (guessed) model. The possibility to include many state points and also many different types of properties in the estimation of new parameters is an important advantage. However, polymer mixture data is scarce and makes exploiting the full potential of the SAFT-γ Mie theory a challenge.

Other complementary methods can be used to inform SAFT-γ Mie parameters. Müller and coworkers speed up the parameter estimation process by relying on the corresponding state principle.[153,156,208] Methods based on *ab-initio* calculations could inform SAFT models about the strength of hydrogen bonding, or could generate pseudoexperimental data for example with COSMO-RS,[18,43] which combines quantum chemical calculations and statistical thermodynamics, for compounds that have not been experimentally characterised. However, the molecular weight which can reliably be described by these complementary methods is usually smaller than what could be considered a polymer.

Parameters can be extrapolated to areas where no information is available based on systematic sets of experimental data. Examples are models for

long alkanes which are extrapolated from models of the homologous series of shorter alkanes.[14,16,80,209] Group-contribution approaches are one way of generating new models by simply scaling the number of parameters.[15,123,184] Often not only the number of beads, but also other SAFT parameters are scaled with the molecular weight.[13,80] However, the development of such continuous models requires a set of systematic data such as a homologous series (monomer, dimer, trimer, tetramer, ...), which is not available for polymers apart from the alkane series for polyethylene.

The balance of enthalpy and entropy can be improved by analysing them separately. White and Lipson[210,211] showed with a lattice-based equation of state that the energetic part of unlike interactions mainly influences the enthalpy of mixing, while the energetic like interactions mainly influence the entropy of mixing. The energetic parameters strongly correlated with the classification of lower critical-solution temperature (LCST) and upper critical-solution temperature (UCST) mixtures. It is unclear how transferable the insights are to the SAFT-γ Mie equation of state as its models entail more parameters than a lattice-based equation of state, but it could help better assess SAFT models and guide parameter estimations where acceptable agreement with experiment can not be found immediately.

The number of beads and number of parameters to optimise can be carefully chosen. The SAFT-γ Mie equation of state offers more parameters than most of its predecessors. The risk of overfitting models is especially present when only a small set of reference data is available. Choosing $\lambda_a = 6$ is one simplification, only allowing one type of Mie potential per compound is another. The step towards group-contribution parameters increases the number of parameters drastically as the number of interactions grows proportional to the number of bead types squared. Combining rules can be used as first estimates for unlike interactions, but especially polymers require individual readjustments.

5.3 Experimental reference data

In this section we try to give an overview of what experimental data types are typically and easily encountered for oligomers and polymers both in scientific literature and from commercial suppliers. We also summarise how helpful the types are in the development of SAFT-γ Mie models and provide a semi-exhaustive list of PVT, V_{mix} and LLE experimental data for a combination of hydrocarbon polymers.

In general, less experimental data is available for polymers than for solvents and other low-molecular-weight compounds. This is at least partially due to the larger number of possible chemical structures for polymers and the increased difficulty to both synthesise and determine the exact chemical structure and composition.

Even less data is available for oligomers than polymers. Two exceptions are polyethylene oligomers (also known as alkanes) and polystyrene oligomers, for which the reader is best referred to Refs 212–214. Some information is available about a range of industrial oligomeric compounds,[215,216] but unfortunately not enough to easily develop a meaningful SAFT model. One additional aspect, which complicates the development of SAFT models for oligomers, is that monodisperse oligomers would be ideal for the model development, but monodisperse oligomers are difficult to synthesise. Typically available oligomers are derived from oil and gas, and therefore consist of monomer units, which often are C_5 or C_9 hydrocarbon units, and can have a few repetitive units up to a number average molecular weight of roughly 3000 g/mol.

Oligomer suppliers such as EASTMAN,[215,216] give cloud-point temperatures of oligomers for selected solvent systems. The specific solvent mixtures methylcyclohexane/aniline, xylene/4-hydroxy-4-methyl-2-pentanone, and a mixture of various aliphatic mineral solvents[216]) are chosen to cover a large range of polarities, so usually only two cloud points are determined for an individual oligomer. As only one composition is used in the experiments, only two data points are provided. Two equilibria data points are not sufficient to confidently obtain a SAFT model, but can only be used as a test for SAFT

models whose parameters where estimated from other data.

In Tab. 5.4, typical oligomer and polymer properties are listed and an overview given whether they are typically provided by manufacturers, easily found in the literature, easily measured and, most importantly, whether they are helpful in the SAFT parametrisation process.

Table 5.4: Types of experimental data of oligomers and polymers. Positive answers are highlighted in green, negative answers in red, and unclear non-binary answers in orange.

type	provided by supplier?	often found in literature?	cheap/easily/quickly measured?	helpful in SAFT model development?
molecular weight	yes	yes	yes, via GPC	yes, the smaller M_w the more important
polydispersity	yes	yes	yes, via GPC	yes, the larger the more important
molecular weight distribution	sometimes	no	yes, via GPC	yes, the less uniform the more important
LLE and cloud points[a]	single data point	yes	yes	yes
glass transition temperature	yes	yes	yes, via DSC	no
softening point	yes	no	ring and ball experiment	no
viscosity	yes	no	yes, via rheology	no
density (PVT)	single data point	yes	yes, various methods	yes
chemical composition	partially	yes	to some degree	yes, for mapping, GC-approaches and it allows the use of data from other systems
isomer ratio	no	yes	yes, via NMR	yes, for mapping, GC-approaches and it allows the use of data from other systems
acid number	yes	no	unclear	no
VLE	no	no, all but small oligomers have no measurable data	no	yes
heat capacity	no	yes	yes, via DSC	no, see Sec.5.4.3
speed of sound	no	no	no, high viscosities are difficult	no, see Sec.5.4.3
SANS	no	rarely	no, very expensive	yes
SAXS	no	rarely	no, expensive	yes
volume of mixing	no	no	needs very high precision and accuracies, see Sec. 5.5.3	yes
block copolymer data	no	yes	yes	no, see Refs 217–219 for comparisons of blends and their block copolymers

[a] Not all mixtures have cloud points or LLE at accessible conditions. Adjusting molecular weights can make cloud points accessible.

5.3.1 Literature compilation of polymer data

A list of the best experimental data found in the course of this work is compiled in Tab. 5.6 accompanied by additional information in Tab. 5.5. The tables provide a semi-comprehensive list of experimental thermodynamic data of homogeneous properties of the most common oligomeric and polymeric hydrocarbons.

The list is aimed both at readers looking for references for polymer data and readers interested in knowing what compounds and mixtures have not been characterised (or not published), yet.

From the compilation of experimental polymer and polymer blend data in Fig. 5.6, it becomes obvious that most data available is for pure polymers. For the binary blends, data was only found for 17 out of the 45 possible blends, although most polymer categories entail several constitutional and stereo isomers. Completely miscible as well as completely immiscible binary pairs can not be easily characterised with LLE and CPC data, as the properties are inaccessible. The missing data for some of the binary blends can be explained by this inaccessibility. However, adjusting the degree of polymerisation or using more extreme temperatures does lead to partial miscibility eventually and the chance to measure LLE and CPC data. Mixtures of compounds with similar structure and higher miscibility are typically better characterised, and the lack of experimental data we found in the course of this work is mainly found for cases of complete immiscibility, as for most aromatic–aliphatic blends (e.g., PS/hPI). However, as seen for PS/PE, an oligomeric pair of PS/PE has accessible liquid–liquid transitions due to the improved miscibility at smaller molecular weights.

Block copolymer properties are not included as they can not be properly captured by SAFT equations of state as they are not homogeneous properties. Block copolymer properties in principle are very attractive sets of data because they are not only available for polymer pairs of similar chemistry (deuterated vs. hydrogenated), but also for more pronounced differences with strong demixing tendencies such as aromatic vs. aliphatic pairs.

No recommendation for particular references is given, as the best ref-

erence data closely depends on target details such as the molecular weight distribution and monomer ratio. The potential details to choose one over the other are too many that listing all of them would make our aim of providing an overview and general reference impractical.

Special attention is reserved for the mixtures of P1B, PE, PP, hPI as they are well characterised by collaborations from the groups around Balsara and Lohse at Exxon Research and Engineering Company, and Krishnamoorti and Graessley at Princeton University,[220–226] who have developed the probably best set of thermodynamic miscibility data of a set of hydrocarbon polymers. For further references, beyond the few given in the table, the reader is referred to the review article by Balsara[36] for a more systematic and comprehensive overview.

Table 5.5: Chemical structure and synonyms of polymers for which experimental data is compiled in Tab. 5.6.

polymer	synonyms	main repeating units
PS	polystyrene	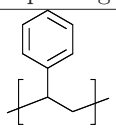
PB	polybutadiene (PB) poly(vinylethylene) (PVE) cis/trans-1,2/1,4-PB	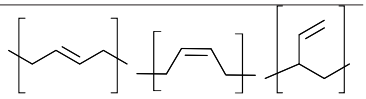
PI	polyisoprene(PI) poly(terpene) terpene resin poly(2-methyl-butadiene)	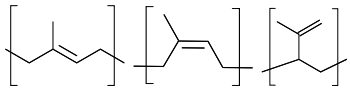
hPI	hydrogenated polyisoprene (hPI) poly(methylbutylene) poly(ethylene-propylene) (PEP)	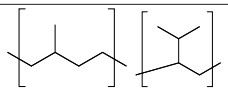
PiB	polyisobutylene polyisobutene	
PE	polyethylene hydrogenated 1,4-polybutadiene (hPB)	
PP	polypropylene	
hPS	hydrogenated polystyrene poly(vinyl-cyclohexane) poly(cyclohexylethylene)	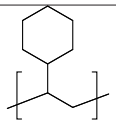
mPM / P(C_9)	poly(methylstyrene) (mPS) hydrogenated poly(methylstyrene) polyindene hydrogenated polyindene poly(aromatic C_9)	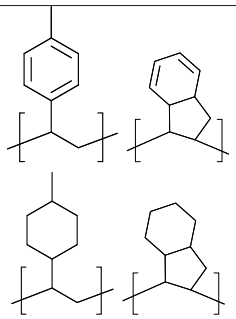
P1B	poly(1-butene) (P1B) poly(ethylethylene) (PEE) hydrogenated 1,2-polybutadiene (hPB)	

Table 5.6: Compilation of selected thermodynamic homogeneous experimental data for selected hydrocarbon oligomers/polymers and binary blends (not block copolymers). References for densities (PVT), vapour–liquid equilibria such as boiling points (VLE), liquid–liquid equilibria such as cloud-point temperatures (LLE), glass transition temperature (T_g), heat capacity (C_P) and small-angle neutron scattering (SANS) are listed. Polymer pairs for which no PVT, VLE, LLE or SANS data could be found are highlighted with a light red cell background. See Tab. 5.5 for more information on the polymer notation.

	PS	PB	PI	hPI	PiB	PE	PP	hPS	mPS	P1B
PS	PVT[211,213,227–230] VLE[212] C_P,[213,214,231] T_g[214]									
PB	LLE[211,230,232–235]	PVT[213,228,230,236–238] VLE[212] LLE,[214,239] C_P[214,240]								
PI	LLE[232,241,242] PVT[242] SAXS[242]	PVT[238,243] LLE[213,244,245] SANS[246] T_g[213]	PVT[213,229,236,238] VLE[212] C_P,[213,214,240] T_g[213]							
hPI		LLE[247]	LLE[248]	PVT[211,220,221,228,249,250] T_g[251]						
PiB				LLE[220]	PVT[220,222,227,228] VLE,[212] C_P[214,240]					
PE	LLE[252]			LLE[218,222,253] SANS[223]		PVT[213,221,222,227,228] VLE[213] C_P,[213,214,254] T_g[213]				
PP				LLE[222] SANS[223]	LLE[221,222]	LLE[214,223] SANS[223]	PVT[214,221,222,227,228] C_P,[213,214,255] T_g[213]			
hPS		LLE[214]						PVT[256]		
mPS	LLE[234,257,258]	LLE[234,257]							PVT[214,227,257] C_P[240]	
P1B				LLE[221,223] SANS[221,223]		PVT[221,224] LLE[221,223–225] SANS[225,226]	PVT[221] LLE[224] SANS[223,224]			PVT[221,225] SANS[225,226]

5.4 Like interactions

This section is concerned with the development of Mie potential interactions between beads of the same type (like interactions). Like interactions are sufficient to describe pure compounds. We discuss different means to develop like interactions and report a range of SAFT-γ Mie models developed with density data (PVT). The impact of each Mie potential parameter on the predicted PVT data is presented, large optimisation sets visualised, and common considerations discussed.

5.4.1 Corresponding state principle

The corresponding state principle (CSP) can be used as a shortcut for the development of SAFT-γ Mie models. With the method by Mejia *et al.*,[156] who provide parametrised explicit expressions, Mie potentials are obtained from just three key experimental data points, without the need for an iterative optimisation algorithm using the full SAFT-γ Mie equations.

The overall VLE curve of most compounds are similar. In fact, they almost perfectly collapse into a single master curve when scaled by a few key features such as the critical temperature and pressure, acentric factor (measure for non-sphericity of compound) and a single absolute density value. This correspondence between different compounds is the so-called corresponding state principle.

In 2014 Mejia *et al.* have reported expressions which translate the rescaling into Mie potential parameters. The method was successfully demonstrated for a couple of example compounds.[156,259] We have implemented the expressions in a small python script and generated a range of Mie potentials for hexane, octane and benzene. The predicted VLE are compared with experimental VLE in Fig. 5.9 and good agreement is found. Recently, also a web application using this corresponding state principle of Mie potentials has been published by Ervik *et al.* providing direct access to Mie potential parameters for thousands of low molecular fluids.[260]

While the method by Mejia and coworkers is limited to $\lambda_a = 6$, there is some flexibility in the choice of Mie potential exponents. As long as the van

der Waals-like attractive value α

$$\alpha = \frac{\lambda_r}{\lambda_r - \lambda_a}\left(\frac{\lambda_r}{\lambda_a}\right)^{\frac{\lambda_a}{\lambda_r - \lambda_a}}\left[\left(\frac{1}{\lambda_a - 3}\right) - \left(\frac{1}{\lambda_r - 3}\right)\right] \tag{5.5}$$

is kept constant,[159] exponents can be varied with little change to the predicted properties. Other exponents of choice can be used, for example, as softer potentials for coarse-grained models, which allow larger MD simulation time steps and effectively reduce the simulation time. Alternative Mie potentials for the single-bead benzene model are used in Fig. 5.10. While Ramrattan *et al.*[159] showed examples with very little impact on the VLE curve obtained from MD simulations and attributed the deviations to theoretical assumptions of the fluid when claiming the same α value results in the same properties. In Fig. 5.10 we see significant changes to the VLE curve as λ_r is changed from 43.97 to 22.37 (at constant $\alpha = 0.4901$), and only minor changes for the other smaller λ_r exponents. This finding suggests that the conversion of Mie(λ_r-λ_a) works best at moderate exponents.

The CSP shortcut can not directly be applied to polymers due to several reasons. Firstly, polymers do not have accessible vapour–liquid equilibria curves and critical conditions. Secondly, developing a model for equivalent low-Mw compounds and scaling the number of beads to meet the polymer weight does not reliably work, as shown in the previous section. Thirdly, no data is available for systematic dimer/trimer/tetramer series to extrapolate polymer model parameters.

One way of using the CSP models for polymers is to combine them to heterogeneous models. A bead for each functional unit is developed based on a solvent molecule with the same or similar structure, all beads are connected and multiplied to make larger molecules and polymers. This approach was used in the recent study by Jimenéz-Serratos and coworkers[259] where they developed a CG MD force field for polystyrene/hexane and polystyrene/heptane mixtures. Polystyrene was assembled from two types of separately developed beads. Their polystyrene model is a branched model, which can not be used in SAFT, but was only used as an MD model. By adjusting some of the unlike interactions in MD simulations they successfully showed both liquid–

liquid phase separation at desired temperatures with both upper critical and lower critical solution temperature in different and also in the same model. Polystyrene units consist of one bead from the two-bead toluene model and one bead from long alkane model. Successful polymer models based developed via the CSP method seem to still need trial and error for the best choice of building blocks. Foremost, the interaction between the connected beads might need further adjustment beyond the combining rule as polymer models are very sensitive to small changes to the Mie parameter values.

In summary, we can confirm that the CSP method is a beautifully quick way to get excellent models for pure compounds of low molecular weight, but the development of polymer models requires testing to find the best low-Mw compounds that capture the chemistry of the building blocks of the polymer structure and further adjustments of the unlike interactions are expected to reproduce most polymer properties.

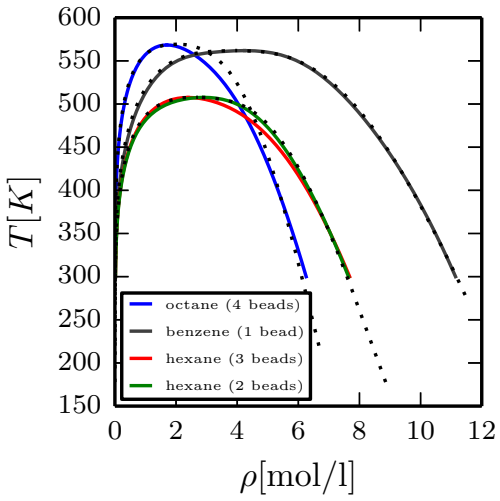

Figure 5.9: VLE predictions for hexane, octane and benzene with SAFT models obtained from the corresponding state method.[156] The number of beads of the model indicated in the legend. Experimental data is plotted as dotted lines.[261]

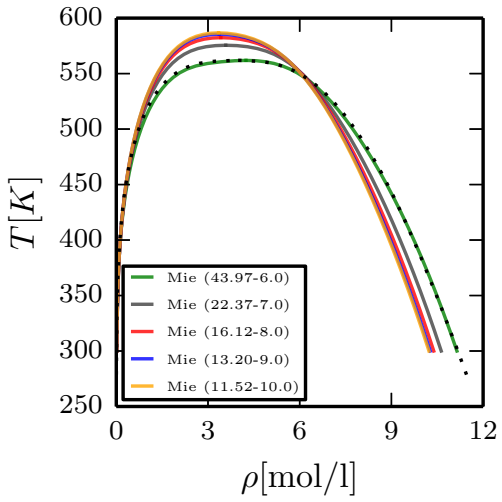

Figure 5.10: Benzene VLE predictions of Mie potentials of constant $\alpha = 0.4901$. Exponent values $\lambda_a = 6, 7, 8, 9$ and 10 are chosen and λ_r adjusted to match the same α. The benzene models consists of a single bead. The model with $\lambda_a = 6$ was obtained via the CSP method. Experimental data is plotted as dotted lines.[261]

5.4.2 Liquid densities (PVT) data

For polymers, unlike for smaller molecules such as solvents, vapour–liquid equilibria data is not available, because polymers have negligible vapour pressures and vapour phases. But liquid densities are accessible and often measured, both as a function of temperature and pressure. Polymers are not only lacking a measurable vapour phase, but the liquid polymer densities show less variations with temperature and pressure than the densities of their low-molecular weight counterparts. For sourcing the most thermodynamic information from liquid densities for a particular polymer, densities across large ranges of both temperatures and pressures are needed.

For the Mie potential optimisations experimental data sets are preferred which were measured both as a function of temperature and pressure.

PVT data is often plotted as several isobars, although it is typically measured as isotherms because pressure differences equilibrate faster than temperature changes. How the position and shape of density isobars is influenced by changes in the four Mie potential parameters is schematically shown

in Fig. 5.11. Most notably, σ shifts the whole isobars almost uniformly. In contrast, ϵ, λ_a and λ_r move, rotate and spread the isobars at the same time. While changes of λ_a and λ_r lead to changes in the same direction, changes in ϵ causes changes in ρ in the opposite direction.

In Fig. 5.12 details of the Mie potential optimisations for a polystyrene oligomer are shown. The (λ_r,λ_a) space is explored by running individual optimisations at fixed (λ_r,λ_a) values and optimising σ and ϵ. The plotted quality of the best fit for all λ exponent combinations in Fig. 5.12 forms a landscape. Further details of the optimisation algorithm and its implementation are described in Chap. 4. The landscape reveals a single minimum with the best model being a Mie(10.5-8.1) potential with $\epsilon = 508.8$ K and $\sigma = 0.4322$ nm for this polystyrene data set.[228] The landscape also shows a groove of fairly good models, which is directly related to the α constant discussed in Sec. 5.4.1. Mie potential exponents can be varied, while models of similar quality can still be obtained.

In Fig. 5.13 details of Mie potential optimisations for a hydrogenated polyisoprene are shown. In this case, the (ϵ,σ) space is explored by running individual optimisations at fixed (ϵ,σ) combinations and optimising λ_r and λ_a. The landscape of the quality of the obtained models reveals a single minimum. The area of fairly good models in this space is narrowly defined for σ and spans across the whole range of tested ϵ values. The narrow σ range shows that the bead size σ is determined to high precision, confirming the expectation that densities foremost carry information about size. The large range of ϵ values that can give fairly good polymer models seems to indicate that ϵ does not have a big influence on the PVT predictions, but rather the opposite is true. The ϵ parameter has a high sensitivity, but λ_r and λ_a can compensate extreme ϵ values as they influence the density isobars in a similar way. By the same argument, there is not a second Mie potential parameter which can compensate extreme σ values which is why σ is narrowly defined for a given PVT set.

Independent of the fact that ϵ, λ_a and λ_r can partially compensate each other's influence on densities, the sensitivity of density predictions with individually changing Mie potential parameters by the same percentage ordered

is

$$\sigma > \epsilon > \lambda_a > \lambda_r. \tag{5.6}$$

As we are aiming to develop coarse-grained models, we try to use fewer beads than the compound's number of heavy atoms. In Fig. 5.14 optimisation results are shown for three mappings, which are 1, 2 and 4 beads per styrene monomer unit. Coarser models move all four Mie potential parameters to larger values: larger bead diameters σ, stronger ϵ interactions and as can easily be seen in Fig. 5.14 both λ_r and λ_a are increased. We want to avoid very coarse-grained models with their very steep potentials as the MD simulations of these Mie potential force fields are slower due to the need for smaller time steps. A balance between coarsening and potential softening has to be struck. We found a mapping of 2-5 heavy atoms per bead a good compromise, for which no numerical issues in the SAFT-γ Mie parameter estimation were encountered, either.

In some cases only one isobar of densities was measured. One isobar effectively corresponds to an absolute density plus several thermal expansion coefficients. No information about the compressibility is included. As can be seen in Fig. 5.15, a single isobar can be captured by a wide range of Mie potentials. Almost all combinations of λ_r and λ_a can form models of fairly good quality. This wide range of good models indicates the four Mie potential parameters overfit the model to what can even be described as essentially two pieces of information, absolute density and thermal expansion. Additional isobars, either by additional measurements or by compressibility coefficients of other very similar polymers (applied to the phPMI and PSαM polymers in this work), are recommended. The additional information about compressibility (slope of $\rho(P)$) and the small variation of thermal expansions and compressibilities (curvature of $\rho(T)$ and $\rho(P)$) justifies using four parameters of the Mie potential in the optimisations.

With the knowledge about the order of sensitivity, and balance of coarse graining, and need for several isobars, we have developed SAFT-γ Mie models for a range of oligomers and polymers. All oligomers and polymers are

hydrocarbons with different degrees of aromaticity and saturation. The Mie potentials and details are tabulated and annotated in Tab. 5.7.

For a selection of polymers, several alternative Mie potentials were chosen and reported in Tab. 5.8. Together with the quality of fit expressed as %AAD, this table allows us to better follow some of the arguments made in this section and gives the reader more choice in picking the most applicable model.

The excellent performance of the SAFT-γ Mie potentials reproducing large ranges of experimental densities used in their development is shown for four example polymers in Fig. 5.16.

In summary, PVT data was successfully used in the development of SAFT-γ Mie models for like interactions of oligomer and polymers employing our own implementation of SAFT-γ Mie and optimisation algorithms.

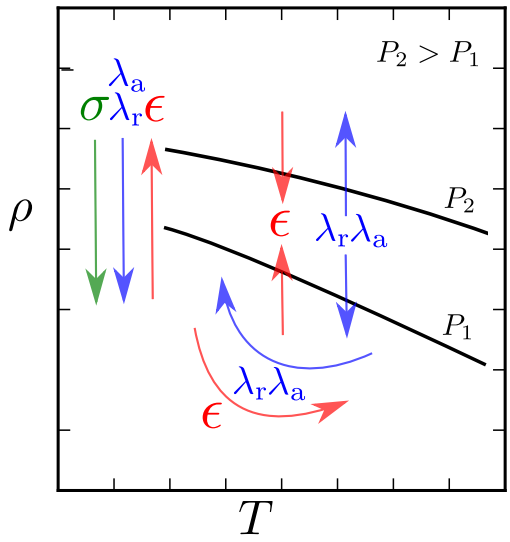

Figure 5.11: Diagram visualising changes of polymer liquid densities (mass per unit volume) caused by varying the four individual Mie potential parameters. The density data is plotted as two isobars at pressures P_1 and P_2 for which $P_2 > P_1$. The bead size σ parameter mainly moves densities at all conditions equally, while ϵ, λ_r and λ_a also rotate and stretch the plotted data. The energetic parameter ϵ causes density changes in the opposite direction compared to the influence of the λ_r and λ_a parameters. Only the most prominent changes are represented in this diagram, which are not enough to explain the very fine differences in model qualities, but to give an overview of how to guide predicted densities by varying the Mie potential parameters to improve the model.

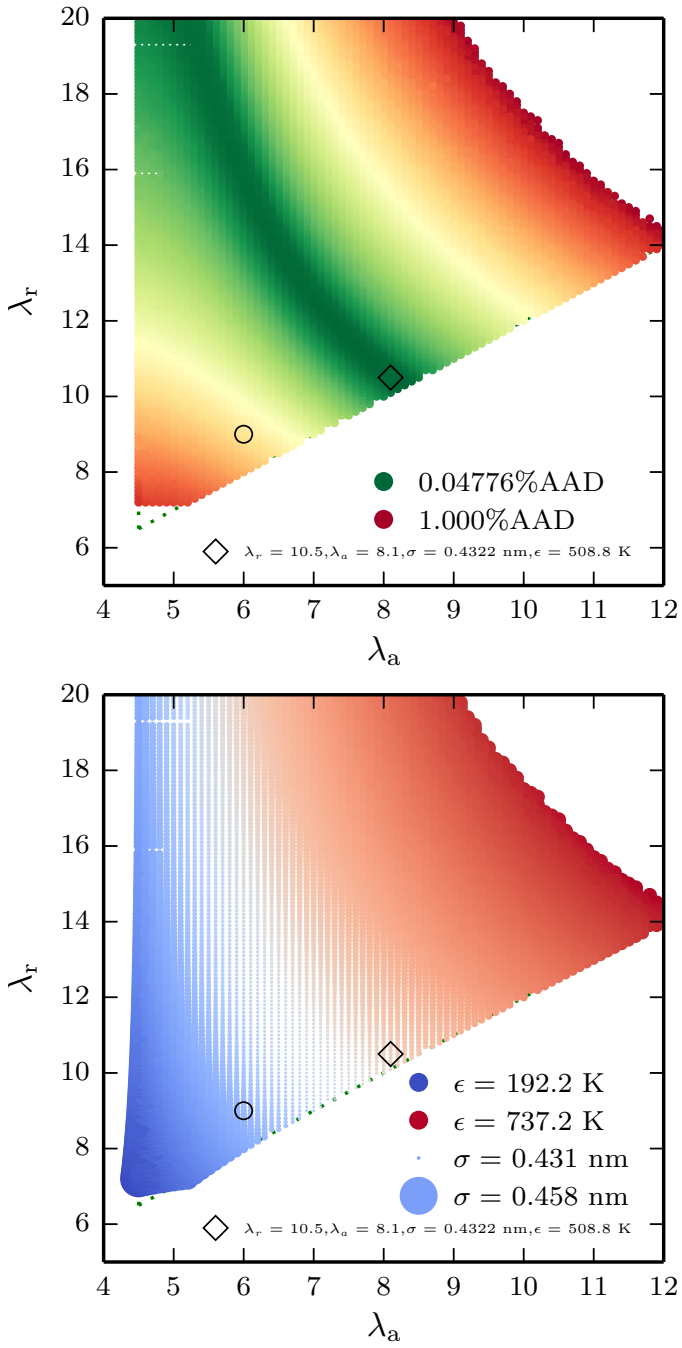

Figure 5.12: SAFT-γ Mie potential optimisations for a polystyrene model using *PVT* data[228] as reference (354.15-514.05 K and 1-2000 bar). Optimisations were performed at fixed (λ_r,λ_a) exponents to systematically sample the Mie potential exponent space adjusting only ϵ and σ. Models which perform better than 1%AAD are plotted in the (λ_r,λ_a) space. (Top) The symbol colours represent the model quality with red (≈1%AAD) and green the best overall model found. (Bottom) The symbol colour represents the energetic ϵ parameter and the symbol size the bead size parameter σ. The best model and Mie(9–6) are highlighted and the best model's parameter values reported.

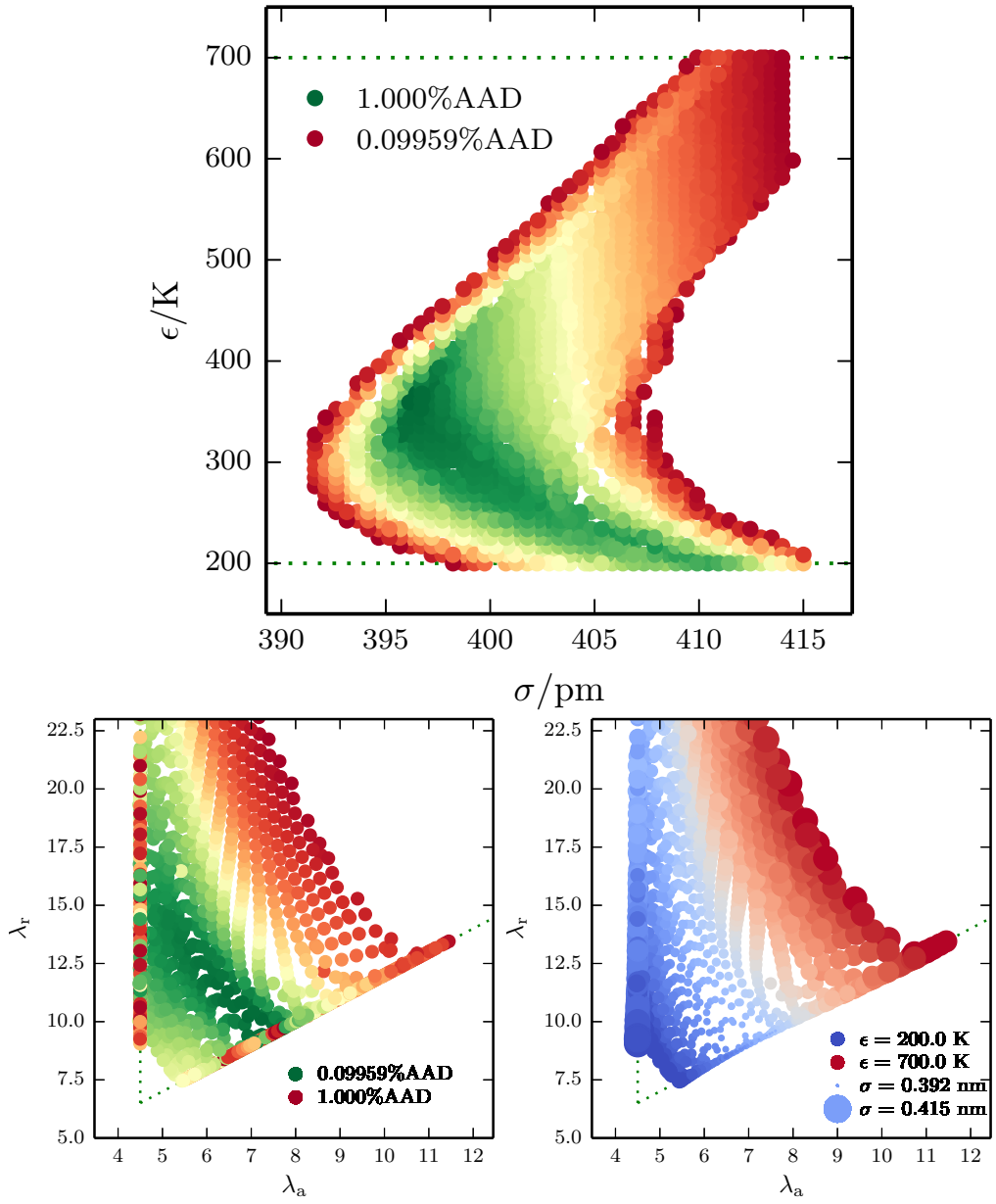

Figure 5.13: SAFT-γ Mie potential optimisations for a hydrogenated polyisoprene (hPI) model using PVT data[228] as reference. Optimisations were forced to sample the (ϵ,σ) space. Reference temperatures 303-543 K and pressures of 1 and 400 bar were used. Only models with qualities better or equal to 1%AAD are plotted. The figure reveals a very narrow σ range and a broad ϵ range with matching quality.

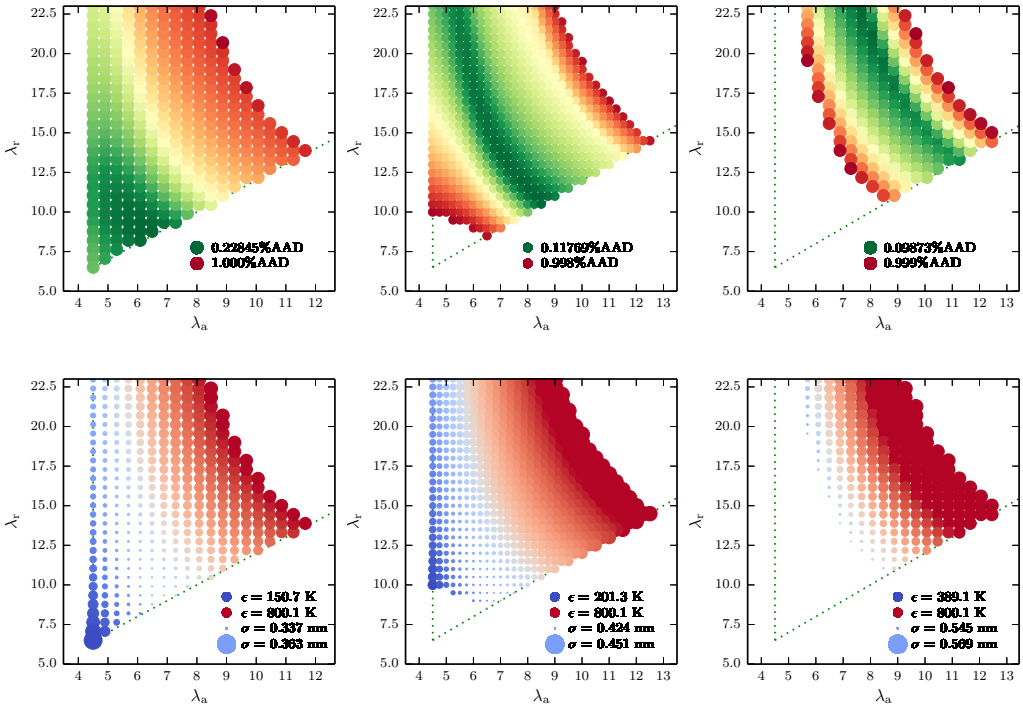

Figure 5.14: SAFT-γ Mie potential optimisations for a polystyrene model with a bead weight of (left) $26\,\mathrm{g\,mol^{-1}}$ (4 beads per monomer), (middle) $52\,\mathrm{g\,mol^{-1}}$ (2 beads per monomer) and (right) $104\,\mathrm{g\,mol^{-1}}$ (1 bead per monomer) using PVT data[228] as reference data. Densities span across temperatures of 303-503 K, and a pressure of 1 bar and 400 bar. The figures reveal that SAFT models with a larger bead weight (fewer beads) require larger values for the Mie potential exponents to achieve similar quality.

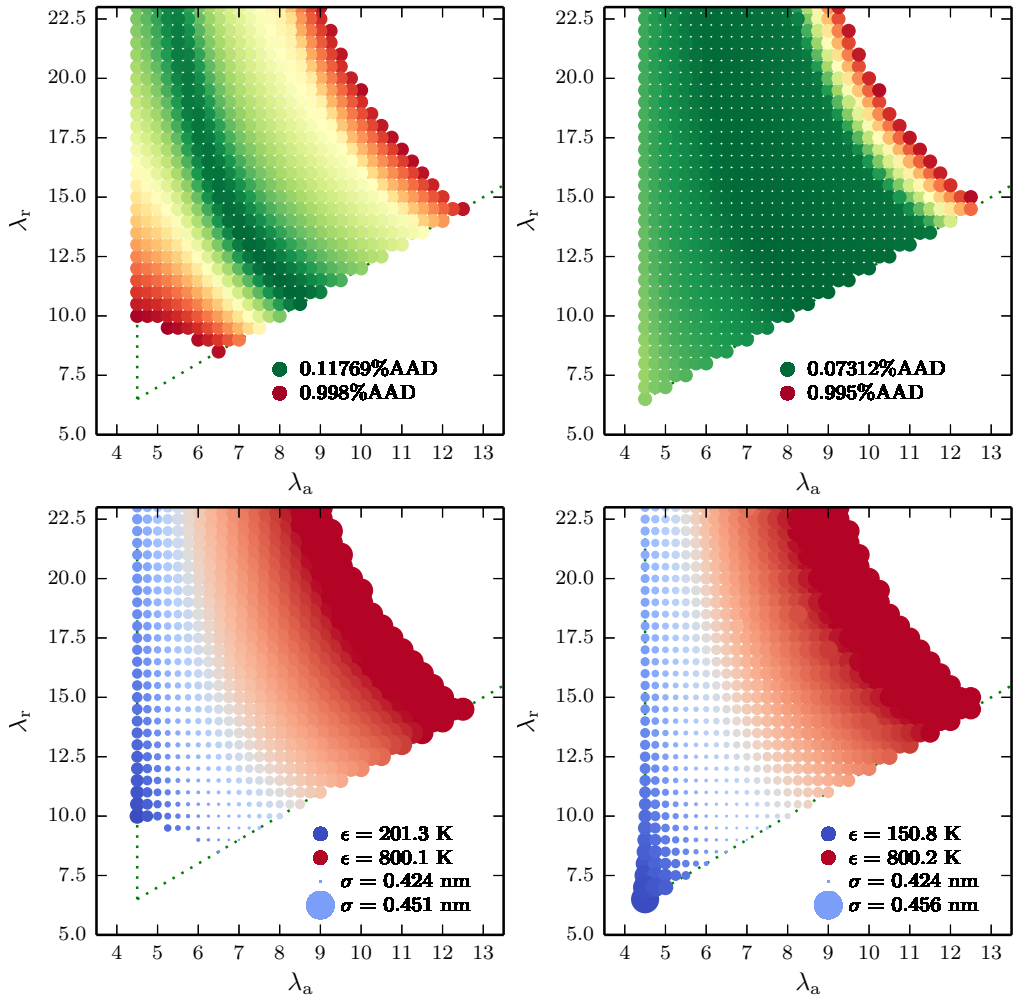

Figure 5.15: SAFT-γ Mie potential optimisations for a polystyrene model using PVT data[228] as reference data. Densities span across temperatures of 303-503 K, and a pressure of (left) 1 bar and 400 bar, and (right) 1 bar only. Therefore, (left) fitting to thermal expansion and compressibility, and (right) thermal expansion.

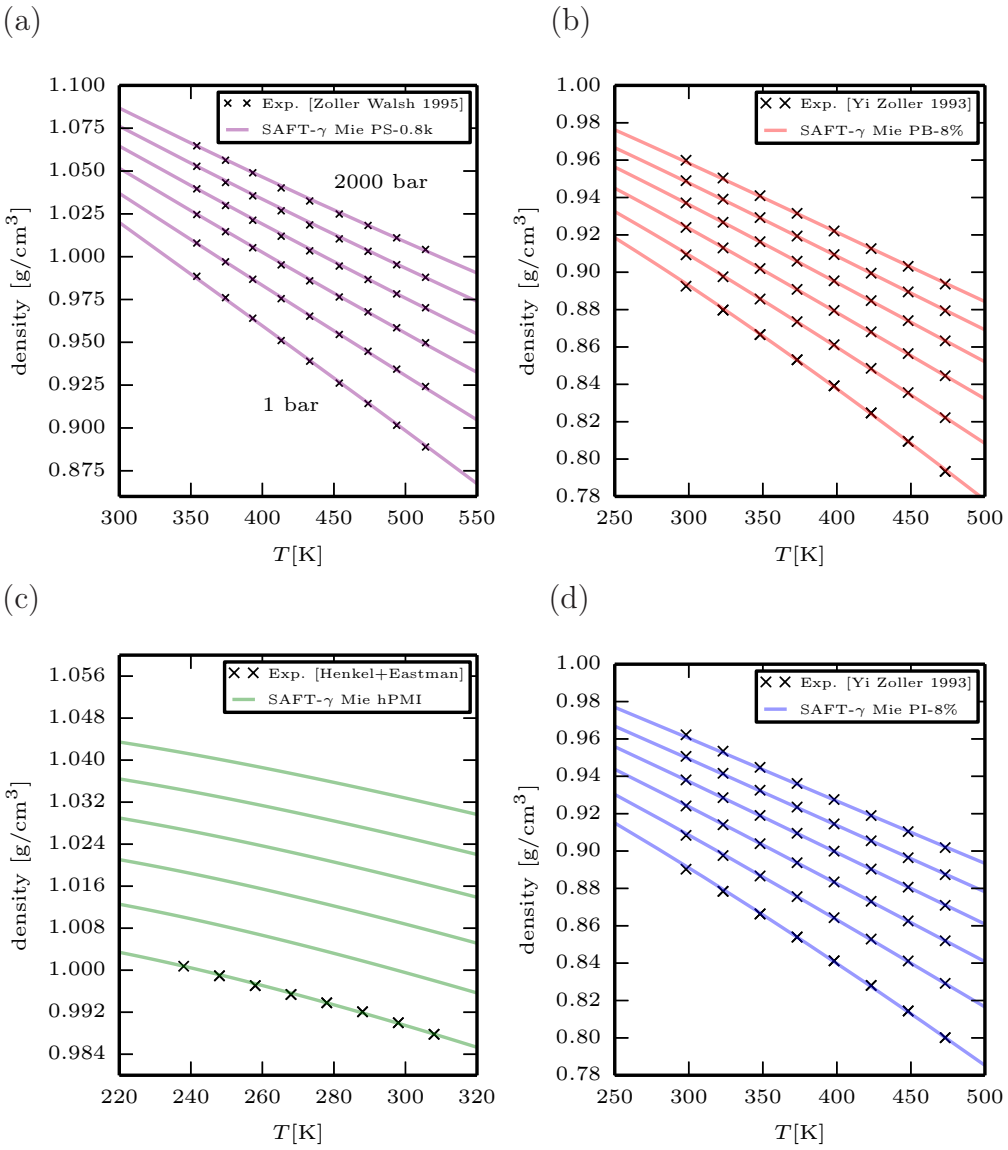

Figure 5.16: Liquid polymer densities compared between SAFT-γ Mie models and the experimental data used in the optimisation of the models. (a) Polystyrene oligomer, (b) polybutadiene with 8% vinyl monomers, (c) hydrogenated poly(methylstyrene-*co*-indene) and (d) polyisoprene with 8% 1-2-linked monomers. Densities are plotted as isobars from 1 bar to 2000 bar in steps of 400 bar. (c) No experimental densities at pressures other than 1 bar were available, which does not complicate the fitting process, but leads to a smaller confidence in the predictions of the high pressure densities.

Table 5.7: SAFT-γ Mie parameters for pure compounds developed with PVT data as reference. For all Mie potentials the shape factor is $S_k = 1$ and the number of segments per group $\nu_k = 1$, which allow the parameters to be used in both SAFT-VR Mie and SAFT-γ Mie. For the notation on the polymer name abbreviations see Tab. 5.1.

compound	σ_{ij} nm	ϵ_{ij}/k_B K	$\lambda_{r,ij}$	$\lambda_{a,ij}$	mass g/mol	experimental reference
PIcis	0.390753	478.933228	10.7	8.7	34	Ref. 238, 397 kDa, *cis*-1,4 isomer
PI-8%	0.387503	315.826263	10.4	6.0	34	Ref. 236, 125 kDa, 8% 3,4 isomer
PI-14%	0.386637	329.685394	11.4	5.9	34	Ref. 236, 124 kDa, 24% 3,4 isomer
PI-41%	0.386773	324.176605	11.5	5.8	34	Ref. 236, 124 kDa, 41% 3,4 isomer
PI-56%	0.387518	318.187103	12.7	5.5	34	Ref. 236, 131 kDa, 56% 3,4 isomer
PB	0.357518	305.702240	8.9	6.8	27	Ref. 228 (D5314), 233 kDa, isomer ratio not reported
PB-32.3%	0.363166	480.716705	10.725371	8.722710	27	Ref. 238, 214 kDa, 32.3% vinyl
PB-9%	0.358172	277.080994	8.5	6.5	27	Ref. 228 (D0517), 200 kDa, 36% cis, 55%trans, 9% vinyl
PBcis	0.357473	282.25589	8.5	6.5	27	Ref. 228 (D0516), 200-300 kDa, cis
PB-3k	0.358062	276.224792	8.6	6.5	27	Ref. 228 (D6051), 3 kDa, isomer ratio not reported
PB-8%	0.358382	272.024628	10.0	5.7	27	Ref. 236, 124 kDa, 8% vinyl, 40% cis, 52% trans
PB-24%	0.358555	271.717957	8.9	6.1	27	Ref. 236, 165 kDa, 24% vinyl, 30% cis, 46% trans
PB-50%	0.363351	219.486954	7.6	5.6	27	Ref. 236, 138 kDa, 50% vinyl, 18% cis, 32% trans
PB-87%	0.367593	196.968475	7.3	5.3	27	Ref. 236, 127 kDa, 87% vinyl, 5% cis, 8% trans
hPI	0.398604	314.201416	12.6	5.5	35	Ref. 228 (D5298), 155 kDa, isomer ratio not reported
sq	0.400619	358.658112	10.2	7.6	35	Ref. 249
PiB-0.3k	0.381979	187.216980	7.2	5.2	28	Ref. 228 (D6109), 300 Da
PiB-0.3k-56g	0.473640	480.424377	10.1	8.0	56	Ref. 228 (D6109), 300 Da
PiB	0.367817	248.197296	7.7	5.6	28	Ref. 228 (D5305), 420 kDa
PiB-56g	0.463982	552.395691	10.6	8.2	56	Ref. 228 (D5305), 420 kDa
hPMI	0.473411	489.834503	15.5	4.5	62	Densities at 1 bar, Ref. 262, 600 Da
phPMI	0.455806	550.626404	12.7	7.1	60	[a]Ref. 228,262, 600 Da
PSαM[b]	0.448646	528.594116	12.7	7.1	60	[a]Ref. 228,262, 700 Da
PS-0.8k	0.432158	508.787262	10.5	8.1	52	Ref. 228 (D5022), 782 Da
PS-9k	0.432417	331.596313	19.8	4.5	52	Ref. 228 (D5037), 9 kDa

[a] Densities at 1 bar obtained from Marc Hamm,[262] compressibilities of PS oligomer from Ref. 228 (D5022)

[b] Poly(styrene-*co*-α-methylstyrene) (PSαM) with $M_n = 700$ Da and $M_w/M_n = 2.1$

Table 5.8: SAFT-γ Mie parameters for pure compounds developed with PVT data as reference. Alternative Mie potential parameters of similar quality are reported for the same reference data set. The quality is reported as the average absolute deviation in percent (%AAD) with comparison to experimental densities. The size of the experimental data set is given in brackets, with nP the being the number of pressure values and nT the number of temperatures. For example (nP=5,nT=8) corresponds to a total of 50 densities for which the SAFT model predictions were compared with experimental values. For all Mie potentials the shape factor is $S_k = 1$ and the number of segments per group $\nu_k = 1$, which allow the parameters to be used in both SAFT-VR Mie and SAFT-γ Mie. For the notation on the polymer name abbreviations see Tab. 5.1.

compound	σ_{ij} nm	$\epsilon_{ij}/k_\mathrm{B}$ K	$\lambda_{\mathrm{r},ij}$	$\lambda_{\mathrm{a},ij}$	mass g/mol	experimental reference	%AAD
PB-6.8	0.357518	305.702240	8.9	6.8	27	Ref. 228 (D5314), 233 kDa	0.112 (nP=6,nT=5)
PB-6	0.358576	287.799347	9.8	6.0	27	Ref. 228 (D5314), 233 kDa	0.118 (nP=6,nT=5)
PB-5	0.362724	240.256165	10.7	5.0	27	Ref. 228 (D5314), 233 kDa	0.152 (nP=6,nT=5)
PB-4.5	0.368058	199.638885	10.7	4.5	27	Ref. 228 (D5314), 233 kDa	0.204 (nP=6,nT=5)
sq-7.8	0.400930	367.006775	10.045913	7.849015	35	Ref. 249	0.023 (nP=5,nT=8), 0.017 (nP=2,nT=4)
sq-7.6	0.400619	358.658112	10.2	7.6	35	Ref. 249	0.016 (nP=5,nT=8)
sq-7	0.400662	352.990967	11.3	7.0	35	Ref. 249	0.018 (nP=5,nT=8)
sq-6	0.400762	329.130829	13.7	6.0	35	Ref. 249	0.020 (nP=5,nT=8)
sq-4.5	0.405078	237.634171	18.0	4.5	35	Ref. 249	0.027 (nP=5,nT=8)
PS-8.1	0.432158	508.787262	10.5	8.1	52	Ref. 228 (D5022), 782 Da	0.060 (nP=6,nT=9)
PS-8.03	0.432736	525.235779	11.390842	8.025436	52	Ref. 228 (D5022), 782 Da	0.124 (nP=6,nT=9), 0.118 (nP=2,nT=6)
PS-8	0.431568	505.748840	11.0	8.0	52	Ref. 228 (D5022), 782 Da	0.146 (nP=2,nT=6)
PS-6	0.433430	491.881500	18.0	6.0	52	Ref. 228 (D5022), 782 Da	0.143 (nP=2,nT=6)
PS-12-6	0.425870	357.278595	12.0	6.0	52	Ref. 228 (D5022), 782 Da	0.618 (nP=2,nT=6)
PS-9-6	0.425669	283.818207	9.0	6.0	52	Ref. 228 (D5022), 782 Da	0.975 (nP=2,nT=6)
PS-4.5	0.432417	331.596313	19.8	4.5	52	Ref. 228 (D5037), 9 kDa	0.028 (nP=6,nT=4)
PS-6	0.428823	459.267059	14.4	6.0	52	Ref. 228 (D5037), 9 kDa	0.036 (nP=6,nT=4)
PS-8	0.428735	503.682404	10.0	8.0	52	Ref. 228 (D5037), 9 kDa	0.032 (nP=6,nT=4)

5.4.3 Heat capacity and speed of sound

Using heat capacities and speed of sound data for the polymer model development is attractive due to the fact that heat capacity measurements are common measurements, easily accessible, and speed of sound data can be measured to very high accuracies which seems to promise polymer models of high quality, too. Why heat capacities and speed of sound data does not live up to these promises in the development of SAFT-γ Mie models for polymers is demonstrated and explained in this section.

For small molecules, very good agreement with experimental results was shown with SAFT-VR Mie 2006,[13] SAFT-VR Mie[14] and SAFT-γ Mie[6,16] models in predicting heat capacities and speed of sound data. Using heat capacities and speed of sound measurements in the parameter estimation was also shown to provide complementary physical information to further guide the model development in the case of methane.[174]

Heat capacities of four oligomers were measured via differential scanning calorimetry (DSC), see Fig. 5.17. As the absolute heat capacity values are of interest here (not only the heat rate changes which reveal phase transitions), additional runs with the empty crucible for a base line and a standard, Sapphire in our case, for calibration, were measured for each sample. The first heat run of each sample shows significant thermal history (blue lines Fig. 5.17). The increased heat capacities at 50 °C to 120 °C correspond to the melting/softening of those samples solid as room temperature, while the decreased heat capacities at around 120 °C correspond to crystallisation/relaxation of the PiBB+fur sample, which is liquid at room temperature. Several repeated measurements of the same sample were run to allow the estimation of uncertainties. Standard deviations of .29%, .4%, .8% and 1.69% were obtained based on at least three runs, excluding the initial run dominated by thermal history. The repeated runs all show a glass transition at 30 °C to 50 °C.

One way of measuring speed of sound is via the echo method. The echoes of two ultrasonic signals send in opposite directions are recorded. By knowing the difference between the distances they travelled and the difference between

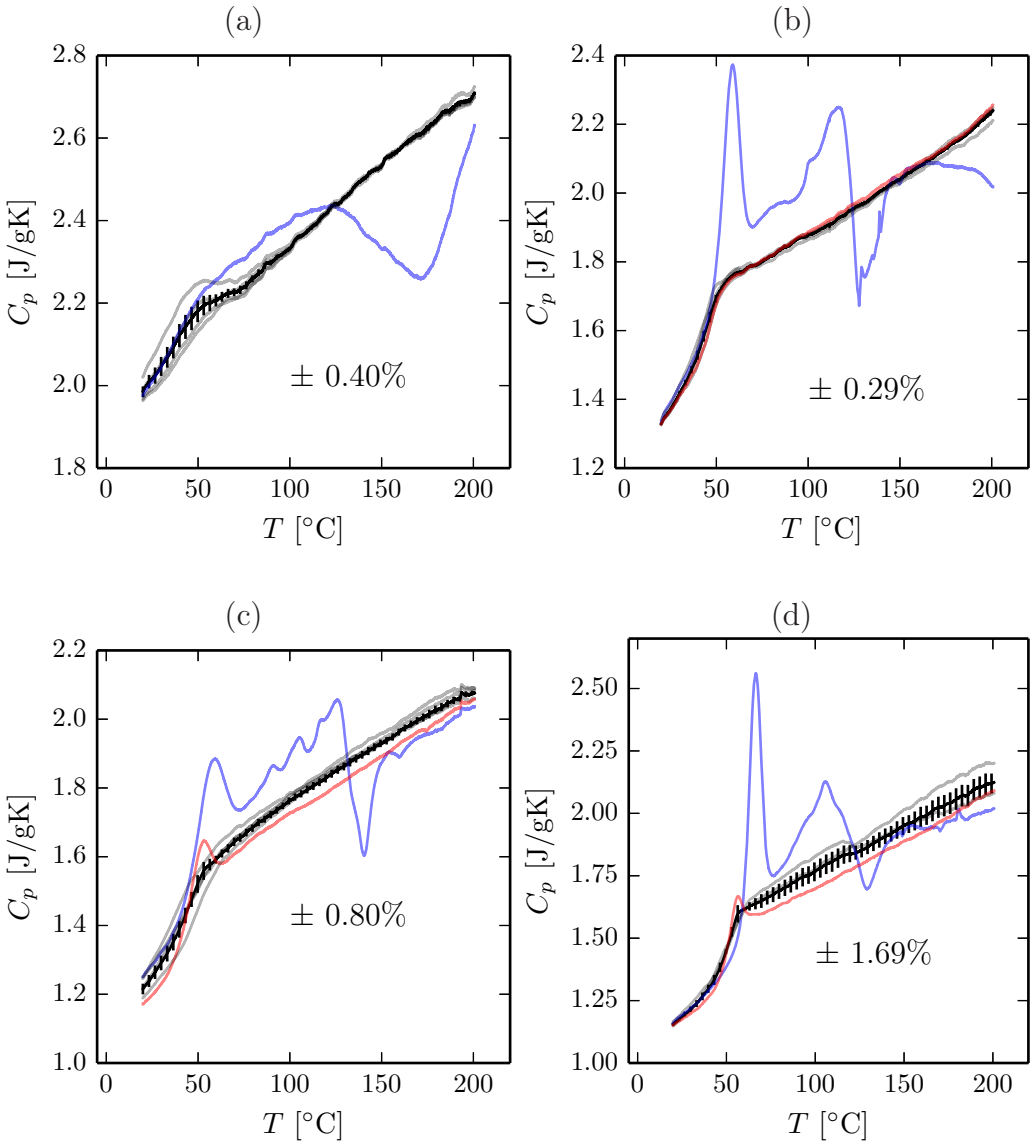

Figure 5.17: Experimental heat capacities C_P determined via differential scanning colorimetry (calibrated via triple measurements: 1. empty crucible, 2. sapphire standard, 3. sample; heat rate $10\,\mathrm{K\,min^{-1}}$) for (a) PiBB+fur (b) hPMI (c) a hydrogenated hydrocarbon resin oligomer with $M_n = 450\,\mathrm{g\,mol^{-1}}$ and $M_w/M_n = 2.3$ and (d) a cycloaliphatic hydrocarbon resin with $M_n = 400\,\mathrm{g\,mol^{-1}}$ and $M_w/M_n = 1.7$. The initial measurement (blue) shows thermal history, the runs after recovering over night (red) show some signs of recrystallisation. Several immediately repeated runs (grey) were averaged and plotted together with the local standard deviation (black). The total averaged standard deviation for each sample is shown below the graphs.

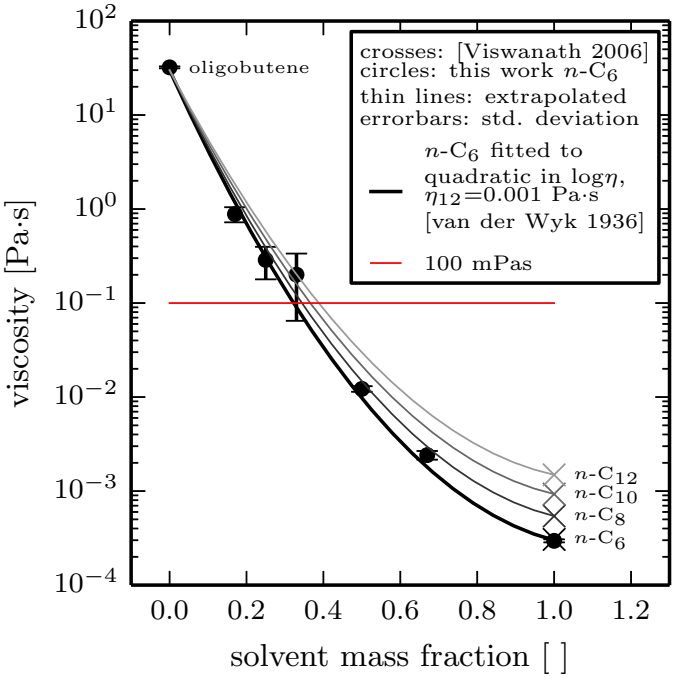

Figure 5.18: Experimental viscosities of PiBB+fur and mixtures with *n*-hexane (95% purity and dried over a silica column) determined on a cone/plate rheometer (Discovery HR-2 hydrid rheometer TA instruments, Peltier 60 mm 2° cone, Peltier plate steel, solvent trap cover for samples of high solvent content) at 20 °C (water cooled) at shear rates of 0.01-100 rad s^{-1}. The experimental viscosities (circles) are well correlated with an analytic function quadratic in $\log \eta$ with a coefficient (effective binary viscosity[263]) of $\eta_{12} = 0.001$ Pa s. Extrapolations for viscosities of PiBB+fur in *n*-octane, *n*-decane and *n*-duodecane are shown based on viscosities of the pure compounds taken from Ref. 264 (crosses). The targeted threshold viscosity of 100 mPa s (red line) is predicted for PiBB+fur solutions of more than 30-40% solvent.

the times of arrival, one can calculate the speed of sound. It was shown that measurements can be reproduced within ±0.002%.[265] Higher sample viscosities lead to larger absorption of the ultrasonic signal and eventually prohibit the determination of speed of sounds. All materials analysed in Fig. 5.17 show larger viscosities than the threshold value of 100 mPa s[266] aimed for to obtain signals of enough resolution, which roughly corresponds to the viscosity of olive oil at room temperature. This threshold viscosity will most likely not be met by any hydrocarbon polymer. Increased temperatures of 100−200 °C could lower the viscosity below the threshold for some oligomers, but most polymers will start decomposing before the viscosity was lowered far enough. Instead, we tested the addition of well-characterised solvents to adjust the viscosity. In Fig. 5.18 viscosities of mixtures of PiBB+fur with *n*-hexane are presented. All PiBB+fur mixtures with more than 35% *n*-hexane by weight show viscosities below the targeted 100 mPa s and are therefore expected to give echo signals of resolutions large enough for the determination of speed of sounds. The addition of solvents can successfully be applied in speed of sound measurements.

In Fig. 5.19, several predictions of PiBB+fur heat capacities are compared. The SAFT-γ Mie method only provides residual heat capacities (see Chap. 4 for more details)

$$C_P = C_P^{\text{ideal}} + C_P^{\text{res}}, \tag{5.7}$$

while the ideal heat capacities can be obtained from correlated experimental datasets or spectroscopic vibrational mode analysis. Because the spectroscopic analysis for oligomers and polymers with a large number of vibrational modes is very tedious, probably even prohibitively challenging for most polymers, we will only test the performance of correlated experimental datasets. The ideal heat capacity sets[9,10] used in this work are group-contribution approaches, which were parametrised on heat capacities of low-M_w compounds. Although not developed explicitly for polymers, group-contributions approaches allow easy scaling to larger molecular weights. The SAFT-γ Mie predictions are calculated with the GC-Dufal2014 parameter set. The pre-

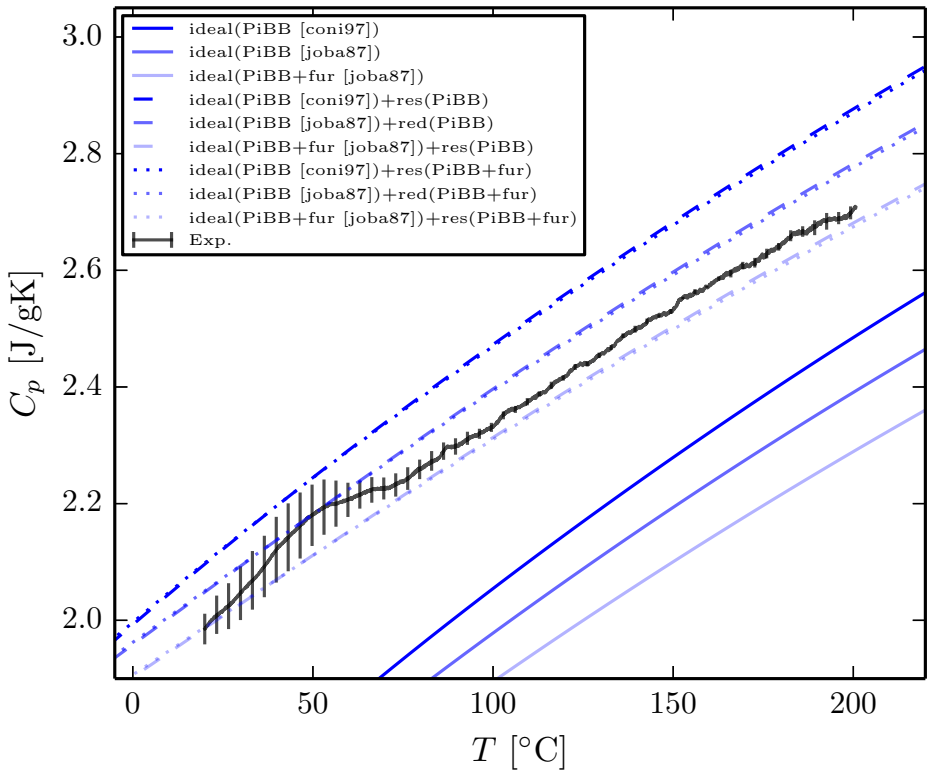

Figure 5.19: Heat capacity SAFT-γ Mie predictions for PiBB+fur using the GC-Dufal2014 parameter set[184] compared with DSC measurements (black line with standard deviation). Predicted ideal heat capacities (continuous lines) are PiBB based on Coniglio and Daridon[10] parameters (dark lines), PiBB based on Joback[9] parameters (medium lines) and PiBB+fur based on Joback and Reis[9] parameters (light lines). Predicted full heat capacities (broken lines) use the GC-Dufal2014 parameter set for the residual SAFT-γ Mie contribution. The SAFT-γ models were PiBB (dashed lines) and PiBB+fur (dotted lines). The plots reveal that the ideal heat capacities dominate the differences seen between the models.

dicted heat capacities are very little influenced by the SAFT-γ Mie model, but significant differences are found between the alternative ideal heat capacities. Roughly 5% differences are found between heat capacities with ideal parts based on the Joback or Coniglio set, and for choice of chemical structure (PiBB vs PiBB+fur) for the ideal part. The heat capacities are dominated by the ideal contribution, which delicately depends on the detailed chemical structure and group-contribution data set. The initial good precision of heat capacity measurements is vastly reduced when 85% of the value with high uncertainty is deducted to give the residual heat capacity which could be used in the parameter estimation.

Speed of sound prediction also require ideal heat capacities, and are subject to the high uncertainties for polymers, too.

In summary, the ideal heat capacities, which can not be predicted by the SAFT-γ Mie theory prohibit the use of experimental heat capacities and speed of sound data for the parameter estimation of polymers. Because the structure of low-M_w compounds is exactly known and GC approaches are optimised for them, ideal heat capacities for low-M_w compounds can be obtained reliably. In contrast, polymeric structures are often not known at molecular detail and no GC approach for polymer weights was found. Predictions of ideal heat capacities are therefore subject to large uncertainties, which substantially diminishes the attractiveness of heat capacities and speed of sound measurements for the SAFT-γ Mie parameter estimation.

5.5 Unlike interactions

In this section, we present means for developing SAFT-γ Mie models for mixtures. We show strategies for estimating the *unlike* interactions for polymer systems, for which the *like* interactions developed in the previous section are used without further adjustments. Results for mixtures of PB/PI, PB/sq, cisPB/sq, PB/PS and PI/phPMI/PSαM are presented. Predictions at other temperature, pressures, compositions and other molecular weights are analysed.

5.5.1 Combining rules

Combining rules predict binary unlike interactions based on only pure-component information. It is very attractive to eliminate the need for mixture data to speed up the development process of SAFT models. Mixture data, as demonstrated for hydrocarbon polymers in Sec. 5.3, is only found in the literature for a few cases and inherently more specific than pure-component data, as pure-component data can be utilised for all mixtures of this component.

Simple and widely-used combining rules for equations of state are the arithmetic mean (Lorentz) for the bead size σ and the geometric mean (Berthelot) for the energetic parameter ϵ (in our case also scaled with the geometric mean of the bead volume).[267] For the Mie potential exponents for a mixture, Lafitte *et al.*[14] have suggested taking the geometric mean of the values of the exponent of the individual species reduced by three units. The combining rules used in Lafitte *et al.*,[14] as introduced in Chap.3, are

$$\sigma_{ij} = \frac{1}{2}(\sigma_{ii} + \sigma_{jj}) \tag{5.8}$$

$$\epsilon_{ij} = (1 - k_{ij}) \frac{\sqrt{\sigma_{ii}^3 \sigma_{jj}^3}}{\sigma_{ij}^3} \sqrt{\epsilon_{ii}\epsilon_{jj}} \tag{5.9}$$

$$\lambda_{r,ij} - 3 = (1 - \gamma_{ij}) \sqrt{(\lambda_{r,ii} - 3)(\lambda_{r,jj} - 3)} \tag{5.10}$$

$$\lambda_{a,ij} - 3 = (1 - \gamma_{ij}) \sqrt{(\lambda_{a,ii} - 3)(\lambda_{a,jj} - 3)}, \tag{5.11}$$

where k_{ij} and γ_{ij} are correction factors to the combining rule. The correction factors are set to zero ($k_{ij} = \gamma_{ij} = 0$) when the combining rules are applied, but can capture and express deviations when needed.

In principle any information about the pure components could be used in the combining rules. Haslam *et al.*[267] have summarised more complex combining rules beyond the Berthelot rule for equations of state, by including pure-component polarisability and ionisation potentials. While one might be tempted to assume deviations to the Lorentz-Berhtelot rules to indicate shortcomings of the theory or specific mixture effects not captured

in the pure-component models, Haslam *et al.*[267] showed how differences in the pure-component bead size σ, differences in the pure-component range of attraction (width of a square-well potential, which is expected to correlate with λ_a of Mie potentials) and differences in the pure-component ionisation potential cause the Berthelot combining rule to break down. Deviations from the Berthelot combining rule, therefore, not only signal uncaptured mixture effects, but also how much the component's like interactions differ. More complex combining rules or experimental data are required to improve the mixture predictions beyond Lorentz-Berthelot combining rules.

In practice, unlike interactions derived with Lorentz-Berthelot combining rules can often be successful or good enough, especially for small molecular weights, properties with large entropic contributions and mixtures of compounds with similar chemistry. However, for LLE of polymer mixtures which are very sensitive to the parameter values, experimental data is required for reliable unlike interaction parameters.

The correction factors k_{ij} and γ_{ij} are usually taken as temperature and composition *in*dependent,[14,16,151] and only a few temperature-dependent correction factors k_{ij} have been published.[144]

We are not aware of more complex combining rules which are successful for polymer mixtures and we have not found experimental ionization potentials for the polymers studied in this work. In this work, Lorentz-Berthelot combining rules are applied and the correction factors k_{ij} and γ_{ij} are invoked and optimised when needed based on experimental mixture data.

The more complex combining rules, as for example discussed in Haslam *et al.*,[267] however, provide general trends to assess the influence of asymmetry, might help to pick pure-component models, recognise unreasonable model parameters and help guess the trend of binary correction factors in the parameter estimation of unlike interactions. One take-away message is that any asymmetry in pure-component models seems to introduce deviations from the Berthelot combining rule, which again supports the aim to introduce as few adjustable parameters as possible. More symmetric models such as Lennard–Jones exponents should be picked if they still reproduce the experimental data sufficiently. To determine where the line between suffi-

cient and insufficient lies is difficult and is influenced by many factors, but smaller corrections factors and more predictive combining rules are expected when models are simplified.

5.5.2 LLE and CPC

Liquid–liquid equilibria (LLE) for monodisperse mixtures and cloud-point curves (CPC) for polydisperse mixtures are the preferred experimental information to estimate and validate unlike interactions in this work. This is due to several reasons. Firstly, compatibility, solubility and cloud points are the target properties we are most interested in predicting. LLE and CPC can therefore be used both in the parameter estimation and for validaton/testing of the models. Secondly, unlike interactions are very sensitive to LLE and CPC phase transition temperatures and compositions, which guarantees unlike interactions of high precision. Thirdly, LLE and CPC are fairly easily measured via temperature sweeps while uncertainties of several Kelvin are often precise enough. The phase transition during the temperature sweep can usually be determined visually.

The influence of each unlike interaction parameter on the shape of LLE and CPC with an upper critical solution temperature is visualised in Fig. 5.20. All parameters significantly change the critical solution temperature, hence all can be used to qualitatively adjust the compatibility of the mixture, i.e., change a fully compatible into a fully incompatible system and vice versa. However, the qualitative adjustment is typically done with the energetic ϵ parameter, while the other parameters are used here for the quantitative adjustment, changing the shape of the curve. The influence of the unlike interaction parameters on the shape of the CPC/LLE curve visualised and discussed here, is not the change of a single parameter, but was adjusted in combination with ϵ to keep an almost constant critical solution temperature, so that the qualitative influence on the overall compatibility is already cancelled out. At constant critical solution temperature, the Mie potential exponents $\lambda_{\mathrm{r},ij}$, $\lambda_{\mathrm{a},ij}$ and the bead size σ_{ij} tilt the UCST plateau in a similar way. However, while $\lambda_{\mathrm{r},ij}$ and $\lambda_{\mathrm{a},ij}$ can change LCST to UCST and vice versa,

we were not able to completely invert the curve with σ_{ij}. Increased polydispersity broadens the UCST plateau, moving the UCST to larger oligomer fractions. The difference in chain length (molecular weight) of the two compounds determines the composition of the UCST, the larger the difference, the larger the weight fraction of the shorter-chain compound at the UCST.

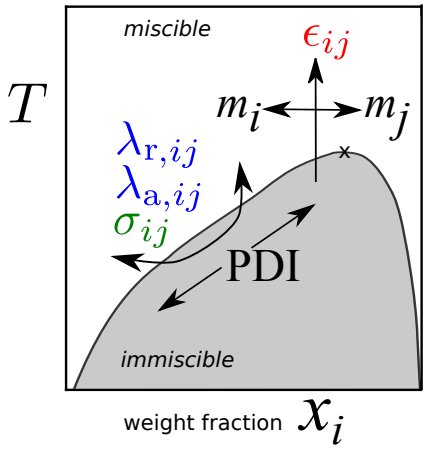

Figure 5.20: Influence of unlike interaction parameters on the shape of CPC (PDI > 1) and LLE (PDI $= 1$) with an upper critical solution temperature (highlighted with a cross) of the binary mixture of polymer i and j. SAFT-γ Mie models with only one type of Mie potential per compound are assumed. The influence of the chain length expressed as number of beads m_i and m_j, the polydispersity (PDI) and the unlike Mie potential parameters are indicated. The like interactions (ii and jj) are kept unchanged. The indicated changes to the LLE curves are such changes that remain after ϵ was adjusted to keep an almost constant critical solution temperature value.

Unlike interactions for the binary pairs PB/PI, PB/sq and PB/PS, and the ternary PI/oligomer/oligomer mixture are developed and validated with LLE and CPC data. Predictions for other properties, conditions or molecular weights are used to assess the transferability of the models.

Some of the unlike interaction parameter estimations were performed with gSAFT[203] to explore large areas of the parameter space. All results plotted in this section, however, were obtained with our implementation of SAFT-γ Mie and solvers.

PB/PI

Mixtures of polybutadiene and polyisoprene show a range of behaviours because both polymers entail several isomers, which are *cis/trans* isomers and 1,4/1,2 linkages.,[238,244,268–272] see Fig. 5.5 for the notation and chemical structure representations. Chemically, PB and PI differ only by a single methyl substitution. The chemical similarity leads to general miscibility. Immiscibility is only found for high-molecular-weight mixtures and some isomer ratios. For the polybutadiene/*cis*-1,4-polyisoprene mixture it was shown[272] that the fraction of 1,2-linkages (vinyl) in polybutadiene crucially influences the compatibility, with immiscibility for low 1,2-PB fractions and miscibility for high 1,2-PB fractions.

In this section, a SAFT-γ Mie model is developed for a PB/PI mixture of partial miscibility. The mixture of polybutadiene with almost equal fractions of *cis*, *trans* and vinyl isomers and *cis*-1,4-polyisoprene shows an LCST at 50-60 °C.[272]

The pure-component models were developed based on PVT data.[238] The density at 25 °C and the thermal expansion coefficient were used to obtain the densities at 0, 25 and 100 °C. The three densities were used in the Mie parameter optimisation. Because of the missing compressibility information (densities only at one pressure), we have not determined a new λ exponent for each compound, but used Mie(12.7–8.1) for PB as it gave the best model in the PI parameter estimation. The parameter values are given with further information as PIcis and PB-32.3% in Tab. 5.7.

The unlike interaction was determined based on LLE data.[272] As the model based on combining rules predicts complete immiscibility, the k_{ij} parameter was adjusted to represent stronger PB/PI unlike interactions. An adjusted model with $k_{ij} = -0.004017$ captures the LCST at 50-60 °C and the miscibility of a few weight percent of each polymer in the other for $T > 60$ °C, see Fig. 5.21. The model LLE predictions agree very well with the experimental results with only adjusting a single unlike interaction parameter. Due to the high molecular weight of the compounds (M_n(PB)=93 kg mol^{-1} and M_n(PI)=397 kg mol^{-1}) the unlike interaction parameter can be fitted to high

precision.

The volume of mixing of the PB/PI blend is correctly predicted with the SAFT-γ Mie model, while no densities of the blend were used in the development of the model, see Fig. 5.22. Kawahara *et al.*[269] show that the negative volume of mixing for this polymer mixture indicates a structural effect of changed relaxation behaviour which can not be explained by enthalpic reasons. The SAFT-γ Mie model seems to effectively capture the effect of the structural effect in the energetic unlike interaction, which correctly predicts the volumes of mixing at 25 °C.

In conclusion, a SAFT-γ Mie model for the PB/PI mixture was successfully developed with limited density data and an LLE phase diagram. The model is in very good agreement with the phase details of the phase diagram and correctly predicts the volumes of mixing at 25 °C.

PB/sq

The mixture of polybutadiene and squalane (sq) studied in this section can be described as a polymer/oligomer binary mixture, where squalane's structure is equivalent to a hexamer of hydrogenated polyisoprene. Two types of polybutadiene are used, poly(*cis*-butadiene) (cisPB) and poly(*cis*-butadiene-*co*-*trans*-butadiene-*co*-1-2-butadiene) (PB).

One type of Mie potential per compound is developed, keeping the number of Mie potential types minimal. Exploiting the structural agreement of the *cis*-PB units, which make almost 100% of cisPB and roughly 33% of the second PB, would allow the prediction of a large range of new PB monomer ratios, but required additional cisPB/PB interactions and more complex models.

The experimental data applied in the parameter estimation of the pure components and mixtures are obtained from different independent sources. They were chosen to have matching PB isomer ratio, but the molecular weight and polydispersity differ. The chain length was individually adjusted to the experimental data to represent the number-average molecular weight. The possibility in SAFT to adjust the chain length as representing the molecu-

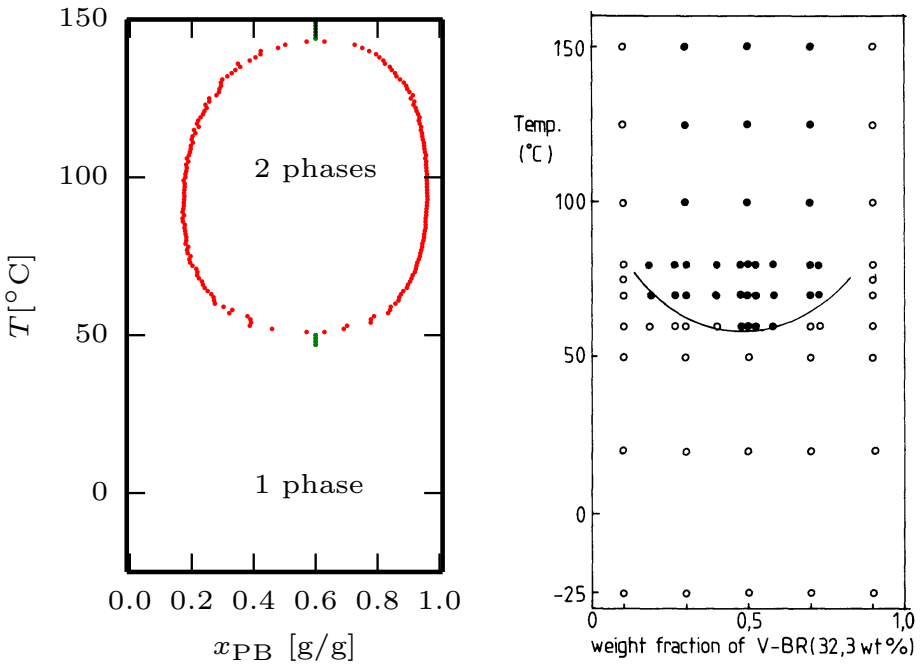

Figure 5.21: Phase diagram of a mixture of PB($93\,\mathrm{kg\,mol^{-1}}$) and PI($397\,\mathrm{kg\,mol^{-1}}$). (Left) SAFT-$\gamma$ Mie results (this work) of PIcis and PB-32.3% (see Tab. 5.7) with $k_{ij} = -0.004017$. (Right) Experimental[272] phase diagram obtained from glass transition temperature T_g measurements after the samples were annealed for two hours at the respective temperature. Two T_g (open symbol), one T_g (filled symbol) and a correlation (line) are shown. Reprinted by permission from Springer Customer Service Centre GmbH: Nature, Polymer Journal, Kawahara *et al.*, Vol. 21, No. 3, pp 221-229. Copyright (1989) Springer Nature.

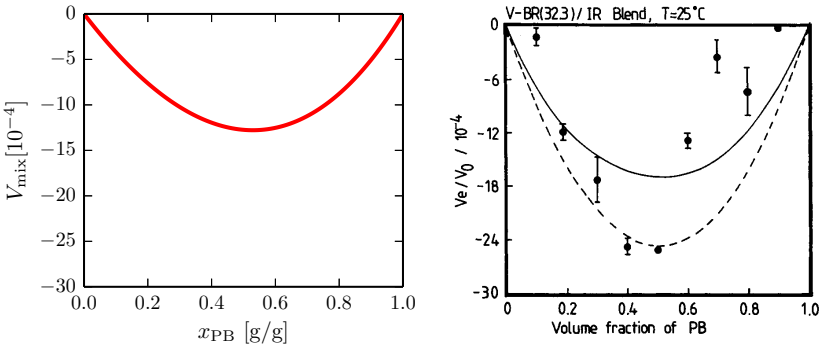

Figure 5.22: Volume of mixing of a mixture of PB(208 kg mol^{-1}) and PI(397 kg mol^{-1}). (Left) SAFT-γ Mie predictions (this work) of PIcis and PB-32.3% (see Tab. 5.7) with $k_{ij} = -0.004017$. (Right) Experimental[269] volumes of mixing (symbols) and two alternative correlations of the experimental data (lines) at 25 °C. Reprinted by permission from Kawahara *et al.*, Journal of Polymer Science, Part B, Polymer Physics, Copyright 1994 John Wiley & Sons, Inc.

lar weight is very valuable in the development of polymer models. Although polymers from different sources, methods and batches usually differ in molecular weight, they can be used in the parameter estimation of the same Mie potential.

The pure-component Mie potentials PB-8%, PBcis and sq were used, whose parameters are given in Tab. 5.7. Using combining rules for all unlike interactions the PB-8%/sq and PBcis/sq are incorrectly predicted to be completly immiscible. Adjusting k_{ij} to increase the PB/sq interactions reveals LCST behaviour, which can not be changed into the UCST behaviour found experimentally by adjusting k_{ij} alone. The other unlike interaction parameters $\lambda_{\mathrm{r},ij}$, $\lambda_{\mathrm{a},ij}$ and σ_{ij}, can all, at least partially, tilt cloud-point curves to change the UCST/LCST behaviour. Adjusting σ_{ij} in addition to k_{ij} allows the correct slope of the cloud-point curve to be obtained, but the UCST disappears to inaccessibly high temperatures with complete immiscibility at high squalane concentrations across the whole accessible temperature range. Adjusting σ_{ij} in the PB/sq mixture to give the best match with the cloud-point temperatures also leads to large volumes of mixing which are about an order of magnitude larger than typically found experimentally for polymer

mixtures. Instead, we adjust $\lambda_{r,ij}$ together with k_{ij}, which correctly reproduces the UCST behaviour, see Fig. 5.23. In the same way, the attractive exponent $\lambda_{a,ij}$ can be optimised instead of the repulsive exponent $\lambda_{r,ij}$, but $\lambda_{r,ij}$ is chosen here as it corresponds to the physical representation of softness of the beads with repect to each other and how easily the beads can overlap. Equivalent values for $\lambda_{a,ij}$ can also become very small, far smaller than $\lambda_{a,ij} = 6$, which is more expensive to model in molecular simulations for which the models are also developed for.[†]

The predicted cloud-point curve in Fig. 5.23 is in good agreement with the experimental data. However, the predicted plateau is flatter than found experimentally and the UCST is shifted towards higher squalane concentrations. Including polydispersity in the PB and cisPB models does not lead to an improved description. Instead, the plateau is elongated and the UCST shifted even further towards high squalane concentrations. The parameters, which have the major influence on the UCST with respect to its squalane concentration, are the chain lengths of the models. Modelling a hypothetical PB with a smaller molecular weight of $13.3\,\mathrm{kg\,mol^{-1}}$ instead of $133.3\,\mathrm{kg\,mol^{-1}}$ gives excellent agreement with the experimental cloud points and the expected position of the UCST, see Fig. 5.24. It is unclear if the effect of the reduced polymer chain length could also be captured by a completely different set of Mie potential parameters, or how much the assumptions in the SAFT-γ Mie theory play a role. It is known,[14] that the SAFT-γ Mie works excellently for compounds of small molecular weight and less well with increasing molecular weights. Another consideration, which can explain the flat plateau, but not the shifted UCST position, is the difference between binodal and spinodal decomposition. While we have plotted the binodal decomposition temperatures in Fig. 5.23-5.24, it is experimentally not guaranteed to observe phase change at the binodal, but, supported by relatively low viscosity and smaller tendency to phase separate, transition can appear further towards the spinodal decomposition temperature where the tendency

[†]The developers of SAFT-γ Mie also adjust $\lambda_{r,ij}$ if necessary to capture mixture properties.[151,184] They keep the attractive exponent constant at $\lambda_{a,ij} = 6$ for all interactions with very few exceptions, such as carbon dioxide and water.[6,151]

to phase separate increases. Generally, cloud-point measurements are expected to lie between the binodal and spinodal conditions and are therefore expected to lead to potentially narrower curves than the predicted binodal curves. While the binodal/spinodal differences could at least partially explain the differences between experiment and prediction in terms of wideness/narrowness of the curves, the position of the critical solution condition is independent of this consideration. The mismatch of the UCST position is the aspect which could not be quantitatively reproduced with the SAFT-γ model and no conclusive explanation was found.

In summary, successful PB/sq and cisPB/sq models were developed, which capture both PVT and cloud-point curves. Two unlike interaction parameters, $\lambda_{\mathrm{r},ij}$ and k_{ij}, need to be adjusted to capture the UCST behaviour. The cause of the remaining differences between experimental and predicted cloud-point temperatures, in particular the position of the UCST, is unclear.

PB/PS

Mixture of polybutadiene (PB) and polystyrene (PS) are less compatible than PB/PI, which can be confirmed by the lower chemical similarity due to the PS aromaticity. PB/PS mixtures phase separate already at smaller molecular weights than PB/PI mixtures.[230]

Experimental data for the SAFT-γ Mie model development was sourced from several independent references. For the pure compounds, we apply the Mie potentials PS-9k and PB-3k (see Tab. 5.7), which were developed with experimental PVT data from Zoller and Walsh 1995[228] in Sec. 5.4.2. For the mixture, experimental cloud-point curves by Rostami *et al.*[230] are used as reference. The unlike interactions require two adjustable parameters to match the UCST behaviour. Only adjusting k_{ij} leads to models predicting closed loop immiscibilities with the loop centre above the experimental UCST. The closed loop behaviour at a similar position is also found when alternative PVT sources are used for the pure parameters, where we have in particular tested the PBD233, PS784, PB-8%, PB-87%, PS-9k and PB-3k models (see Tab. 5.7), which supports the need for a second adjustable unlike interac-

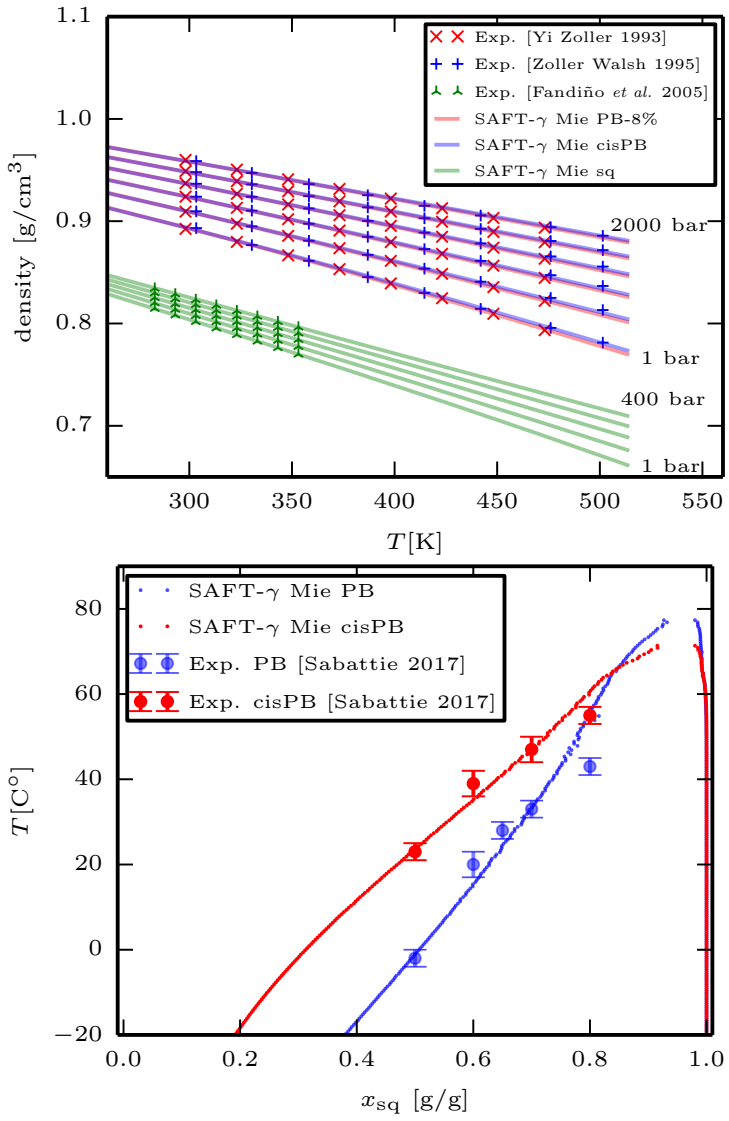

Figure 5.23: Pure-component PVT of polybutadiene (M_n^{PB} = 123.6 kg mol^{-1},[236] M_n^{cisPB} = 200 kg mol^{-1} [228]) and squalane (422 g mol^{-1}) (top) and cloud-point temperatures of PB(133.3 kg mol^{-1})/sq and cisPB(127.2 kg mol^{-1})/sq mixtures (bottom). The SAFT-γ Mie models are PB-8%, PBcis and sq (Tab. 5.7) with $k_{\mathrm{PB-8\%/sq}}$=0.030877, $k_{\mathrm{cisPB/sq}}$=0.070205, $\lambda_{\mathrm{r,PB-8\%/sq}}$=9.3026, $\lambda_{\mathrm{r,cisPB/sq}}$=8.2083. The experimental data is taken from Refs 228,236,249,273.

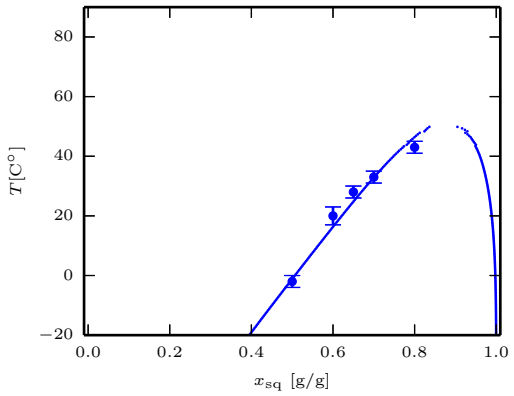

Figure 5.24: Cloud-point curve of polybutandiene and squalane compared between experimental data[273] and a SAFT-γ Mie model of PB-8% and sq (Tab. 5.7) where PB-8% is modelled with a 10× smaller molecular weight than in Fig. 5.23. The unlike interaction parameters are adjusted to $k_{\mathrm{PB-8\%/sq}}$=0.021528, $\lambda_{\mathrm{r,PB-8\%/sq}}$=9.4503.

tion parameter. The best model was obtained with $k_{\mathrm{PB-3k/PS-9k}}$=0.177 and $\lambda_{\mathrm{r,PB-3k/PS-9k}}$=8.0, which correctly captures the UCST behaviour and the slope around the critical region, see Fig. 5.25. However, the predicted mixture composition at the UCST deviates from the experimental observations, i.e. the PS composition at the UCST is overpredicted. Still, it is also worth noting that fitting across a full composition range is very tough with limited experimental data, as with the five points for the PB/PS in this section.

Experimental LLE data of the same PB/PS mixture at higher pressure, 1000 bar,[230] allows validation of the model at another condition. The prediction for 1000 bar correctly shows reduced miscibility compared to 1 bar, but slightly overshoots the UCST, see Fig. 5.25.

In summary, a model for a PB/PS mixture was successfully developed which captures PVT and LLE data. The model predictions for an LLE at a higher pressure agrees well with experiment.

PI/oligomer/oligomer

A ternary mixture is described in SAFT-γ Mie as three pure compounds with three pair-wise unlike interactions. In this section a ternary model is

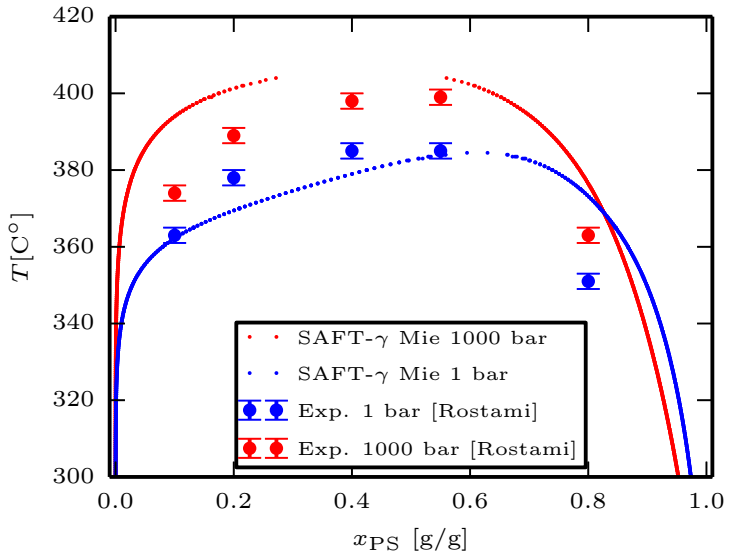

Figure 5.25: Cloud-point curve of polybutandiene and polystyrene compared between experimental data[230] and a SAFT-γ Mie model of PB-3k and PS-9k (see Tab. 5.7). The unlike interaction parameters which best reproduced the LLE at 1 bar are $k_{\mathrm{PB-3k/PS-9k}} = 0.177$ and $\lambda_{\mathrm{r,PB-3k/PS-9k}} = 8.0$. The LLE at 1000 bar is predicted with the same SAFT-γ Mie model.

developed for the mixture of polyisoprene of high molecular weight with two oligomers, which are both polystyrene derivatives. One of the PI/oligomer pairs is miscible at room temperature, while the other PI/oligomer pair shows immiscibility with UCST behaviour up to high temperatures. The two oligomers appear to be immiscible, but experimental evidence is not conclusive.[262] The addition of the first oligomer to the immiscible PI/olgiomer mixture improves the overall miscibility.[262] A good SAFT-γ Mie model would therefore ideally capture the effect of improved miscibility, the UCST behaviour and reproduce the ternary cloud-point temperatures as quantitatively as possible, while using a SAFT-γ Mie model with only one Mie potential type per compound and as few adjusted unlike interactions as necessary. Compared to the binary mixtures analysed in the previous sections, the addition of the third compound in this ternary mixture requires significantly more computational time for the LLE calculations and the parameter estimations, especially for the polydisperse description.

The oligomers are polystyrene derivatives. The first oligomer is a partially hydrogenated poly(methylstyrene-*co*-indene) (phPMI), which is, when blended with styrene-isoprene-styrene (SIS) block copolymers, more miscible with the polyisoprene midblock, and therefore also referred to as a midblock tackifier (MT). The second oligomer is a poly(styrene-*co*-α-methylstyrene) (PSαM), which is more miscible with the endblocks of SIS block copolymers and, hence, referred to as an endblock tackifier (ET). See Tab. 5.7 for more information.

The experimental reference data are shown in Fig. 5.26.[262] For the mixture, 27 cloud-point temperatures are available for samples of different compositions. PI/ET mixtures phase separate at room temperature at ET concentrations larger than 5% by weight. No phase separation for PI/MT mixtures was observed. MT/ET mixtures appear to phase separate into a yellow and a colourless phase at some conditions. While the precise determination of a cloud point visually is difficult for the 9% MT/91% ET sample, it appears to be at approximately 160 °C, which suggests a surprisingly steep cloud-point curve for the ET/MT binary pair at low MT concentrations.[262] Liquid densities of both pure oligomers at ambient pressure for several temperatures were measured.[262] Liquid densities for polyisoprene with a similar monomer ratio were taken from Yi and Zoller.[236]

The pure-component Mie potentials where developed purely with liquid densities as described in Sec. 5.4.2. As no compressibility information was available for the oligomers, compressibilities from a polystyrene oligomer of similar molecular weight measured by Zoller and Walsh[228] were included in the parameter estimation procedure for both oligomers. The PVT data set for polyisoprene already included information about thermal expansion and compressibility and was used without changes. The Mie potentials are referred to as phPMI, PSαM and PI-8%. See Tab. 5.7 for more information.

We have also attempted to develop a *polydisperse* model for the ternary mixture. The oligomers are modelled with three pseudocomponents each, i.e. in total seven components for the ternary mixture. Calculations for the three binary pairs using combining rules for all unlike interactions predict UCST behaviour for the oligomer mixture ET/MT, but LCST behaviour for both

PI/oligomer pairs. The shape of the experimental immiscibility area can be captured qualitatively at room temperature for the adjusted interactions $k_{\mathrm{ET/MT}} = 0.0065$, $k_{\mathrm{PI/MT}} = -0.1$ and $k_{\mathrm{PI/ET}} = -0.006$. The cloud-point curve at room temperature is shown in Fig. 5.27. In agreement with the experimental evidence, the PI/ET and ET/MT pairs are partially miscible, the MT/PI pair is fully miscible, and the immiscibility area spans across the majority of the composition space. While the overall shape of the immiscibility area is captured qualitatively correct at one temperature, the temperature dependency, i.e. the LCST behaviour of the PI/ET pair, disagrees with the experimental observation of an UCST. The improved miscibility upon addition of MT to the PI/ET mixture, which is observed experimentally, is captured by the SAFT-γ Mie model for most, but not all compositions. The SAFT-γ Mie model, for example, predicts the miscible mixture of 60% PI and 40% ET to phase separate upon addition of MT, which contradicts experiment.

An improved polydisperse model would require the adjustment of additional unlike interactions and a more elaborate parameter estimation. The available SAFT-γ Mie programs, however, are already pushed to their limits with this polydisperse ternary polymer mixture. The cloud-point calculations of this mixture of 7 pseudocomponents are computationally demanding for our SAFT-γ Mie software using the HammR algorithm. The calculations for the results in Fig. 5.27 take about one week (i.e. about 13 min per PT-flash calculation) on a single CPU core (i5-2400S 2.5 GHz). While this allows the determination of the cloud-point curve for a given SAFT-γ Mie model in a production run, it is prohibitively expensive to iteratively optimise the model parameters with automated algorithms. With our parallelised HammR algorithm with optimised Intel compiler settings and using powerful processors on the Durham high performance cluster, HammR calculations run effectively 50−60 times faster (about 15 s per PT-flash calculation) than running in serial on a typical desktop machine compiled with gfortran. This speed-up is the first crucial step towards the goal of successfully running elaborate parameter optimisations on ternary mixtures. The development of an algorithm for automated parameter optimisations for binary and ternary mixtures was

not attempted in the course of this work, but could be part of future work.[‡]

We have also attempted to develop a SAFT-γ Mie model with reduced complexity for faster calculations and, at the same time, aim for a better agreement with the experimental miscibilities. All three materials are modelled *monodisperse* for reduced complexity. Additionally, the oligomer mixture ET/MT is assumed to be miscible. Unlike interaction parameters for the PI/ET mixture are adjusted to improve upon the previously obtained LCST behaviour which is in conflict with experiment. With $k_{\mathrm{ET/MT}} = 0.206$, $k_{\mathrm{PI/MT}} = 0.0065$, $k_{\mathrm{PI/ET}} = -0.01$ and $\lambda_{\mathrm{r,PI/ET}} = 8.0$ the improved phase diagram in Fig. 5.28 is obtained. The UCST behaviour of the PI/ET pair is successfully obtained due to the adjusted λ_{r}. As a result, the trend of increased overall miscibility for higher temperatures (ternary UCST) is also captured. In addition, the improved miscibility upon adding MT is correctly predicted for all compositions. While the trends with respect to temperature and MT addition are correctly captured with this model, the quantitative shape of the phase diagram still significantly deviates from the experimental results. Especially the mixture composition at the UCST is predicted to be at ET concentrations >90%, while experimentally found at roughly 60% ET. The observation that SAFT-γ Mie models show deviating mixture compositions at the critical solution temperature for all Mie potential parameter values was also made for the binary models developed in the previous sections.

Another interesting observation during the development of ternary polymer mixture models was made about the shape of immiscibility areas. Possibly counter to intuition, the reduced miscibility of one pair AB can increase the miscibility of the ternary mixture ABC. Expressed in free energies of mixing, the larger free energies of mixing of AB (more favourable mixing), can increase the mixture composition area where the mixture ABC has smaller

[‡]The commercial SAFT-γ Mie software gSAFTmm[203] version from 2016 which was kindly provided by PSE, calculates fast and reliable LLE predictions for strictly binary and ternary mixtures which were in agreement with results from our HammR code. For polydisperse mixtures, however, unreliable miscibility predictions were observed with gSAFTmm. The deviations were acknowledged by the developers. Since this work was completed a new version of the software has been released that has been stated to address the problems.

free energies of mixing (less favourable mixing) than the phase separated AB+C, because AB+C has become less favourable. This simple, but possibly counter-intuitive example, demonstrates the increased complexity of ternary systems compared to binary systems and hints at the additional insights that are expected to be made when complex polymer mixtures are studied with computational approaches such as SAFT-γ Mie.

In summary, a successful SAFT-γ Mie model for a ternary polymer mixture was developed. The model, while not quantitatively capturing the experimental phase diagram, captures the overall phase diagram shape at room temperature correctly and reproduces the trends for increasing temperatures and addition of MT. We have made the first step towards automated iterative parameter optimisations for complex polydisperse models with our own algorithms by speeding up the HammR calculations with a parallelised HammR version. Similar to the findings in the previous sections, the mixture composition at the UCST is predicted to have significantly larger oligomer concentrations than found experimentally.

5.5.3 Volumes of mixing

It is very appealing to use volumes of mixing V_{mix} for validating and optimising unlike interactions in SAFT-γ Mie polymer models as the same experimental equipment used for the pure-component PVT data can also be used for measuring V_{mix}. A single experimental technique for the complete characterisation of polymers and polymer mixtures for the development of polymer SAFT-γ Mie models might reduce the cost for the overall development. The very high precision needed for valuable measurements of V_{mix} and the unclear transferability of V_{mix}-based SAFT models for the prediction of polymer miscibilities unfortunately reduces the appeal and makes LLE and CPC the data of choice. However, as V_{mix} are measured only for miscible blends, and LLE and CPC determinations require the access to phase transitions, V_{mix} data can be the best choice for highly miscible systems.

Volumes of mixing have successfully been used in the context of polymer models. V_{mix} data of PB/PI mixture of high molecular weight was cor-

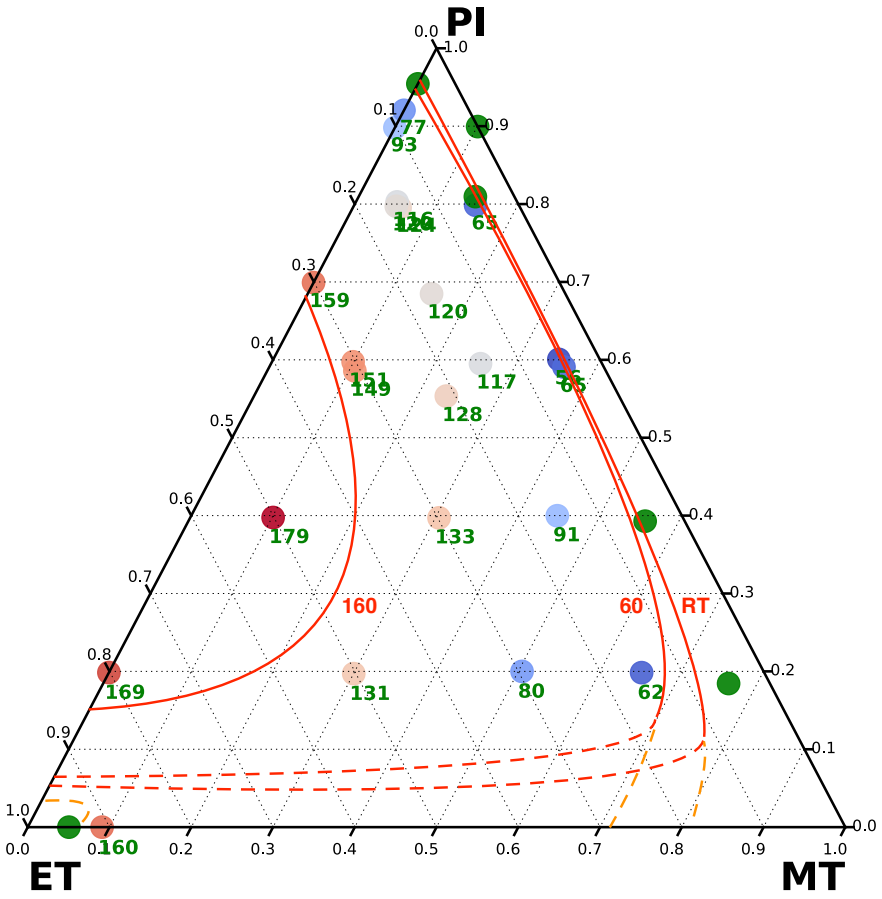

Figure 5.26: Experimental cloud-point temperatures for the ternary mixture of polyisoprene (PI), a partially hydrogenated poly(methylstyrene-*co*-indene) (MT) and a poly(styrene-*co*-α-methylstyrene) (ET).[262] The cloud-point temperatures are given in °C. The samples are miscible above the cloud-point temperature (UCST behaviour). The symbol colouring from green to red correlates with the cloud-point temperature values. Samples represented with green circles (no temperature value given) were miscible at room temperature. The expected cloud-point curves for room temperature (RT), 60 °C and 160 °C are added as hand-drawn lines to guide the eye. The dashed lines indicate two alternative cloud-point curve continuations which both agree with the inconclusive experimental evidence of the ET/MT miscibility.

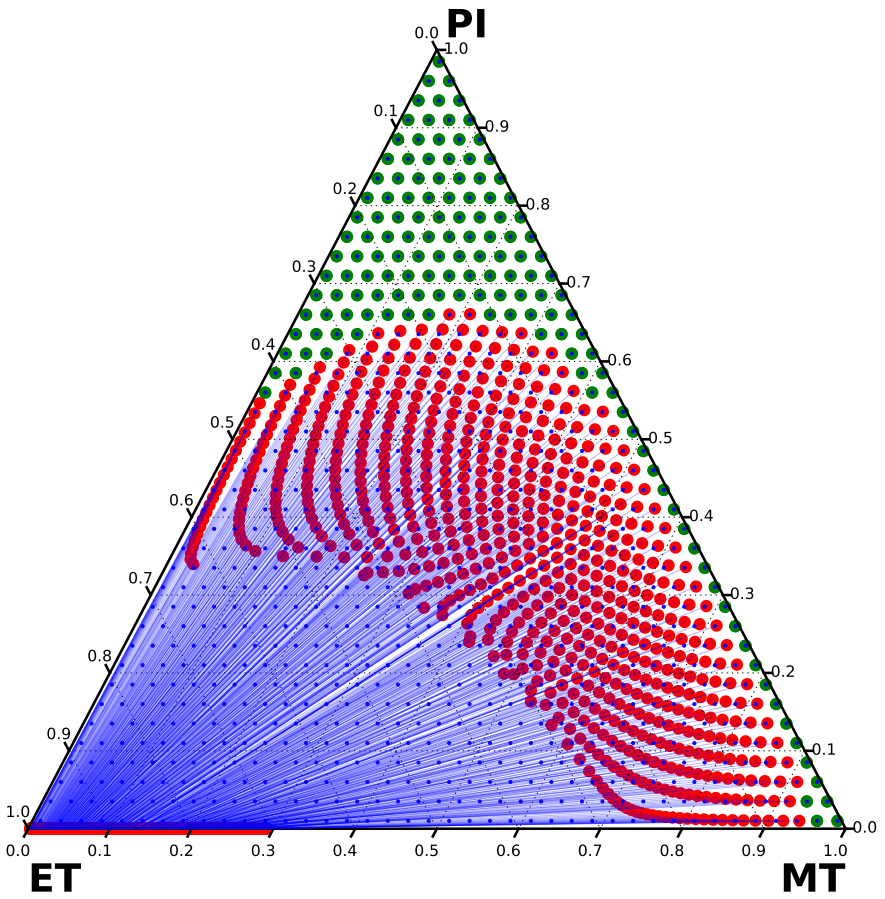

Figure 5.27: Cloud-point curve predictions at 25 °C with a polydisperse SAFT-γ Mie model indicating the computational procedure for obtaining cloud points. The composition of the coexisting phases (red sphere) are plotted for a grid of equally-spaced initial global compositions (blue point). Phases in equilibrium are connected by thin blue lines. The cloud-point curve corresponds to the boundary between green (miscible/stable compositions) and red (phase separated phase) compositions. The composition of the phases in equilibrium (red spheres) do not all collapse into a single cloud-point curve in this figure as the system consists of 7 pseudocomponents and the results were expressed as only 3 materials. The unlike interactions deviate from the combining rules by $k_{\mathrm{ET/MT}} = 0.0065$, $k_{\mathrm{PI/MT}} = -0.1$ and $k_{\mathrm{PI/ET}} = -0.006$.

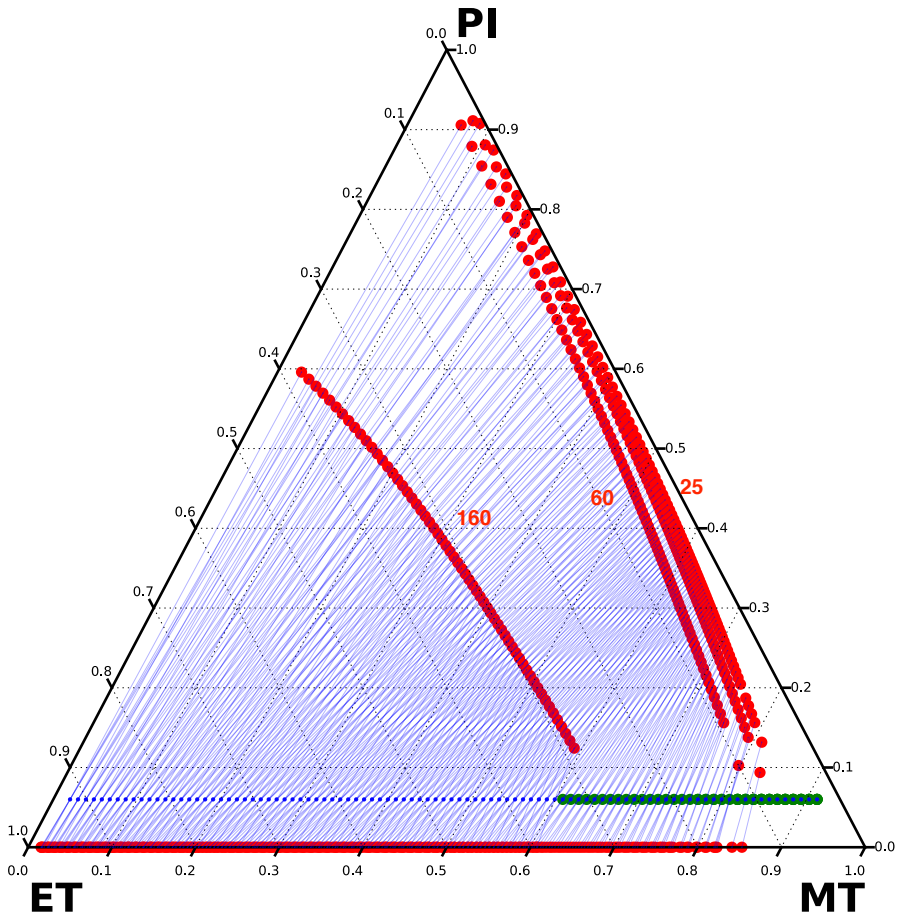

Figure 5.28: LLE predictions at 25 °C, 40 °C, 60 °C and 160 °C with a monodisperse SAFT-γ Mie model. The composition of the coexisting phases (red sphere) were obtained for a range of initial global compositions (blue point). Phases in equilibrium are connected by thin blue lines. The compositions of the phases in equilibrium correspond to the phase boundaries as all components are modelled monodisperse. The unlike interactions deviate from the combining rules by $k_{\mathrm{ET/MT}} = 0.206$, $k_{\mathrm{PI/MT}} = 0.0065$, $k_{\mathrm{PI/ET}} = -0.01$ and $\lambda_{\mathrm{r,PI/ET}} = 8.0$. Data shown in this figure was calculated with the gSAFT program.[203]

rectly predicted with a SAFT-γ Mie model fitted to PVT and LLE data in Sec. 5.5.2. In addition, Higgins *et al.* in 2010 successfully developed a PS/poly(vinylmethylether) model based on V_{mix} data for an equation of state.[233] A SAFT-γ Mie sensitivity analysis of the energetic unlike interaction k_{ij} on V_{mix} data of oligomer and polymer mixtures showed V_{mix} to capture energetic differences of unlike interactions. The influence on V_{mix} data, however, is significantly smaller than on LLE/CPC temperatures and even smaller V_{mix} changes are found with increasing molecular weights, sometimes orders of magnitude smaller than the relative changes in temperature.

Volumes of mixing can carry both structural and energetic information about polymer mixtures. If structural information are not sufficiently captured by the choice of number of beads and Mie potentials in the SAFT-γ Mie model, the energetic fitting parameter k_{ij} might be forced to effectively capture some of the structural information, which can result in a model with a poor balance of entropy and enthalpy. Such a model is not expected to correctly predict partitioning and solubilities of polymers.

Experimental methods for measuring volumes of mixing are, for example, the density gradient column (e.g., described in ASTM D1505) and the vibrating tube densimeter (e.g., used by Fandiño *et al.*[249]). V_{mix} values are calculated from the densities of both pure compounds and the mixture. Density gradient columns are a long column of two liquids whose composition—and therefore density—smoothly changes with height. Densities are determined by the position of a sample compared to reference specimens floating in the column. Both setting up the density gradient and changing temperature can be time-consuming. The vibrating tube densimeter requires regularly performed time-consuming calibration across the whole density, temperature and pressure range it is used for.

In summary, the methods for measuring high-precision densities are expected to be more expensive and time-consuming than cloud-point temperature measurements. In addition, it is unclear how reliable LLE/CPC are predicted with unlike interactions that are obtained from V_{mix}-based models as the balance of entropy and enthalpy might not be correctly captured. For highly miscible mixtures, however, V_{mix} data might be the best experimental

data when no LLE/CPC are accessible.

5.6 Summary and conclusion

We have tested whether available SAFT-γ Mie parameters correctly predict solubilities and partitioning of polymer mixtures. We found the low molecular weight parameters not to be transferable to solubility and partitioning of polymers.

We presented a semi-exhaustive set of thermodynamic experimental data of hydrocarbon polymers and their mixtures, which can be used in the development of polymer models, and highlighted areas that have not been characterised. We developed pure-component Mie potentials for a range of polymers based on PVT data. We developed mixture models for three binary and one ternary polymer mixture based on LLE/CPC data. An overview over the usefulness of experimental data other than PVT and LLE/CPC was given, while heat capacities, speed of sound and volumes of mixing are discussed in particular. Other strategies for speeding up the parameter estimation procedure, such as the corresponding state principle and combining rules are also analysed.

We find the best methodology for developing SAFT-γ Mie models for polymer mixtures to be a two-step process. Firstly, the pure-component parameters are optimised to best reproduce PVT data. The larger the PVT data set, the more Mie potential parameters can be estimated. Secondly, the unlike interactions are tested and adjusted with the help of LLE/CPC mixture data, where k_{ij} alone, or k_{ij} and $\lambda_{\mathrm{r},ij}$ are adjusted together to best reproduce the phase transition temperatures.

While correct qualitative predictions have been obtained throughout with the methodology presented above, quantitative extrapolations and predictions for LLE and CPC properties are challenging within SAFT-γ Mie. We see a systematic deviation for all polymer mixture models studied in this work. The concentration of the lower-molecular weight compound is consistently overpredicted at the critical solution condition. The available Mie potential interactions do not include a parameter to adjust the mixture com-

position at the critical solution temperature. No Mie potential parameter other than the chain length (i.e., molecular weight) can significantly influence the mixture composition at the critical solution temperature. The molecular weight is well known from experiments and when adjusted, leads to less physical presentation for other properties. The limited set of experimental data typically encountered for polymers, however, does not justify making the model more complex by increasing the number of Mie potential types. Several reasons for the deviations seen between LLE/CPC experimental data and SAFT-γ Mie predictions around the critical solution temperature are possible. First, SAFT often does not capture critical vapour–liquid region well and often overshoots critical temperatures (larger curvature predicted than found in experiment).[14] Second, SAFT is best for spherical monomers/dimers/trimers, and larger deviations and shortcomings were found for longer molecules such as polymers. Third, experimental cloud-point temperatures are not expected to exactly represent binodal separation, but can lie between binodal and spinodal temperatures.

Chapter 6

Application of Mie potentials in molecular dynamics simulations

This chapter covers the application of SAFT-γ Mie potentials in coarse-grained molecular dynamics simulations. We investigate the advantages and also challenges faced when coarse graining force fields are developed using a top-down approach via the SAFT-γ Mie EoS. Systems ranging from pure-component solvents and polymer melts, to mixtures of solvents, oligomer/ polymer mixtures and polymer/polymer mixtures are studied. Prior to the SAFT-γ Mie work, we present results from a generic coarse-grained model showing the influence of oligomer length and oligomer/polymer interaction on miscibility. Again, the main properties of interest are the bulk miscibility and phase separation characteristics. In addition, also surface phenomena are studied using an oligomer/polymer system showing surface enrichment and wetting layers.

The excellent recent series of publications from the Imperial College group centred around Prof. George Jackson and Prof. Erich Müller "SAFT-γ Force Field for Simulation of Molecular Fluids",[6,114,115,151,152,274] is the most comprehensive and systematic work published on using SAFT-γ Mie potentials in molecular simulations. Including other publications, the list of studied systems range from CO_2,[6] refrigerants,[115] alkanes,[114,115,155] water,[151] binary and ternary systems[152] and hetero group models.[114,274] In addition, a successful

coarse-grained SAFT-γ Mie model for a polystyrene solution in hexane and nonane showing LLE was published recently.[259]

We introduce a shorthand notation to distinguish Mie potentials used in equations of state and in MD simulations. SAFT-γ Mie potentials used with the SAFT-γ Mie equation of state (EoS) are referred to as SAFT-γ Mie EoS, and SAFT-γ Mie potentials used as force fields in coarse-grained molecular dynamics simulations are referred to as SAFT-γ Mie CG. As in previous chapters, if EoS or CG is not specified, SAFT-γ Mie is used as a short form of SAFT-γ Mie EoS.

All molecular dynamics simulations in this chapter were carried out using GROMACS 4.6.7.[275,276] Simulation snapshots were rendered with VMD.[277,278]

6.1 Converting SAFT-γ Mie models into a molecular force field model

SAFT-γ Mie potentials translate directly to the non-bonded interactions to be used in a molecular force field. In the simplest case of a single-bead model, the force fields only consists of the Mie potential. For multi-bead models, bonded potentials are added. The Mie potential parameter σ is equivalent to the bond length. While no bond-stretching force constant is needed for Monte-Carlo simulations, they are required for MD simulations. In the SAFT-γ Mie EoS bonds are infinitely stiff, which is why bond constraints such as LINCS are the closest translation. However, fairly stiff representations taken from off-the-shelf bottom-up force fields of similar resolution can also be used and do not change typical properties at reasonable conditions. If not stated otherwise, in this chapter we use a bond-stretching force constant of $1.5 \times 10^5\,\mathrm{kJ\,mol^{-1}\,nm^{-2}}$, which was chosen to be stiff enough to represent the constant bond lengths of SAFT models and MC simulation models, but soft enough to not require smaller MD time steps. SAFT-γ Mie models are fully flexible without angle or dihedral constraint, which is why no angle and torsion potentials were applied. In Sec. 6.8 we address the motivation to add additional bonded potentials and discuss the advantageous and challenges

for several examples.

6.2 Generic coarse-grained model system for oligomer/polymer miscibility

A simple polymer mixture model system is presented for which the influence of unlike interactions and molecular weight on bulk miscibilities are investigated. Phase separation is demonstrated in a polymer–oligomer system using a coarse-grained model description. A polymer made of 100 Lennard–Jones beads and an oligomer of 5, 10 and 25 Lennard–Jones beads are used for this study. Their structure is represented in Fig. 6.1.

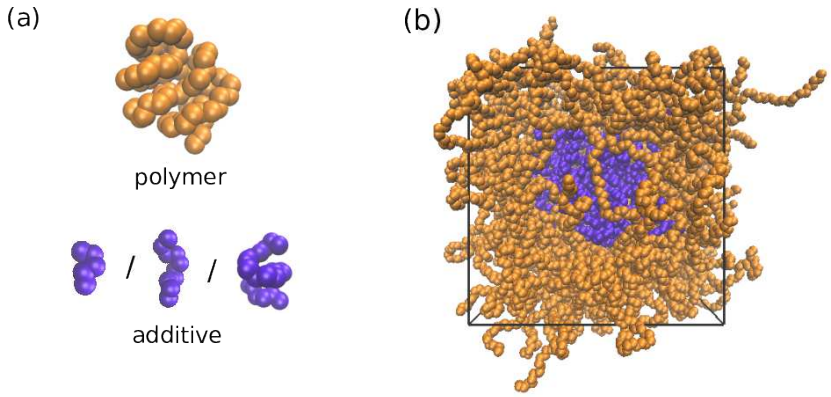

Figure 6.1: The polymer/oligomer model system used, comprising (a) 100 polymer chains each with 100 beads and 100 oligomer molecules of 5, 10 or 25 beads. (b) An MD snapshot from an equilibrated simulation showing a phase separated state in a condensed polymer system.

Coarse-grained model

The simulations were performed at 500 K to ensure relatively fast equilibration times. The force field used was based on parameters of the TraPPE[279] force field for the CH_2 united-atom bead, i.e. with a bond length $d = 0.154\,\mathrm{nm}$, bond angles of $\theta = 114°$ with a force constant of $k_\theta/k_\mathrm{B} = 62\,500\,\mathrm{K\,rad^{-2}}$ and non-bonded Lennard–Jones interactions with $\epsilon/k_\mathrm{B} = 46\,\mathrm{K}$ and $\sigma =$

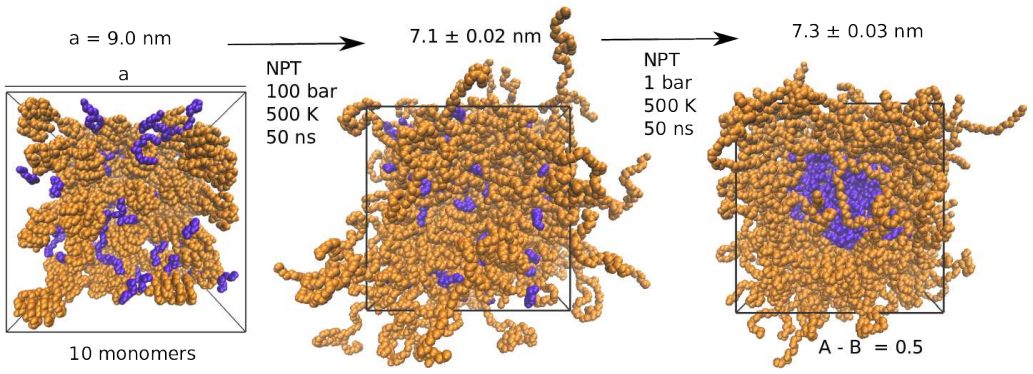

Figure 6.2: MD simulation methodology. Left, a low density system of oligomers and polymers. Middle, a condensed system obtained with a relative interaction of $a = 1.0$. Right, a phase separated system found after adjusting the relative interaction to $= 0.5$. The box dimensions and ensemble conditions for the simulations are indicated.

0.395 nm. No dihedral angles were applied to increase the chain's flexibility further. The same like interactions (interaction between beads of the same type) were used for both polymer and oligomers. The unlike interactions between polymer and oligomer units was systematically varied in this study. We define the relative interaction parameter a as $\epsilon_{\text{unlike}} = a\epsilon_{\text{like}}$ and use values of $a = 1.0$, 0.85, 0.75 and 0.5. The relative interaction is therefore the ratio of polymer–additive and polymer–polymer interactions.

Methodology

The MD simulation methodology is visualised in Fig. 6.2. Firstly, single molecules of oligomer and polymers were simulated in short NVT MD simulations leading to coiled conformations (see Fig. 6.1a). The coiled-up structures were multiplied and randomly arranged in a low-density conformation in a large simulation box to meet an oligomer number concentration of 0.11 mol/mol. Secondly, the condensed phase was obtained from an NPT ensemble MD simulation at high pressures of 100 bar. The simulation was run for 50 ns at time steps of 2 fs. Thirdly, a short equilibration run of 1 ns was performed at 1 bar. The resulting configuration was taken as the result for the relative interaction of $a = 1.0$. Fourthly, the relative interaction was

adjusted and MD simulations were carried out for 50 ns.

Results

The oligomer chain length and the oligomer/polymer interaction strength were systematically varied in this study and the impact on the bulk miscibility analysed. Both parameters influence the compatibility/phase behaviour significantly, see Fig. 6.3. Weaker polymer–additive interactions, as well as longer oligomers lead to stronger phase separations. The lower miscibility for weaker unlike interactions can be explained by enthalpic arguments, while the lower miscibility for larger oligomers can be explained by both enthalpic and entropic contributions as the effective interaction between oligomers is increased and the entropy of mixing is reduced.

An estimation of the phase boundary as a function of chain length m_s and relative interaction a was developed. A simple hyperbolic function has been used to describe the results, see Fig. 6.4. The prefactor of the hyperbolic function has been fitted to the arithmetic averages of the adjacent mixed/phase-separated parameters for each of the three additive lengths. The good hyperbolic fit $m_s = 1.89/(1 - a)$ suggests that the product of $(1 - a)$ and additive length m_s is constant at the phase boundary.

Conclusion

In summary, this model system of an oligomer/polymer system successfully demonstrated the influence of oligomer chain length and oligomer/polymer interaction strength on the bulk miscibility. The model allowed clear visual differentiation between compatible and incompatible conditions although relatively small MD simulations were performed.

6.3 Polymer-melt densities

In this section the transferability of SAFT-γ Mie potentials for polymer-melt densities across temperature, pressure and molecular weight ranges is

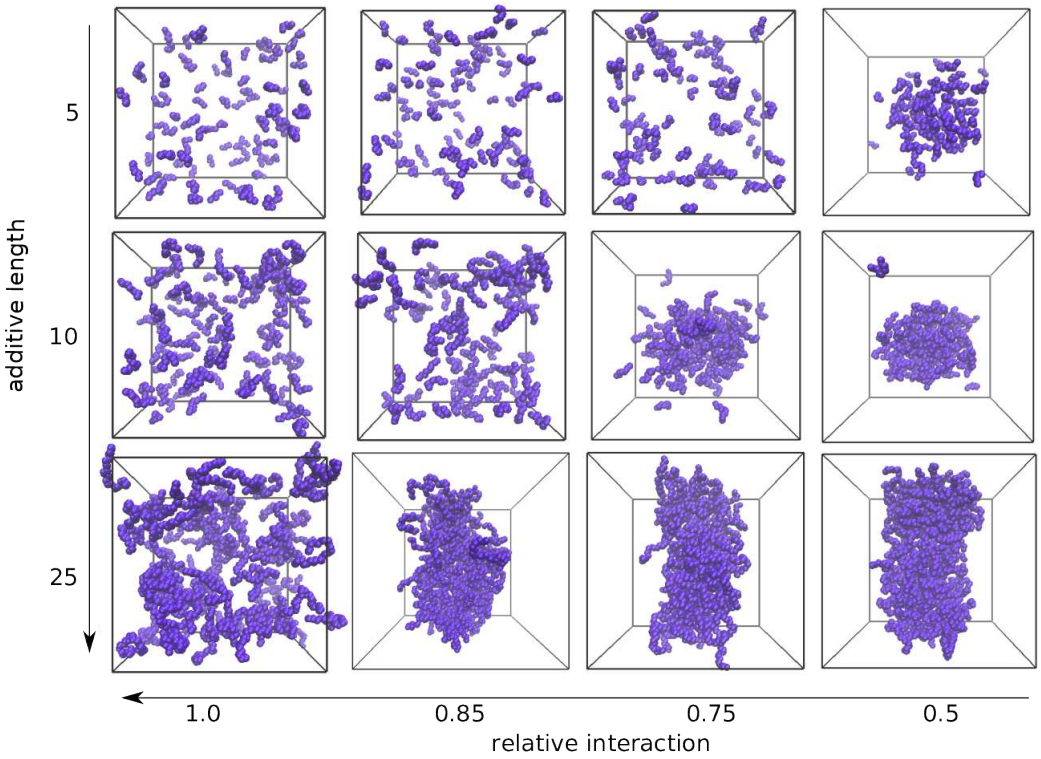

Figure 6.3: MD simulation snapshots for oligomer/polymer mixtures as a function of oligomer chain length and oligomer/polymer interaction strength. The polymer chains are not shown for clarity. Systems were prepared with constant number concentration and a single simplified Lennard–Jones potential as the basis for all interactions.

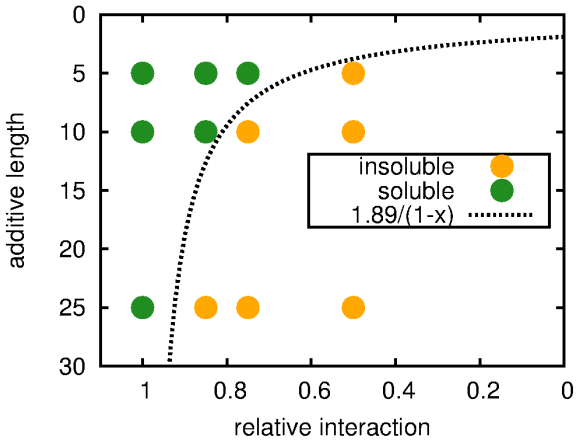

Figure 6.4: Representation of miscible conditions (green) and immiscible conditions (amber) quantitatively mapped in the oligomer-length and unlike interaction space. A simple hyperbola function was fitted to the results as an estimate of the phase boundary.

tested. Polystyrene density predictions are compared between SAFT-γ Mie EoS calculations and SAFT-γ Mie CG simulations.

SAFT-γ Mie CG model

Mie potential parameters were estimated with our parallel optimisation algorithm (see Sec. 4.6.5) and are designed to reproduce experimental PVT data.[228] The Mie potential Mie(10.5-8.1) (PS-0.8k in Tab. 5.7) was developed to best reproduce experimental data of a polystyrene with $M_n = 784\,\mathrm{g\,mol^{-1}}$. The Mie potential Mie(9-6) (PS-9-6 in Tab. 5.8) was developed with the same experimental data, but was chosen to have smaller Mie potential exponents. See Sec. 5.4.2 for more details on the parameter values. The Mie potentials are used without further adjustments. The number of beads was adjusted to meet the target molecular weight, with the mass of a single bead set to $52\,\mathrm{g\,mol^{-1}}$.

Methodology

The polymer chains and initial configurations were build with the Assemble! program.[280] The number of chains was set to give a box of 6k–7k

beads. The energy of the configurations was minimised with the steepest decent algorithm for 1000 steps with an interaction cut-off of 1.5 nm. The energy-minimised boxes of low density were compressed at 500 bar with the Berendsen barostat and at 500 K with the velocity rescale method for 2 ns to give a condensed fluid. The target pressure and temperature were then applied in a subsequent short MD run of 1 ns at otherwise unchanged conditions. The boxes were stacked $2 \times 2 \times 2$ to give a simulation size of 50k–54k beads. The production run was performed in the NPT ensemble with the Nosé-Hoover thermostat controlling the target temperature with a coupling constant of $\tau_T = 1$ ps and the target pressure controlled by the Parrinello-Rahman barostat with a coupling constant of $\tau_P = 5$ ps and compressibility of 9×10^{-5} bar^{-1}. The mixtures were run for 10 ns of which the first nanosecond was discarded for the purposes of further equilibration. All MD simulations were performed with the GROMACS suite version 4.6.7. The equations of motion were integrated with the leap-frog algorithm with a time step of 2 fs. Cut-off distances of 2 nm for interactions and neighbour lists were used.

Results

In Fig. 6.5c-d excellent agreement is found between SAFT-γ Mie EoS calculations and the coarse-grained simulations for Mie(10.5-8.1) at all tested pressures, temperatures and molecular weights. Very good agreement is also found for the second CG model Mie(9-6) which correctly captures the thermal expansion coefficient (temperature dependence), but slightly underpredicts the densities at 1 bar by about 1%.

Conclusion

Polymer-melt densities of polystyrene at different pressures, temperatures and molecular weights are compared between SAFT-γ Mie EoS and SAFT-γ Mie CG simulations. Excellent agreement is found between experiment, theory and simulation. The polymer model is this section demonstrates that polymer CG force fields for polymer-melt densities can be developed with the SAFT-γ Mie EoS and converted to SAFT-γ Mie CG force fields without the

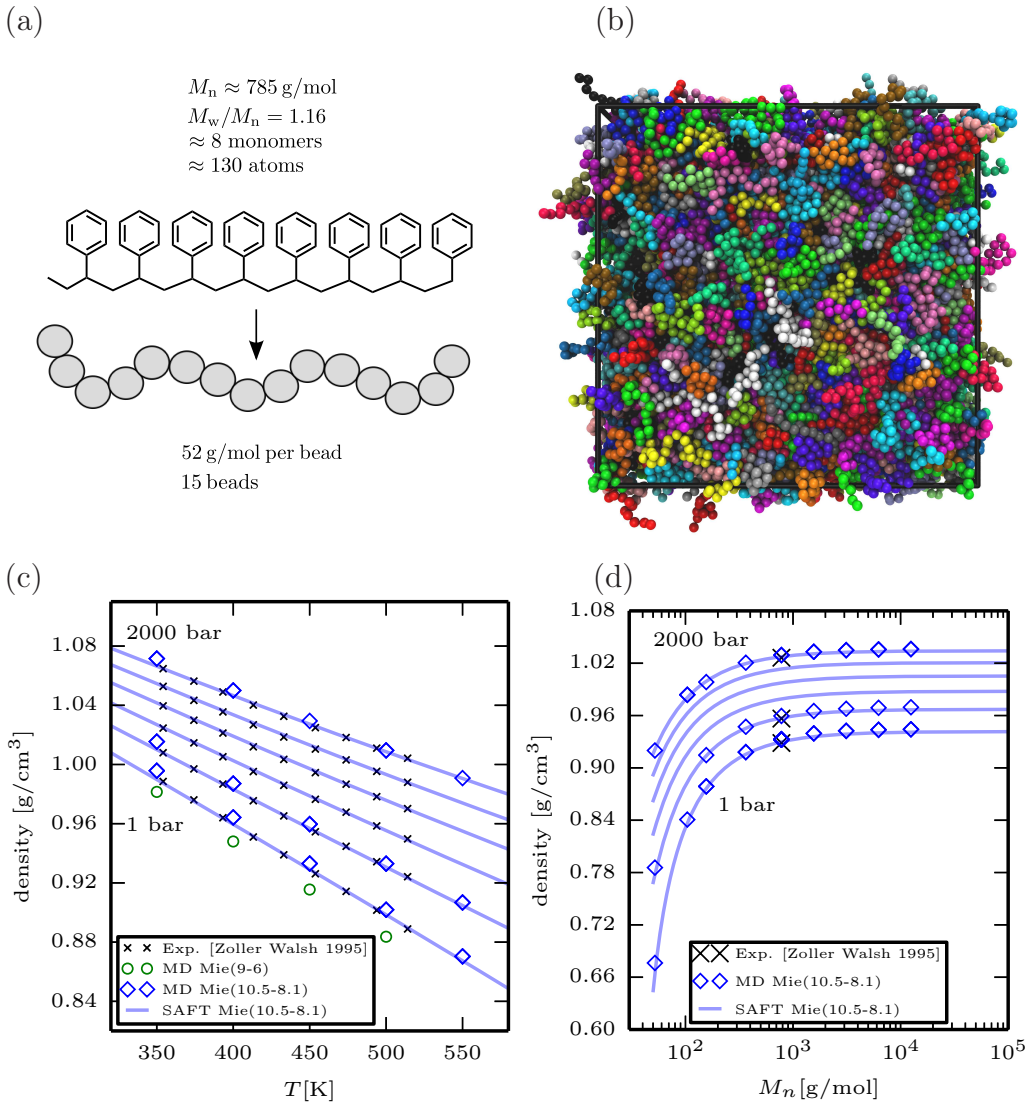

Figure 6.5: Polystyrene density comparison. (a) SAFT-γ Mie CG model for a polystyrene with $M_n = 785\,\mathrm{g\,mol^{-1}}$ as a 15mer, whose experimental data[228] was used in the development of the Mie potentials. (b) MD snapshot of a systems with 15mers with 50k beads in total. Each chain is coloured differently. Polystyrene densities of the (c) 15mer ($M_n = 785\,\mathrm{g\,mol^{-1}}$) and (d) several molecular weights compared between experiment[228] (crosses), SAFT-γ Mie EoS results (lines) and SAFT-γ Mie CG simulations (diamonds and circles). Results for chains of 1, 2, 3, 7, 15, 30, 60, 120 and 240 beads are shown. Pressure values in steps of 400 bar from 1 bar to 2000 bar are applied.

need for further adjustments in MD. In addition, SAFT-γ Mie CG models correctly capture thermal expansion and compressibility at the same time, which is very challenging to achieve with other coarse-graining methods such as IBI and force matching.

6.4 Benzene/octane mixture

A coarse-grained SAFT-γ Mie force field is developed in this section for a mixture of *n*-octane and benzene. The corresponding state principle parametrisation by Müller *et al.*[156] is employed to study one of the fastest means of developing SAFT-γ Mie CG mixture models.

SAFT-γ Mie CG model

Mie potentials were obtained with the CSP method[156] introduced in Sec. 5.4.1. Mie potential parameters are listed in Tab. 6.1.

Table 6.1: SAFT-γ Mie parameters for pure compounds used in this section. For all Mie potentials the shape factor is $S_k = 1$ and the number of segments per group $\nu_k = 1$, which allow the parameters to be used in both SAFT-VR Mie and SAFT-γ Mie. Mie potential parameters were obtained with the CSP method[156]

compound	σ_{ij} nm	$\epsilon_{ij}/k_\mathrm{B}$ K	$\lambda_{\mathrm{r},ij}$	$\lambda_{\mathrm{a},ij}$	mass g/mol	#beads
octane (oct-4b)	0.3768	255.92	12.70	6.0	28	4
benzene (benz-1b)	0.5329	686.15	43.97	6.0	78	1
benzene (benz-2b)	0.3978	349.79	13.96	6.0	39	2

Methodology

Simulations for pure-component properties were prepared by placing 500 molecules in an initial small box at low density with GROMACS scripts. For all systems, the equations of motion were integrated with the leap-frog algorithm with a time step of 2 fs. Cut-off distances of 2 nm for interactions

and neighbour lists were used. The configurations were compressed at 100 bar with the Berendsen barostat and simulated at 280 K with the velocity rescale method for 2 ns to give a condensed fluid; then relaxed at 1 bar at otherwise unchanged conditions. The initial box was stacked $1 \times 1 \times 3$ and extended three more box lengths to add vacuuum and create two vacuum/liquid interfaces.

Simulations for the octane/benzene mixture properties were prepared by combining 100 molecules (with the target composition) to an initial small box at low density, which was compressed at 500 bar and 328 K and relaxed at 1 bar as in the pure-component preparations. The relaxed configuration of 100 molecules was stacked $6 \times 6 \times 6$ for the 10%, 30% and 50% of benzene, $7 \times 7 \times 7$ for 70% benzene and $8 \times 8 \times 8$ for 90% of benzene. The cubic boxes were extended by three box lengths to add vacuum and create two interfaces. The final simulation boxes comprised 63k–66k beads.

The production run was performed in the NVT ensemble with the Nosé-Hoover thermostat controlling the target temperature. The first 20 ns were discarded and the remaining 180 ns (pure components) and 60–160 ns (mixture) analysed.

The pure octane systems with 6k beads at $T < 350$ K were stacked again ($3 \times 3 \times 1$ to give $15 \times 15 \times 30\,\mathrm{nm}^3$) and rerun to improve the sampling of the vapour phase. Benzene systems with 1.5k beads at 325 K and 328 K were stacked again ($5 \times 5 \times 1$ to give $42 \times 42 \times 25\,\mathrm{nm}^3$) to improve the sampling for the vapour pressure predictions.

Results

Pure-component Mie potentials obtained with the corresponding state principle (CSP) as presented in Sec. 5.4.1 are used to predict pure-component VLE, vapour pressures, isobaric mixture VLE and isothermal mixture VLE in Fig. 6.6 and 6.7. See Tab. 6.1 for the Mie potential parameters.

As can be seen in Fig. 6.6, the pure-component properties agree very well with experiment. Deviations are found for the vapour pressures, which is very slightly overpredicted by SAFT-γ Mie EoS calculations and slightly

overpredicted by SAFT-γ Mie CG simulations. The melting temperature (can not be captured by the fluid theory SAFT-γ Mie) is overpredicted for benzene by about 40 K ($T_\mathrm{m} = 279\,\mathrm{K}$)[261] as can be seen by the jump in density in Fig. 6.6b at about 320 K. The melting point of octane (experimentally at $T_\mathrm{m} = 216\,\mathrm{K}$)[261] was expected within the studied range, but is underpredicted at least by 20 K.

It is interesting to point out that simulations of only 1500 molecules run for 200 ns already give acceptable levels of precision for most VLE properties. As expected, closer to the critical conditions the density errors increase due to larger density fluctuations, and at lower temperatures the vapour pressure errors rise due to lower concentrations in the vapour phase. Larger simulations were performed on a few selected low temperature systems to improve the vapour pressure predictions.

Predicted binary vapour–liquid equilibria at 1 bar show an azeotropic mixture and a liquid–liquid immiscibility area when relying purely on combining rules. A single adjusted unlike interaction parameter $k_{ij} = -0.007$ gives an excellent representation of the experimental isobaric mixture in Fig. 6.7b. The dew (upper curve) and bubble (lower curve) points in Fig. 6.7b are not as conveniently modelled in MD simulations because they are phase transitions at constant pressure. Vapour pressures at constant temperatures can conveniently be obtained from canonical NVT ensemble simulations. MD simulation results are therefore presented at constant temperature in Fig. 6.7c. The vapour pressure results are in fair agreement with the experimental data, but are overpredicted due to the poor pure benzene vapour pressure (cf. Fig. 6.6). An alternative benzene model with 2 beads instead of one leads to an improved description of the isothermal VLE without the need for a correction factor for the unlike interaction, but corresponds to a smaller degree of coarse graining.

Conclusion

The coarse-grained simulations of octane and benzene not only give good agreement for pure-component properties, but also predict isothermal VLE

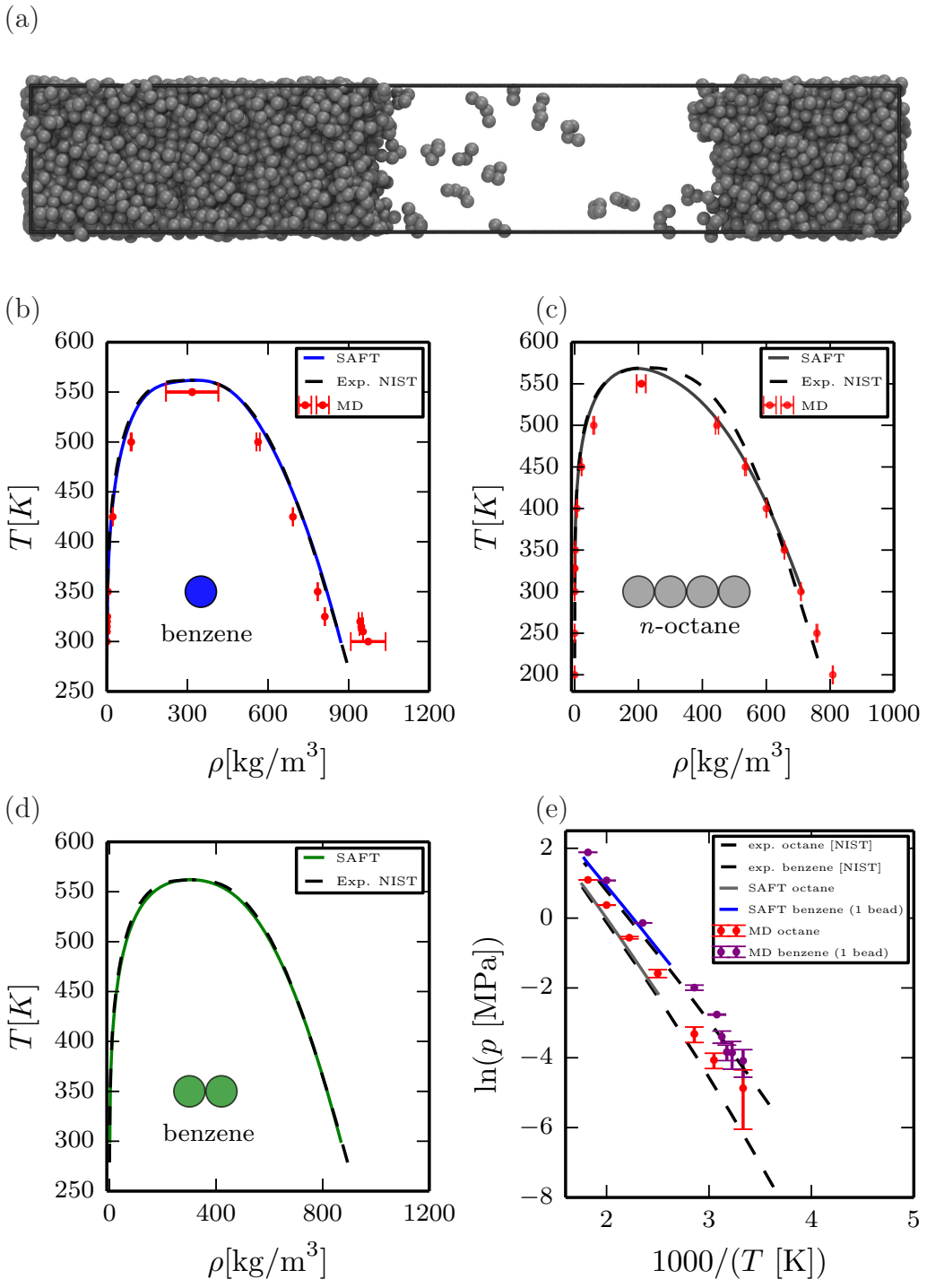

Figure 6.6: Pure-component vapour–liquid equilibra (VLE) of n-octane and benzene. (a) MD simulation snapshot of an octane system of 6k beads at 300 K (b,c,d) pure-component VLE compositions and (e) vapour pressures of octane and benzene are compared between experiment[207] (dotted lines and circles), SAFT-γ Mie EoS (continuous lines) and SAFT-γ Mie CG simulations (symbols with error bars). SAFT-γ Mie EoS results in (b–e) are obtained with our Maxwell construction algorithm.

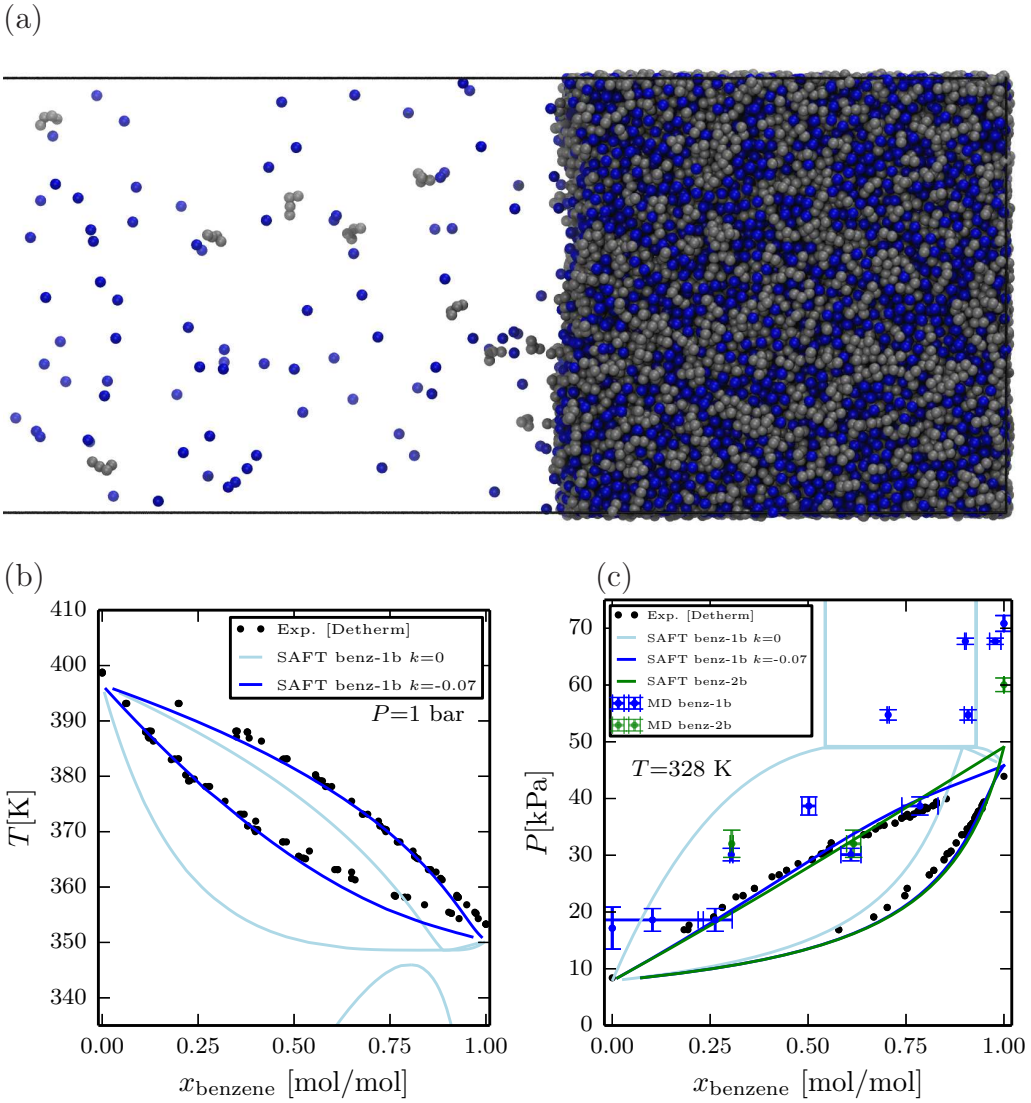

Figure 6.7: Vapour–liquid equilibra at (a,c) isothermal conditions of 328 K and (b) at isobaric conditions of 1 bar for a mixture of *n*-octane and benzene are compared between experiment[207] (dotted lines and circles), SAFT-γ Mie EoS (continous lines) and SAFT-γ Mie CG simulations (symbols with error bars). (b) VLE results at 1 bar are shown for the predicted unlike interaction k_{ij}=0 and for the improved unlike interaction k_{ij}=-0.07. (c) VLE results are shown for a benzene model made of one bead (benz-1b, k_{ij}=-0.07) and two beads (benz-2b, k_{ij}=0). Additional liquid–liquid immiscibility areas are found for benz-1b with k_{ij}=0 at 328 K and 1 bar. The HELD[195] algorithm together with our SAFT-γ Mie implementation was used to calculate the SAFT-γ Mie EoS VLE and LLE data. (a) MD snapshot of the SAFT-γ Mie CG simulation with 70% benzene at 328 K and a vapour pressure of roughly 55 kPa. The snapshot shows the liquid phase and part of the vapour phase. The whole box contains 65k beads.

in good agreement with experiment. The solvent mixture example in this section demonstrates how well SAFT-γ Mie calculations can be used to speed up the coarse graining of MD force fields for low molecular weight compounds. While a correction factor is needed for benzene modelled with a single bead, more predictive mixture results are obtained for benzene modelled with two beads.

6.5 Polystyrene/octane mixture

In this section we combine SAFT-γ Mie potentials to a heterogeneous CG model of a polymer solution in octane and test how well the liquid–liquid immiscibility and UCST are reproduced. The polystyrene model is branched and can therefore not be used in the SAFT-γ Mie EoS. Although model improvements with the help of the SAFT-γ Mie EoS are desirable, branched models are expected to represent chemical structures better than linear chains. It is therefore of high interest to see how well assembled heterogeneous branched polymer models perform in CG MD simulations as further improvements are more expensive if the predictions are not acceptable. The example system in this section is a mixture of polystyrene and octane, which shows UCST behaviour.

While several bottom-up coarse-grained models of polystyrene exist,[281,282] a SAFT-γ Mie CG model has only recently been published for a hexane and heptane solution by Jimenez *et al.*[259] The authors also used the CSP method for the pure-component Mie potentials. They adjusted two solvent/polymer interaction parameters based on MD simulations and were able to capture both LCST and UCST behaviour. Discussions with the author suggested many attempts were needed. In this section we are testing how well a model with little to no adjustments performs.

SAFT-γ Mie CG model

All Mie potentials used for the octane and polystyrene force fields were obtained with the CSP method,[156] see Tab. 6.1 for parameter values of benz-

1b and oct-4b. Polystyrene of $M_n = 1\,\mathrm{kg\,mol^{-1}}$ corresponds to 12 styrene monomers, which are build from the octane and benzene beads. The backbone is modelled with 12 octane beads (oct-4b) and the phenyl side chains with 12 benzene beads (benz-1b). See Fig. 6.8 for a SAFT-γ Mie CG model representation. Combining rules are applied to all benz-1b/oct-4b interactions.

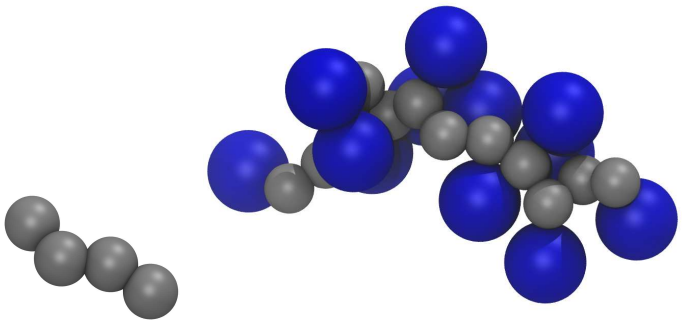

Figure 6.8: Coarse-grained models of octane (left) and polystyrene (right). Bead of the same colour are modelled with the same Mie potentials.

Methodology

Simulations were started from a phase separated state. Conformations were prepared by separately simulating pure-component boxes, which are then combined and run at the targeted conditions and interactions. A global composition of 35% by weight of polystyrene close to the experimental UCST[252] was set for all mixtures.

The pure-component phases were prepared by combining 2413 octane and 119 polystyrene chains separately in initial boxes at low density. The configurations were compressed at 500 bar with the Berendsen barostat and at 500 K with the velocity rescale method for 2 ns to give a condensed fluid. The systems were relaxed at 1 bar at otherwise unchanged conditions. The relaxed boxes were separately stacked $1 \times 2 \times 2$, a thin layer of vacuum added such that no chain crosses box boundaries and then joined from the shorter box side by translating one phase's coordinates and appending them to the

other phase's coordinate file. The mixture configuration comprises 50k beads in the form of two pure condensed phases separated and surrounded by a thin layer of vacuum.

The production run was performed in the NPT ensemble with the Nosé-Hoover thermostat controlling the target temperature and at 1 bar controlled by the Parrinello-Rahman barostat. The mixtures were run for at least 200 ns of which the last 20–50 ns were used to determine the phase compositions once the compositions converged.

The equations of motion were integrated with the leap-frog algorithm with a time step of 2 fs. Cut-off distances of 2 nm for interactions and neighbour lists were used.

Results

Using the adjusted unlike interaction parameter $k_{ij} = -0.07$, which gave the best representation of octane/benzene VLE, results in completely miscible polystyrene/octane mixtures at 200 K to 280 K where immiscibility is found experimentally.[252] Using combining rules for all unlike interactions an immiscibility area is predicted with UCST behaviour, see Fig. 6.8. While the temperature of the critical solution condition is higher than found experimentally, it is remarkable to capture the UCST in a similar temperature range. The UCST behaviour was confirmed by simulations at 360, 400, 450 and 500 K, which revealed miscibility. While the mixture at 360 K showed large density fluctuations, the fluctuations decrease in magnitude with larger temperatures. Also worth noting, the mixture composition of the critical solution condition appears to be similar to the experimentally observed composition. This mixture composition was shown in Chap. 5 to be very challenging to capture by SAFT-γ Mie EoS models.

The octane/benzene VLE was better described with $k_{ij} = -0.07$, while the polystyrene/octane LLE is better described with $k_{ij} = 0$. As both models use the same Mie potentials which were obtained for benzene and octane with the corresponding state principle, the conclusion has to be that the combined benzene and octane beads are not a perfect representation of the

chemistry of a polystyrene solution. In particular the influence of the connection between aliphatic backbone and aromatic residue on the chemistry of each individual group might not be captured by simply connecting a benzene and octane representation. In addition, 50% of the beads in the octane model are terminal groups, while the polystyrene is less influenced by chain ends. Our considerations are supported by the results of Jimenez *et al.*[259] who presented a successful model based on toluene and long alkane beads, whose unlike interaction was additionally adjusted with the help of MD simulations.

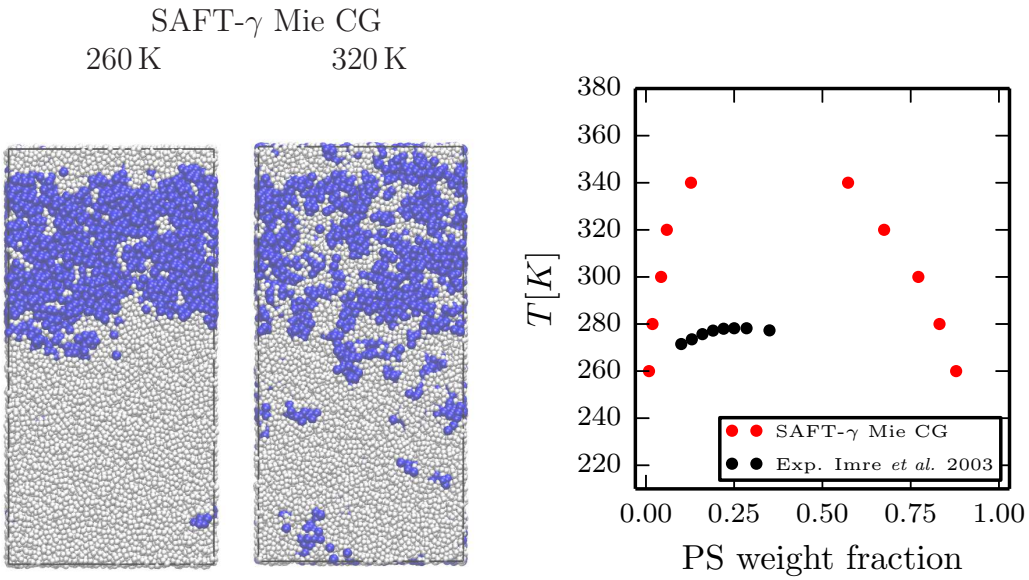

Figure 6.9: LLE predictions from SAFT-γ Mie CG simulations with a coarse-grained model of a mixture of polystyrene and octane. (left) MD snapshots at 260 K and 320 K. (right) LLE phase diagram comparing experimental results[252] with SAFT-γ Mie CG predictions.

Conclusion

A simple coarse-grained model based on SAFT-γ Mie potentials of benzene and octane was used to predict LLE. The model captured the UCST behaviour correctly and predicted a critical temperature within 100 K of the experimentally observed results. Although this deviation is unacceptable in practical experimental terms, it is remarkable to obtain this degree of agree-

ment with such a simple predictive SAFT-γ Mie CG model which is expected to only imperfectly capture the chemistry of the polystyrene chains. The example in this section also highlights the fact that more care is required for developing polymer models than for solvent models.

6.6 Surfaces of oligomer/polymer mixtures

This section describes the development of a SAFT-γ Mie CG model for an oligomer/polymer mixture. Oligomer/polymer surface concentration profiles are compared with experimental neutron reflectometry measurements. Surface properties in polymer systems are especially important for adhesive systems and at conditions where at least a part of the polymer mixture is above their glass transition temperature. The migration of the lower-molecular weight component can change the elasticity, tack, viscosity, smell, touch and visual appearance of the mixture. The larger the molecular weight and the smaller the viscosity of the components, the slower the migration process can be. The migration and all associated property changes can takes more than several months to finish.

The prediction of surface properties with the help of computational models could speed up the development and formulation of polymer mixtures if the slowly evolving properties can be simulated and calculated faster and cheaper than in experiments.

The coarse-grained MD model of polybutadiene and squalane in this section are the first SAFT-γ Mie CG polymer surface simulations we are aware of. The model successfully captures surface enrichments, wetting transition and bulk immiscibility of the oligomer/polymer model.

SAFT-γ Mie CG model

The chain length of the MD polymer model is chosen to be ten times longer than the oligomer chain (12 and 120 beads), see Fig. 6.10. The full experimental polymer weight of $M_{\mathrm{n}}^{\mathrm{PB}} = 133.3\,\mathrm{kg\,mol^{-1}}$ corresponds to a model of almost 5000 beads per chain and would lead to prohibitively long equilibra-

tion times and a prohibitively large simulation size. The Mie potential types are sq and PB-8%. See Tab. 5.7 for more details and parameter values.

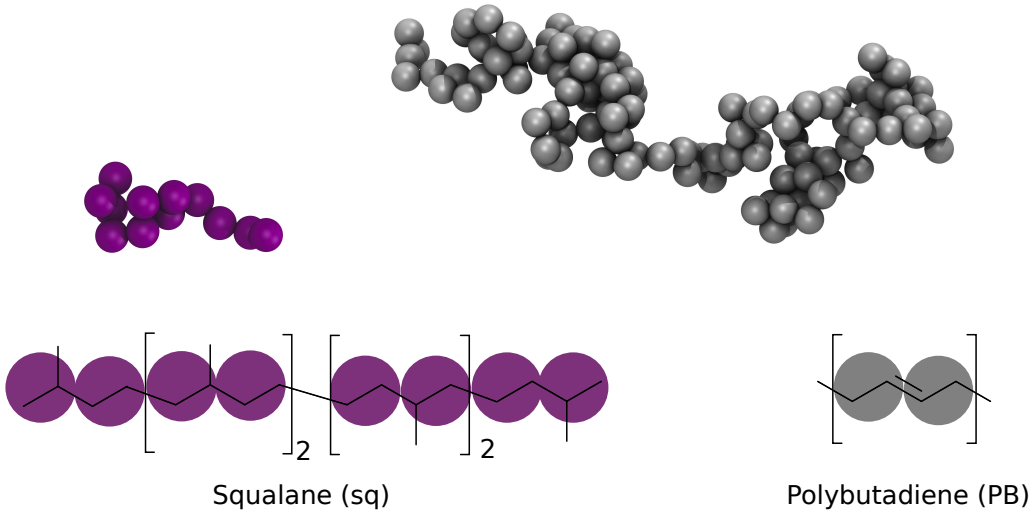

Figure 6.10: (top) SAFT-γ Mie CG models of squalane (left, palatinate) with 12 sq beads and polybutadiene (right, grey) with 120 PB-8% beads. (bottom) Mapping of SAFT-γ Mie beads PB-8% (grey) and sq (palatinate) to the chemical structure of squalane and polybutadiene. Two beads per repetitive unit are used and one Mie potential type per compound.

Methodology

The MD simulations can only model surfaces/interfaces in pairs, not just one surface. Periodic boundary conditions help reduce the number down to just two surfaces. We choose a longer dimension normal to the surface plain to stabilise the two surfaces. The two surfaces are equivalent and are therefore averaged during our analysis. The averaging requires a smart analysis which determines the surface position, chops the layer in half, inverts one of them and aligns the surfaces before averaging.

The production runs were performed at higher temperatures of 450 K to further speed up the migration process. Slightly reduced cut-off distances of 1.5 nm and a larger time step of 5 fs were used to reduce the computational costs per simulated time unit.

The methodology of MD simulations and density profile analysis is schematically visualised in Fig. 6.11. Randomly generated vapour mixture configurations of the target composition of 10% to 90% oligomer by weight were prepared. The initial box size ranged from 6372 (40%) to 7032 (10%) beads. The cubic box was compressed at 500 bar and 450 K for 1 ns and relaxed at 450 K and 1 bar for 1 ns using the Berendsen thermostat and Berendsen barostat in the NPT ensemble.

The equilibrated cubic box was stacked $1 \times 1 \times 4$ to give a system size of 25.5k–28.1k beads depending on the composition. A larger system size with 40% oligomer stacked $1 \times 2 \times 4$ with over 102k beads was analysed to study the influence of finite size effects. The full size equilibration/migration runs were carried out for at least 1.4 µs with the Nosé–Hoover thermostat in the NVT ensemble.

The equations of motion were solved using the leap-frog integrator with a time step of 5 fs applying the LINCS constraint algorithm on all bonds. Cut-off distances of 1.5 nm for interactions and neighbour lists were used. If not stated otherwise simulations were carried out at a temperature of 450 K using the Nosé–Hoover thermostat.

Density profiles were obtained with the GROMACS tools, which were further aligned and normalised in a subsequent python script.

Results

Oligomer surface concentration profiles are calculated for oligomer/polymer films as a function of unlike interaction and as a function of global mixture composition.

Interaction strength

The oligomer/polymer unlike interaction is systematically varied to simulate oligomer/polymer mixtures of different chemistry and test which surface phenomena are captured by the SAFT-γ Mie CG model. The oligomer surface profiles in Fig. 6.12 show different degrees of oligomer surface enrichment. Models with favourable unlike interactions ($k_{ij} = -0.01$) show a small surface

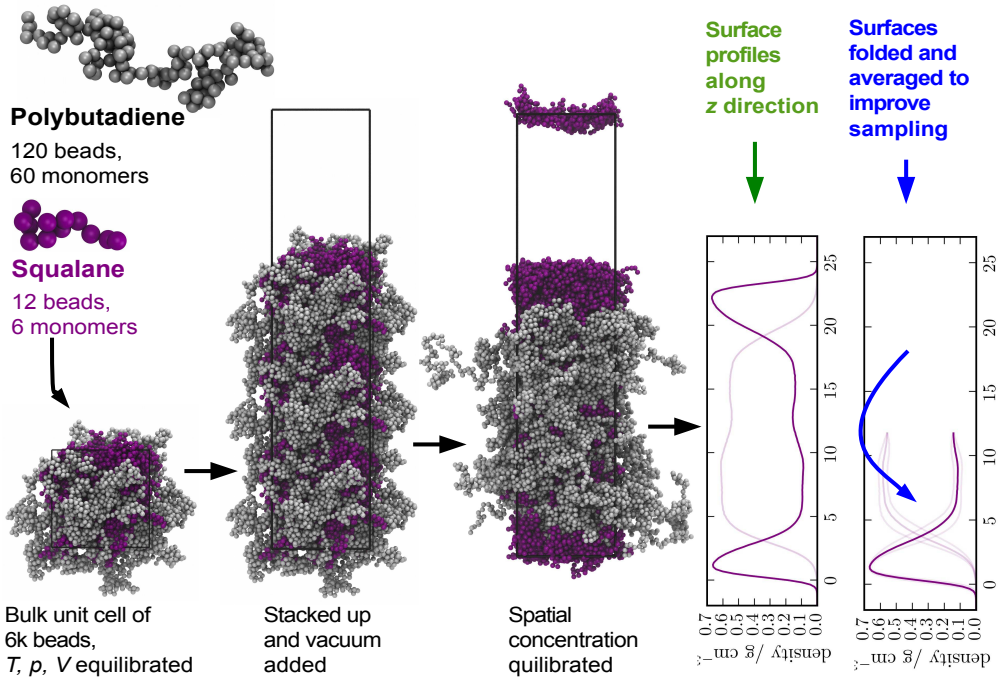

Figure 6.11: Process for generating surface density profiles of polymer mixtures. A polybutadiene coarse-grained model (grey) and a squalane model (palatinate) comprised of 12 beads were multiplied and equilibrated in a microcanonical (NPT) simulation in a box of 6k-7k beads. The equilibrated unit was stacked up four times and two surfaces created by adding vacuum. The process was carried out for different concentrations and interaction strengths. The last part of the simulation was analysed by averaging the density across the x, y plane. As both surfaces are equivalent, they were combined and averaged.

enrichment, and models with less favourable unlike interactions ($k_{ij} = 0.005$) show a larger surface enrichment which corresponds to an almost continuous monolayer of oligomers on the surface. Models with even less favourable unlike interactions ($k_{ij} > 0.005$) show bulk phase separation, which results in the formation of layers in the bulk facilitated by the periodic boundaries and the limited box size. Results with bulk layering are not shown as they are metastable conformations which are challenging to equilibrate in MD simulations. The less favourable the unlike interactions, the more metastable bulk layers appear.

Larger box sizes with 102k beads (instead of 25k) allow the study of less favourable systems as droplets are formed instead of layers. The diffusion of an oligomer droplet from the bulk to the surface was observed in Fig. 6.13, which merged with the surface and resulted in a thick oligomer surface layer. While the droplet was formed within 80 ns when started from a homogeneous mixture, the droplet slowly reduced in size over 700 ns due to migration of individual oligomer chains, before it merged with the surface. A process which took 100 ns to complete. The thick oligomer surface layer is referred to as wetting layer. The wetting layer is a continuous surface layer thicker than one molecule.

Almost identical surface concentration profiles are obtained in Fig. 6.13d for $k_{ij} = -0.01$ and $k_{ij} = 0$ for the 25k and 102k bead systems, whose surface area differs by a factor of four. The agreement suggests that the surface areas of the 25k bead systems are large enough for studying oligomer surface enrichment and negligible finite-size effects are present.

Oligomer concentration

Sets of different global mixture composition are modelled for two different unlike interaction strength, i.e. $k_{ij} = -0.01$ and $k_{ij} = 0$. While the mixtures with $k_{ij} = -0.01$ are miscible at all concentrations they show small oligomer surface enrichment in Fig. 6.14a thinner than a wetting layer. Mixtures with $k_{ij} = 0$ show surface enrichment at low oligomer compositions and wetting layers at high compositions. The wetting transition occurs between 40% and

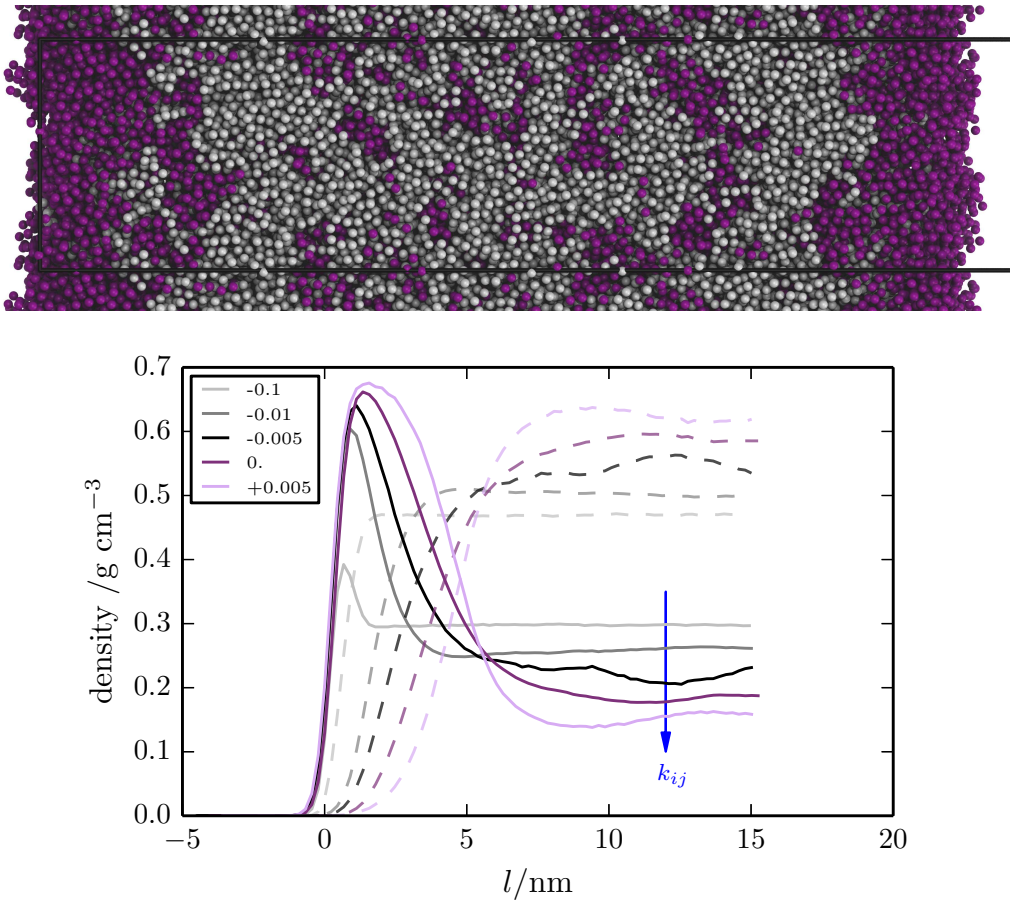

Figure 6.12: (top) Coarse-grained MD snapshot of the squalane/polybutadiene mixture with 40% oligomer by weight after 1.5 µs with $k_{ij} = 0$ showing oligomer surface enrichment. Oligomer beads are coloured palatinate, polymer beads are grey. (bottom) Density profiles for several unlike interaction strengths k_{ij}. k_{ij} values are given in the legend. Oligomer (continuous lines) and polymer (dashed line) density profiles are obtained from SAFT-γ Mie CG simulations. All mixtures have 40% oligomer by weight.

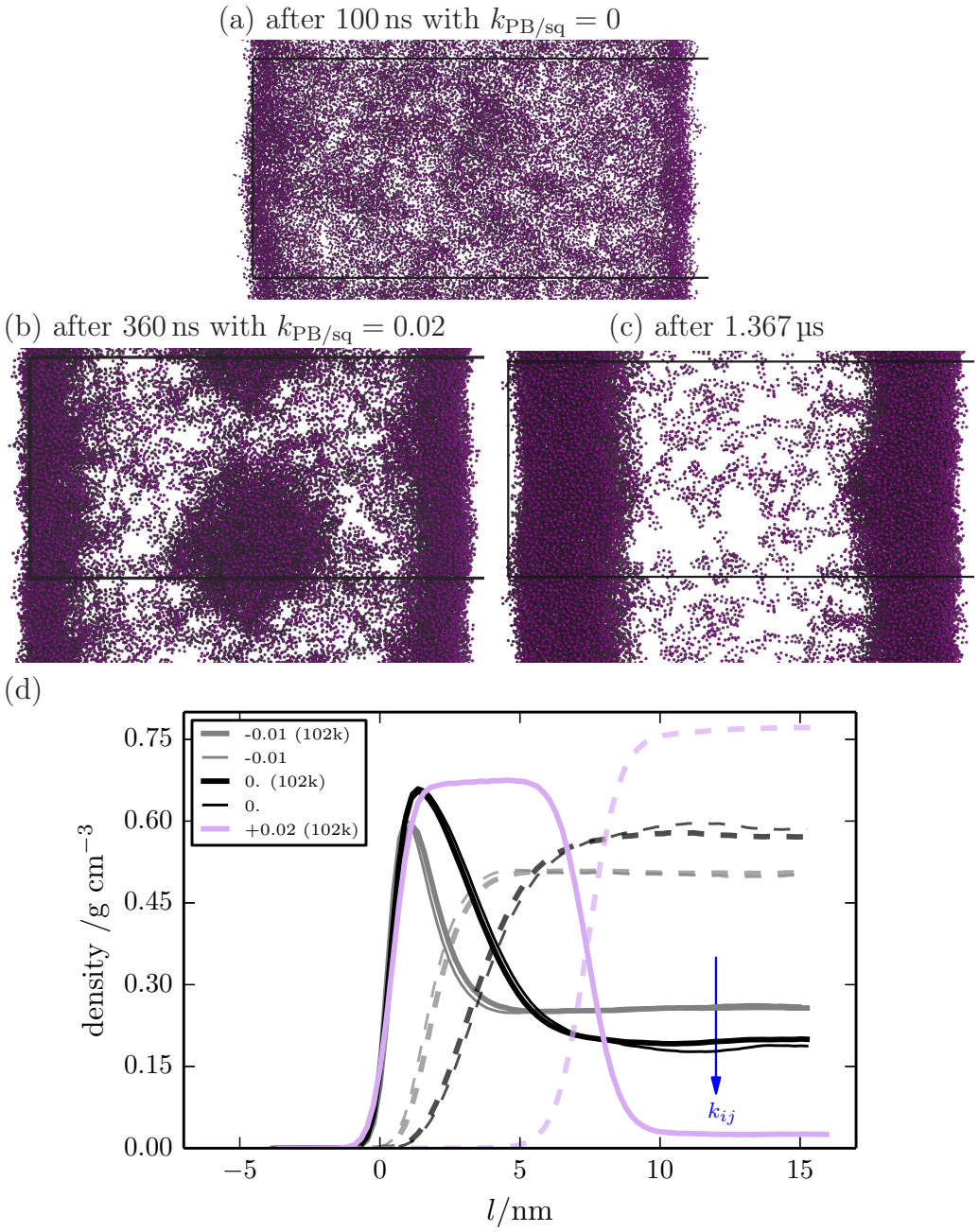

Figure 6.13: Larger oligomer/polymer simulations with 102k beads at 40% oligomer by weight. (a) Miscible condition with $k_{PB/sq} = 0$ show surface enrichment of the oligomer and (b) immiscible conditions with $k_{ij} = 0.02$ started from a mixed phase first forms a droplet of squalane in the bulk within less than 100 ns, (c) but takes approximately 900 ns before the droplet has completely merged with the (left) surface layer. (d) Density surface profiles for oligomer and polymer mixtures for $k_{ij} = -0.01$, 0 and 0.02. Profiles for $k_{ij} = -0.01$ and 0 are also shown for the smaller simulations sizes of 25k beads (cf. Fig. 6.12). The profiles $k_{ij} = 0.02$ were not obtained from averaging both surfaces, but only one surface (left in (b,c)) as the droplet caused the surfaces to be asymmetric.

60% oligomer, see Fig. 6.14.

The oligomer concentration profiles are compared in Fig. 6.14c with experimental profiles of a mixture of deuterated squalane and polybutadiene measured with neutron reflectometry.[273] Good agreement is found between experiment and simulation. The simulations capture surface enrichment, wetting transitions and wetting layers. While the agreement is not quantitative, the steepness of the profiles are matched at several conditions. It is important to emphasize that the length scales of the simulation results were not adjusted. The agreement is remarkable when considering that the model parameters are only based on liquid densities and the unlike interaction predicted with combining rules. The predictive power of the combining rule might also be influenced by fortunate values picked for the polymer chain length and temperature of 450 K which were deviated from experimental conditions to facilitate the CG MD simulations. More favourable interactions with correction factors $k_{ij} < 0$ are expected for simulations at experimental conditions.

The migration of oligomer chains is significantly faster than the migration of the polymer chains. Conditions which require the migration of the polymer chains to reach equilibrium conditions take longer than 1 µs (eg. 80% at $k_{ij} = 0$ in Fig 6.14b). Conditions, which only require the oligomer to migrate (miscible conditions, with only surface enrichment), equilibrate within a couple of 100 ns.

Conclusion

SAFT-γ Mie CG simulations of oligomer/polymer surfaces were presented, which are—to the best of our knowledge—the first of their kind. Small oligomer surface enrichment was found for small oligomer bulk concentrations or favourable oligomer/polymer interactions (small k_{ij}). Wetting layers were found for high oligomer bulk concentrations and unfavourable oligomer/-polymer interactions (high k_{ij}). Good agreement with experimental squalane surface concentration profiles is seen. The agreement is in particular remarkable due to the simplicity of the model and the agreement of the length scales.

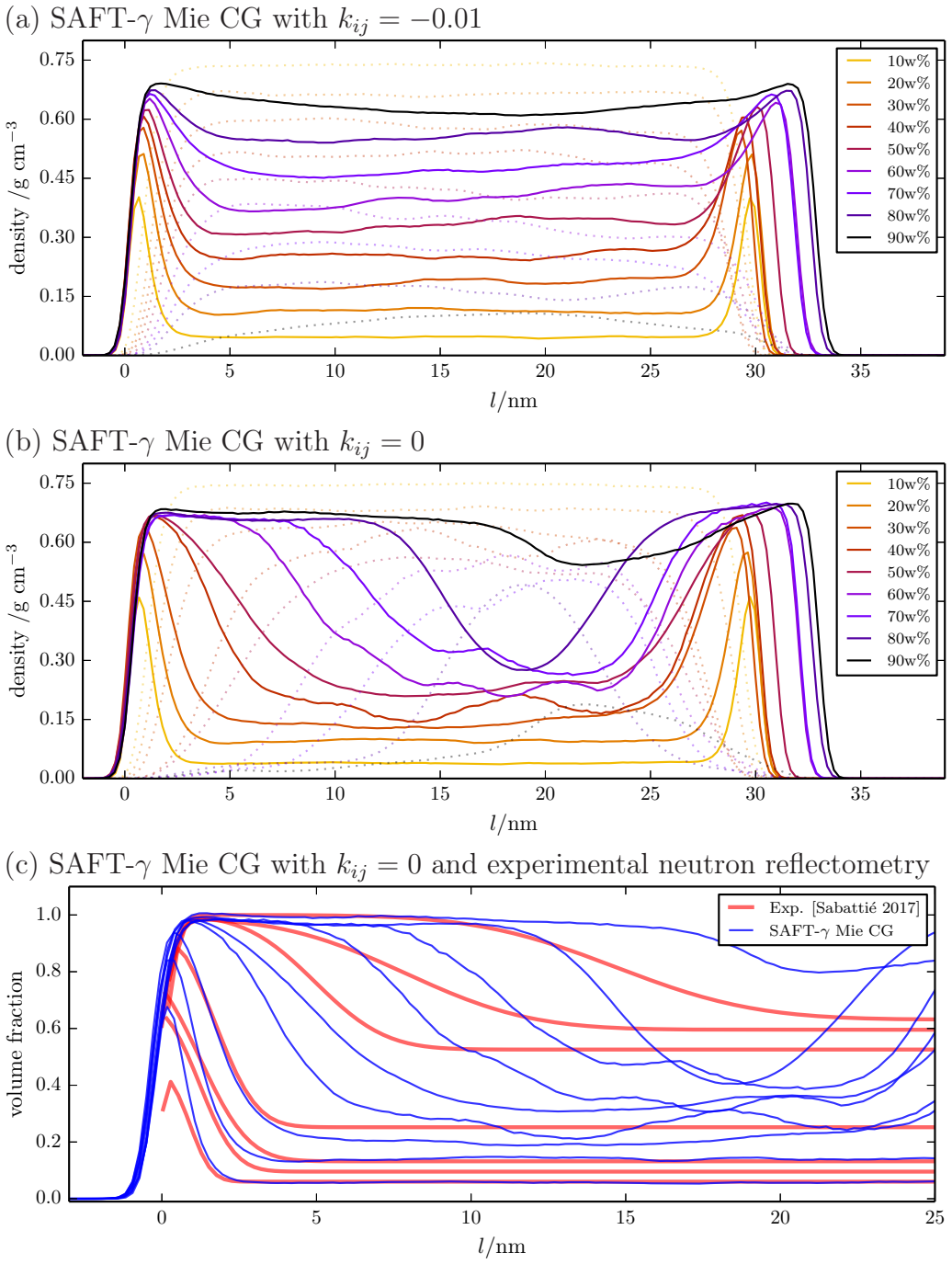

Figure 6.14: Oligomer (continuous lines) and polymer (dotted lines) density profiles in a thin oligomer/polymer film as a function of global oligomer concentration. (a) SAFT-γ Mie CG results for $k_{ij} = -0.01$ and (b) SAFT-γ Mie CG results for $k_{ij} = 0$. (c) Squalane surface concentration profiles obtained from neutron reflectometry[273] (bold red lines) are compared with SAFT-γ Mie CG results (thin blue lines) with $k_{ij} = 0$. All profiles were shifted to align for the left surface. Overall SAFT-γ Mie CG film thickness varies due to differences in composition and total number of beads. Experimental film thicknesses are significantly larger than in the MD simulations.

The presented SAFT-γ Mie CG simulations successfully capture surface enrichment, a wetting transition and wetting layers within a single model.

6.7 Polymer/polymer mixtures

This section describes the development of a SAFT-γ Mie CG model for a polymer/polymer mixture. We successfully show models with miscible and immiscible equilibrium states. We also demonstrate that models close to the phase boundary and close to the critical solution condition are challenging to simulate even for polymer models with relatively short chain lengths.

SAFT-γ Mie CG model

We have chosen to build the polymer mixture model based on polyisoprene and polystyrene data as their mixtures already show immiscible conditions at relatively low molecular weights.[241] Both polymer models were developed with large sets of polymer-melt densities, as presented in Chap. 5.4.2. The Mie potential types are referred to as PI-8% and PS-0.8k. Parameter values and more details can be found in Tab. 5.7. For simplicity we have chosen symmetric models with chain lengths of 25 and 40 beads per chain. The models map 2 beads per isoprene and styrene unit. No angle or dihedral potentials were applied.

Methodology

Randomly generated vapour mixture configurations of a 50/50 mixture by weight of polyisoprene chains and polystyrene chains were prepared. The initial box sizes contained 6300 (25 bead chains) and 6720 (40 bead chains) beads. The cubic boxes were compressed at 500 bar and 450 K for 1 ns and relaxed at 450 K and 1 bar for 1 ns using the Berendsen thermostat and Berendsen barostat in the NPT ensemble.

The equilibrated cubic box was stacked $1 \times 1 \times 3$, $1 \times 2 \times 4$ and $2 \times 3 \times 4$ to give system sizes of 20k, 54k and 161k beads, respectively. The full size

equilibration/migration runs were carried out with the Nosé–Hoover thermostat at 450 K and the Parrinello–Rahman barostat at 1 bar. The equations of motion were solved using the leap-frog integrator with a time step of 5 fs applying the LINCS constraint algorithm on all bonds. Cut-off distances of 2 nm for interactions and neighbour lists were used.

Results

The mixture of chains with 25 beads is predicted to be partially miscible (10-20%w solubility limit) by the SAFT-γ Mie EoS using combining rules for the unlike interactions ($k_{ij} = 0$). In the SAFT-γ Mie CG simulations with the same model, a single homogeneous phase is observed. Changing the unlike interactions to describe less favourable polymer/polymer interactions leads to partial miscibility with $k_{ij} = 0.01$ and complete immiscibility with $k_{ij} = 0.1$, see Fib. 6.15.

The mixture of chains with 40 beads is predicted to be completely immiscible (< 3%w solubility limit) by the SAFT-γ Mie EoS with $k_{ij} = 0$. However, only a single homogeneous phase is observed in SAFT-γ Mie CG simulations, see Fig. 6.16. Also running larger simulations with up to 161k beads does not reveal two stable phases. While snapshots, as in Fig. 6.16, hint at immiscibility, they do not show phase separation, but the peak of large density fluctuations. The wave length of the fluctuations increases with the simulation size. The density fluctuations indicate conditions close to the critical conditions. As for the 25-bead-mixture, readjusted unlike interactions within MD simulations are necessary to reproduce both qualitative compatibility and quantitative solubility limits found with the SAFT-γ Mie EoS.

Conclusion

The simulations in this section demonstrate some of the challenges faced with SAFT-γ Mie CG models for polymer/polymer mixtures. At least k_{ij} needs to be rescaled for a successful transfer of a SAFT-γ Mie EoS to a SAFT-γ Mie CG model to obtain similar solubility predictions. The rescaling requires it-

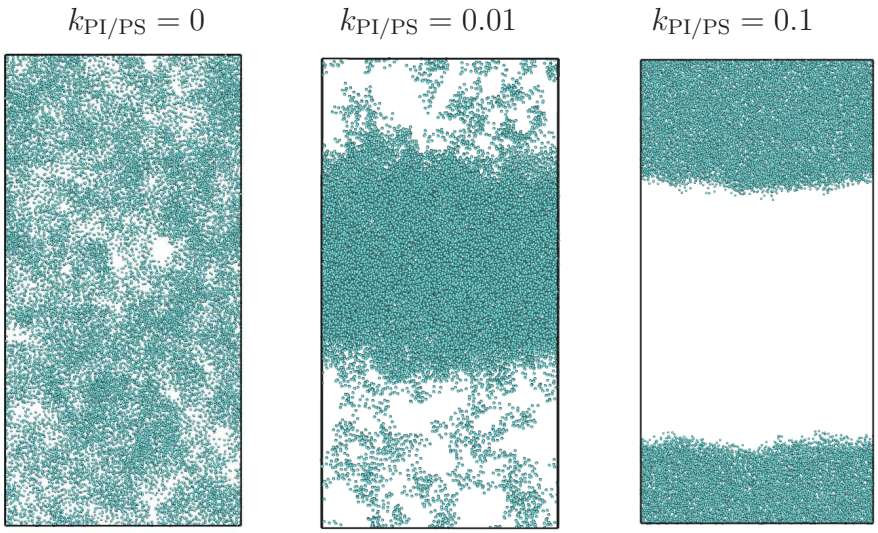

Figure 6.15: Symmetric mixtures of polyisoprene and polystyrene with 25 beads per chain with 50k beads in total. Only polyisoprene beads are shown. The simulations box's third dimension is as long as the shorter of the other two. Unlike interaction parameter were set to (left) $k_{\mathrm{PI/PS}} = 0$, (middle) $k_{\mathrm{PI/PS}} = 0.01$ and (right) $k_{\mathrm{PI/PS}} = 0.1$; snapshots were taken after 425 ns, 260 ns and 25 ns, respectively.

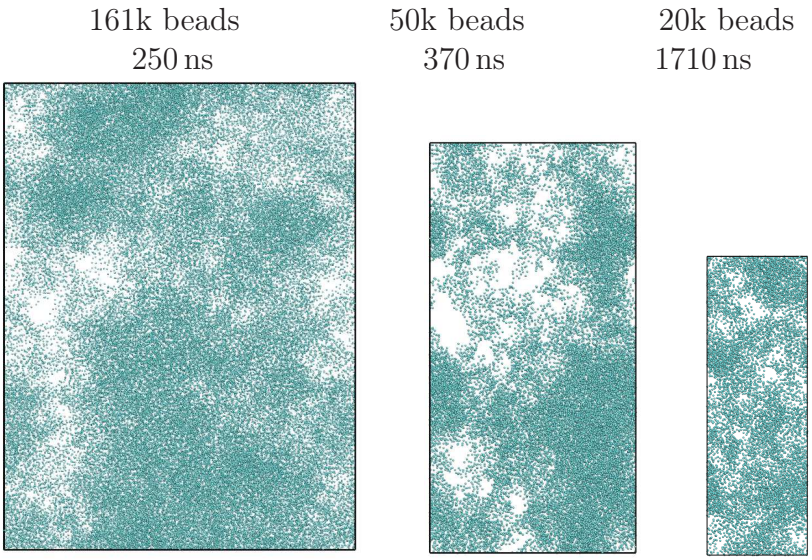

Figure 6.16: Symmetric mixture of polyisoprene and polystyrene with 40 beads per chain with unlike interactions obtained from combining rules only $k_{\mathrm{PI/PS}} = 0$. Only polyisoprene beads are shown. The size of the simulation is changed to compare visibility of density fluctuations and possible phase boundaries. Although large density differences can be seen, they are strongly fluctuating such that pair correlation functions do not allow differentiation of compatible and (partially) incompatible conditions. Boxes comprise 161k, 54k and 20k beads from left to right.

erative MD simulations. Polymer/polymer simulations are expensive due to the slow equilibration, poor sampling and the need for large simulation sizes. Phase transition and conditions close to the critical solution temperature, which are of special interest experimentally, are especially challenging. Further coarse graining within MD simulations, or other methods such as DPD simulations could help speed up simulations of polymer/polymer mixtures.

The degree of coarse graining was chosen to best reproduce polymer-melt densities both as a function of temperature and pressure (thermal expansion and compressibility) for the best thermodynamic representation and transferability. With SAFT-γ Mie this choice allows lumping together 2–5 heavy atoms per bead, which significantly reduces the number of beads compared to united-atom force fields (1 bead per heavy atom). A stronger coarse graining with fewer beads would result in Mie potentials which reproduce pure-component data less well, but would allow further speed up.

A method with a coarser description and faster diffusion is Dissipative Particle Dynamics (DPD). A coarser and softer DPD model could be parametrised based on fitting to initial SAFT-γ Mie potentials. For example see bottom-up coarse-grained DPD models of n-pentane.[283,284] DPD simulations are faster because the potential at the bead cores are finite, which allows beads and chains to overlap and penetrate each over, and therefore allows chains to cross. In MD simulations with infinite potential values at the bead cores, overlap and chain crosses are negligible. DPD and MD-DPD are promising methods for simulating more challenging polymer/polymer mixtures.

6.8 Angles and dihedrals for SAFT-γ Mie CG force fields

The SAFT-γ Mie EoS 2013[14,16] does not include restrictions on angles and dihedrals. Bonded potentials such as angle and dihedral potentials for MD force fields can therefore not be developed with the SAFT-γ Mie EoS alone. This limitation is based on the fact that only the first-order term of Wertheim's

thermodynamic perturbation theory (Wertheim's TPT1) is included. Future versions of SAFT might include 3-body and 4-body interactions which allow for restricted angles and dihedrals. However, a derivation of the corresponding equations, and a simplified version which can be added to the existing SAFT equations, has so far not been achieved due to the complex nature of the equations that arise.

Angle and dihedral potentials for SAFT-γ Mie CG models are of interest to improve upon the predicted structural properties. For polymers, certainly angle potentials and possibly dihedral potentials should be added. The potentials are effectively changing the chain flexibility and are therefore expected to improve the description of the radius of gyration, which quantifies the chain's state between completely stretched and completely collapsed. The radius of gyration influences both bulk miscibility as well as surface layers.

With increasing chain length of SAFT-γ Mie models, i.e. a larger deviation from the spherical shape, the importance of intramolecular interactions such as angle potentials increases. So far, without a direct link between angle potentials and the SAFT-γ Mie EoS, mainly two approaches are used to account for the missing intramolecular restrictions.

Firstly, the nonbonding Mie potential parameters are rescaled to best reproduce the properties in MD simulations, effectively accouting for *all* differences between the SAFT-γ Mie EoS and MD simulations. Rescaled Mie potentials were shown to perform excellently for the VLE properties of benzene[114] and alkanes.[115] Also in this chapter, the pointed-out improvements for mixture properties by adjusting k_{ij} correspond to the same approach.

Secondly, additional angle and dihedral potentials, which were independently obtained from other methods, are added to the SAFT-γ Mie CG models. The potential can for example be generated with MD simulations with other (higher-resolution) force fields. The potentials are obtained by analysing and Boltzmann inverting the angle distributions for the target mapping. Similarly obtained angles were successfully added to SAFT-γ Mie CG models.[154,208] In this work, we have applied angle and dihedral potentials obtained from TraPPE-UA[285,286] single molecule reference stochastic

dynamic simulations. We found no significant influence on the VLE properties at 300 K for the *n*-octane model in Sec. 6.4, which is supported by simulations on Lennard–Jones chains[287] and references therein. However, for the mixture of PS and octane* in Sec. 6.5 the added angle and dihedral potentials led to the freezing and vitrification of polystyrene and octane at 300–350 K. This occurs approximately 100 K higher than the experimental melting temperature of octane. The drastically reduced diffusion led to inaccessible equilibrium states. Reduced diffusion coefficients were also found in other polymer MD simulation studies.[288]

Angles and dihedral potentials are crucially important for liquid crystals. In liquid crystals, the structural flexibility, rigidity and shape influences the orientation and stacking properties of molecules. In additional work (not part of this thesis)[107] we have developed a successful SAFT-γ Mie CG model with additional angle and dihedral potentials for a chromonic liquid crystal whose stacking behaviour crucially depends on the rigidity of the molecule's core.

6.9 Summary and Conclusions

In this chapter, SAFT-γ Mie CG models are presented for solvent mixtures, polymer melts, polymer solutions, oligomer/polymer surfaces and polymer/polymer mixtures. Deviations between the results obtained from SAFT-γ Mie EoS calculations and SAFT-γ Mie CG simulations seem to increase with molecular weight. Larger deviations are found for miscibility predictions than for melt densities. While further SAFT-γ Mie CG model adjustments within MD simulations are required for matching solubilities such as LLE, excellent agreement was found for melt densities and surface profiles with little or no readjusting.

Compatibilities at conditions close to phase transitions or critical solution conditions are especially challenging to simulate in MD simulations. Coarser methods such as DPD simulations could be reparametrised based on Mie

*Boltzmann inversion was performed with the VOTCA package[104,105] on stochastic dynamic simulation trajectories of single molecules of *n*-octane and PS in vacuum.

potentials. Chemical potentials are a target property which can easily be simulated in DPD simulations via particle insertion. DPD interactions would be tuned to reproduce the chemical potentials obtained from SAFT models. Due to a coarser and more abstract representation, the DPD simulations are significantly faster than MD simulations and could be a promising avenue for developing polymer/polymer models for solubilities and phase separation.

The simulations in this chapter confirm the types of properties SAFT methods and MD simulations are best at. SAFT EoS are best at phase equilibria, phase separation and other macroscopic equilibrium properties, but can not be used for structural, non-equilibrium and other heterogeneous properties without the help of additional methods and theories (see Chap. 3.7). In contrast, MD simulations are limited in describing phase separation and macroscopic properties, but are an excellent method for surfaces and "structured fluids". Within MD excellent coarse-grained polymer models have been developed for polymer types discussed in this chapter, which are long alkanes[48,99,110,289,290] PI,[93,281,291–293] PB[294] and PS.[34,96,97,281,295–298]

Chapter 7

Conclusion and future work

In this thesis, theory, simulations and experiments were used to study the solubility and partitioning of polymer systems. Oligomers and polymers show complex behaviours such as coils and entanglements, and have, hence, been challenging systems to model computationally. The impact of enthalpic contributions to phase equilibria becomes more important, the larger the molecular weight. Small chemical and structural differences between typical hydrocarbon polymer types already drastically influences the miscibility and partitioning behaviour. Polymer systems also remain challenging to characterise experimentally, as for example, low viscosities and slow diffusion processes lead to property changes of mixtures even after several days or weeks. The aim of this work was to analyse the predictive capabilities of the SAFT-γ Mie theory and MD simulations to determine the solubility and partitioning in polymer systems, potentially faster than via experimental measurements.

In Chap. 4, one of the most sophisticated SAFT versions, SAFT-γ Mie[16] EoS, was implemented into a stand-alone program. Special care was taken with comparisons with the data of the authors of the original publications presented to ensure the highest precision and accuracy for the basic Helmholtz energies obtained from the SAFT-γ Mie theory. Simple numerical derivatives were added and dedicated numerical optimisation algorithms and solver developed to give access to thermodynamic properties such as pressure, chemical potential and phase equilibria. Most relevant to the later applications,

a multicomponent, multiphase equilibrium solver (HammR) was developed for the calculation of polymer phase equilibria. Also an optimisation routine for estimating new pure-component SAFT-γ Mie model parameters was developed and extensively applied in later chapters.

Potential future work extending the efforts of Chap. 4 would be an optimisation routine for the automated estimation of binary interaction parameters. The HammR routine, which is so far limited to liquid phases, could be extended to vapour phases, to allow the calculation of VLE and VLLE properties, which would allow the description of polymer solutions of higher vapour pressure.

In Chap. 5, polymer models within the SAFT-γ Mie EoS were studied. The SAFT-γ Mie group-contribution parameter set[184] originally developed for low-molecular weight compounds was tested on polymer miscibilities and partition coefficients. As only trends and not quantitative miscibility results were matched with experimental findings, we developed new dedicated SAFT-γ Mie polymer models. A semi-comprehensive overview of experimental thermodynamic data of hydrocarbon polymers and their mixtures was compiled. A large range of SAFT-γ Mie models was developed for polymer melts and polymer blends, even including a ternary mixture. Excellent agreement was achieved for reproducing polymer-melt densities, very good agreement was found for reproducing polymer cloud-point curves, and good agreement was found for predicting cloud-point curves and other thermodynamic properties for new molecular weights and new conditions. A systematic deviation in reproducing and predicting cloud-point curves was observed which seems to be connected to the molecular weight of the model and also, does not appear to be influenced by any of the other Mie potential parameters.

Potential future work extending the efforts of Chap. 5 would be developing SAFT-γ Mie EoS models with parameters as a function of molecular weight, similar to the models developed in Refs 80,127. Synthesising and characterising a set polymers of different molecular weight but of the same polymer type, would be hugely beneficial. The systematic deviation found for cloud-point curves, which is connected to the molecular weight, could be

further analysed by testing if a universal scaling factor for the SAFT chain length can systematically improve cloud-point predictions. A physical representation of this scaling factor could be the compensation for the unphysically extended chain conformation in the SAFT theory (TPT1 versions). A scaling factor could effectively capture the coiling of polymer chains found experimentally. The idea is similar to the effect of the shape factor in SAFT-γ Mie. The shape factor, however, was not enough to mitigate the deviations found for the polymers in this work.

In Chap. 6, coarse-grained force fields based on SAFT-γ Mie EoS models were studied in molecular dynamics simulations. Excellent agreement was found for the direct translation of Mie potentials to CG force fields for modelling properties of low-molecular weight compounds and densities of polymer melts. Only a single unlike interaction parameter required adjustment within MD simulations to obtain excellent SAFT-γ Mie CG force fields. The complementary power of SAFT and molecular simulation was demonstrated by modelling surfaces of an oligomer/polymer system. First, pure-component parameters were optimised within the SAFT-γ Mie EoS. Second, simple model adjustments were made within MD to reduce the computational demand. The SAFT-γ Mie CG model reproduced experimental partial-density surface profiles as a function of blend composition without the need to rescale length scales. Oligomer surface enrichment, wetting transition and wetting layers were correctly predicted with a single model.

Potential future work extending the efforts of Chap. 6 would be to employ mesoscale DPD simulations for modelling polymer phase equilibria in the bulk of larger molecular weight. DPD models could be parametrised to reproduce chemical potentials obtained from the SAFT-γ Mie EoS. The larger time and length scales, which can be modelled in DPD models, would allow researchers to study more complex heterogeneous phase equilibria and structural properties.

Bibliography

[1] F. Vilaplana and S. Karlsson, Quality Concepts for the Improved Use of Recycled Polymeric Materials: A Review, *Macromolecular Materials and Engineering*, 2008, **293**, 274–297, DOI: 10.1002/mame.200700393.

[2] R. G. Adams, R. Lohmann, L. A. Fernandez and J. K. MacFarlane, Polyethylene Devices: Passive Samplers for Measuring Dissolved Hydrophobic Organic Compounds in Aquatic Environments, *Environmental Science & Technology*, 2007, **41**, 1317–1323, DOI: 10.1021/es0621593.

[3] C. M. Hansen, *Hansen Solubility Parameters: A User's Handbook*, CRC Press, Boca Raton, 2nd edn., 2007.

[4] R. H. DeVane, M. S. Wagner and B. P. Murch, in *Materials Research for Manufacturing*, ed. L. D. Madsen and E. B. Svedberg, Springer International Publishing, Cham, 2016, vol. 224, pp. 303–328.

[5] A. Eslamimanesh and F. Esmaeilzadeh, Estimation of Solubility Parameter by the Modified ER Equation of State, *Fluid Phase Equilibria*, 2010, **291**, 141–150, DOI: 10.1016/j.fluid.2009.12.031.

[6] C. Avendaño, T. Lafitte, A. Galindo, C. S. Adjiman, G. Jackson and E. A. Müller, SAFT-γ Force Field for the Simulation of Molecular Fluids. 1. A Single-Site Coarse Grained Model of Carbon Dioxide, *The Journal of Physical Chemistry B*, 2011, **115**, 11154–11169, DOI: 10.1021/jp204908d.

[7] M. Michelsen and J. Mollerup, *Thermodynamic Models: Fundamentals & Computational Aspects*, Tie-Line Publications, www.tie-tech.net, 2007, (accessed 06/2014).

[8] J. M. Prausnitz, R. N. Lichtenthaler and E. G. de Azevedo, *Molecular Thermodynamics of Fluid-Phase Equilibria*, Prentice Hall PTR, Upper Saddle River, N.J, 3rd edn., 1999.

[9] K. G. Joback and R. C. Reid, Estimation of Pure-Component Properties from Group-Contributions, *Chemical Engineering Communications*, 1987, **57**, 233–243, DOI: 10.1080/00986448708960487.

[10] L. Coniglio and J. L. Daridon, A Group Contribution Method for Estimating Ideal Gas Heat Capacities of Hydrocarbons, *Fluid Phase Equilibria*, 1997, **139**, 15–35, DOI: 10.1016/S0378-3812(97)00143-X.

[11] D. S. Abrams and J. M. Prausnitz, Statistical Thermodynamics of Liquid Mixtures: A New Expression for the Excess Gibbs Energy of Partly or Completely Miscible Systems, *AIChE Journal*, 1975, **21**, 116–128, DOI: 10.1002/aic.690210115.

[12] A. Fredenslund, R. L. Jones and J. M. Prausnitz, Group-contribution estimation of activity coefficients in nonideal liquid mixtures, *AIChE Journal*, 1975, **21**, 1086–1099, DOI: 10.1002/aic.690210607.

[13] T. Lafitte, D. Bessieres, M. M. Piñeiro and J.-L. Daridon, Simultaneous Estimation of Phase Behavior and Second-Derivative Properties Using the Statistical Associating Fluid Theory with Variable Range Approach, *The Journal of Chemical Physics*, 2006, **124**, 024509, DOI: 10.1063/1.2140276.

[14] T. Lafitte, A. Apostolakou, C. Avendaño, A. Galindo, C. S. Adjiman, E. A. Müller and G. Jackson, Accurate Statistical Associating Fluid Theory for Chain Molecules Formed from Mie Segments, *The Journal of Chemical Physics*, 2013, **139**, 154504, DOI: 10.1063/1.4819786.

[15] A. Lymperiadis, C. S. Adjiman, A. Galindo and G. Jackson, A Group Contribution Method for Associating Chain Molecules Based on the Statistical Associating Fluid Theory (SAFT-γ), *The Journal of Chemical Physics*, 2007, **127**, 234903, DOI: 10.1063/1.2813894.

[16] V. Papaioannou, T. Lafitte, C. Avendaño, C. S. Adjiman, G. Jackson, E. A. Müller and A. Galindo, Group Contribution Methodology Based on the Statistical Associating Fluid Theory for Heteronuclear Molecules Formed from Mie Segments, *The Journal of Chemical Physics*, 2014, **140**, 054107, DOI: 10.1063/1.4851455.

[17] G. M. Wilson, Vapor-Liquid Equilibrium. XI. A New Expression for the Excess Free Energy of Mixing, *Journal of the American Chemical Society*, 1964, **86**, 127–130, DOI: 10.1021/ja01056a002.

[18] A. Klamt, Conductor-like Screening Model for Real Solvents: A New Approach to the Quantitative Calculation of Solvation Phenomena, *The Journal of Physical Chemistry*, 1995, **99**, 2224–2235, DOI: 10.1021/j100007a062.

[19] M. Hornig and A. Klamt, COSMOfrag : A Novel Tool for High-Throughput ADME Property Prediction and Similarity Screening Based on Quantum Chemistry, *Journal of Chemical Information and Modeling*, 2005, **45**, 1169–1177, DOI: 10.1021/ci0501948.

[20] J. H. Hildebrand, A Critique of the Theory of Solubility of Non-Electrolytes., *Chemical Reviews*, 1949, **44**, 37–45, DOI: 10.1021/cr60137a003.

[21] C. Hansen, *The Three Dimensional Solubility Parameter and Solvent Diffusion Coefficient: Their Importance in Surface Coating Formalution*, Doctoral Dissertation, Danish Technical Press, Copenhagen, 1967.

[22] M. Belmares, M. Blanco, W. A. Goddard, R. B. Ross, G. Caldwell, S.-H. Chou, J. Pham, P. M. Olofson and C. Thomas, Hildebrand and

Hansen Solubility Parameters from Molecular Dynamics with Applications to Electronic Nose Polymer Sensors, *Journal of Computational Chemistry*, 2004, **25**, 1814–1826, DOI: 10.1002/jcc.20098.

[23] N. Rai and J. I. Siepmann, Transferable Potentials for Phase Equilibria. 9. Explicit Hydrogen Description of Benzene and Five-Membered and Six-Membered Heterocyclic Aromatic Compounds, *The Journal of Physical Chemistry B*, 2007, **111**, 10790–10799, DOI: 10.1021/jp073586l.

[24] I. Tsivintzelis, I. G. Economou and G. M. Kontogeorgis, Modeling the Solid-Liquid Equilibrium in Pharmaceutical-Solvent Mixtures: Systems with Complex Hydrogen Bonding Behavior, *AIChE Journal*, 2009, **55**, 756–770, DOI: 10.1002/aic.11716.

[25] G. Járvás, C. Quellet and A. Dallos, Estimation of Hansen Solubility Parameters Using Multivariate Nonlinear QSPR Modeling with COSMO Screening Charge Density Moments, *Fluid Phase Equilibria*, 2011, **309**, 8–14, DOI: 10.1016/j.fluid.2011.06.030.

[26] C. M. Hansen, *Hansen Solubility Parameters in Practice (HSPiP)*, `http://www.hansen-solubility.com`, Mai 2014.

[27] C. Hansen, *Hansen Solubility Parameters: A User's Handbook, Second Edition*, CRC Press, Taylor & Francis Group, 2007.

[28] T. Lindvig, I. G. Economou, R. P. Danner, M. L. Michelsen and G. M. Kontogeorgis, Modeling of Multicomponent Vapor–liquid Equilibria for Polymer–solvent Systems, *Fluid Phase Equilibria*, 2004, **220**, 11–20, DOI: 10.1016/j.fluid.2004.02.017.

[29] T. Lindvig, M. L. Michelsen and G. M. Kontogeorgis, A Flory–Huggins model based on the Hansen solubility parameters, *Fluid Phase Equilibria*, 2002, **203**, 247–260, DOI: http://dx.doi.org/10.1016/S0378-3812(02)00184-X.

[30] J. Gupta, C. Nunes, S. Vyas and S. Jonnalagadda, Prediction of Solubility Parameters and Miscibility of Pharmaceutical Compounds by Molecular Dynamics Simulations, *The Journal of Physical Chemistry B*, 2011, **115**, 2014–2023, DOI: 10.1021/jp108540n.

[31] J. M. Hughes, D. Aherne and J. N. Coleman, Generalizing Solubility Parameter Theory to Apply to One- and Two-Dimensional Solutes and to Incorporate Dipolar Interactions, *Journal of Applied Polymer Science*, 2013, **127**, 4483–4491, DOI: 10.1002/app.38051.

[32] K. Pajula, M. Taskinen, V.-P. Lehto, J. Ketolainen and O. Korhonen, Predicting the Formation and Stability of Amorphous Small Molecule Binary Mixtures from Computationally Determined Flory-Huggins Interaction Parameter and Phase Diagram, *Molecular Pharmaceutics*, 2010, **7**, 795–804, DOI: 10.1021/mp900304p.

[33] G. Gillet, O. Vitrac and S. Desobry, Prediction of Solute Partition Coefficients between Polyolefins and Alcohols Using a Generalized Flory-Huggins Approach, *Industrial & Engineering Chemistry Research*, 2009, **48**, 5285–5301, DOI: 10.1021/ie801141h.

[34] N. F. A. van der Vegt, V. A. Kusuma and B. D. Freeman, Basis of Solubility versus T_C Correlations in Polymeric Gas Separation Membranes, *Macromolecules*, 2010, **43**, 1473–1479, DOI: 10.1021/ma9024653.

[35] S. T. Milner, M.-D. Lacasse and W. W. Graessley, Why χ Is Seldom Zero for Polymer-Solvent Mixtures, *Macromolecules*, 2009, **42**, 876–886, DOI: 10.1021/ma801091b.

[36] N. P. Balsara, in *Physical Properties of Polymers Handbook*, ed. J. Mark E., AIP Press, New York, 1996, pp. 339–356.

[37] G. M. Kontogeorgis and G. K. Folas, *Thermodynamic Models for Industrial Applications: From Classical and Advanced Mixing Rules to Association Theories*, Wiley, Chichester, U.K, 2010.

[38] J. Elliott and C. Lira, *Introductory Chemical Engineering Thermodynamics, Second Edition*, Pearson Education, 2012.

[39] H. Renon and J. M. Prausnitz, Estimation of Parameters for the NRTL Equation for Excess Gibbs Energies of Strongly Nonideal Liquid Mixtures, *Industrial & Engineering Chemistry Process Design and Development*, 1969, **8**, 413–419, DOI: 10.1021/i260031a019.

[40] H. S. Elbro, A. Fredenslund and P. Rasmussen, A new simple equation for the prediction of solvent activities in polymer solutions, *Macromolecules*, 1990, **23**, 4707–4714, DOI: 10.1021/ma00223a031.

[41] T. Oishi and J. M. Prausnitz, Estimation of Solvent Activities in Polymer Solutions Using a Group-Contribution Method, *Industrial & Engineering Chemistry Process Design and Development*, 1978, **17**, 333–339, DOI: 10.1021/i260067a021.

[42] G. M. Kontogeorgis, A. Fredenslund and D. P. Tassios, Simple activity coefficient model for the prediction of solvent activities in polymer solutions, *Industrial & Engineering Chemistry Research*, 1993, **32**, 362–372, DOI: 10.1021/ie00014a013.

[43] A. Klamt and G. Schüürmann, COSMO: A New Approach to Dielectric Screening in Solvents with Explicit Expressions for the Screening Energy and Its Gradient, *J. Chem. Soc., Perkin Trans. 2*, 1993, 799–805, DOI: 10.1039/P29930000799.

[44] A. Klamt, F. Eckert and W. Arlt, COSMO-RS: An Alternative to Simulation for Calculating Thermodynamic Properties of Liquid Mixtures, *Annual Review of Chemical and Biomolecular Engineering*, 2010, **1**, 101–122, DOI: 10.1146/annurev-chembioeng-073009-100903.

[45] A. Klamt, V. Jonas, T. Bürger and J. C. W. Lohrenz, Refinement and Parametrization of COSMO-RS, *The Journal of Physical Chemistry A*, 1998, **102**, 5074–5085, DOI: 10.1021/jp980017s.

[46] J. Reinisch, *personal communication*, Houston, 2015.

[47] J. McCarty, A. J. Clark, I. Y. Lyubimov and M. G. Guenza, Thermodynamic Consistency between Analytic Integral Equation Theory and Coarse-Grained Molecular Dynamics Simulations of Homopolymer Melts, *Macromolecules*, 2012, **45**, 8482–8493, DOI: 10.1021/ma301502w.

[48] J. McCarty, A. J. Clark, J. Copperman and M. G. Guenza, An Analytical Coarse-Graining Method Which Preserves the Free Energy, Structural Correlations, and Thermodynamic State of Polymer Melts from the Atomistic to the Mesoscale, *The Journal of Chemical Physics*, 2014, **140**, 204913, DOI: 10.1063/1.4875923.

[49] J. McCarty, I. Y. Lyubimov and M. G. Guenza, Effective Soft-Core Potentials and Mesoscopic Simulations of Binary Polymer Mixtures, *Macromolecules*, 2010, **43**, 3964–3979, DOI: 10.1021/ma100052z.

[50] G. Yatsenko, E. J. Sambriski and M. G. Guenza, Coarse-Grained Description of Polymer Blends as Interacting Soft-Colloidal Particles, *The Journal of Chemical Physics*, 2005, **122**, 054907, DOI: 10.1063/1.1835271.

[51] N. M. Garrido, A. J. Queimada, M. Jorge, E. A. Macedo and I. G. Economou, 1-Octanol/Water Partition Coefficients of *n*-Alkanes from Molecular Simulations of Absolute Solvation Free Energies, *Journal of Chemical Theory and Computation*, 2009, **5**, 2436–2446, DOI: 10.1021/ct900214y.

[52] E. Zervopoulou, V. G. Mavrantzas and D. N. Theodorou, A New Monte Carlo Simulation Approach for the Prediction of Sorption Equilibria of Oligomers in Polymer Melts: Solubility of Long Alkanes in Linear Polyethylene, *The Journal of Chemical Physics*, 2001, **115**, 2860–2875, DOI: 10.1063/1.1383050.

[53] P. J. Hoogerbrugge and J. M. V. A. Koelman, Simulating Microscopic Hydrodynamic Phenomena with Dissipative Particle Dynam-

ics, *EPL (Europhysics Letters)*, 1992, **19**, 155, DOI: 10.1209/0295-5075/19/3/001.

[54] Z. G. Mills, W. Mao and A. Alexeev, Mesoscale Modeling: Solving Complex Flows in Biology and Biotechnology, *Trends in Biotechnology*, 2013, **31**, 426–434, DOI: 10.1016/j.tibtech.2013.05.001.

[55] R. D. Groot and P. B. Warren, Dissipative Particle Dynamics: Bridging the Gap between Atomistic and Mesoscopic Simulation, *The Journal of Chemical Physics*, 1997, **107**, 4423, DOI: 10.1063/1.474784.

[56] J. G. E. M. Fraaije, J. van Male, P. Becherer and R. Serral Gracià, Coarse-Grained Models for Automated Fragmentation and Parametrization of Molecular Databases, *Journal of Chemical Information and Modeling*, 2016, **56**, 2361–2377, DOI: 10.1021/acs.jcim.6b00003.

[57] I. Pagonabarraga and D. Frenkel, Non-Ideal DPD Fluids, *Molecular Simulation*, 2000, **25**, 167–175, DOI: 10.1080/08927020008044122.

[58] I. Pagonabarraga and D. Frenkel, Dissipative Particle Dynamics for Interacting Systems, *The Journal of Chemical Physics*, 2001, **115**, 5015–5026, DOI: 10.1063/1.1396848.

[59] P. B. Warren, Vapour-Liquid Coexistence in Many-Body Dissipative Particle Dynamics, *Physical Review E*, 2003, **68**, year, DOI: 10.1103/PhysRevE.68.066702.

[60] J. R. Spaeth, T. Dale, I. G. Kevrekidis and A. Z. Panagiotopoulos, Coarse-Graining of Chain Models in Dissipative Particle Dynamics Simulations, *Industrial & Engineering Chemistry Research*, 2011, **50**, 69–77, DOI: 10.1021/ie100337r.

[61] M. B. Liu, G. R. Liu, L. W. Zhou and J. Z. Chang, Dissipative Particle Dynamics (DPD): An Overview and Recent Developments, *Archives of Computational Methods in Engineering*, 2015, **22**, 529–556, DOI: 10.1007/s11831-014-9124-x.

[62] J. D. Van der Waals and J. D. van der Waals, *Over de Continuiteit van den Gas- en Vloeistoftoestand*, AW Sijthoff, 1873.

[63] S. P. Tan, H. Adidharma and M. Radosz, Recent Advances and Applications of Statistical Associating Fluid Theory, *Industrial & Engineering Chemistry Research*, 2008, **47**, 8063–8082, DOI: 10.1021/ie8008764.

[64] E. A. Müller and K. E. Gubbins, Molecular-Based Equations of State for Associating Fluids: A Review of SAFT and Related Approaches, *Industrial & Engineering Chemistry Research*, 2001, **40**, 2193–2211, DOI: 10.1021/ie000773w.

[65] I. G. Economou, Statistical Associating Fluid Theory: A Successful Model for the Calculation of Thermodynamic and Phase Equilibrium Properties of Complex Fluid Mixtures, *Industrial & Engineering Chemistry Research*, 2002, **41**, 953–962, DOI: 10.1021/ie0102201.

[66] C. McCabe and A. Galindo, in *Applied Thermodynamics of Fluids*, ed. A. Goodwin, J. Sengers and C. J. Peters, Royal Society of Chemistry, Cambridge, 2010, pp. 215–279.

[67] W. G. Chapman, S. G. Sauer, D. Ting and A. Ghosh, Phase Behavior Applications of SAFT Based Equations of State—from Associating Fluids to Polydisperse, Polar Copolymers, *Fluid Phase Equilibria*, 2004, **217**, 137–143, DOI: 10.1016/j.fluid.2003.05.001.

[68] P. Paricaud, A. Galindo and G. Jackson, Recent Advances in the Use of the SAFT Approach in Describing Electrolytes, Interfaces, Liquid Crystals and Polymers, *Fluid Phase Equilibria*, 2002, **194-197**, 87–96, DOI: 10.1016/S0378-3812(01)00659-8.

[69] M. B. Oliveira, L. A. Follegatti–Romero, M. Lanza, F. R. Batista, E. A. Batista and A. J. Meirelles, Low Pressure Vapor–liquid Equilibria Modeling of Biodiesel Related Systems with the Cubic–Plus–Association (CPA) Equation of State, *Fuel*, 2014, **133**, 224–231, DOI: 10.1016/j.fuel.2014.05.016.

[70] G. Kontogeorgis, I. Yakoumis and P. Vlamos, Application of the sCPA equation of state for polymer solutions, *Computational and Theoretical Polymer Science*, 2000, **10**, 501–506, DOI: http://dx.doi.org/10.1016/S1089-3156(99)00053-7.

[71] W. Chapman, K. Gubbins, G. Jackson and M. Radosz, SAFT: Equation-of-State Solution Model for Associating Fluids, *Fluid Phase Equilibria*, 1989, **52**, 31–38, DOI: 10.1016/0378-3812(89)80308-5.

[72] J. A. Barker and D. Henderson, What Is "Liquid"? Understanding the States of Matter, *Reviews of Modern Physics*, 1976, **48**, 587.

[73] N. F. Carnahan, Equation of State for Nonattracting Rigid Spheres, *The Journal of Chemical Physics*, 1969, **51**, 635, DOI: 10.1063/1.1672048.

[74] M. Wertheim, Fluids with highly directional attractive forces. I. Statistical thermodynamics, *Journal of Statistical Physics*, 1984, **35**, 19–34, DOI: 10.1007/BF01017362.

[75] M. Wertheim, Fluids with highly directional attractive forces. II. Thermodynamic perturbation theory and integral equations, *Journal of Statistical Physics*, 1984, **35**, 35–47, DOI: 10.1007/BF01017363.

[76] M. Wertheim, Fluids with highly directional attractive forces. III. Multiple attraction sites, *Journal of Statistical Physics*, 1986, **42**, 459–476, DOI: 10.1007/BF01127721.

[77] M. Wertheim, Fluids with highly directional attractive forces. IV. Equilibrium polymerization, *Journal of Statistical Physics*, 1986, **42**, 477–492, DOI: 10.1007/BF01127722.

[78] M. S. Wertheim, Fluids of dimerizing hard spheres, and fluid mixtures of hard spheres and dispheres, *The Journal of Chemical Physics*, 1986, **85**, 2929–2936, DOI: http://dx.doi.org/10.1063/1.451002.

[79] M. S. Wertheim, Thermodynamic perturbation theory of polymerization, *The Journal of Chemical Physics*, 1987, **87**, 7323–7331, DOI: http://dx.doi.org/10.1063/1.453326.

[80] S. H. Huang and M. Radosz, Equation of State for Small, Large, Polydisperse, and Associating Molecules, *Industrial & Engineering Chemistry Research*, 1990, **29**, 2284–2294.

[81] J. Gross and G. Sadowski, Modeling Polymer Systems Using the Perturbed-Chain Statistical Associating Fluid Theory Equation of State, *Industrial & Engineering Chemistry Research*, 2002, **41**, 1084–1093, DOI: 10.1021/ie010449g.

[82] J. Gross and G. Sadowski, Perturbed-Chain SAFT: An Equation of State Based on a Perturbation Theory for Chain Molecules, *Industrial & Engineering Chemistry Research*, 2001, **40**, 1244–1260, DOI: 10.1021/ie0003887.

[83] P. Paricaud, A. Galindo and G. Jackson, Modeling the Cloud Curves and the Solubility of Gases in Amorphous and Semicrystalline Polyethylene with the SAFT-VR Approach and Flory Theory of Crystallization, *Industrial & Engineering Chemistry Research*, 2004, **43**, 6871–6889, DOI: 10.1021/ie049592a.

[84] W. G. Noid, J.-W. Chu, G. S. Ayton and G. A. Voth, Multiscale Coarse-Graining and Structural Correlations: Connections to Liquid-State Theory, *The Journal of Physical Chemistry B*, 2007, **111**, 4116–4127, DOI: 10.1021/jp068549t.

[85] M. G. Martin and J. I. Siepmann, Transferable Potentials for Phase Equilibria. 1. United-Atom Description of n-Alkanes, *The Journal of Physical Chemistry B*, 1998, **102**, 2569–2577.

[86] S. K. Nath, B. J. Banaszak and J. J. de Pablo, A New United Atom Force Field for α-Olefins, *The Journal of Chemical Physics*, 2001, **114**, 3612, DOI: 10.1063/1.1343487.

[87] A. Gooneie, S. Schuschnigg and C. Holzer, A Review of Multiscale Computational Methods in Polymeric Materials, *Polymers*, 2017, **9**, 16, DOI: 10.3390/polym9010016.

[88] D. Rosenberger, M. Hanke and N. F. A. van der Vegt, Comparison of Iterative Inverse Coarse-Graining Methods, *The European Physical Journal Special Topics*, 2016, **225**, 1323–1345, DOI: 10.1140/epjst/e2016-60120-1.

[89] F. Müller-Plathe, Coarse-Graining in Polymer Simulation: From the Atomistic to the Mesoscopic Scale and Back, *ChemPhysChem*, 2002, **3**, 754–769, DOI: 10.1002/1439-7641(20020916)3:9<754::AID-CPHC754>3.0.CO;2-U.

[90] E. Brini, E. A. Algaer, P. Ganguly, C. Li, F. Rodríguez-Ropero and N. F. A. van der Vegt, Systematic Coarse-Graining Methods for Soft Matter Simulations – a Review, *Soft Matter*, 2013, **9**, 2108–2119, DOI: 10.1039/C2SM27201F.

[91] Z. Li, X. Bian, X. Yang and G. E. Karniadakis, A Comparative Study of Coarse-Graining Methods for Polymeric Fluids: Mori-Zwanzig vs. Iterative Boltzmann Inversion vs. Stochastic Parametric Optimization, *The Journal of Chemical Physics*, 2016, **145**, 044102, DOI: 10.1063/1.4959121.

[92] L. Vlcek and A. A. Chialvo, Rigorous Force Field Optimization Principles Based on Statistical Distance Minimization, *The Journal of Chemical Physics*, 2015, **143**, 144110, DOI: 10.1063/1.4932360.

[93] D. Reith, M. Pütz and F. Müller-Plathe, Deriving Effective Mesoscale Potentials from Atomistic Simulations: Mesoscale Potentials from Atomistic Simulations, *Journal of Computational Chemistry*, 2003, **24**, 1624–1636, DOI: 10.1002/jcc.10307.

[94] K. Prasitnok and M. R. Wilson, A Coarse-Grained Model for Polyethylene Glycol in Bulk Water and at a Water/Air Inter-

face, *Physical Chemistry Chemical Physics*, 2013, **15**, 17093, DOI: 10.1039/c3cp52958d.

[95] V. Agrawal, P. Peralta, Y. Li and J. Oswald, A Pressure-Transferable Coarse-Grained Potential for Modeling the Shock Hugoniot of Polyethylene, *The Journal of Chemical Physics*, 2016, **145**, 104903, DOI: 10.1063/1.4962255.

[96] V. A. Harmandaris, D. Reith, N. F. A. van der Vegt and K. Kremer, Comparison Between Coarse-Graining Models for Polymer Systems: Two Mapping Schemes for Polystyrene, *Macromolecular Chemistry and Physics*, 2007, **208**, 2109–2120, DOI: 10.1002/macp.200700245.

[97] A. Agrawal, D. Aryal, D. Perahia, T. Ge and G. S. Grest, Coarse-Graining Atactic Polystyrene and Its Analogues, *Macromolecules*, 2014, **47**, 3210–3218, DOI: 10.1021/ma500319v.

[98] P. Carbone, H. A. K. Varzaneh, X. Chen and F. Müller-Plathe, Transferability of Coarse-Grained Force Fields: The Polymer Case, *The Journal of Chemical Physics*, 2008, **128**, 064904, DOI: 10.1063/1.2829409.

[99] T. C. Moore, C. R. Iacovella and C. McCabe, Derivation of Coarse-Grained Potentials via Multistate Iterative Boltzmann Inversion, *The Journal of Chemical Physics*, 2014, **140**, 224104, DOI: 10.1063/1.4880555.

[100] M. S. Shell, The Relative Entropy Is Fundamental to Multiscale and Inverse Thermodynamic Problems, *The Journal of Chemical Physics*, 2008, **129**, 144108, DOI: 10.1063/1.2992060.

[101] S. Y. Mashayak, M. N. Jochum, K. Koschke, N. R. Aluru, V. Rühle and C. Junghans, Relative Entropy and Optimization-Driven Coarse-Graining Methods in VOTCA, *PLOS ONE*, 2015, **10**, e0131754, DOI: 10.1371/journal.pone.0131754.

[102] S. Izvekov and G. A. Voth, A Multiscale Coarse-Graining Method for Biomolecular Systems, *The Journal of Physical Chemistry B*, 2005, **109**, 2469–2473, DOI: 10.1021/jp044629q.

[103] S. Izvekov, A. Violi and G. A. Voth, Systematic Coarse-Graining of Nanoparticle Interactions in Molecular Dynamics Simulation, *The Journal of Physical Chemistry B*, 2005, **109**, 17019–17024, DOI: 10.1021/jp0530496.

[104] V. Rühle and C. Junghans, Hybrid Approaches to Coarse-Graining Using the VOTCA Package: Liquid Hexane, *Macromolecular Theory and Simulations*, 2011, **20**, 472–477, DOI: 10.1002/mats.201100011.

[105] V. Rühle, C. Junghans, A. Lukyanov, K. Kremer and D. Andrienko, Versatile Object-Oriented Toolkit for Coarse-Graining Applications, *Journal of Chemical Theory and Computation*, 2009, **5**, 3211–3223, DOI: 10.1021/ct900369w.

[106] S. J. Marrink, H. J. Risselada, S. Yefimov, D. P. Tieleman and A. H. de Vries, The MARTINI Force Field: Coarse Grained Model for Biomolecular Simulations, *The Journal of Physical Chemistry B*, 2007, **111**, 7812–7824, DOI: 10.1021/jp071097f.

[107] T. D. Potter, J. Tasche, E. L. Barrett, M. Walker and M. R. Wilson, Development of New Coarse-Grained Models for Chromonic Liquid Crystals: Insights from Top-down Approaches, *Liquid Crystals*, 2017, **0**, 1–11, DOI: 10.1080/02678292.2017.1342005.

[108] L. Monticelli, S. K. Kandasamy, X. Periole, R. G. Larson, D. P. Tieleman and S.-J. Marrink, The MARTINI Coarse-Grained Force Field: Extension to Proteins, *Journal of Chemical Theory and Computation*, 2008, **4**, 819–834, DOI: 10.1021/ct700324x.

[109] X. Periole and S.-J. Marrink, in *Biomolecular Simulations*, ed. L. Monticelli and E. Salonen, Humana Press, Totowa, NJ, 2013, vol. 924, pp. 533–565.

[110] E. Panizon, D. Bochicchio, L. Monticelli and G. Rossi, MARTINI Coarse-Grained Models of Polyethylene and Polypropylene, *The Journal of Physical Chemistry B*, 2015, **119**, 8209–8216, DOI: 10.1021/acs.jpcb.5b03611.

[111] H. Lee, A. H. de Vries, S.-J. Marrink and R. W. Pastor, A Coarse-Grained Model for Polyethylene Oxide and Polyethylene Glycol: Conformation and Hydrodynamics, *The Journal of Physical Chemistry B*, 2009, **113**, 13186–13194, DOI: 10.1021/jp9058966.

[112] G. Rossi, L. Monticelli, S. R. Puisto, I. Vattulainen and T. Ala-Nissila, Coarse-Graining Polymers with the MARTINI Force-Field: Polystyrene as a Benchmark Case, *Soft Matter*, 2011, **7**, 698–708, DOI: 10.1039/C0SM00481B.

[113] E. A. Müller and G. Jackson, Force-Field Parameters from the SAFT-γ Equation of State for Use in Coarse-Grained Molecular Simulations, *Annual Review of Chemical and Biomolecular Engineering*, 2014, **5**, 405–427, DOI: 10.1146/annurev-chembioeng-061312-103314.

[114] T. Lafitte, C. Avendaño, V. Papaioannou, A. Galindo, C. S. Adjiman, G. Jackson and E. A. Müller, SAFT- γ Force Field for the Simulation of Molecular Fluids: 3. Coarse-Grained Models of Benzene and Hetero-Group Models of *n* -Decylbenzene, *Molecular Physics*, 2012, **110**, 1189–1203, DOI: 10.1080/00268976.2012.662303.

[115] C. Avendaño, T. Lafitte, C. S. Adjiman, A. Galindo, E. A. Müller and G. Jackson, SAFT-γ Force Field for the Simulation of Molecular Fluids: 2. Coarse-Grained Models of Greenhouse Gases, Refrigerants, and Long Alkanes, *The Journal of Physical Chemistry B*, 2013, **117**, 2717–2733, DOI: 10.1021/jp306442b.

[116] G. Sadowski, in *Polymer Thermodynamics*, Springer, Berlin, Heidelberg, 2010, pp. 389–418.

[117] W. G. Chapman, K. E. Gubbins, G. Jackson and M. Radosz, New Reference Equation of State for Associating Liquids, *Industrial & Engineering Chemistry Research*, 1990, **29**, 1709–1721, DOI: 10.1021/ie00104a021.

[118] W. Zmpitas and J. Gross, Detailed Pedagogical Review and Analysis of Wertheim's Thermodynamic Perturbation Theory, *Fluid Phase Equilibria*, 2016, **428**, 121–152, DOI: 10.1016/j.fluid.2016.07.033.

[119] S. Dufal, T. Lafitte, A. J. Haslam, A. Galindo, G. N. Clark, C. Vega and G. Jackson, The A in SAFT: Developing the Contribution of Association to the Helmholtz Free Energy within a Wertheim TPT1 Treatment of Generic Mie Fluids, *Molecular Physics*, 2015, **113**, 948–984, DOI: 10.1080/00268976.2015.1029027.

[120] A. Lymperiadis, C. S. Adjiman, G. Jackson and A. Galindo, A Generalisation of the SAFT- Group Contribution Method for Groups Comprising Multiple Spherical Segments, *Fluid Phase Equilibria*, 2008, **274**, 85–104, DOI: 10.1016/j.fluid.2008.08.005.

[121] G. A. Mansoori, N. F. Carnahan, K. E. Starling and T. W. Leland, Equilibrium Thermodynamic Properties of the Mixture of Hard Spheres, *The Journal of Chemical Physics*, 1971, **54**, 1523–1525, DOI: 10.1063/1.1675048.

[122] R. L. Cotterman, B. J. Schwarz and J. M. Prausnitz, Molecular Thermodynamics for Fluids at Low and High Densities. Part I: Pure Fluids Containing Small or Large Molecules, *AIChE Journal*, 1986, **32**, 1787–1798, DOI: 10.1002/aic.690321104.

[123] A. F. Ghobadi and J. R. Elliott, Adapting SAFT-γ Perturbation Theory to Site-Based Molecular Dynamics Simulation. I. Homogeneous Fluids, *The Journal of Chemical Physics*, 2013, **139**, 234104, DOI: 10.1063/1.4838457.

[124] M. Banaszak, C. K. Chen and M. Radosz, Copolymer SAFT Equation of State. Thermodynamic Perturbation Theory Extended to

Heterobonded Chains, *Macromolecules*, 1996, **29**, 6481–6486, DOI: 10.1021/ma9517815.

[125] A. Gil-Villegas, A. Galindo, P. J. Whitehead, S. J. Mills, G. Jackson and A. N. Burgess, Statistical Associating Fluid Theory for Chain Molecules with Attractive Potentials of Variable Range, *The Journal of Chemical Physics*, 1997, **106**, 4168, DOI: 10.1063/1.473101.

[126] Y. Peng, K. D. Goff, M. C. dos Ramos and C. McCabe, Predicting the Phase Behavior of Polymer Systems with the GC-SAFT-VR Approach, *Industrial & Engineering Chemistry Research*, 2010, **49**, 1378–1394, DOI: 10.1021/ie900795x.

[127] H. Adidharma and M. Radosz, Prototype of an Engineering Equation of State for Heterosegmented Polymers, *Industrial & Engineering Chemistry Research*, 1998, **37**, 4453–4462, DOI: 10.1021/ie980345e.

[128] D. Ghonasgi and W. G. Chapman, Prediction of the Properties of Model Polymer Solutions and Blends, *AIChE Journal*, 1994, **40**, 878–887, DOI: 10.1002/aic.690400514.

[129] J. K. Johnson, E. A. Mueller and K. E. Gubbins, Equation of State for Lennard-Jones Chains, *The Journal of Physical Chemistry*, 1994, **98**, 6413–6419, DOI: 10.1021/j100076a028.

[130] T. Kraska and K. E. Gubbins, Phase Equilibria Calculations with a Modified SAFT Equation of State. 1. Pure Alkanes, Alkanols, and Water, *Industrial & Engineering Chemistry Research*, 1996, **35**, 4727–4737, DOI: 10.1021/ie9602320.

[131] L. A. Davies, A. Gil-Villegas and G. Jackson, Describing the Properties of Chains of Segments Interacting Via Soft-Core Potentials of Variable Range with the SAFT-VR Approach, *International Journal of Thermophysics*, 1998, **19**, 675–686, DOI: 10.1023/A:1022662116418.

[132] L. A. Davies, A. Gil-Villegas and G. Jackson, An Analytical Equation of State for Chain Molecules Formed from Yukawa Segments,

The Journal of Chemical Physics, 1999, **111**, 8659–8665, DOI: 10.1063/1.480205.

[133] I. Nezbeda, R. Melnyk and A. Trokhymchuk, Augmented van Der Waals Equations of State: SAFT-VR versus Yukawa Based van Der Waals Equation, *Fluid Phase Equilibria*, 2011, **309**, 174–178, DOI: 10.1016/j.fluid.2011.07.006.

[134] I. M. Zerón, L. A. Padilla, F. Gámez, J. Torres-Arenas and A. L. Benavides, Discrete Perturbation Theory for Mie Potentials, *Journal of Molecular Liquids*, 2017, **229**, 125–136, DOI: 10.1016/j.molliq.2016.12.026.

[135] R. Shahriari and M. R. Dehghani, New SAFT-VR Equation of State Based on Morse Potential, *Journal of Molecular Liquids*, 2017, **231**, 430–439, DOI: 10.1016/j.molliq.2017.02.018.

[136] W. G. Chapman, G. Jackson and K. E. Gubbins, Phase Equilibria of Associating Fluids: Chain Molecules with Multiple Bonding Sites, *Molecular Physics*, 1988, **65**, 1057–1079, DOI: 10.1080/00268978800101601.

[137] G. Jackson, W. G. Chapman and K. E. Gubbins, Phase Equilibria of Associating Fluids: Spherical Molecules with Multiple Bonding Sites, *Molecular Physics*, 1988, **65**, 1–31, DOI: 10.1080/00268978800100821.

[138] C. Joslin, C. Gray, W. Chapman and K. Gubbins, Theory and Simulation of Associating Liquid Mixtures. II, *Molecular Physics*, 1987, **62**, 843–860, DOI: 10.1080/00268978700102621.

[139] W. G. Chapman, K. E. Gubbins, C. G. Joslin and C. G. Gray, Mixtures of Polar and Associating Molecules, *Pure and Applied Chemistry*, 1987, **59**, year, DOI: 10.1351/pac198759010053.

[140] W. Chapman, K. Gubbins, C. Joslin and C. Gray, Theory and Simulation of Associating Liquid Mixtures, *Fluid Phase Equilibria*, 1986, **29**, 337–346, DOI: 10.1016/0378-3812(86)85033-6.

[141] C. McCabe and G. Jackson, SAFT-VR Modelling of the Phase Equilibrium of Long-Chain n-Alkanes, *Physical Chemistry Chemical Physics*, 1999, **1**, 2057–2064, DOI: 10.1039/a808085b.

[142] C.-k. Chen, M. Banaszak and M. Radosz, Statistical Associating Fluid Theory Equation of State with Lennard-Jones Reference Applied to Pure and Binary *n* -Alkane Systems, *The Journal of Physical Chemistry B*, 1998, **102**, 2427–2431, DOI: 10.1021/jp9731819.

[143] J. Gross, O. Spuhl, F. Tumakaka and G. Sadowski, Modeling Copolymer Systems Using the Perturbed-Chain SAFT Equation of State, *Industrial & Engineering Chemistry Research*, 2003, **42**, 1266–1274, DOI: 10.1021/ie020509y.

[144] C.-S. Wu and Y.-P. Chen, Calculation of Vapor-Liquid Equilibria of Polymer Solutions Using the SAFT Equation of State, *Fluid Phase Equilibria*, 1994, **100**, 103–119, DOI: 10.1016/0378-3812(94)80004-9.

[145] P. K. Jog, W. G. Chapman, S. K. Gupta and R. D. Swindoll, Modeling of Liquid-Liquid-Phase Separation in Linear Low-Density Polyethylene-Solvent Systems Using the Statistical Associating Fluid Theory Equation of State, *Industrial & Engineering Chemistry Research*, 2002, **41**, 887–891, DOI: 10.1021/ie000604b.

[146] R. A. Heidemann, R. A. Krenz, T. Laursen and E. L. Cheluget, An Approach to Expediting Phase Equilibrium Calculations for Polydisperse Polymers, *Fluid Phase Equilibria*, 2006, **241**, 70–80, DOI: 10.1016/j.fluid.2005.12.030.

[147] P. K. Jog and W. G. Chapman, An Algorithm for Calculation of Phase Equilibria in Polydisperse Polymer Solutions Using the SAFT Equation of State, *Macromolecules*, 2002, **35**, 1002–1011, DOI: 10.1021/ma000974b.

[148] P. Paricaud, A. Galindo and G. Jackson, Examining the Effect of Chain Length Polydispersity on the Phase Behavior of Polymer Solutions with

the Statistical Associating Fluid Theory (Wertheim TPT1) Using Discrete and Continuous Distributions, *The Journal of Chemical Physics*, 2007, **127**, 154906, DOI: 10.1063/1.2772600.

[149] L. Sun, H. Zhao and C. McCabe, Predicting the Phase Equilibria of Petroleum Fluids with the SAFT-VR Approach, *AIChE Journal*, 2007, **53**, 720–731, DOI: 10.1002/aic.11110.

[150] T. Boublík, Hard-Sphere Equation of State, *The Journal of Chemical Physics*, 1970, **53**, 471–472, DOI: 10.1063/1.1673824.

[151] O. Lobanova, C. Avendaño, T. Lafitte, E. A. Müller and G. Jackson, SAFT-γ Force Field for the Simulation of Molecular Fluids: 4. A Single-Site Coarse-Grained Model of Water Applicable over a Wide Temperature Range, *Molecular Physics*, 2015, **113**, 1228–1249, DOI: 10.1080/00268976.2015.1004804.

[152] O. Lobanova, A. Mejía, G. Jackson and E. A. Müller, SAFT-γ Force Field for the Simulation of Molecular Fluids 6: Binary and Ternary Mixtures Comprising Water, Carbon Dioxide, and n-Alkanes, *The Journal of Chemical Thermodynamics*, 2016, **93**, 320–336, DOI: 10.1016/j.jct.2015.10.011.

[153] E. A. Müller, C. Herdes and T. S. Totton, author, 2015, DOI: 10.4043/26155-MS.

[154] C. Herdes, T. S. Totton and E. A. Müller, Coarse Grained Force Field for the Molecular Simulation of Natural Gases and Condensates, *Fluid Phase Equilibria*, 2015, **406**, 91–100, DOI: 10.1016/j.fluid.2015.07.014.

[155] A. Mejía, M. Cartes, H. Segura and E. A. Müller, Use of Equations of State and Coarse Grained Simulations to Complement Experiments: Describing the Interfacial Properties of Carbon Dioxide + Decane and Carbon Dioxide + Eicosane Mixtures, *Journal of Chemical & Engineering Data*, 2014, **59**, 2928–2941, DOI: 10.1021/je5000764.

[156] A. Mejía, C. Herdes and E. A. Müller, Force Fields for Coarse-Grained Molecular Simulations from a Corresponding States Correlation, *Industrial & Engineering Chemistry Research*, 2014, **53**, 4131–4141, DOI: 10.1021/ie404247e.

[157] E. A. Müller and A. Mejía, Resolving Discrepancies in the Measurements of the Interfacial Tension for the CO_2 + H_2O Mixture by Computer Simulation, *The Journal of Physical Chemistry Letters*, 2014, **5**, 1267–1271, DOI: 10.1021/jz500417w.

[158] M. Chorążewski, J. Troncoso and J. Jacquemin, Thermodynamic Properties of Dichloromethane, Bromochloromethane, and Dibromomethane under Elevated Pressure: Experimental Results and SAFT-VR Mie Predictions, *Industrial & Engineering Chemistry Research*, 2015, **54**, 720–730, DOI: 10.1021/ie5038903.

[159] N. Ramrattan, C. Avendaño, E. Müller and A. Galindo, A Corresponding-States Framework for the Description of the Mie Family of Intermolecular Potentials, *Molecular Physics*, 2015, **113**, 932–947, DOI: 10.1080/00268976.2015.1025112.

[160] A. Hemmen and J. Gross, Transferable Anisotropic United-Atom Force Field Based on the Mie Potential for Phase Equilibrium Calculations: N-Alkanes and n-Olefins, *The Journal of Physical Chemistry B*, 2015, **119**, 11695–11707, DOI: 10.1021/acs.jpcb.5b01354.

[161] Y. Zhou, C. K. Hall and G. Stell, Thermodynamic Perturbation Theory for Fused Hard-sphere and Hard-disk Chain Fluids, *The Journal of Chemical Physics*, 1995, **103**, 2688–2695, DOI: 10.1063/1.470528.

[162] E. A. Müller and K. E. Gubbins, Simulation of Hard Triatomic and Tetratomic Molecules: A Test of Associating Fluid Theories, *Molecular Physics*, 1993, **80**, 957–976, DOI: 10.1080/00268979300102791.

[163] C. Pan and M. Radosz, Modeling of Solid–liquid Equilibria in Naphthalene, Normal-Alkane and Polyethylene Solutions, *Fluid Phase Equilibria*, 1999, **155**, 57–73, DOI: 10.1016/S0378-3812(98)00454-3.

[164] M. G. De Angelis and G. C. Sarti, Solubility of Gases and Liquids in Glassy Polymers, *Annual Review of Chemical and Biomolecular Engineering*, 2011, **2**, 97–120, DOI: 10.1146/annurev-chembioeng-061010-114247.

[165] T. Lafitte, B. Mendiboure, M. M. Piñeiro, D. Bessières and C. Miqueu, Interfacial Properties of Water/CO_2 : A Comprehensive Description through a Gradient Theory-SAFT-VR Mie Approach, *The Journal of Physical Chemistry B*, 2010, **114**, 11110–11116, DOI: 10.1021/jp103292e.

[166] E. A. Müller and A. Mejía, Interfacial Properties of Selected Binary Mixtures Containing N-Alkanes, *Fluid Phase Equilibria*, 2009, **282**, 68–81, DOI: 10.1016/j.fluid.2009.04.022.

[167] J. M. Míguez, J. M. Garrido, F. J. Blas, H. Segura, A. Mejía and M. M. Piñeiro, Comprehensive Characterization of Interfacial Behavior for the Mixture CO $_2$ + H $_2$ O + CH $_4$: Comparison between Atomistic and Coarse Grained Molecular Simulation Models and Density Gradient Theory, *The Journal of Physical Chemistry C*, 2014, **118**, 24504–24519, DOI: 10.1021/jp507107a.

[168] F. Llovell, A. Galindo, F. J. Blas and G. Jackson, Classical Density Functional Theory for the Prediction of the Surface Tension and Interfacial Properties of Fluids Mixtures of Chain Molecules Based on the Statistical Associating Fluid Theory for Potentials of Variable Range, *The Journal of Chemical Physics*, 2010, **133**, 024704, DOI: 10.1063/1.3449143.

[169] G. J. Gloor, F. J. Blas, E. M. del Rıó, E. de Miguel and G. Jackson, A SAFT–DFT Approach for the Vapour–liquid Interface of Associating Fluids, *Fluid Phase Equilibria*, 2002, **194-197**, 521–530, DOI: 10.1016/S0378-3812(01)00774-9.

[170] L. A. Mitchell, B. J. Schindler, G. Das, M. C. dos Ramos, C. McCabe, P. T. Cummings and M. D. LeVan, Prediction of *n* -Alkane Ad-

sorption on Activated Carbon Using the SAFT–FMT–DFT Approach, *The Journal of Physical Chemistry C*, 2015, **119**, 1457–1463, DOI: 10.1021/jp510515m.

[171] L. Wang, H. Zhou, X. Wang and J. Mi, Modeling Solubility and Interfacial Properties of Carbon Dioxide Dissolved in Polymers, *Industrial & Engineering Chemistry Research*, 2016, **55**, 1126–1133, DOI: 10.1021/acs.iecr.5b04343.

[172] B. J. Schindler, L. A. Mitchell, C. McCabe, P. T. Cummings and M. D. LeVan, Adsorption of Chain Molecules in Slit-Shaped Pores: Development of a SAFT-FMT-DFT Approach, *The Journal of Physical Chemistry C*, 2013, **117**, 21337–21350, DOI: 10.1021/jp406572d.

[173] A. Dominik, S. Tripathi and W. G. Chapman, Bulk and Interfacial Properties of Polymers from Interfacial SAFT Density Functional Theory, *Industrial & Engineering Chemistry Research*, 2006, **45**, 6785–6792, DOI: 10.1021/ie060329e.

[174] S. Dufal, T. Lafitte, A. Galindo, G. Jackson and A. J. Haslam, Developing Intermolecular-Potential Models for Use with the SAFT-VRMie Equation of State, *AIChE Journal*, 2015, **61**, 2891–2912, DOI: 10.1002/aic.14808.

[175] E. Lindahl, B. Hess and D. van der Spoel, GROMACS 3.0: a package for molecular simulation and trajectory analysis, *Molecular modeling annual*, 2001, **7**, 306–317, DOI: 10.1007/s008940100045.

[176] D. Van Der Spoel, E. Lindahl, B. Hess, G. Groenhof, A. E. Mark and H. J. C. Berendsen, GROMACS: Fast, flexible, and free, *Journal of Computational Chemistry*, 2005, **26**, 1701–1718, DOI: 10.1002/jcc.20291.

[177] H. Berendsen, D. van der Spoel and R. van Drunen, GROMACS: A message-passing parallel molecular dynamics implementation, *Computer Physics Communications*, 1995, **91**, 43–56, DOI: http://dx.doi.org/10.1016/0010-4655(95)00042-E.

[178] D. Kondepudi, *Introduction to Modern Thermodynamics*, Wiley, Chichester, England ; Hoboken, NJ, 1st edn., 2008.

[179] F. E. Pereira, G. Jackson, A. Galindo and C. S. Adjiman, A Duality-Based Optimisation Approach for the Reliable Solution of (P, T) Phase Equilibrium in Volume-Composition Space, *Fluid Phase Equilibria*, 2010, **299**, 1–23, DOI: 10.1016/j.fluid.2010.08.001.

[180] P. Paricaud, A General Perturbation Approach for Equation of State Development: Applications to Simple Fluids, Ab Initio Potentials, and Fullerenes, *The Journal of Chemical Physics*, 2006, **124**, 154505, DOI: 10.1063/1.2181979.

[181] The Numerical Algorithms Group (NAG), *The NAG Fortran Library Mark 22*, Oxford, United Kingdom, www.nag.com, 2013.

[182] T. N. L. Patterson, The optimum addition of points to quadrature formulae, *Mathematics of Computation*, 1968, **22**, 847–856.

[183] W. Press, S. Teukolsky, W. Vetterling and B. Flannery, *Numerical Recipes in Fortran 90 Version 2.10*, Cambridge University Press, 2001.

[184] S. Dufal, V. Papaioannou, M. Sadeqzadeh, T. Pogiatzis, A. Chremos, C. S. Adjiman, G. Jackson and A. Galindo, Prediction of Thermodynamic Properties and Phase Behavior of Fluids and Mixtures with the SAFT-γ Mie Group-Contribution Equation of State, *Journal of Chemical & Engineering Data*, 2014, **59**, 3272–3288, DOI: 10.1021/je500248h.

[185] G. Jackson, E. Müller and S. Dufal, *private communication*, 2014.

[186] Y. Peng, K. D. Goff, M. C. dos Ramos and C. McCabe, Developing a Predictive Group-Contribution-Based SAFT-VR Equation of State, *Fluid Phase Equilibria*, 2009, **277**, 131–144, DOI: 10.1016/j.fluid.2008.11.008.

[187] B. Fornberg, Generation of Finite Difference Formulas on Arbitrarily Spaced Grids, *Mathematics of Computation*, 1988, **51**, 699–699, DOI: 10.1090/S0025-5718-1988-0935077-0.

[188] H. Tetrode, Die chemische Konstante der Gase und das elementare Wirkungsquantum, *Annalen der Physik*, 1912, **343**, 434–442, DOI: 10.1002/andp.19123430708.

[189] H. Tetrode, Berichtigung zu meiner Arbeit: „Die chemische Konstante der Gase und das elementare Wirkungsquantum", *Annalen der Physik*, 1912, **344**, 255–256, DOI: 10.1002/andp.19123441112.

[190] O. Sackur, Die Anwendung der kinetischen Theorie der Gase auf chemische Probleme, *Annalen der Physik*, 1911, **341**, 958–980, DOI: 10.1002/andp.19113411505.

[191] O. Sackur, Die Bedeutung Des Elementaren Wirkungsquantums Für Die Gastheorie Und Die Berechnung Der Chemischen Konstanten, *Nernst Festschrift*, 1912, 405–423.

[192] O. Sackur, Die universelle Bedeutung des sog. elementaren Wirkungsquantums, *Annalen der Physik*, 1913, **345**, 67–86, DOI: 10.1002/andp.19133450103.

[193] K. Rajendran and R. Ravi, Critical Analysis of Maxwell's Equal Area Rule: Implications for Phase Equilibrium Calculations, *Industrial & Engineering Chemistry Research*, 2010, **49**, 7687–7692, DOI: 10.1021/ie100571m.

[194] T. Jindrová and J. Mikyška, Fast and Robust Algorithm for Calculation of Two-Phase Equilibria at given Volume, Temperature, and Moles, *Fluid Phase Equilibria*, 2013, **353**, 101–114, DOI: 10.1016/j.fluid.2013.05.036.

[195] F. E. Pereira, G. Jackson, A. Galindo and C. S. Adjiman, The HELD Algorithm for Multicomponent, Multiphase Equilibrium Calculations with Generic Equations of State, *Computers & Chemical Engineering*, 2012, **36**, 99–118, DOI: 10.1016/j.compchemeng.2011.07.009.

[196] C. G. Broyden, The Convergence of a Class of Double-Rank Minimization Algorithms 1. General Considerations, *IMA Journal of Applied Mathematics*, 1970, **6**, 76–90, DOI: 10.1093/imamat/6.1.76.

[197] R. Fletcher, A New Approach to Variable Metric Algorithms, *The Computer Journal*, 1970, **13**, 317–322, DOI: 10.1093/comjnl/13.3.317.

[198] D. Goldfarb, A Family of Variable-Metric Methods Derived by Variational Means, *Mathematics of Computation*, 1970, **24**, 23–26, DOI: 10.1090/S0025-5718-1970-0258249-6.

[199] D. F. Shanno, Conditioning of Quasi-Newton Methods for Function Minimization, *Mathematics of Computation*, 1970, **24**, 647–656, DOI: 10.1090/S0025-5718-1970-0274029-X.

[200] W. R. Mebane and J. S. Sekhon, Genetic Optimization Using Derivatives: The **Rgenoud** Package for *R*, *Journal of Statistical Software*, 2011, **42**, year, DOI: 10.18637/jss.v042.i11.

[201] J. A. Nelder and R. Mead, A Simplex Method for Function Minimization, *The Computer Journal*, 1965, **7**, 308–313, DOI: 10.1093/comjnl/7.4.308.

[202] D. van der Spoel, E. Lindahl, B. Hess, A. R. van Buuren, P. J. M. E. Apol, D. P. Tieleman, A. L. T. M. Sijbers, K. A. Feenstra, R. van Drunen and H. J. C. Berendsen, *Gromacs User Manual version 4.5.6*, `www.gromacs.org`, (2010).

[203] gSAFT Advanced Thermodynamics, https://www.psenterprise.com/products/gsaft/, 2017.

[204] E. F. D. Sabattié, J. Tasche, M. R. Wilson, M. W. A. Skoda, A. Hughes, T. Lindner and R. L. Thompson, Predicting Oligomer/Polymer Compatibility and the Impact on Nanoscale Segregation in Thin Films, *Soft Matter*, 2017, DOI: 10.1039/C7SM00048K.

[205] T. Mansfield, *unpublished results*, 2015.

[206] M. Hamm and T. Mansfield, *unpublished results*, 2014.

[207] DECHEMA e.V. DETHERM, *Thermophysical Properties of Pure Substances & Mixtures.*, 2005-2017, accessed 2015, http://i-systems.dechema.de/detherm/.

[208] C. Herdes, E. E. Santiso, C. James, J. Eastoe and E. A. Müller, Modelling the Interfacial Behaviour of Dilute Light-Switching Surfactant Solutions, *Journal of Colloid and Interface Science*, 2015, **445**, 16–23, DOI: 10.1016/j.jcis.2014.12.040.

[209] R. P. White and J. E. G. Lipson, Chain Fluids: Contrasts of Theoretical and Simulation Approaches, and Comparison with Experimental Alkane Properties, *The Journal of Chemical Physics*, 2009, **131**, 074109, DOI: 10.1063/1.3200925.

[210] R. P. White, J. E. G. Lipson and J. S. Higgins, How Pure Components Control Polymer Blend Miscibility, *Macromolecules*, 2012, **45**, 8861–8871, DOI: 10.1021/ma3018124.

[211] R. P. White, J. E. G. Lipson and J. S. Higgins, New Correlations in Polymer Blend Miscibility, *Macromolecules*, 2012, **45**, 1076–1084, DOI: 10.1021/ma202393f.

[212] *Polymer Handbook*, ed. J. Brandrup, E. H. Immergut and E. A. Grulke, Wiley, New York, 4th edn., 1999, vol. 1, chap. IV.

[213] *Polymer Handbook*, ed. J. Brandrup, E. H. Immergut and E. A. Grulke, Wiley, New York, 4th edn., 1999, vol. 1, chap. V.

[214] *Polymer Handbook*, ed. J. Brandrup, E. H. Immergut and E. A. Grulke, Wiley, New York, 4th edn., 1999, vol. 2.

[215] D. Bamborough and C. Donker, *The Chemistry of Tackifying Resins, 2002/2003*, http://www.specialchem4adhesives.com, (accessed 08/2012).

[216] Eastman Chemical Company, *Eastman's spectrum of hydrocarbon resins, 2004*, http://www.eastman.com/literature_center/w/WA86.pdf, (accessed 06/2014).

[217] J. Dudowicz and K. F. Freed, Relation of Effective Interaction Parameters for Binary Blends and Diblock Copolymers: Lattice Cluster Theory Predictions and Comparisons with Experiment, *Macromolecules*, 1993, **26**, 213–220, DOI: 10.1021/ma00053a033.

[218] W. W. Maurer, F. S. Bates, T. P. Lodge, K. Almdal, K. Mortensen and G. H. Fredrickson, Can a Single Function for χ Account for Block Copolymer and Homopolymer Blend Phase Behavior?, *The Journal of Chemical Physics*, 1998, **108**, 2989–3000, DOI: 10.1063/1.475704.

[219] R. E. Cohen and A. R. Ramos, Homogeneous and Heterogeneous Blends of Polybutadiene, Polyisoprene, and Corresponding Diblock Copolymers, *Macromolecules*, 1979, **12**, 131–134, DOI: 10.1021/ma60067a027.

[220] R. Krishnamoorti, W. W. Graessley, L. J. Fetters, R. T. Garner and D. J. Lohse, Anomalous Mixing Behavior of Polyisobutylene with Other Polyolefins, *Macromolecules*, 1995, **28**, 1252–1259, DOI: 10.1021/ma00108a064.

[221] R. Krishnamoorti, W. W. Graessley, N. P. Balsara and D. J. Lohse, Structural Origin of Thermodynamic Interactions in Blends of Saturated Hydrocarbon Polymers, *Macromolecules*, 1994, **27**, 3073–3081, DOI: 10.1021/ma00089a026.

[222] R. Krishnamoorti, W. W. Graessley, G. T. Dee, D. J. Walsh, L. J. Fetters and D. J. Lohse, Pure Component Properties and Mixing Behavior in Polyolefin Blends, *Macromolecules*, 1996, **29**, 367–376, DOI: 10.1021/ma950754b.

[223] W. W. Graessley, R. Krishnamoorti, N. P. Balsara, L. J. Fetters, D. J. Lohse, D. N. Schulz and J. A. Sissano, Deuteration Effects and Solubil-

ity Parameter Ordering in Blends of Saturated Hydrocarbon Polymers, *Macromolecules*, 1994, **27**, 2574–2579, DOI: 10.1021/ma00087a028.

[224] R. Krishnamoorti, W. W. Graessley, N. P. Balsara and D. J. Lohse, The Compositional Dependence of Thermodynamic Interactions in Blends of Model Polyolefins, *The Journal of Chemical Physics*, 1994, **100**, 3894–3904, DOI: 10.1063/1.466324.

[225] N. P. Balsara, L. J. Fetters, N. Hadjichristidis, D. J. Lohse, C. C. Han, W. W. Graessley and R. Krishnamoorti, Thermodynamic Interactions in Model Polyolefin Blends Obtained by Small-Angle Neutron Scattering, *Macromolecules*, 1992, **25**, 6137–6147, DOI: 10.1021/ma00049a009.

[226] N. P. Balsara, D. J. Lohse, W. W. Graessley and R. Krishnamoorti, Small-angle Neutron Scattering by Partially Deuterated Polymers and Their Blends, *The Journal of Chemical Physics*, 1994, **100**, 3905–3910, DOI: 10.1063/1.466325.

[227] P. A. Rodgers, Pressure–volume–temperature Relationships for Polymeric Liquids: A Review of Equations of State and Their Characteristic Parameters for 56 Polymers, *Journal of Applied Polymer Science*, 1993, **48**, 1061–1080, DOI: 10.1002/app.1993.070480613.

[228] P. Zoller and D. J. Walsh, *Standard Pressure-Volume-Temperature Data for Polymers*, Technomic Pub. Co, Lancaster, PA, 1995.

[229] B. Rudolf, J. Kressler, K. Shimomai, T. Ougizawa and T. Inoue, Evaluation of Equation-of-State Parameters from PVT Data, *Acta Polymerica*, 1995, **46**, 312–318, DOI: 10.1002/actp.1995.010460405.

[230] S. Rostami and D. J. Walsh, Simulation of Upper and Lower Critical Phase Diagrams for Polymer Mixtures at Various Pressures, *Macromolecules*, 1985, **18**, 1228–1235, DOI: 10.1021/ma00148a032.

[231] U. Gaur and B. Wunderlich, Heat Capacity and Other Thermodynamic Properties of Linear Macromolecules. V. Polystyrene, *Journal*

of Physical and Chemical Reference Data, 1982, **11**, 313–325, DOI: 10.1063/1.555663.

[232] R. Koningsveld, W. H. Stockmayer and E. Nies, *Polymer Phase Diagrams: A Textbook*, Oxford University Press, Oxford ; New York, 2001.

[233] J. S. Higgins, J. E. G. Lipson and R. P. White, A Simple Approach to Polymer Mixture Miscibility, *Philosophical Transactions of the Royal Society A: Mathematical, Physical and Engineering Sciences*, 2010, **368**, 1009–1025, DOI: 10.1098/rsta.2009.0215.

[234] J. L. Lin, D. Rigby and R. J. Roe, Deuterium Isotope Effect on the Compatibility between Polystyrene and Polybutadiene, *Macromolecules*, 1985, **18**, 1609–1611, DOI: 10.1021/ma00150a015.

[235] P. E. Tomlins and J. S. Higgins, Late Stage Spinodal Decomposition in an Oligomeric Blend of Polystyrene/Polybutadiene: A Test of the Scaling Law for the Structure Function, *The Journal of Chemical Physics*, 1989, **90**, 6691–6700, DOI: 10.1063/1.456288.

[236] Y. X. Yi and P. Zoller, An Experimental and Theoretical Study of the PVT Equation of State of Butadiene and Isoprene Elastomers to 200°C and 200 MPa, *Journal of Polymer Science Part B: Polymer Physics*, 1993, **31**, 779–788, DOI: 10.1002/polb.1993.090310705.

[237] J. W. Barlow, Measurement of the PVT Behavior of Cis-1,4-Polybutadiene, *Polymer Engineering & Science*, 1978, **18**, 238–245, DOI: 10.1002/pen.760180311.

[238] S. Kawahara and S. Akiyama, Volume Contraction on Mixing in Poly(Vinyl Ethylene-Co-1,4-Butadiene)/Polyisoprene Blends, *Polymer Journal*, 1991, **23**, 7–14, DOI: 10.1295/polymj.23.7.

[239] D. Schwahn and L. Willner, Phase Behavior and Flory-Huggins Interaction Parameter of Binary Polybutadiene Copolymer Mixtures with Different Vinyl Content and Molar Volume, *Macromolecules*, 2002, **35**, 239–247, DOI: 10.1021/ma010379p.

[240] U. Gaur, B. B. Wunderlich and B. Wunderlich, Heat Capacity and Other Thermodynamic Properties of Linear Macromolecules. VII. Other Carbon Backbone Polymers, *Journal of Physical and Chemical Reference Data*, 1983, **12**, 29–63, DOI: 10.1063/1.555677.

[241] B. Rudolf and H.-J. Cantow, Description of Phase Behavior of Polymer Blends by Different Equation-of-State Theories. 1. Phase Diagrams and Thermodynamic Reasons for Mixing and Demixing, *Macromolecules*, 1995, **28**, 6586–6594, DOI: 10.1021/ma00123a028.

[242] B. Rudolf, Temperature Dependence of the χ-Parameter between Polystyrene and Polyisoprene, *Macromolecular Chemistry and Physics*, 1995, **196**, 4057–4068, DOI: 10.1002/macp.1995.021961215.

[243] C. A. Trask and C. M. Roland, Lower Critical Solution Temperatures in the Absence of Specific Interactions, *Polymer communications*, 1988, **29**, 332–334.

[244] H. Hasegawa, S. Sakurai, M. Takenaka, T. Hashimoto and C. C. Han, Small-Angle Neutron Scattering and Light Scattering Studies on the Miscibility of Protonated Polyisoprene/Deuterated Polybutadiene Blends, *Macromolecules*, 1991, **24**, 1813–1819, DOI: 10.1021/ma00008a019.

[245] H. Grüll, L. Sung, A. Karim, J. F. Douglas, S. K. Satija, M. Hayashi, H. Jinnai, T. Hashimoto and C. C. Han, Finite-Size Effects on Surface Segregation in Polymer Blend Films above and below the Critical Point of Phase Separation, *Europhysics Letters (EPL)*, 2004, **65**, 671–677, DOI: 10.1209/epl/i2003-10176-1.

[246] D. W. Tomlin and C. M. Roland, Negative Excess Enthalpy in a van Der Waals Polymer Mixture, *Macromolecules*, 1992, **25**, 2994–2996, DOI: 10.1021/ma00037a033.

[247] S. Kawahara and S. Akiyama, UCST Phase Behavior and the Miscibility Valley in Blends of Poly(Vinyl Ethylene-Co-1,4-Butadiene) and

Hydrogenated Terpene Resin, *Macromolecules*, 1993, **26**, 2428–2432, DOI: 10.1021/ma00062a006.

[248] A. Cumming, P. Wiltzius and F. S. Bates, Nucleation and Growth of Monodisperse Droplets in a Binary-Fluid System, *Physical Review Letters*, 1990, **65**, 863–866, DOI: 10.1103/PhysRevLett.65.863.

[249] O. Fandiño, A. S. Pensado, L. Lugo, M. J. P. Comuñas and J. Fernández, Compressed Liquid Densities of Squalane and Pentaerythritol Tetra(2-Ethylhexanoate), *Journal of Chemical & Engineering Data*, 2005, **50**, 939–946, DOI: 10.1021/je049580w.

[250] S.-J. Chen, Y. C. Chiew, J. A. Gardecki, S. Nilsen and M. Radosz, P-V-T Properties of Alternating Poly(Ethylene-Propylene) Liquids, *Journal of Polymer Science Part B: Polymer Physics*, 1994, **32**, 1791–1798, DOI: 10.1002/polb.1994.090321012.

[251] S. J. Han, C. J. Gregg and M. Radosz, How the Solute Polydispersity Affects the Cloud-Point and Coexistence Pressures in Propylene and Ethylene Solutions of Alternating Poly (Ethylene-Co-Propylene), *Industrial & engineering chemistry research*, 1997, **36**, 5520–5525.

[252] A. R. Imre, W. A. V. Hook, B. H. Chang and Y. C. Bae, The Effect of Alkane Chain Length on the Liquid–Liquid Critical Temperatures of Oligostyrene/Linear-Alkane Mixtures, *Monatshefte für Chemie / Chemical Monthly*, 2003, **134**, 1529–1539, DOI: 10.1007/s00706-003-0077-2.

[253] F. S. Bates, M. F. Schulz, J. H. Rosedale and K. Almdal, Correlation of Binary Polyolefin Phase Behavior with Statistical Segment Length Asymmetry, *Macromolecules*, 1992, **25**, 5547–5550, DOI: 10.1021/ma00046a070.

[254] U. Gaur and B. Wunderlich, Heat Capacity and Other Thermodynamic Properties of Linear Macromolecules. II. Polyethylene, *Journal of Physical and Chemical Reference Data*, 1981, **10**, 119–152, DOI: 10.1063/1.555636.

[255] U. Gaur and B. Wunderlich, Heat Capacity and Other Thermodynamic Properties of Linear Macromolecules. IV. Polypropylene, *Journal of Physical and Chemical Reference Data*, 1981, **10**, 1051–1064, DOI: 10.1063/1.555650.

[256] E. W. Cochran and F. S. Bates, Thermodynamic Behavior of Poly(Cyclohexylethylene) in Polyolefin Diblock Copolymers, *Macromolecules*, 2002, **35**, 7368–7374, DOI: 10.1021/ma020227+.

[257] J. K. Kim, D. Y. Ryu and K.-H. Lee, The Aromatic Hydrocarbon Resins with Various Hydrogenation Degrees Part 1. The Phase Behavior and Miscibility with Polybutadiene and with Polystyrene, *Polymer*, 2000, **41**, 5195–5205, DOI: 10.1016/S0032-3861(99)00614-X.

[258] M. Antonietti, S. Lang and H. Sillescu, Miscibility Behaviour of Polystyrene and Polystyrene Derivatives, *Die Makromolekulare Chemie, Rapid Communications*, 1986, **7**, 415–419, DOI: 10.1002/marc.1986.030070616.

[259] G. Jiménez-Serratos, C. Herdes, A. J. Haslam, G. Jackson and E. A. Müller, Group Contribution Coarse-Grained Molecular Simulations of Polystyrene Melts and Polystyrene Solutions in Alkanes Using the SAFT-γ Force Field, *Macromolecules*, 2017, DOI: 10.1021/acs.macromol.6b02072.

[260] A. Ervik, A. Mejía and E. A. Müller, Bottled SAFT: A Web App Providing SAFT-γ Mie Force Field Parameters for Thousands of Molecular Fluids, *Journal of Chemical Information and Modeling*, 2016, **56**, 1609–1614, DOI: 10.1021/acs.jcim.6b00149.

[261] P. Linstrom, W. Mallard and Eds., *NIST Chemistry WebBook, NIST Standard Reference Database Number 69, National Institute of Standards and Technology, Gaithersburg MD, 20899*, `http://webbook.nist.gov`, (accessed 6/2014).

[262] M. Hamm, *unpublished results*, 2016.

[263] A. J. A. Van Der Wyk, Viscosity of Binary Mixtures, *Nature*, 1936, **138**, 845–846, DOI: 10.1038/138845b0.

[264] *Viscosity of Liquids: Theory, Estimation, Experiment, and Data*, ed. D. S. Viswanath, Springer, Dordrecht, 2007.

[265] M. Trusler, *The Speed of Sound and Derived Thermodynamic Properties of Compressed Liquids, 2007*, http://www3.imperial.ac.uk/pls/portallive/docs/1/40167704.PDF, (accessed 05/2014).

[266] M. Trusler, *private communication*, 2014.

[267] A. J. Haslam, A. Galindo and G. Jackson, Prediction of Binary Intermolecular Potential Parameters for Use in Modelling Fluid Mixtures, *Fluid Phase Equilibria*, 2008, **266**, 105–128, DOI: 10.1016/j.fluid.2008.02.004.

[268] S. Kawahara, Y. Asada, Y. Isono, K. Muraoka and Y. Minagawa, Lower Critical Solution Temperature Phase Behavior of Natural Rubber/Polybutadiene Blend, *Polymer Journal*, 2002, **34**, 1–8, DOI: 10.1295/polymj.34.1.

[269] S. Kawahara, K. Sato and S. Akiyama, Negative Excess Volume of Mixing in Polybutadiene/Polyisoprene Blends, *Journal of Polymer Science Part B: Polymer Physics*, 1994, **32**, 15–20, DOI: 10.1002/polb.1994.090320103.

[270] S. Kawahara and S. Akiyama, in *Advances in Polymer Blends and Alloys Technology. Vol. 5*, ed. K. Finlayson, Technomic Publ. Co, Lancaster, Pa., 1994, p. chap. 9.

[271] S. Kawahara and S. Akiyama, Thermal Reversibility in Liquid–Liquid Phase Transition in Poly (Vinyl Ethylene-Co-1, 4-Butadiene)/Polyisoprene Blends, *Polymer Journal*, 1990, **22**, 361–368.

[272] S. Kawahara, S. Akiyama and A. Ueda, Miscibility and LCST Behavior of Polyisoprene/Poly (Cis-Butadiene-Co-1, 2-Vinylbutadiene), *Polymer journal*, 1989, **21**, 22lf229.

[273] E. F. D. Sabattié, *Ph.D. thesis*, Durham University, 2017.

[274] P. Morgado, O. Lobanova, E. A. Müller, G. Jackson, M. Almeida and E. J. M. Filipe, SAFT-γ Force Field for the Simulation of Molecular Fluids: 8. Hetero-Segmented Coarse-Grained Models of Perfluoroalkylalkanes Assessed with New Vapour–liquid Interfacial Tension Data, *Molecular Physics*, 2016, **114**, 2597–2614, DOI: 10.1080/00268976.2016.1218077.

[275] B. Hess, C. Kutzner, D. van der Spoel and E. Lindahl, GROMACS 4: Algorithms for Highly Efficient, Load-Balanced, and Scalable Molecular Simulation, *Journal of Chemical Theory and Computation*, 2008, **4**, 435–447, DOI: 10.1021/ct700301q.

[276] S. Pronk, S. Páll, R. Schulz, P. Larsson, P. Bjelkmar, R. Apostolov, M. R. Shirts, J. C. Smith, P. M. Kasson, D. van der Spoel, B. Hess and E. Lindahl, GROMACS 4.5: A High-Throughput and Highly Parallel Open Source Molecular Simulation Toolkit, *Bioinformatics*, 2013, **29**, 845–854, DOI: 10.1093/bioinformatics/btt055.

[277] W. Humphrey, A. Dalke and K. Schulten, VMD – Visual Molecular Dynamics, *Journal of Molecular Graphics*, 1996, **14**, 33–38.

[278] J. Stone, *M.Sc. thesis*, Computer Science Department, University of Missouri-Rolla, 1998.

[279] M. G. Martin and J. I. Siepmann, Transferable Potentials for Phase Equilibria. 1. United-Atom Description of n-Alkanes, *The Journal of Physical Chemistry B*, 1998, **102**, 2569–2577, DOI: 10.1021/jp972543+.

[280] M. T. Degiacomi, V. Erastova and M. R. Wilson, Easy Creation of Polymeric Systems for Molecular Dynamics with Assemble!, *Computer Physics Communications*, 2016, **202**, 304–309, DOI: 10.1016/j.cpc.2015.12.026.

[281] Q. Sun and R. Faller, Systematic Coarse-Graining of a Polymer Blend: Polyisoprene and Polystyrene, *Journal of Chemical Theory and Computation*, 2006, **2**, 607–615, DOI: 10.1021/ct600065v.

[282] Q. Sun and R. Faller, Phase Separation in Polyisoprene/Polystyrene Blends by a Systematically Coarse-Grained Model, *The Journal of Chemical Physics*, 2007, **126**, 144908, DOI: 10.1063/1.2715588.

[283] J. G. Solano Canchaya, A. Dequidt, F. Goujon and P. Malfreyt, Development of DPD Coarse-Grained Models: From Bulk to Interfacial Properties, *The Journal of Chemical Physics*, 2016, **145**, 054107, DOI: 10.1063/1.4960114.

[284] A. Dequidt and J. G. Solano Canchaya, Bayesian Parametrization of Coarse-Grain Dissipative Dynamics Models, *The Journal of Chemical Physics*, 2015, **143**, 084122, DOI: 10.1063/1.4929557.

[285] M. G. Martin and J. I. Siepmann, Novel Configurational-Bias Monte Carlo Method for Branched Molecules. Transferable Potentials for Phase Equilibria. 2. United-Atom Description of Branched Alkanes, *The Journal of Physical Chemistry B*, 1999, **103**, 4508–4517, DOI: 10.1021/jp984742e.

[286] C. D. Wick, M. G. Martin and J. I. Siepmann, Transferable Potentials for Phase Equilibria. 4. United-Atom Description of Linear and Branched Alkenes and Alkylbenzenes, *The Journal of Physical Chemistry B*, 2000, **104**, 8008–8016, DOI: 10.1021/jp001044x.

[287] T. van Westen, T. J. H. Vlugt and J. Gross, On the Vapor-Liquid Equilibrium of Attractive Chain Fluids with Variable Degree of Molecular Flexibility, *The Journal of Chemical Physics*, 2015, **142**, 224504, DOI: 10.1063/1.4922264.

[288] K. Choi and W. H. Jo, Effect of Chain Flexibility on Selectivity in the Gas Separation Process: Molecular Dynamics Simulation, *Macromolecules*, 1995, **28**, 8598–8603, DOI: 10.1021/ma00129a019.

[289] H. S. Ashbaugh, H. A. Patel, S. K. Kumar and S. Garde, Mesoscale Model of Polymer Melt Structure: Self-Consistent Mapping of Molecular Correlations to Coarse-Grained Potentials, *The Journal of Chemical Physics*, 2005, **122**, 104908, DOI: 10.1063/1.1861455.

[290] S. O. Nielsen, C. F. Lopez, G. Srinivas and M. L. Klein, A Coarse Grain Model for N-Alkanes Parameterized from Surface Tension Data, *The Journal of Chemical Physics*, 2003, **119**, 7043, DOI: 10.1063/1.1607955.

[291] R. Faller, Automatic Coarse Graining of Polymers, *Polymer*, 2004, **45**, 3869–3876, DOI: 10.1016/j.polymer.2003.11.053.

[292] R. Faller, F. Müller-Plathe, M. Doxastakis and D. Theodorou, Local Structure and Dynamics of *Trans* -Polyisoprene Oligomers, *Macromolecules*, 2001, **34**, 1436–1448, DOI: 10.1021/ma0016782.

[293] R. Faller and D. Reith, Properties of Poly(Isoprene): Model Building in the Melt and in Solution, *Macromolecules*, 2003, **36**, 5406–5414, DOI: 10.1021/ma025877s.

[294] P. Gao and H. Guo, Developing Coarse-Grained Potentials for the Prediction of Multi-Properties of Trans-1,4-Polybutadiene Melt, *Polymer*, 2015, **69**, 25–38, DOI: 10.1016/j.polymer.2015.05.023.

[295] G. Milano and F. Müller-Plathe, Mapping Atomistic Simulations to Mesoscopic Models: A Systematic Coarse-Graining Procedure for Vinyl Polymer Chains, *The Journal of Physical Chemistry B*, 2005, **109**, 18609–18619, DOI: 10.1021/jp0523571.

[296] Q. Sun and R. Faller, Systematic Coarse-Graining of Atomistic Models for Simulation of Polymeric Systems, *Computers & Chemical Engineering*, 2005, **29**, 2380–2385, DOI: 10.1016/j.compchemeng.2005.05.026.

[297] E. Brini, C. R. Herbers, G. Deichmann and N. F. A. van der Vegt, Thermodynamic Transferability of Coarse-Grained Potentials for Poly-

mer–additive Systems, *Physical Chemistry Chemical Physics*, 2012, **14**, 11896, DOI: 10.1039/c2cp40735c.

[298] D. Fritz, V. A. Harmandaris, K. Kremer and N. F. A. van der Vegt, Coarse-Grained Polymer Melts Based on Isolated Atomistic Chains: Simulation of Polystyrene of Different Tacticities, *Macromolecules*, 2009, **42**, 7579–7588, DOI: 10.1021/ma901242h.